Author:
Wang, Jian-nong

Title:
Cathodoluminescence and transmission electron microscopy characterization of GaAs/A1GaAs and InGaAS/InP quantum well structures.

Cathodoluminescence and Transmission Electron Microscopy Characterization of GaAs/AlGaAs and InGaAs/InP Quantum Well Structures

Jian-nong Wang, M.Sc

H.H.Wills Physics Laboratory

University of Bristol

A thesis submitted in partial fulfilment of the requirement for admission to the degree of Doctor of Philosophy of the University of Bristol

February 1990

MEMORANDUM

This thesis is submitted to the University of Bristol in support of an application for admission to the degree of Doctor of Philosophy. The work was carried out by myself between November 1986 and January 1990 under the supervision of Professor J.W.Steeds. No part of this thesis has previously been submitted to this or any other University for the award of a degree.

J.N.Wang

王建农 Jianong Wang

February 1990

ACKNOWLEDGEMENT

I should like to thank my supervisor, Professor J.W.Steeds, for his constant encouragement and never-ending supply of suggestions through out this project, especially for his patient corrections of this manuscript. Many members of the Bristol Microstructural Analysis Group (or Electron Microscopy Group), past and present, have contributed to this work through sharing of expertise and discussions. However, special thanks must go to a lot people: to Dr.A.R.Preston for his constant help and discussions in all aspects; to Dr.Y.P.Lin for introducing me to getting around in this laboratory and teaching me to perform CBED and LACBED work; to Dr.S.J.Bailey for sharing his expertise on using TEM-CL system and selective etching specimen preparation; to Dr.J.C.C.Day for his carefully looking after the CL system and setting-up a temporary PL system; to Dr.R.Vincent for his helpful discussions of diffraction work and excellent maintenance of EM430 and EM400 microscopes and to Mr.A.B.Kendrick, Miss.F.Johnson, Mr.P.Spellward and Mr.S.Diamond for their friendly help in various occasions.

I should like to extend my thanks to AT&T Bell Laboratory, the Physics Dept. of Nottingham University, RSRE, Plessey Research Ltd. and E.E.E. Dept. of Glasgow University for supplying samples.

The financial support of the Academy of Science of China during the period from Oct.1986 to Oct.1989 and the financial support of Prof.J.W.Steeds (Nov.1989-Jan.1990) are gratefully acknowledged.

ABSTRACT

Transmission electron microscopy, cathodoluminescence and photoluminescence spectroscopy and TEM-CL imaging technique have been employed in this work in order to investigate the microstructure and optical properties of GaAs/AlGaAs and InGaAs/InP multilayer structures.

LACBED patterns, obtained from plan view specimens of the GaAs/AlGaAs and InGaAs/InP multiple quantum well structures, were explained qualitatively by a kinematic theory. A linear contrast feature was observed in a GaAs/AlGaAs multiple quantum well structure along one in-plane [110] direction in dark field image formed by multilayer structure reflections and was related to the fluctuations of the quantum well thickness.

By applying LACBED to [001] and [011] cross-section specimens of an InGaAs/InP single QW structure, residual misfit strain in the quantum well was measured based on a tetragonal distortion model. This misfit strain was also illustrated in a diffraction contrast analysis of the interface fringes observed from inclined interfaces of the structure.

A degradation of CL spectra, induced in long period air exposure and in the specimen preparation process, was observed from a GaAs/AlGaAs MQW structure. TEM-CL spectra and images were first obtained from thin cross-section specimens of the structure and revealed an uneven distribution of impurities in the structure. Carrier capture and confinement effects in the QW structures were studied by the dependence of CL spectra on the barrier layer thickness and quantum well width.

Interface smoothing effect due to growth interruption was investigated by CL spectroscopy from a series MBE grown GaAs/AlGaAs SQW samples. High resolution TEM-CL images were obtained from a SQW structure grown

with interruptions and showed local bright and dark contrast resulting from monolayer changes in the thickness of the QW. We also noted a decreasing Stokes shift of the QW luminescence as a result of growth interruption in a temperature dependent PL experiment.

Impurity distributions were investigated around a particular type of oval defect in a GaAs/AlGaAs SQW structure by TEM and TEM-CL.

The characterisation of free-standing quantum dots was carried out by applying the STEM-CL spectroscopy and imaging technique.

CONTENTS

Chapter 1 Introduction and Experimental Principles

1-1 Introduction

The advancement of modern growth techniques, such as molecular beam epitaxy (MBE) and metal organic chemical vapour deposition (MOCVD), opened the way to the growth of semiconductors atomic layer upon atomic layer. As a result, a new class of artificial layer materials, called semiconductor quantum wells (QW's) or superlattices, with unique electronic and optical properties emerged and have attracted the attention for both basic physics research and also for exploiting new or high performance devices. The most common QW structure is of undoped, lattice matched layers which consist of alternating layers with different composition. Modulation doped QWs are prepared by selective doping of certain layers in an otherwise undoped QW structures. Strain layer superlattices are formed by alternating layers with both different composition and lattice constant, where the mismatch strain is accommodated by the crystal lattice relaxation, rather then by nucleation of misfit dislocations. There are many potential devices which are based on the quasi-two dimensional carrier motion in QW structures, charge transfer in modulation doped QW structures and the tunnelling effect in superlattice structures. These include QW lasers, high electron mobility

transistors (HEMT), two-dimensional electron gas FETs (TEGFETs) and negative differential resistance (NDR) tunnelling diodes (W.T.Tsang 1987; M.Abe 1987; N.T.Linh 1987; T.C.L.G.Sollner 1983). Motivated by the device applications and seeking a good understanding of basic physics of the structures, studies of the electronic, optical and electrical properties of QW structures there has been a dramatic increase of both theoretical and experimental investigation of quantum wells during last decade. The early interests in QW structures were summarized by Dingle (R.Dingle 1975). The recent progress has been reviewed by Weisbuch, Bastard and Ploog (C.Weisbuch 1987; G.Bastard 1988; K.Ploog 1983).

In this work transmission electron microscopy, cathodoluminescence and photoluminescence were employed for investigations of microstructure and optical properties of GaAs/AlGaAs and InGaAs/InP quantum well structures. The radiative transition processes in semiconductor materials, the fundamental properties of semiconductor multilayer structures and cathodoluminescence mechanisms are discussed in this chapter. The experimental techniques and equipment are introduced in the next chapter. Chapter 3, 4 and 5 contain the results obtained and their evaluation. Finally the achievements of this work are summarized in chapter 6.

1-2 Radiative Transitions in Semiconductors

In semiconductors light is emitted as a result of electronic transitions from high energy states to low energy states, while optical absorption corresponds electronic transitions from low energy states to high energy states. Detailed discussions of optical absorption and emission processes in

semiconductors can be found in many semiconductor physics textbooks (J.I.Pankove 1971; S.H.Smith 1978; M.Balkanki 1980)

One unavoidable requirement for light emission at room temperature or lower is that the system must not be in equilibrium, i.e. there must be excess carriers in the system. Recombination of these excess carriers may be accompanied by many types of radiative and non-radiative transitions. In Fig.1-1, the transitions which commonly lead to light emission are numbered 1-5.

Process 1 is a band to band transition, electrons in the conduction band recombine with holes in the valence band. For a direct gap semiconductor, emitted photon energy is $h\nu=E_g$, where E_g is the band gap energy of the semiconductor. For a indirect gap semiconductor, the participation of one or more phonons is necessary in order to conserve momentum in the transition and the emitted photon has energy $h\nu=E_g-n\cdot E_{pn}$ where $n=1,2,\cdots$ and E_{pn} is phonon energy.

Process 2 is an excitonic transition. The Coulombic interaction between a free electron in the conduction band and a free hole in the valence band can result in a series of bound states E_{xn} just below the conduction band called excitons. The ground state ionization energy of an exciton may be obtained by analogy with the hydrogen atom as

$$E_x=\frac{m_r^* q^4}{2\hbar^2\epsilon^2} \qquad 1\text{-}1$$

where m_r^* $(=m_e^* m_h^*/(m_e^*+m_h^*))$ is the reduced mass for exciton, m_e^* is the effective mass of electrons in the conduction band and m_h^* is the effective mass of holes in the valence band, ϵ is the material dielectric constant, q is the

electron charge and h is Planck's constant. Excitonic levels are observable at low temperatures where kT is smaller than exciton ionization energy, k is Boltzmann's constant. Excitonic recombination emission from a free exciton produces a photon with energy $h\nu=E_g-E_x$. In the presence of impurities and defects in a semiconductor, free excitons can be bound by them to form bound excitons. The emission energy of a bound exciton is then equal to $E_g-E_x-E_{xb}$, E_{xb} is the binding energy of a free exciton to the impurity or a defect.

Processes 4 and 3 are transitions which start or finish on localized states of impurities in the energy gap. These include the recombination of electrons at shallow donor levels with holes in the valence band and the recombination of electrons in the conduction band with holes at acceptor levels. The photon energy in these processes is given by E_g-E_D (or E_A), where E_D and E_A are the ionization energies of donors and acceptors respectively. Deep donor and deep acceptor levels can introduce radiative transitions with emitted photon energies well below the energy of the band gap. Apart from the above impurity related transitions, lattice defects introduce localized levels into the band gap which can also be involved in light emission processes.

Process 5 is the recombination between electrons on donor levels and holes on acceptor levels. When donors and acceptors occur in a semiconductor at the same time, they can form pairs due to the Coulombic interaction between them. This interaction also results in a lowering of their ionization energy by an amount ΔE, where

$$\Delta E = \frac{q^2}{\epsilon r} \qquad 1\text{-}2$$

r is the distance between them. So the emitted photon energy becomes $h\nu = E_g - E_D - E_A + \Delta E$

Apart from the phonon assistant transitions in the indirect gap semiconductors, one or more phonon replicas of excitonic emission and impurity related emissions are also observed in some direct gap semiconductors. For those impurity related emissions with large binding energies, phonon replicas are especially strong due to the strong interaction between those impurities and crystal lattice.

It is worth mentioning that it is not always possible to observe all these radiative transitions in one material at the same time and under the same conditions of excitation and temperature. Further these transitions can also be quenched by non-radiative recombination processes such as multiple phonon recombination and Auger electron emission, including defect Auger processes.

1-3 Semiconductor Multilayer Structures

Semiconductor multilayer structures are composed of periodic sequences of ultrathin layers of alternating composition, or of alternating doping, or of the combination of both. In the case of compositional multilayer structures, the materials with different compositions can either be lattice matched to form common multilayer structures, or mismatched to form strain layer superlattices. The band structures of these multilayers are modulated along the direction normal to the layers (often referred to as the z direction), since the band discontinuity or bending occurs at the interfaces of the layers due to the different band gaps of the materials with different compositions, or the different Fermi levels in the materials with different doping types. As a result, the potential wells and barriers are formed along the z direction and

the movement of electrons are modulated in these multilayer structures. The electron movement parallel to the layers is unchanged while the motion along the z direction is confined within the potential wells. A quantum size effect emerges when the widths of the potential wells are comparable to the DeBroglie wavelength of an electron. The quantization creates changes in the macroscopic properties of the layers and produces new effects which are not present in the bulk materials.

1-3-1 Types of Semiconductor Multilayer Structures

Generally speaking, there are three basic types of semiconductor multilayer structures. These are widely referred to as Type-I and Type-II compositional multilayer structures and doping multilayer structures (K.Ploog 1983). Fig.1-2 shows the real space band structures along z direction for these three types of multilayers.

In Type-I multilayer structures, the band structure is modulated such that both electrons in the conduction band and holes in the valence band are confined in the material with smaller energy gap. Both GaAs/AlGaAs and InGaAs/InP systems belong to this type (see Fig.1-2(a)).

The Type-II multilayer structure is shown in Fig.1-2(b) taking the $Ga_xIn_{1-x}As/GaAs_ySb_{1-y}$ multilayer structure as an example. In this case, the electrons in the conduction band and holes in the valence band are confined separately in $Ga_xIn_{1-x}As$ layers and $GaAs_ySb_{1-y}$ layers respectively. The effective energy gap of this system is indirect in real space. In the case of x and y being sufficiently small, the top of valence band of $GaAs_ySb_{1-y}$ is even higher than the bottom of conduction band of $Ga_xIn_{1-x}As$.

Both Type-I and Type-II multilayers shown in the figure are undoped. The doping can be applied to all of the layers or some of the layers of these

multilayer structures. In modulation doped multilayer structures, impurities are deliberately kept away from the quantum wells, where the extrinsic carriers are gathered, in order to improve carrier mobility.

Fig.1-2(c) shows the doping multilayer structure taking GaAs as an example. The carrier confinement is similar to that of the Type-II multilayer structures.

Semiconductor multilayer structures are usually called quantum wells (QWs) when the potential barrier layer thickness is large enough to prevent carriers tunnelling across. When this is not the case the structures are simply called superlattices.

1-3-2 Energy Levels of Quantum Well Structures

The restriction of electronic carrier motion in the z direction can be considered as carrier confining in a one dimensional potential well. For simplicity, considering a one dimensional Type-I single QW structure (see Fig.1-3), a single layer of A is embedded between two thick layers of material B where B has a band gap large than that of A. In the approximation of an infinitely deep well, the carriers are strictly confined to the well. The confining energy E_n is given as (C.Weisbuch 1987)

$$E_n = \frac{\hbar^2}{2m^*}\left(\frac{n\pi}{L_z}\right)^2 \qquad (n=1,2,3,\cdots) \qquad 1\text{-}3$$

where m^* is the carrier effective mass in well material A, L_z is well width.

In reality, the carrier potential wells formed by the band discontinuities are finite. The confining energy E is then determined by the expression (H.Jung 1984)

$$\left(\frac{2m_A^{*}E}{\hbar^2}\right)^{1/2}\tan\left[\left(\frac{2m_A^{*}E}{\hbar^2}\right)^{1/2}\frac{L_z}{2}\right]=\left[\frac{2m_B^{*}(V_o-E)}{\hbar^2}\right]^{1/2} \qquad 1\text{-}4$$

where m_A^{*} and m_B^{*} are the carrier effective mass in material A and B respectively, V_o is the potential barrier height and is V_o^{c} for electrons in the conduction band or V_o^{v} for holes in the valence band (see Fig.1-3). There is always one bound state in the well for electrons or holes. The total number of bound states for electrons or holes is equal to

$$1 + \text{Int.}\left[\left(\frac{2m_A^{*}V_oL_z^{2}}{\pi^2\hbar^2}\right)^{1/2}\right] \qquad 1\text{-}5$$

where Int.[x] indicates the integer part of x.

For electrons in the conduction band, their motion parallel to the layer (in the x, y plane) is unchanged from bulk with $E_{x,y}=\hbar^2k_{x,y}^{2}/2m_A^{*}$. Therefore the electron energy levels in the conduction band can be expressed as $E=E_{x,y}+E_z$ where E_z is determined by Equation 1-4. The discrete values of E_z indicate that a series of two dimensional sub-bands are formed in the QW instead of one continuous band. Similar results are obtained for the heavy holes (hh) and light holes (lh) of the valence band. As a result, the band to band luminescence transition, which is usually between n=1 electrons and n=1 heavy holes, produces photons with energy $h\upsilon=E_g+E_1^{e}+E_1^{hh}$, where E_g is the band gap of material A and E_1^{e}, E_1^{hh} are the confining energies for n=1 electrons and n=1 heavy holes respectively. This QW emission energy is greater than the band gap of bulk material with the quantum well composition and lower than the band gap of bulk material with the barrier composition. The

exact value of the emission energy is controlled by the well width and increases with well width decreases.

1-3-3 Excitons and Shallow Impurities in QW

In the bulk, the exciton states and shallow impurity states in the effective mass approximation resemble hydrogen atoms and have a characteristic radius (Bohr radius) of a_B (C.Weisbuch 1987) where

$$a_B = \epsilon \hbar / (m^* e^2) \approx 100 \text{ Å} \qquad 1\text{-}6$$

m^* is either the reduced mass for the excitons or the effective mass for impurities, ϵ is the dielectric constant. In QW structures, because the well width is usually of the order of or smaller than the Bohr diameter $2a_B$ the wave function and the energy levels of excitons and impurities are modified (C.Weisbuch 1987; R.L.Greene 1984; C.Delalande 1987; B.V.Sharabrook 1987; L.E.Oliveira 1988, 1989).

In Fig.1-4 exciton binding energy as a function of well thickness is shown (R.L.Greene 1984). In the case of excitons in an infinite well, the ground state binding energy increases when the well width L_z decreases and reaches a limited value of $E_x^{2D}=4E_x^{3D}$ when $L_z=0$. In the case of finite well, exciton binding energy increases with the decreasing of L_z until it reaches a maximum and then decreases rapidly as L_z decreases.

In the case of shallow impurities, the problem is somewhat more complicated since the impurity energy levels not only depend on the well width but also on the impurities positions in the well. When $L_z>2a_B$, well centre impurities have enough space to display 1-s bulk-like hydrogenic wave functions. When L_z decreases the impurity binding energy E_b increases because the electron is held close to the impurity centre by QW barrier. As is shown in Fig.1-5 (B.V.Shanabrook 1987), if the barrier is infinitely high,

this increase will last until L_z=0 where a two dimensional binding energy E_b^{2D}=4E_b^{3D} would be attained, and in the case of finite barrier, instead of monotonically increasing with decreasing L_z, E_b reaches a maximum value, then decreases with decreasing L_z. At L_z=0, the binding energy is reached of an impurity in bulk material with barrier composition. Off-centre impurities have qualitatively similar behaviour with L_z variation as well centre impurities the binding energies are lower. At a fixed L_z, the impurity binding energy decreases monotonically with the increasing distance from the centre of the well, as is shown in Fig.1-6 (B.V.Shanabrook 1987).

1-4 Cathodoluminescence

The emission of light from a semiconductor results from electron hole recombination. To excite luminescence, the generation of high concentration excess electron-hole pairs is required. According to the different excitation forms, luminescence is sometimes called electroluminescence (EL) if it is excited by carrier injection at a p-n junction, or photoluminescence (PL) if the electron-hole pairs are produced by optical excitation, or cathodoluminescence (CL) if the electron-hole pairs are generated by energetic electron beam bombardment. For the different excitation forms, the mechanisms leading to the emission of light are similar and their results are broadly compatible.

Interaction of highly energetic electrons with a semiconductor produces many useful signals for material characterization such as backscattered electrons, secondary electrons, x-rays and photons (or CL). The main advantages of CL analysis are its high spatial resolution, its ability to obtain depth resolved information and the possibility to correlate its results with the

information obtained from other analysis available in a electron microscope. The CL analysis can be performed either in a scanning electron microscope (SEM) or a transmission electron microscope (TEM). The SEM-CL study and its application to semiconductors have been thoroughly reviewed by Spivak and Yacobi (G.V.Spivak 1986; B.G.Yacobi 1986). In SEM-CL the collection of emitted light from a sample is more efficient and the sample cooling system is relatively easy to install since there is more space in the SEM chamber, but only a bulk specimen can be used. The advantage of a TEM-CL system is that it can use a thin electron transparent specimen so that the spatial resolution of CL is improved and the direct correlation study of crystal defects with their luminescence properties can be carried out. For thin specimens, the surface recombination effect is much larger than for a bulk specimen and the electron-hole pair generation volume is greatly reduced.

1-4-1 The Formation of CL Signal

The formation of a CL signal is determined by three fundamental processes. These are the generation, diffusion and recombination of electron-hole pairs. In principle all material properties which are related to these processes can be investigated through CL characterization. A general descriptions of these processes can be found in many references (see B.G.Yacobi 1986 and D.B.Holt 1980 for example). Most efforts have been devoted to the CL contrast formation at localized defects (C.Schiller 1975; M.Dupuy 1983; K.Löhnert 1984; A.Jakubowicz 1986) and the determination of semiconductor parameters (W.Hergert 1987, 1984; C.Opdorp 1977) from a semi-infinite (bulk) sample. More recently, the effect of thickness on the CL signal generated in thin film has been discussed by Yuan et.al.(J.Yuan 1989).

For continuous electron beam bombardment of a fixed position, a stationary excess carrier distribution can be reached by the actions of the processes mentioned above. The distribution function of the excess carrier concentration $\Delta n(r)$ can be evaluated from the continuity equation with appropriate boundary conditions,

$$D \nabla^2 \Delta n(r) - \frac{\Delta n(r)}{\tau} + g(r) = 0 \qquad 1\text{-}7$$

τ is the carrier lifetime after taking into account both non-radiative and radiative recombinations, i.e.

$$\frac{1}{\tau} = \frac{1}{\tau_r} + \frac{1}{\tau_n} = \left(\frac{1}{\tau_{r1}} + \frac{1}{\tau_{r2}} + \cdots\right) + \left(\frac{1}{\tau_{n1}} + \frac{1}{\tau_{n2}} + \cdots\right) \qquad 1\text{-}8$$

where τ_r is the total radiative recombination lifetime and τ_n is the total non-radiative recombination lifetime. D is the electron diffusion coefficient or hole diffusion coefficient for doped p-type or n-type materials or is equal to $2D_e \cdot D_h/(D_e+D_h)$ for intrinsic material as given by Leamy (H.J.Leamy 1982). g(r) is the carrier generation function determined by electron beam parameters and the energy dissipation process. The carrier diffusion length L_D is defined as $L_D^2=(D\,\tau)$. According to recombination mechanism, the excess carrier distribution is determined by minority carrier behaviours for the doped materials. The recombination efficiency η_r for a certain radiative transition τ_r is

$$\eta_r = \tau / \tau_r \qquad 1\text{-}9$$

The local intensity of this radiative luminescence I_{CL} can then be written as (D.B.Holt 1980)

$$I_{CL} \propto \Delta n \, \eta_r \qquad 1\text{-}10$$

This is a simplified expression. Many factors such as surface recombination, optical reabsorption inside the material, surface reflection etc. have to be take into account for a truly quantitative analysis. It may be noted that η_r also varies with many factors such as temperature, the presence of lattice defects and impurities, their concentrations and the excess carrier concentration Δn. As a result, the quantitative analysis of CL results is very complicated. Equation 1-9 also indicates that the non-radiative transitions compete with the light emission process so that information about non-radiative recombination processes in the material is very important in determining the CL intensity. Lack of the information about non-radiative recombination in the material under study and lack of an accurate form of generation function for electron-hole pairs further adds to the difficulty of performing quantitative analysis of CL results.

1-4-2 The Spatial Resolution of CL

The spatial resolution of CL is related to three factors; the electron beam probe size d_p, the diameter of the electron-hole pair generation volume d_g, and the carrier diffusion length L_D. The over-all spatial resolution of CL is then given by (S.J.Pennycook 1981)

$$d = (d_p^2 + d_g^2 + L_D^2)^{1/2} \qquad 1\text{-}11$$

For a bulk specimen, the incident electron undergoes a series of elastic and inelastic scattering events before it loses all of its energy. To describe this

process, we suppose that the electrons penetrate to a depth Z_D in the specimen without loss of energy, and then scatter in all direction within a sphere of radius R_e-Z_D, where R_e is the range of the electron penetration. We have (C.Schiller 1975; B.G.Yacobi 1986)

$$Z_D = \frac{4\ R_e}{Z + 4} \qquad 1\text{-}12$$

$$R_e = \frac{0.0276\ A}{\rho\ Z^{0.89}}\ E_b^{1.67} \quad (\mu m) \qquad 1\text{-}13$$

where A is the atomic weight in g/ml, ρ is the density of the material in g/cm^3, Z is the atomic number and E_b is the electron beam energy in keV. For GaAs, we have R_e=2.5μm for E_b=20keV.

In practice the spatial resolution of CL may be determined by one particular factor of these described or by a combination of these factors depending on material under study and the electron beam energy. For a bulk sample it is often given by R_e.

For a thin, electron transparent specimen, the electron beam spreads as it passes through the specimen. The diameter of the electron beam at bottom of a specimen (averaging atomic number Z) with thickness t is given (L.M.Brown 1981; J.I.Goldstein 1977)

$$\phi = 6*10^{-6}\frac{Z\ N^{1/2}\ t^{3/2}}{E_b\ a_0^{3/2}} \quad (\mu m) \qquad 1\text{-}14$$

where N is the number of atoms in a unit cell, a_0 is the lattice parameter of that unit cell and E_b is electron beam energy in keV. For a 2000Å thick GaAs film, if the primary electron beam energy is 120keV, the beam spreading ϕ is about 300Å. The high surface non-radiative recombination velocity of a thin film also reduces the carrier diffusion length to L_D=t/2.2 (S.J.Pennycook 1981). Therefore the spatial resolution of CL can be improved by reducing specimen thickness. However this improvement is accompanied by a reduction in CL intensity which is proportional to t^2. A suitable compromise has to be made in the analysis of TEM-CL

1-4-3 The CL from Multilayer Structures

The discussion given above is based on homogeneous semiconductor specimens. For the semiconductor multilayer structures studied here, the excess carrier distribution will be modified due to the band structure modification of the material. The transfer of excess carriers from the barrier layers to the well layers and the effect of carrier confinement in the well layers lead to a great enhancement of the electron-hole recombination rate in the quantum wells in plan view specimens. The existence of barrier layers reduces the effect of surface recombination on the well emission. The reabsorption effect is also decreased since the wells are usually located within a distance of less than 1μm from the surfaces and the well emission energy is less than the band gap energy of barrier material. The restriction of carrier movement along the z direction also reduces the exciton diffusion coefficient D, following the relation of H.Hillmer (1988)

$$D \propto L_z^{5/2} \qquad 1\text{-}15$$

where L_z is the well width. As a result, the spatial resolution of CL is improved for multilayer structures.

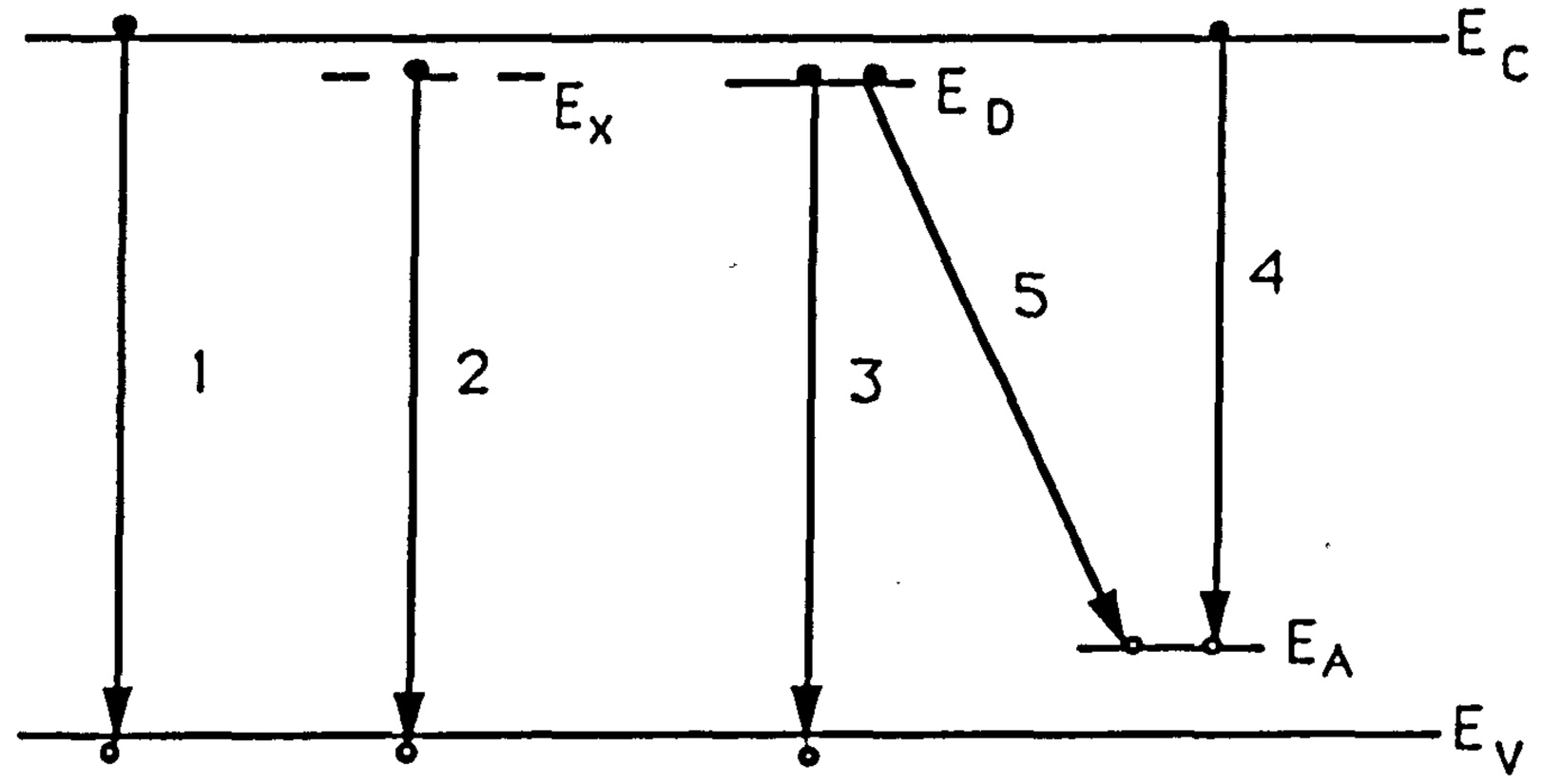

Fig.1-1 Schematic diagram showing the main radiative transition processes in a semiconductor.

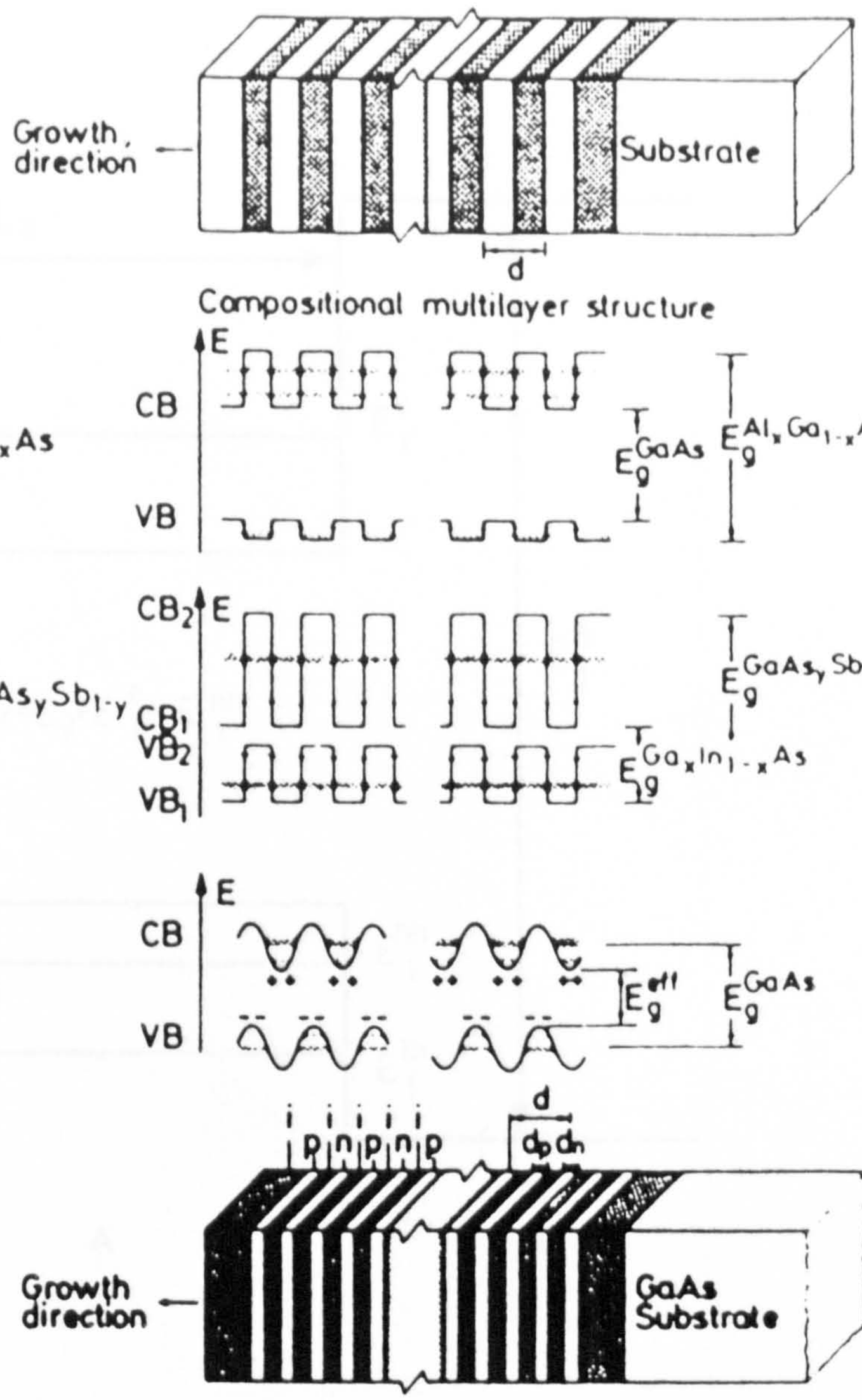

Fig.1-2 Schematic diagrams of real space band structure modulation along growth direction of three basic types of semiconductor multilayer structures. a) Type-I compositional multilayer structure; b) Type-II compositional multilayer structure; c) Doping multilayer structure. (After K.Ploog 1983)

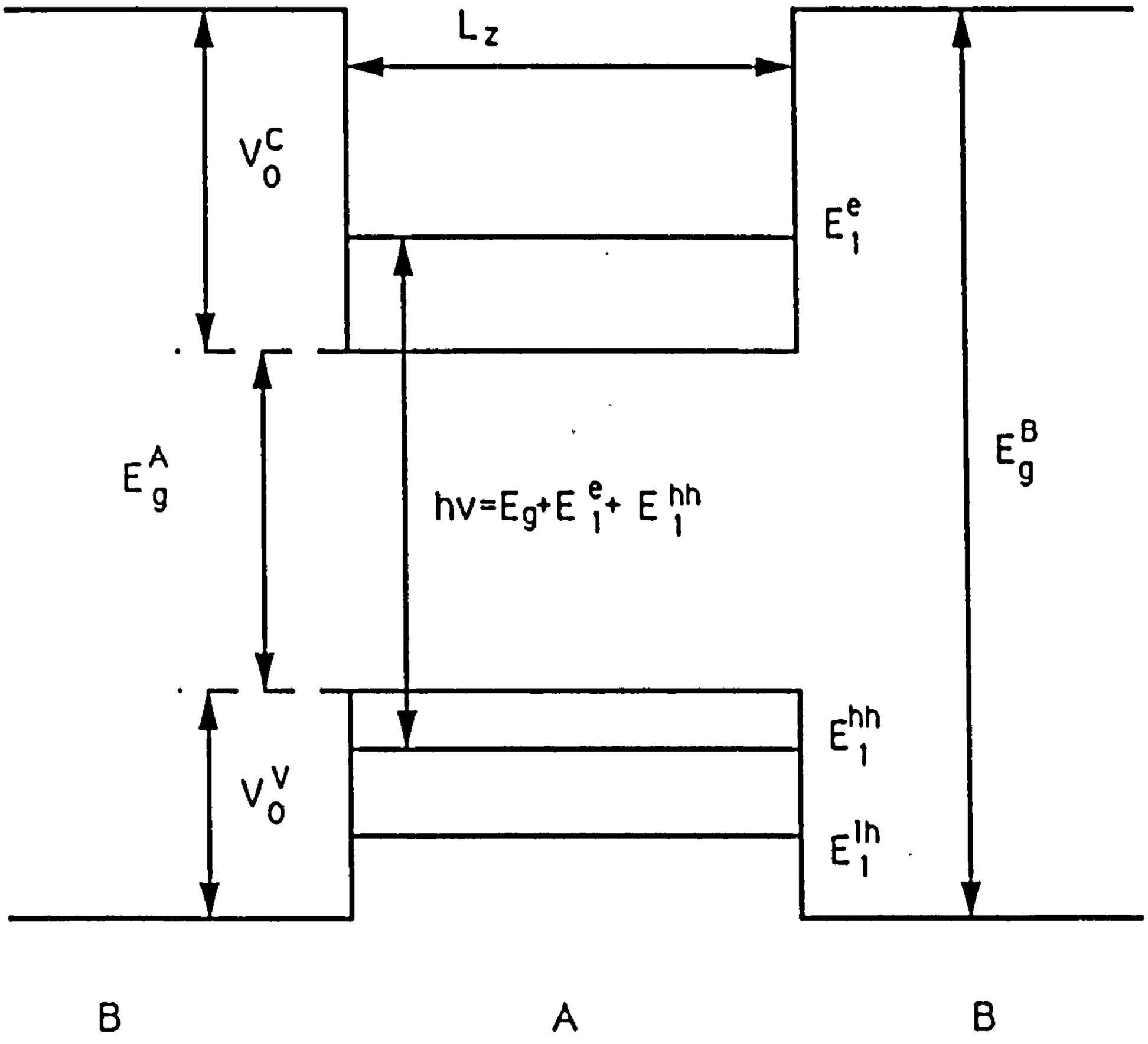

Fig.1-3 Band structure of a single Type-I quantum well.

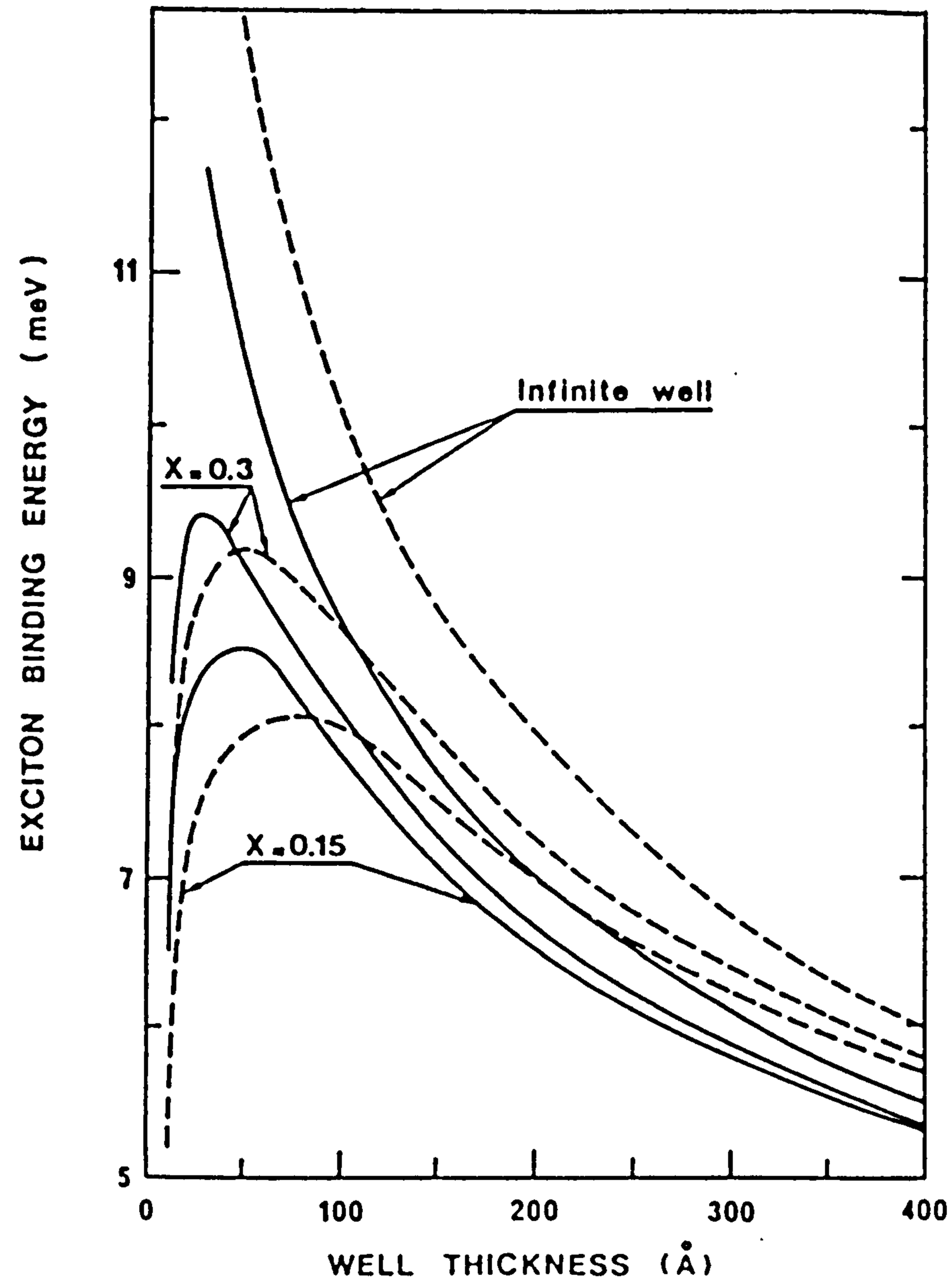

Fig.1-4 Exciton binding energy for finite quatum wells as a function of well thickness. Three barrier potentials are shown corresponding to x=0.15 and 0.30 and the infinite barrier case. Heavy-hole excitons (————) and light-hole excitons (-------) are displayed. (After R.L.Greene 1984)

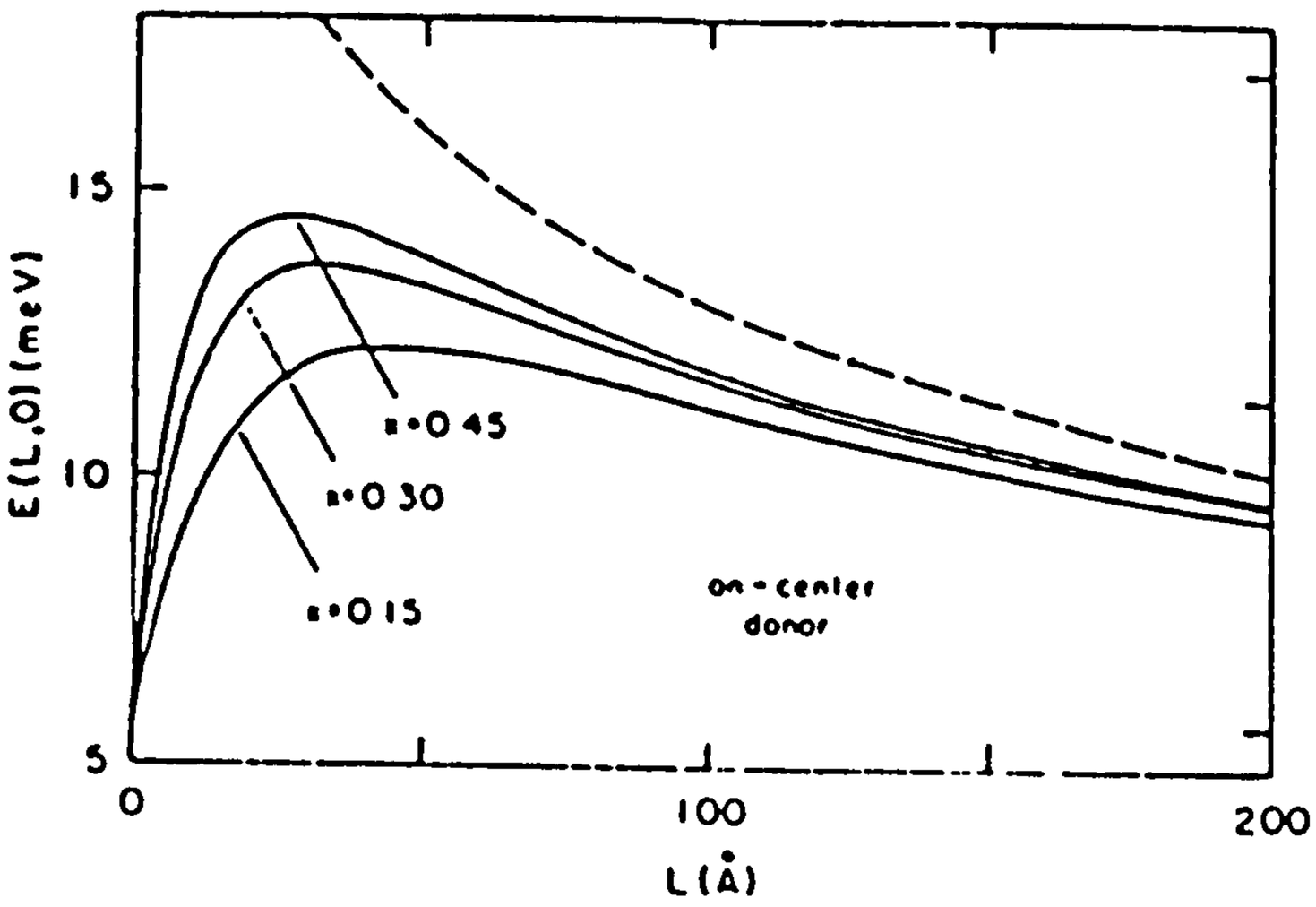

Fig.1-5 Thickness dependence of the on-centre donor binding energies in a GaAs-AlGaAs quantum well for various Al concentrations. The dashed lines correspond to the GaAs quantum well of infinite depth. (After B.V.Shanabrook 1987)

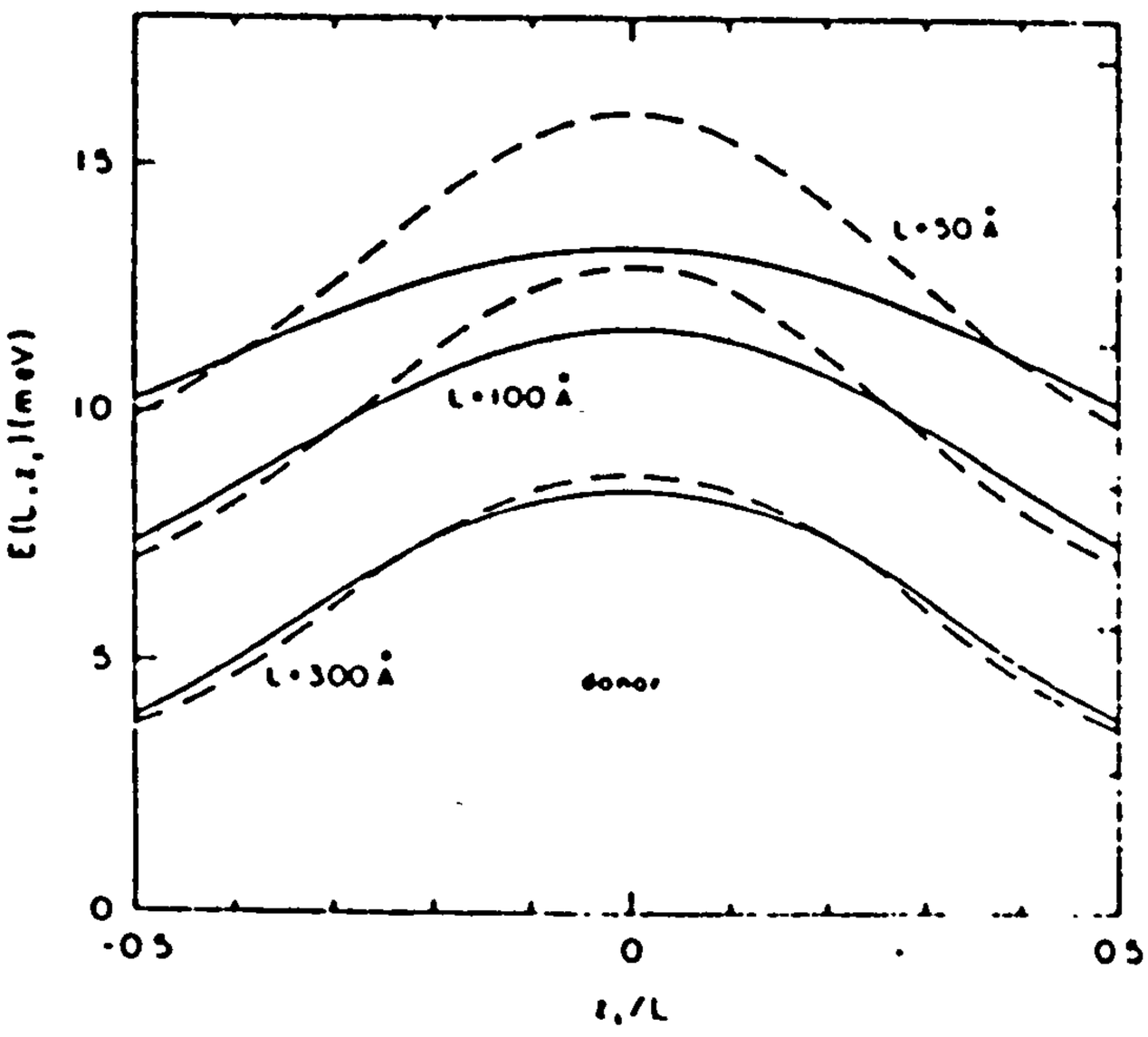

Fig.1-6 Binding energies for the ground state of a donor as function of the impurity position Zi within the GaAs -AlGaAs quantum well for various Quantum well thickness. The Al concentration is 0.30. The solid lines are for finite barrier potentials; the dashed lines are for infinite barrier potentials. (After B.V.Shanabrook 1987)

Chapter 2 Experimental Techniques

The principal techniques employed in this work are TEM and TEM-CL. Such techniques require thin, electron transparent specimens. The outline of this chapter is to describe the specimen preparation from an as-grown sample and to introduce the main techniques and equipments used. A simple account of all as-grown samples investigated is also given.

2-1 Sample Preparation

All sample studied here are GaAs/AlGaAs, InGaAs/InP multilayer structures. They were grown by either molecular beam epitaxy (MBE) or metal-organic chemical vapour deposition (MOCVD) on [100] substrates and were supplied by different growers.

Both MBE and MOCVD are newly developed growth techniques and allow very low growth rates, thus providing good control for desired layer thickness, abrupt changes and exact compositions. MBE is carried out in a UHV chamber with the implementation of powerful in situ analytical techniques, such as SIMS, AES, and RHEED in order to precisely control the crystal growth. So far it has successfully grown flat interfaces to within one atomic layer. The MOCVD process is based on the pyrolysis of alkyls of group

three elements in a atmosphere of hydrides of group five elements. Although it is not as well monitored as that of MBE, recent progress shows that MOCVD has similar control of crystal growth. Detailed description and information of them can be found in many articles (see L.L.Chang 1980; P.D.Dapkus 1982; K.Ploog 1982; M.Razeghi 1985; W.T.Tsang 1985).

In Table 2-1, the number of samples used in this work, their growth methods and growers are listed. Other details of these samples will be given in later discussions.

2-2 Specimen Preparation

Three types, plan view, cross section and cleavage specimens were used. The descriptions of preparation procedures of these specimens and the further treatments of them are given below. All specimens ready for observation in electron microscope were mounted into brass cups which are suitable for use either in a helium cold specimen holder or a normal tilt-rotate holder. Impurity contamination due to the epoxy was first found in the cross section specimen preparation. Full discussion of this will be presented in Chapter 4.

2-2-1 Plan View Specimen

Plan view specimens are most widely used in this work. Its advantages are large observable area, even thickness, a relatively easy controllable process and less surface damage.

Full accounts of preparation procedures for the GaAs/AlGaAs system plan view specimen have been given by Bailey (S.J.Bailey 1987). For other systems the procedure is the same except different etchants are applied. The

usual procedure is simply shown in Fig.2-1. The as-grown sample is cleaved into 2mm by 2mm pieces, and mechanically thinned to 50μm-70μm thickness at the centre from the substrate side by a Gatan model 656 precision dimple grinder. After being thoroughly cleaned, the specimen is chemical polished down to 10μm-20μm thickness at the centre. The remaining substrate is removed by a selective etchant, which attacks one material more rapidly than another. The etching will stop at a certain epitaxial layer where the selective etchant does not attack effectively. Usually the specimen is thin enough at this stage for TEM analysis, but sometimes further thinning is needed depending on the remaining film thickness and can be carried out by etching from either side of the film according to the specific structure of the original sample.

For the GaAs/AlGaAs system, H_2SO_4:H_2O_2:H_2O at 3:1:1 is an excellent polishing etchant, which can also be used as a further thinning etchant and NH_4OH :H_2O_2 at 1:19 is a selective etchant which removes GaAs much more rapidly than AlGaAs and allows the etching process to stop at the AlGaAs layer.

Corresponding etchants have been found for the InGaAs/InP system. 5% Br in methanol is a good polishing etchant and HCl:H_2O at 1:3 is a good selective etchant for stopping at the InGaAs layer. Bromine methanol is highly volatile and a newly mixed etchant has to be used each time in order to keep a proper polishing speed and surface quality.

For ~~the~~ systems, for which no suitable selective etchant has been found, a plan view specimen containing a reasonable thin area can be obtained with great care and constant watching by following the same procedure and using a proper polishing etchant. A few seconds distraction can cause a loss of a whole thin area in the specimen.

A properly made plan view specimen usually contains a quite big thin area of a few hundreds micrometers in diameter and should always be handled very carefully. Square 50 mesh copper grids are recommended, especially for the InGaAs/InP specimen, since it is easier to crack than the GaAs/AlGaAs one.

2-2-2 Cross Section Specimen

Although the cross section specimen preparation is a time consuming procedure and its observation area is small compared with the plan view specimen, it contains information which is not available from the other and allows the direct observations of growth profile and interfaces. In this study, all samples were grown along the [100] direction and two cross section view directions, [001] and [011], are available. Fig.2-2 illustrates the cross section specimen preparation procedure used in this work. It is given in detail as below:

1. Depending on the cross section view direction required, as-grown samples are cleaved or cut into rectangular strips. The usual size of a strip is about 6mm by 1mm and can be smaller if the sample supply is short, but this may cause difficulty in handling it. The strips are cleaned by acetone solvent in an ultrasonic bath to insure that no dust and particles are left on their growth surfaces before being stuck together, see Fig.2-2.

2. The tools employed to hold the strips tightly together are either a pair of heat sink, cross-over pattern tweezers or a home-made press as shown in Fig.2-3(a)&(b). The latter is only used for standard strips while the former is good for smaller strips. The glue used here is 5 minutes fast epoxy but anything similar can be used instead. According to availability, two more

strips of similar size from the same material as the sample substrates are often stuck to the sides in order to support the sample strips during the following mechanical thinning. To stick strips onto one specimen, first take all strips needed out of solvent, let them dry in air, make sure that the growth surfaces of sample strips are free from dust and particles visible to the naked eyes. Then mix some fresh epoxy, stack the strips with a little epoxy on their surfaces one by one into the press or between the tips of the tweezers, note that the growth surfaces of the sample strips must be face to face and in the middle when supporting strips are used, and they must be pressed tightly together to let any extra epoxy be squeezed out without breaking them. This process has to be finished quickly so that the epoxy does not get sticky and can be squeezed out easily. To let the epoxy dry and reach full strength, the strips are kept in the press or tweezers at about 100°C for about 10 minutes. After cooling in air the strips are freed from the holders as one specimen and are ready for mechanical thinning, see Fig.2-2. In order to save time and energy, two strips from the two samples, which should have the same substrate materials and can be easily identified in a microscope according to information given by growers, are usually stuck together face to face to form one specimen.

3. A home made specimen polishing stage, as is shown in Fig.2-3(c), is used to carry out mechanical thinning. The stage is consisted of a big flat cylinder with a hole in the middle and a small stub fitted into the hole. The heights of the cylinder and stub are the same and their horizontal surfaces are flat and very well polished. The specimen is laid on one surface of the stub and is fixed by using white wax and the gap of the strips is kept vertical to the stub surface. Then put the stub into the hole and let the side with

specimen down, hold the cylinder by hand with one finger pushing on the stub and grind on water proof silicon carbide paper back and forth. The specimen is thinned evenly since the cylinder around acts like a balance. P400C-P1200C silicon carbide papers are used in turn. After the zigzag surface of the specimen has become smooth, transfer to a polishing unit to polish the specimen surface and start with 6μm diamond paste then go down to 1μm until the surface is shining. During each transfer process, the cylinder and the stub with the specimen must be washed thoroughly by water to prevent the mixing of particles and pastes of different grades. The specimen is then turned over and thinned down to 20-50μm by grinding on silicon carbide paper. The minimum thickness which can be reached in this way depends on the specimen material. Great care must be taken when the specimen gets thinner during this final grinding process since many micrometers thickness material can be ground away by each back and forth movement. After being well polished, the specimen is glued, depending on its length, on one or more slot nickel grids. After rinsing in solvents like acetone and ethonal, the specimen or specimens are ready for ion thinning.

4. The ion thinners used here are Gatan Model 600 Dual Ion Mill with argon ion beam and liquid nitrogen cold specimen stage and Ion Tech Iodine Ion Thinner. For GaAs based specimens, using a cold stage and under proper milling conditions the argon ion beam thinning quality is good enough to carry out TEM and TEM-CL study. The best results are achieved by using the Gatan Mill at 4kV beam energy and 0.5mA gun current with incident beam angles of 20 degrees for the first few hours and 10 degrees for the rest, depending on the specimen thickness. The close watching of every 20 minutes is necessary during the final stage in order to turn off the ion beam at the

right moment. For InP based specimens, the severe surface damage due to argon ions cannot be ignored. To eliminate this damage, the Ion Tech iodine ion thinner is employed. There are two ways to produce a good InP based specimen. One is to carry out iodine ion thinning directly after the mechanical thinning of the specimen. Another is to apply iodine ion milling after the specimen has already been thinned by argon ions. For the latter, the first stage of the argon ion milling is the same as the GaAs one. The specimen taken out from the Gatan Mill is then put into the Ion Tech Thinner to continue milling using the iodine ion beam for about 10 minutes so that the surface ion damage created by argon ion can be wiped out. The preferred iodine ion milling is at 6kV in energy and 0.8mA of gun current and the incident angle of the ion beam is 15 degrees.

It is important to emphasize here that the gap between two sample strips must be made as narrow as possible, and the specimen thickness left after mechanical grinding should be as thin as possible, especially in the cases where the sample's epitaxial layer is softer or harder than its substrata. Otherwise, the epitaxial layer region in the specimen may be thinned away first to leave the thick substrata behind, or a bridge or a needle may be formed at the region of the epitaxial layer, resulting in a very limited or even no view area in the specimen.

2-2-3 Cleavage Specimen

A schematic illustration of a wedge-shaped specimen used for TEM observation and the geometry of its imaging condition is shown in Fig.2-4. The growth profile of the sample and interface abruptness can be evaluated by dependence of thickness fringe on composition. The thickness of the

observed region can be determined geometrically, i.e. thickness d is equal to 2t where t is distance from the region to the edge. Comparison with standard cross section specimen preparation, the preparation of the 90° wedge-shaped specimen by the cleavage of (100) wafers along (011) planes is relatively easy. Basically a piece of the sample of 2mm by 2mm is ground down to about 50μm thickness which is then cleaved by placing the sample on a flexible surface and applying pressure at the edge of the sample with the tip of a sharp knife. The sample is split into two pieces. In this way a few pieces of the specimens can be produced and then are mounted on the modified slot grids with the self-cleaved edge over the slot, see Fig.2-5. The modified slot grid is made by cutting off one third of the grid and bending the edge of about 0.5mm width, to 90°.

2-2-4 Na_2S Specimen Surface Treatment For TEM-CL

The TEM-CL investigation requires a low recombination velocity of the specimen surfaces, i.e. a low density of the surface states which locate in the middle of the energy gap as the carrier trap centres. Recently, a dramatic reduction of the surface states and a great increasing of PL spectral intensity due to a $Na_2S{:}9H_2O$ chemical passivation treatment of the GaAs (100) surface were reported (C.J.Sandroff 1987; R.S.Besser 1988; C.J.Spindt 1989). In their work, the $Na_2S{:}9H_2O$ solution was dropped on the wafer surface and spin dried. A colourless Na_2S film with the even thickness was left on the wafer surface. They found that the surface passivation effect was sensitive to the Na_2S film thickness. In this work, the Na_2S surface passivation experiment was done by immersing the specimens, which have already been thinned, in the Na_2S solutions of various concentrations for the different time from a few

seconds to a few minutes. The specimens were dried in air, and then the TEM-CL investigations were carried out right away and later up to 20 hours. The results are variable perhaps due to the uncontrollable and uneven thickness of the Na_2S films being left on the specimens surfaces. No great improvement of the CL spectral intensity has been observed. The best improvement was obtained on a GaAs based cross section specimen where the CL spectral intensity was doubled, but it has not been possible to repeat this on the other specimens. So far the way to control the Na_2S layer thickness and to get a even film over the thin specimens has not been found yet.

2-2-5 PIMS

A Gatan model 645 Precision Ion Milling System(PIMS) enables a desired area in a specimen to be thinned by the argon ion beam with a considerable accuracy. The minimum ion beam size of the PIMS can be as small as 2μm. The standard specimen holder of a Philips electron microscope can be used directly in the PIMS. So it is convenient to transfer the specimen between the microscope and the PIMS and to carry out further thinning or surface cleaning over a certain area in the specimen.

2-3 Transmission Electron Microscope

In this study, a Philips EM430 and a Philips EM400 transmission electron microscopes were used. The EM430 microscope is a medium voltage TEM, the operating voltage of the electron probe is from 50kV to 300kV and the minimum probe size which can be obtained is 20Å. The Bristol EM430 is implemented with a Link AN 10000 energy dispersive X-ray (EDS) analysis

system and a Gatan model 607 electron energy loss (EELS) spectrometer. The operating voltage of the EM400 is from 20kV to 120kV. The Bristol EM400 is constructed with a TEM-CL system and also equipped with a EDS detector controlled by a Link systems 860 minicomputer, a scanning unit, and a secondary electron detector. The microscope can be operated in both TEM and STEM modes. Most of the microscopy and analysis was carried out on the EM430 while the TEM-CL investigation was done on the EM400 with its associated CL system.

The general descriptions of the microscope construction and the conventional TEM diffraction and image analysis can be found in many books on electron microscopy (see M.H.Loretto; J.W.Edington; P.B.Hirsch and G.Thomas for example). Here only a description of the large angle convergent beam electron diffraction (LACBED) technique is given.

The LACBED technique used was first proposed by M.Tanaka and coworkers in 1980 (M.Tanaka 1980). A ray diagram of LACBED is shown in Fig.2-6. To get a LACBED (Tanaka) pattern on EM430, a specimen is placed at the eucentric height s and a highly converged electron beam is obtained in the nanoprobe mode. The excitation current of the second condenser lens was set at about 0.8A, the beam focussed using the image focus control and the specimen raised to the position s' by using the height control of the goniometer. The transmitted and diffracted images split from each other in the image plane. Dark field deflection and tilt controls were used to obtain a symmetric transmitted image. Then a bright field or a dark field LACBED pattern could be formed without disturbance from the other beams by choosing the transmitted image or a particular diffracted image using the selected area aperture and finally switching the microscope to the diffraction mode. In a

LACBED pattern, real space information about the specimen is displayed as a shadow image simultaneously with reciprocal space information. The spatial resolution is of the order of the probe size. A LACBED pattern is formally equivalent to a bend contour image.

2-4 CL System And Experiment

All CL investigations in this work were performed on a TEM-CL system constructed in 1981 and later modified in 1983 and 1987 by the researchers in this group (S.Roberts 1981; P.Aplin 1983; S.Myhajlenko 1984; J.C.C.Day 1988). The optical arrangement of the system is shown in Fig.2-7. A retractable and adjustable ellipsoidal mirror, with a small hole to allow the electron beam pass through, is used to collect the light, which is generated by the specimen when the electron beam impinges, at one focus above the specimen. The light is then deflected out of the microscope and can be detected directly by a S20 photomultiplier to form an integrated CL image displayed on the scanning unit video screen of the microscope, or can be detected by one of three detectors after passing through a spectrometer to form a CL spectrum, a monochromatic line scan and a monochromatic image. The three detectors used here are a RCA 31034A photomultiplier with a GaAs photocathode, a liquid nitrogen cooled North Coast EO 817 Germanium photodiode and a CCD parallel detection system. Three of them are all interfaced to the Link 860 computer for the controlling of data acquisition. The data acquired by the Link 860 computer can be transferred to a VAX 11/750 computer for manipulating. It should be note that the data has been rescaled during the transfer. The operating energy range is about 300nm-

880nm for the RCA photomultiplier, 900nm-1800nm for the Ge photodiode, and 400nm-1100nm for the CCD parallel detection system.

In CL study, a liquid helium cooled specimen holder is usually used in order to get the maximum possible light out of a specimen and to get high resolution spectra. The specimen is cooled by pumping a continuous flow of liquid helium through the holder from a container. It was noticed that when the container was full, very unstable helium flow could occur which would cause severe vibration of the specimen and make the CL experiments impossible. To minimize such effects, a very slow cooling rate was usually taken of more than one and half hours in duration. The minimum temperature of the specimen normally reached was found to be approximately 40°K by comparing CL experimental results with those obtained by PL of the same sample.

The operating voltage of the electron beam is usually 120kV for thin specimens and 20kV for bulk specimens. Irregular deteriorations of CL spectra and images sometimes appeared during this work. Some of the factors which may be responsible are electron beam damage, ion damage or specimen contamination. Ion damage occurs when ions come down from the microscope gun area under conditions of poor gun vacuum. Specimen contamination occurs as a result of poor specimen vacuum or as a result of specimen preparation. However it is unlikely that electron beam damage is responsible since the operating voltage was below the radiation damage threshold for the material and the deteriorations only happened occasionally. A test of the ions in the microscope was carried out by using TASTRAK (CR39) plastic supplied by Track Analysis Group in this Department. No traces of the ions were observed, but the possibility remains of temporary ion damage, due to poor

vacuum condition in the gun area caused by filament changes or by filament instabilities at near the end of its life. Specimen contamination is another possibility. The irregular and unpredictable character of the deteriorations makes it difficulty find the real causes.

During the study of CL emitted from thin film it has to be remembered that the intensity of CL emission is film thickness-dependent. Fig.2-8 shows the monochromatic CL images acquired with different emission wavelengths at the edge of a thin specimen. The film thickness incraeses away from the edge. Optical interference fringes are clearly seen in these images. We note that the intensity oscillations of these fringes are also emission wavelength dependent, so the care must be taken in comparing the intensities of different images obtained from different peaks of the spectrum. Apart from optical interference effect, thickness dependence of the diffusion length of electron-hole pairs generated by the electron beam in the specimen can affect the CL emission intensity as well. A recent account of this is given by Yuan (J.Yuan 1989).

Samples	Growth Method	Supplied By
G43 GaAs/AlGaAs MQW	MBE	Philips Research Laboratory
OE61 InGaAs/InP MQW	MOCVD	Plessey Research Ltd.
5902A InGaAs/InP SQW	MOCVD	RSRE
NU210S & NU305 GaAs/AlGaAs MQW	MBE	Physics Dept. University of Nottingham
86004, 86005, **86048 & 86049** GaAs/AlGaAs SQW	MBE	AT&T Bell Laboratory
DB36 GaAs/AlGaAs QW-Dots	MBE	E&E Engineering Dept. University of Glasgow

Table 2-1 The list of the samples studied in this work, the preparation methods and the sources.

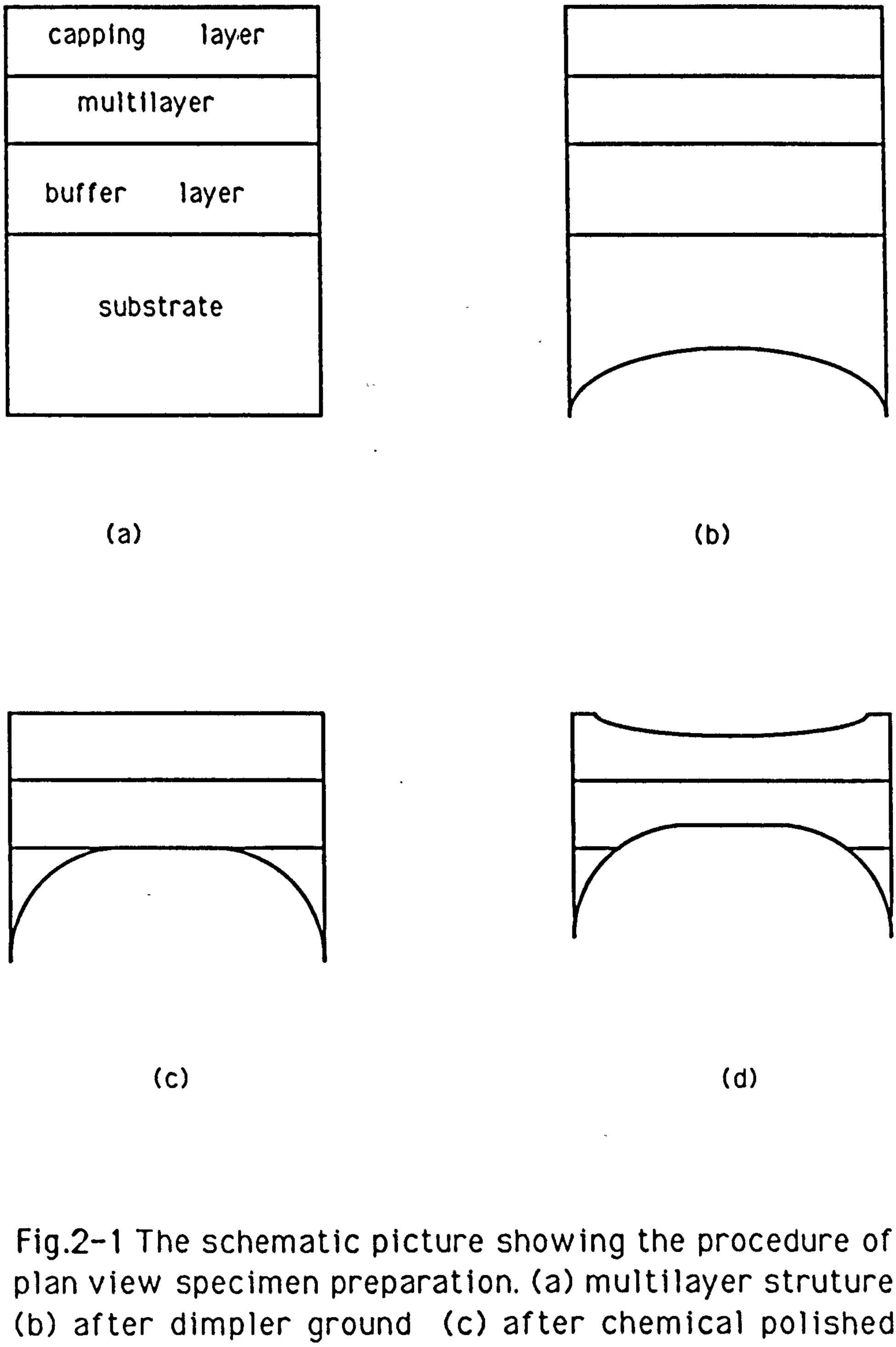

Fig.2-1 The schematic picture showing the procedure of plan view specimen preparation. (a) multilayer struture (b) after dimpler ground (c) after chemical polished and selective etched (d) further thinning from either sides.

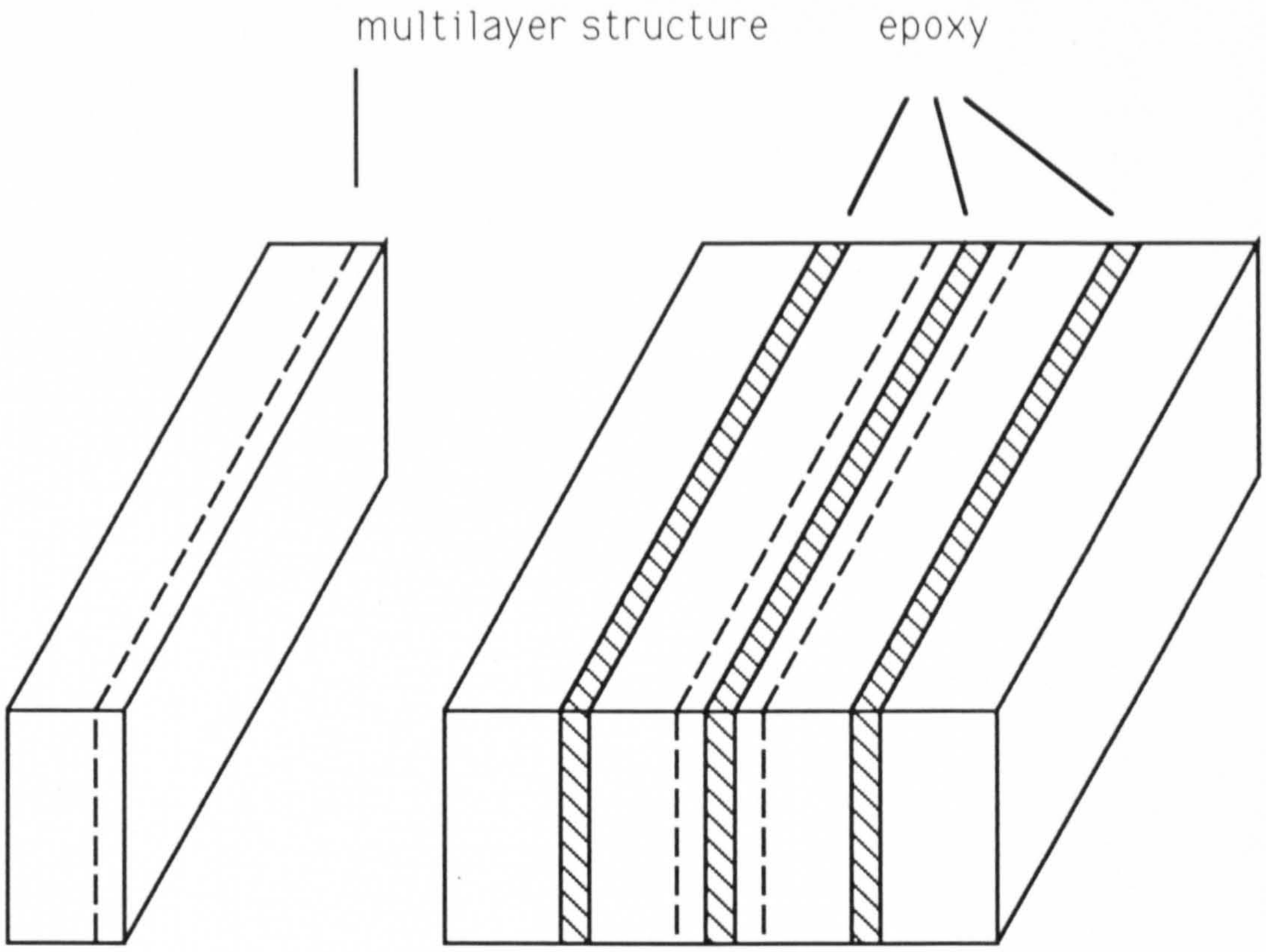

Fig.2-2 The schematic picture of the procedure of croos section specimen preparation

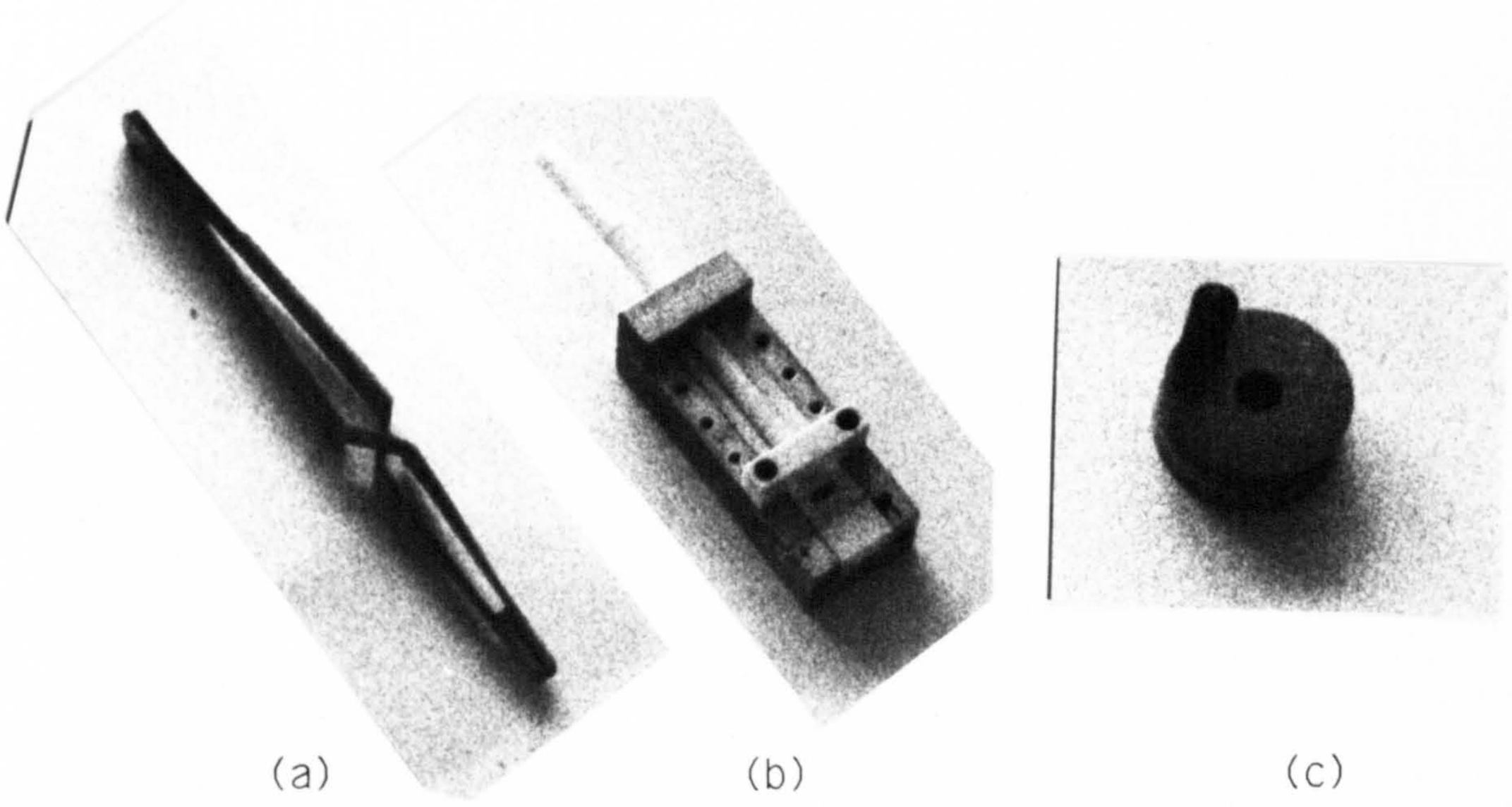

Fig.2-3 The tools for cross section specimen preparation: (a) crossover pattern tweezers (b) the press (c) the polishing stage

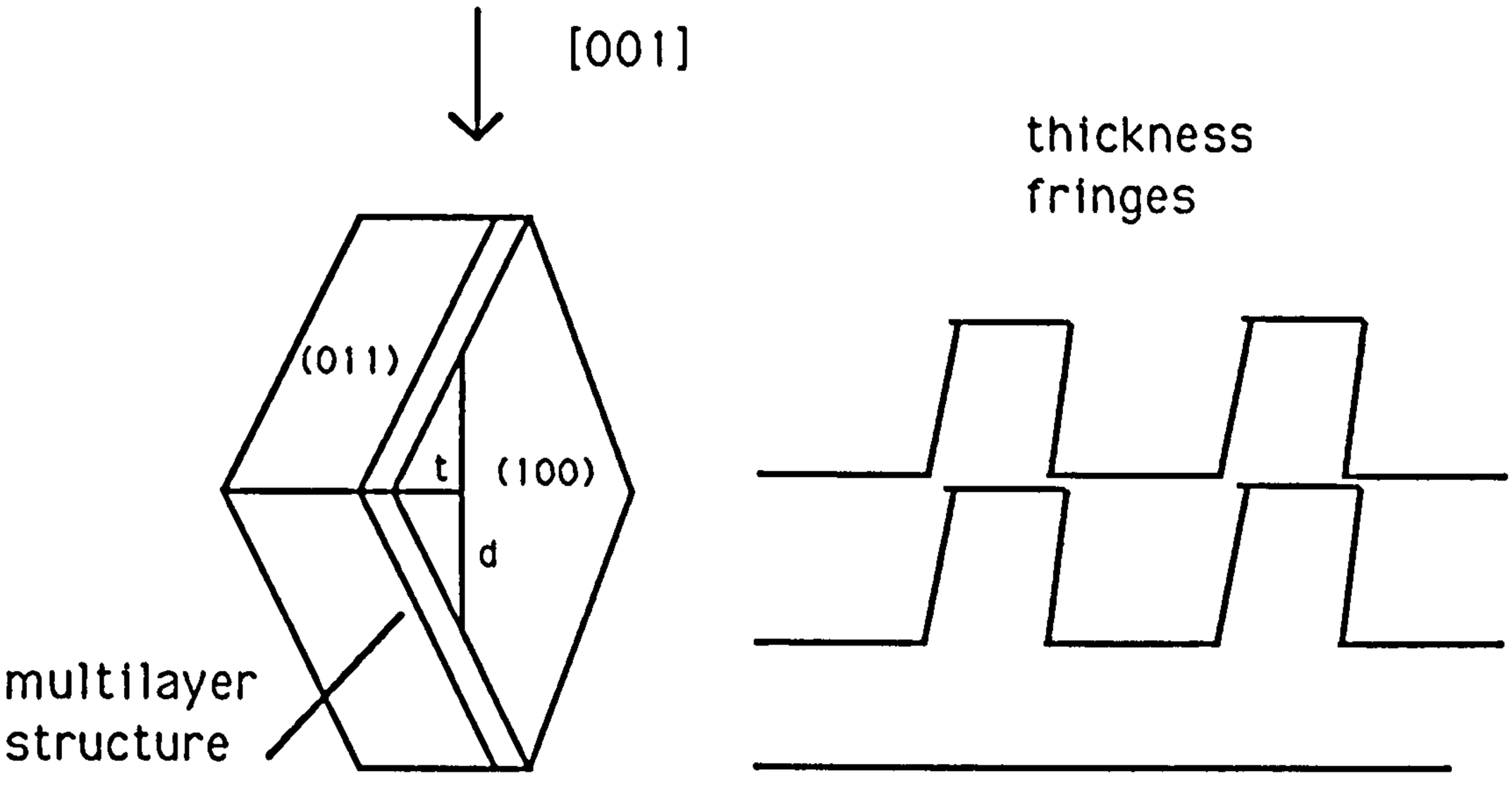

Fig.2-4 The schematic picture illustrating the geometry arrangement of the cleavaged specimen in TEM

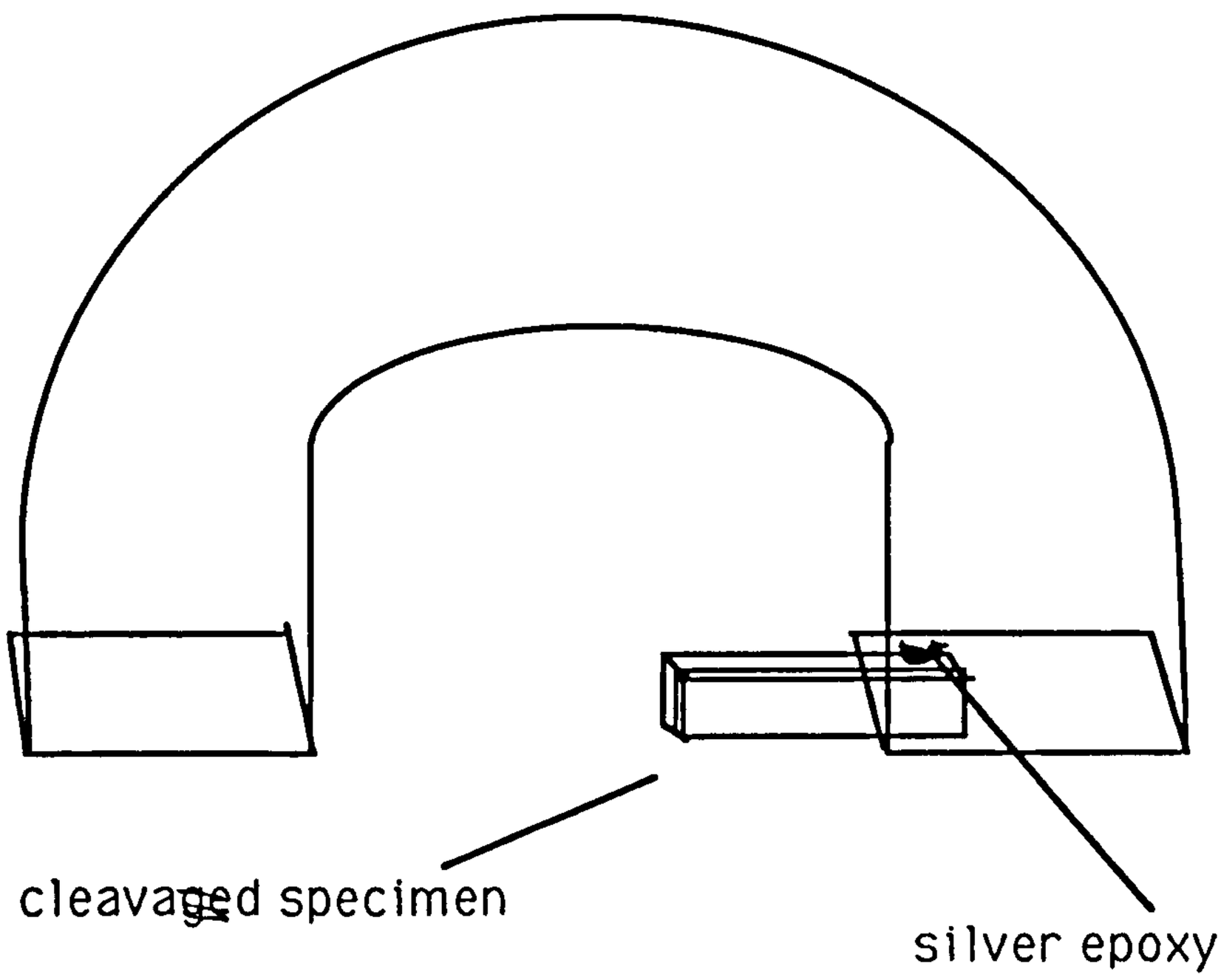

Fig.2-5 The modified slot grid with a cleavaged specimen

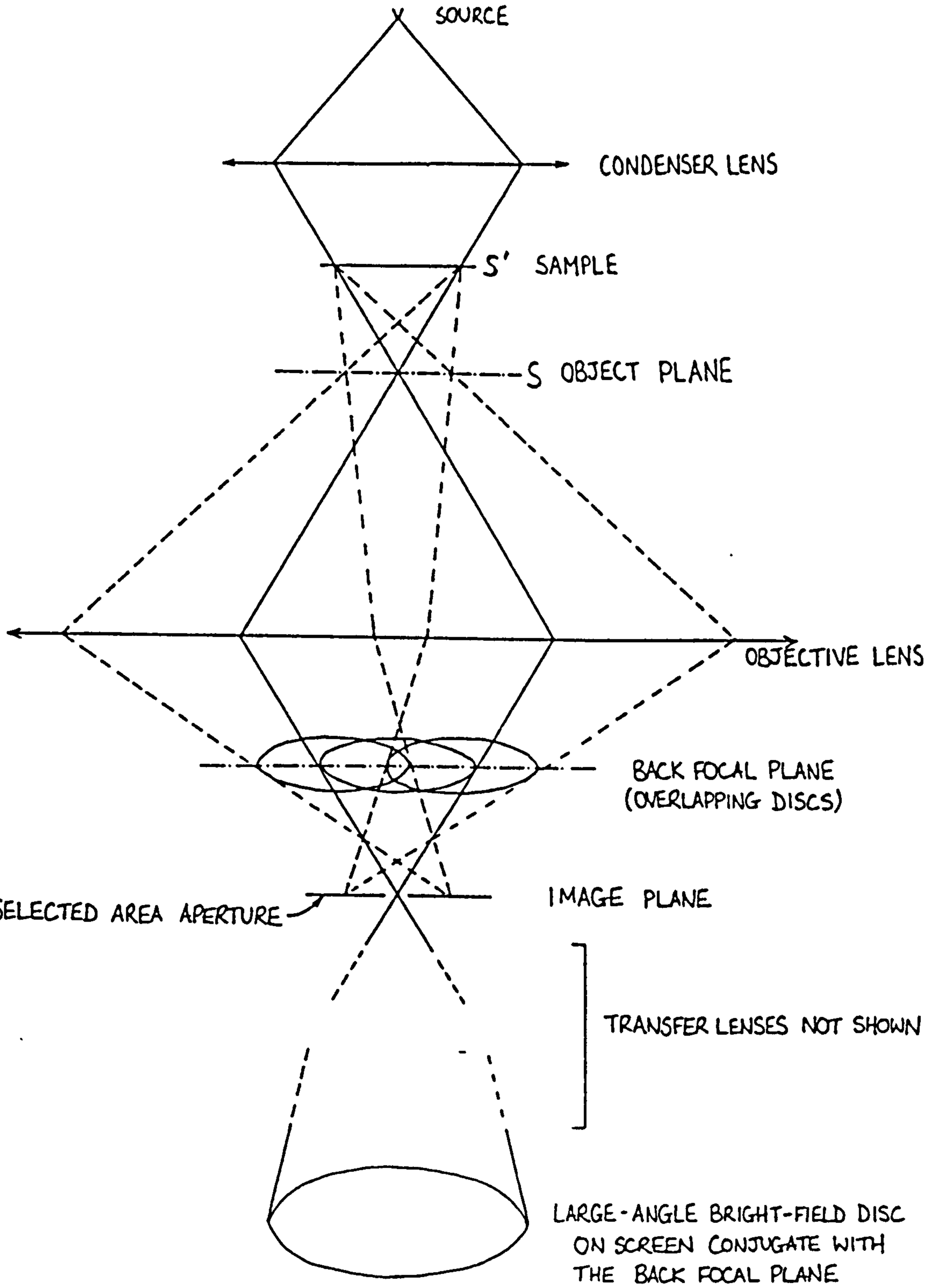

Fig.2-6 The ray diagram of LACBED (Courtesy A.R.Preston).

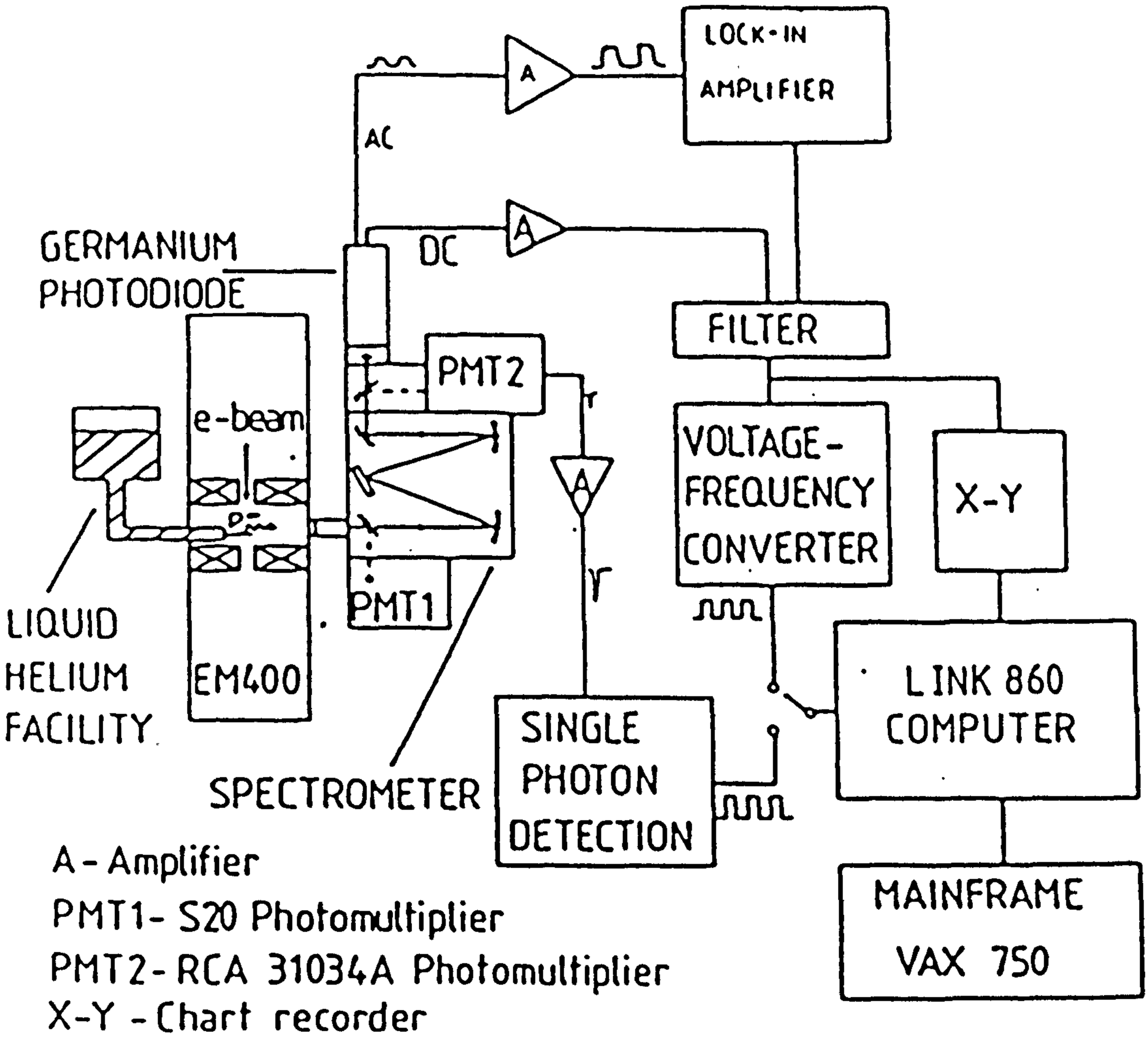

Fig.2-7 Schematic diagram of detectors and signal processing arrangment of TEM-CL system in EM400. (Courtesy of S.Myhajlenko)

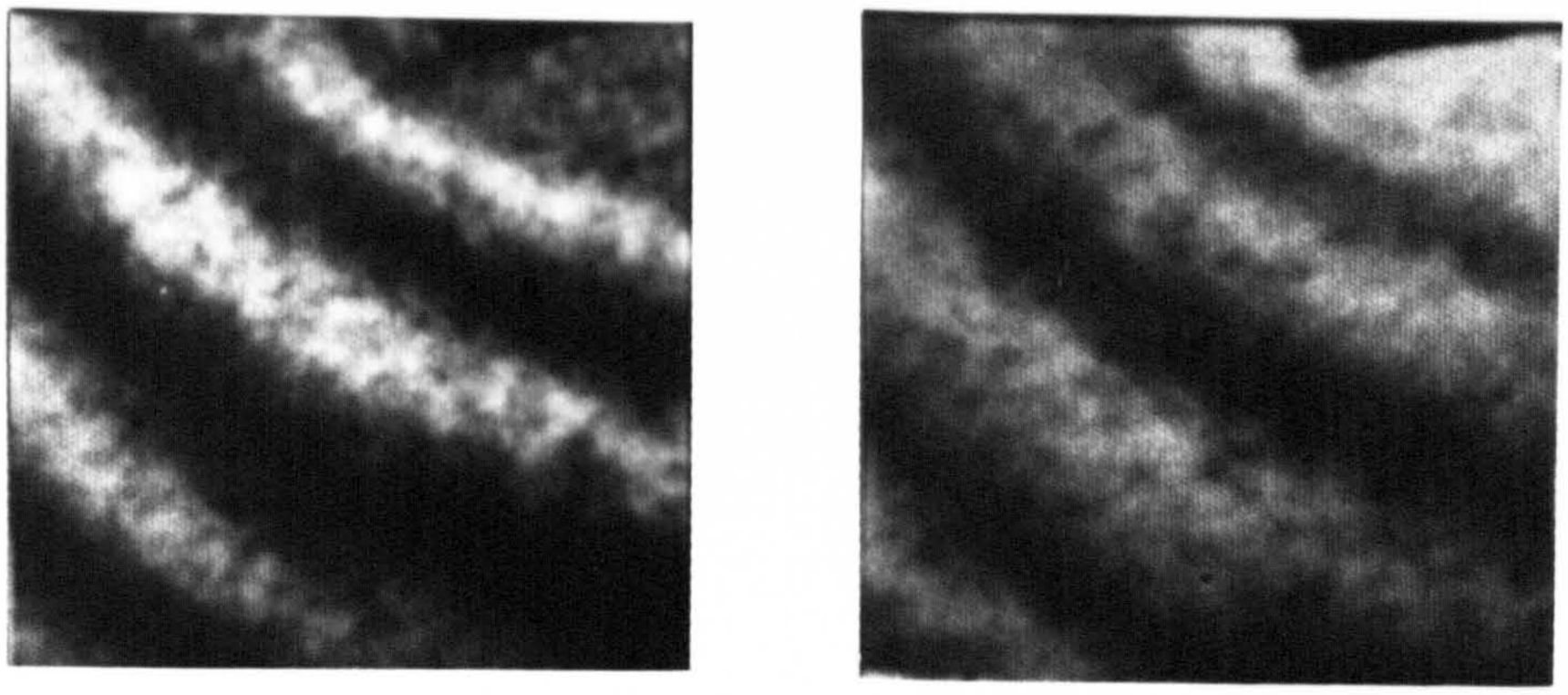

(a) 693.8nm

(b) 729.2nm

10um

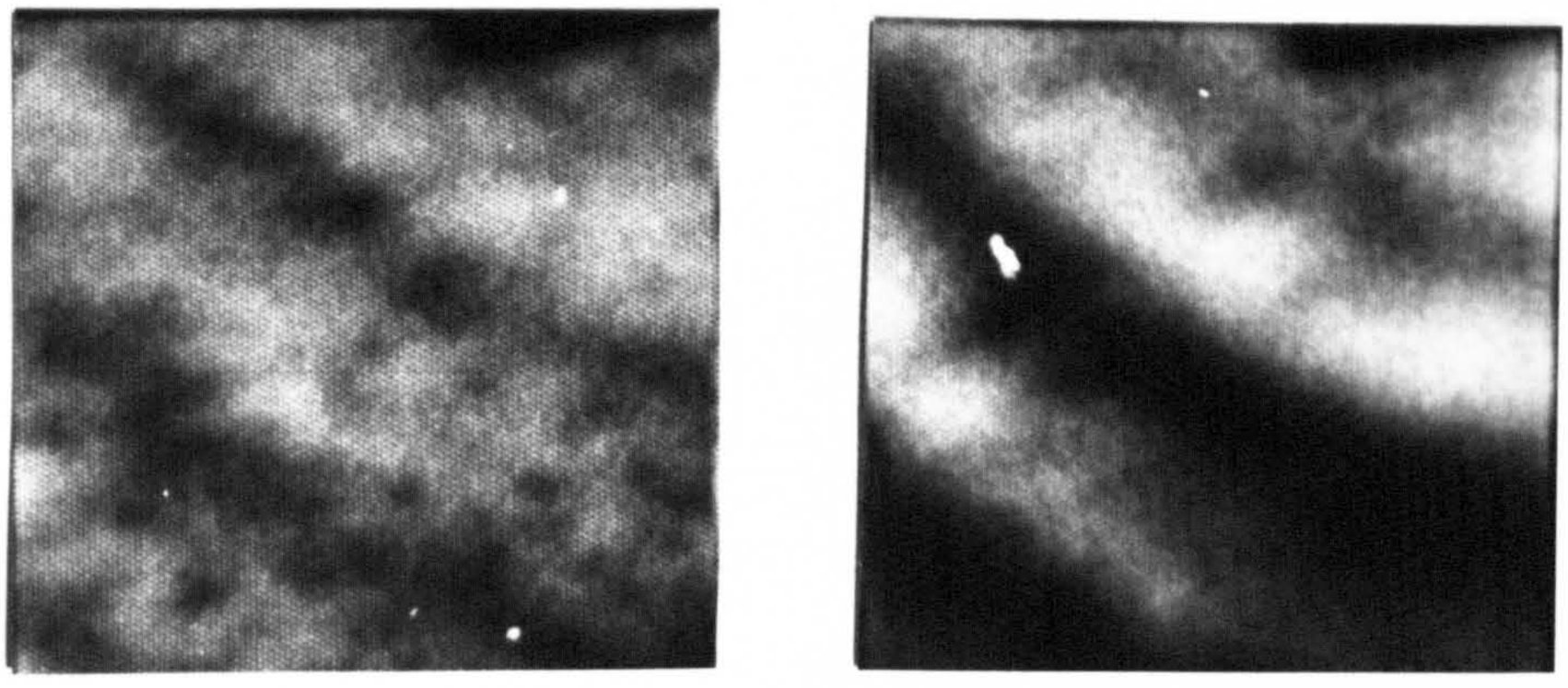

(c) 771.4nm

(d) 803.6nm

Fig.2-8 The monochromatic CL images obtained at same area with diffrent wavelength as indicated.

Chapter 3 TEM Studies OF GaAs/AlGaAs and InGaAs/InP Multilayer Structures

The structure information of semiconductor multilayers is very important in their technology applications and physics studies. A few techniques based on transmission electron microscopy (TEM) are often used to study the structure of semiconductor multilayers. The techniques employed in this work include cross sectional transmission electron microscopy (XTEM), composition analysis by thickness-fringe (CAT), large angle convergent beam electron diffraction (LACBED) and imaging from multilayer structure reflections.

For the conventional cross sectional observations, the specimens are generally viewed along the interfaces, where the interface defects, growth steps, and composition profiles can be examined by diffraction contrast images and lattice images (W.M.Stobbs 1988; A.Ourmazd 1987), but in this work we studied the interfaces of multilayer structure from a cross section specimen by applying LACBED technique and we also studied the inclined interfaces of multilayer structure by using fringe contrast analysis. The CAT is a new technique proposed by Kakibayshi and Nagata (H.Kakibayshi 1985), in which a wedge-shaped specimen is made by a cleavage method and the composition

dependence on the thickness fringe is used to evaluate the interface abruptness. In both XTEM and CAT, the suitable observation areas are sometimes rather small. In contrast, the plan view specimens, which are often prepared by a selected etching, contain a larger transparent area with uniform thickness and are convenient for defect analysis. But conventional diffraction contrast fails to reveal the interface steps and composition modulation. A method based on LACBED for diffraction and imaging from multilayer structure reflections offers a possible way to evaluate structure information from plan view specimen. The method was introduced by Vincent and ~~being~~ was developed in this group (R.Vincent 1987[1]&[2]).

In this chapter, some preliminary work of LACBED pattern and imaging from multilayer structures reflections is presented first. A simple qualitative kinematic explanation of the diffraction pattern is presented with applications to GaAs/AlGaAs and InGaAs/InP multilayer structures. Imaging from GaAs/AlGaAs multilayer reflections is also described. Then, in Section 3-3, studies of InGaAs/InP interfaces by LACBED and XTEM of inclined interfaces are discussed. Finally an example of the applications of CAT is given.

The samples investigated here include G43, OE61B, 5902A and NU210S. Their structures are sketched in Fig.3-1. The details of specimen preparation can be found in Chapter 2.

3-1 LACBED Patterns of GaAs/AlGaAs, InGaAs/InP Multilayer Structures

Semiconductor multilayer structures considered here are formed by a series of alternating layers with different compositions and thickness but with

matching lattice parameters. If the repeat period of these layers is d, such a periodic composition modulation acts like a diffraction grating and results in the reciprocal lattice vector g being decorated with sets of satellite reflections $g+nq(n=\pm1,\pm2,.....)$, where q is parallel to the growth direction with magnitude $1/d$. X-ray diffraction has been successfully used to reveal the existence of such artificial superstructures and to determine their characteristic parameters such as the period and composition (J.Kervarec 1983; M.A.G.Halliwell 1984; W.J.Bartels 1986), but the parameters obtained by X-ray diffraction are average values and unable to show fine scale variations. In this aspect, transmission electron diffraction is an attractive candidate to approach this problem.

In a conventional electron diffraction pattern obtained with parallel illumination of a tilted plan view specimen, the evidence of composition modulation is invisible due to the geometrical arrangement. In the case of a thin film specimen with thickness t, all reflections g which are in the growth plane are accompanied by decaying intensity oscillations which are perpendicular to g and the growth plane (see Fig.3-2(a)). The composition modulation in the thin film adds extra maxima at $g\pm nq$ to the oscillations (see Fig.3-2(b)). By tilting the specimen around Bragg condition for g, the Ewald sphere is able to intersect these lines of intensity oscillation (the rocking curve). By taking a series diffraction patterns it is possible to examine the intensity oscillation and the measured intensities are, to a first approximation, related to the structure factor F_g. In reality, the bending of the thin films, inelastic scattering around the Bragg reflections, and multiple diffraction effects broaden and distort the intensity oscillations making them completely unobservable.

However in LACBED, as described in Chapter 2, the convergent incident electron beam makes the intensity distribution of a Bragg reflection directly available in its diffraction disk. The defocused probe i.e. lifted specimen, permits the isolation of the direct or a chosen diffracted beam by insertion of a small aperture in the area selecting plane and a LACBED pattern can be formed from one beam without disturbance of others. The higher is the specimen lifted, the larger is the splitting of beams and the more is the inelastic diffuse scattering excluded. So in dark field LACBED patterns of 200 satellites the composition modulation is clearly visible as sidebands in the rocking curves; see Fig.3-5 for an example.

The appearance of sidebands and their behaviour can be modelled qualitatively by a simple kinematic phased sum of the scattered amplitudes along a column parallel to growth direction z, which is [001] here. For a slab of thickness t and for any composition modulation along z, the amplitude diffracted around g can be written as

$$\psi_g \propto \int_0^t F_g(z) \exp(-2\pi i s z)\, dz \qquad 3\text{-}1$$

according to the usual kinematic rocking curve theory. s is the deviation from Bragg condition and is approximately equal to q at the limit of small tilting angle away from [001], $F_g(z)$ is the structure factor function. For the zincblende structure, $F_g(z)$ is determined by a phased sum of the scattering from the two fcc sublattices, which adds in phase for reflections such as 400 and 220 and in antiphase for 200. For the GaAs/AlGaAs and InGaAs/InP multilayers considered here, the relative amplitudes of structure factors $f_a(z)$ and $f_c(z)$ of the anion and cation sublattices modulations along z are sketched

in Fig.3-3 and Fig.3-4 respectively, where the values of $f(z)$ are taken at $s=0.2A^{-1}$ and a relative phase shift of π is represented by changing the sign of $f(z)$ for one sublattice. In Fig.3-3 the resultant Δf of $F_g(z)$ is similar for both in-phase reflections like 400 and anti-phase reflections like 200. We therefore expect that the sidebands to both types of reflections will be similar too. Fig.3-7 and Fig.3-8 show the LACBED patterns obtained from a GaAs/AlGaAs structure (sample G43) for 200 and 400 reflections. As can be seen, the extent of the sidebands is up to $3q$ in both case. However the resultant Δf of $F_g(z)$ from the InGaAs/InP structure in Fig.3-4 is obviously small for 400 reflections and large for 200 reflections. Experimentally, sidebands extending to $17q$ were visible from a InGaAs/InP structure (sample OE61B) around 200 reflections as is shown in Fig.3-5, whereas around 400 reflections only a few sidebands were visible, (see Fig.3-6). For this reason LACBED patterns of 200 reflections were often chosen to carry out more detailed analysis.

Equation (3-1) is a Fourier transform of the structure factor function $F_g(z)$. Consider a rectangular variation of composition modulation along z i.e. a rectangular variation of scattered amplitude Δf with period d and components d_1 and d_2, where $d=d_1+d_2$. Then for reflections $g\pm nq$, the nth Fourier component of equation(3-1) with $s=nq$ $(n\neq 0)$ is

$$\psi_n \propto \frac{\sin(n\pi d_1/d)}{n\pi} \qquad 3\text{-}2$$

which is proportional to the modulation structure factor. If d/d_1 or d/d_2 is an exact integer m, then ψ_n with n satisfying $n/m=i$ $(i=1,2,3,....)$ are identically zero. A good illustration of this effect is shown in Fig.3-5 for the

InGaAs/InP multilayer sample OE61B with d_1=95Å (InGaAs) and d_2=350Å (InP). As $m\approx5$, although the sidebands are visible up to 17q (n=17) n=5, 10 & 15 are missing.

Look at Fig.3-7, which is a 200 reflection LACBED pattern obtained from sample G43. It contains 5 GaAs quantum wells of 55Å width separated by 175Å AlGaAs barriers and enclosed by 1500Å cladding layers of AlGaAs. The principal sidebands of n=1,2&3 are clearly shown, and between q and $2q$ three fine subsidiary bands are visible. These bands are related to the 5 layer structure as was proved by experiment described below. A plan view specimen was made by selective etching, and then put into the PIMS (precise ion milling system) to further thin it locally until a small hole was created. In the area around the hole the thickness of the 5 layer structure was reduced gradually to zero. Taking 200 LACBED pattern from such an area, we expected that the fine subsidiary bands should be reduced from 3 to 2 to 1 as the edge of the hole was approached, this result is shown in Fig.3-9, indicated by arrows. The appearance of these fine bands can also be understood by elementary theory of diffraction gratings. Due to the limited number of repeats in the modulated structure, we should multiply Equation 3-2 by the term $\sin NV/\sin V$, where N is the number of repeats in the modulated structure and V is related to s. Between q and nq the term creates N-1 minima, in other word N-2 maxima. In the case above, N=5, so three fine subsidiary bands appear.

This simple kinematic analysis is successful in understanding qualitatively the details of the LACBED patterns of multilayer structures, more rigorous theoretical analysis should take into account deviations of the actual multilayer structure from a rectangular modulation, the effects of the cladding layers, and the perturbations caused by dynamical diffraction. Such

factors have to be taken into account in order to obtain useful quantitative information from the experimental results and to explain the detailed structure of LACBED patterns such as splitting of the *q* lines, deviations from the exact Bragg positions and the relative intensities of the *q* lines. Such work has not been undertaken for the purposes of this thesis but is now under investigation by others.

3-2 Imaging Of Multilayer Sidebands From GaAs/AlGaAs QW

Apart from LACBED patterns, the DF images of bend contours from any lattice reflection g contain composition modulation sidebands as well, as long as the objective aperture is large enough for them to pass through. By comparison with LACBED pattern, the sidebands may be distinguished from dynamical diffraction into higher order systematic Bragg reflections and used to form DF images. In some GaAs/AlGaAs samples the DF images from sidebands of 200 reflections show an unusual linear contrast along a single [110] direction. Fig.3-10 is a example of such contrast taken from the sample with 5 QW's described above. To indicate that this is not a surface effect, the PIMS technique was applied to both surfaces, to produce the results shown in Fig.3-11; the linear contrast remained unchanged although ion damaged surface contrast appeared after 115 minutes ion thinning of both surfaces. It was also noticed that no similar linear contrast appeared in DF images formed from regular lattice reflections. It may be inferred that the linear contrast must be related to the multilayer structure itself. The fact that the contrast only appeared in the DF images formed from multilayer sideband reflections implies that layer thickness fluctuations with associated interface steps are

responsible. Moreover the sidebands are directly related to the layer thickness. The fact that the contrast was only observed along one of the two possible [110] directions is possibly due to the polar GaAs subcell. The CL imaging technique has been used repeatedly in an effort to observe similar linear contrast effects in this sample without success. This failure may be due to carrier diffusion resulting in limited spatial resolution of CL images and the limited energy resolution of CL spectrum since the change of the emission energy caused by monolayer fluctuation in well thickness is very small in this case. For a single QW sample with growth interruption, we have observed the interface step contrast in CL images, but failed to observe similar contrast in sideband reflection images, the detailed results will be discussed in Chapter 5. So far the contrast in sideband reflection images has only been observed in two samples (for the result of another sample see R.Vincent 1987[1]). The complicated structure of these samples with the overlap of many interfaces on projection along the zone axis direction adds ambiguity to the final explanation of the contrast. However the relative simplicity of making these observations and the importance of interface sharpness makes these new results of considerable potential interest as a way to complement information obtained by cross sectional TEM.

3-3 TEM Study of $In_{1-x}Ga_xAs/InP$ SQW

For the $In_{1-x}Ga_xAs/InP$ system, a perfect lattice match can be achieved for an alloy composition with X=0.47, but a variation of 1% from this value will cause a lattice mismatch of 0.07%. As has been studied by other researchers (P.Franzosi 1986; N.G.Chew 1987), in $In_{1-x}Ga_xAs$ layers with

X<0.47, where the lattice constant a_0' of $In_{1-x}Ga_xAs$ layer is larger than that of InP layers (a_0), a compressing stress is applied to $In_{1-x}Ga_xAs$ layer. In this case interface misfit dislocations were observed which relieved part of the misfit strain. However, with X>0.47, a_0'<a_0 and a tensile stress is applied to $In_{1-x}Ga_xAs$ layer. No misfit dislocations were observed but cracking of $In_{1-x}Ga_xAs$ layer occurred as a strain relieving mechanism.

In this work, $In_{1-x}Ga_xAs$/InP single quantum well samples were supplied by RSRE. The typical structure of the samples is shown in Fig.3-1(c). The $In_{1-x}Ga_xAs$ wells had widths varying from 100Å to 800Å and were sandwiched between the InP substrate and a 2000Å InP capping layer. PL studies of these samples have been carried out by RSRE researchers. Their results revealed that in these samples the variation from the composition X=0.47 of $In_{1-x}Ga_xAs$ was less than 1%. They also deduced that small subsidiary peaks in the PL spectra from these samples were the result of phonon replication caused by the presence of alloy clusters in the material. Here, [001] and [011] cross-section specimens were prepared together with plan view specimens to investigate the microstructure of the samples and to correlate the observations with the RSRE PL studies. Our experimental results were rather similar for all the samples and no definite microstructural differences have been observed. We can not therefore confirm that the phonon assisted emission, evident in PL, is related to alloy clusters. Here only the experimental results for sample 5902A are given. An investigation was made of the strain measurement in the $In_{1-x}Ga_xAs$ layer by applying the LACBED technique to the [001] and [011] cross-sections. The results are discussed first and then a diffraction contrast analysis of the interfaces fringes observed in

the same specimens is presented. Finally, a discussion of these experiment results is given.

3-3-1 The Application of LACBED to Sample 5902A

The technique of LACBED has been described in Section 2-3. 020 and 220 BF LACBED patterns, which were taken from a [001] orientation cross-section specimen, together with a $02\bar{2}$ BF LACBED pattern, which was taken from a [011] orientation cross section specimen, are shown in Fig.3-12. The InGaAs/InP sandwich structure is clearly seen in the shadow images of the patterns. As we can see in these figures, those contours, which correspond groups of planes perpendicular to the InGaAs/InP interface such as 020, 040, etc. and 022, 044, etc., pass rather smoothly through InGaAs layer from the InP substrate to the InP capping layer. On the other hand, those contours, which correspond groups of planes inclined to the InGaAs/InP interface such as 220, 440, etc., and oblique lines in 020 and 022 LACBED patterns are displaced on crossing InGaAs layer from the InP substrate to the InP capping layer. This effect is caused by the rotation of the same planes in the InGaAs layer. These observations indicate that lattice misfit strain exists between the InP and InGaAs layers in the sample. This strain causes tetragonal distortion of the InGaAs layer which results in planes inclined to the interface being rotated and planes perpendicular or parallel to the interface remaining unrotated.

For simplicity, we suppose that all misfit strain $\Delta a/a_0$ is accommodated by tetragonal distortion in $In_{1-x}Ga_xAs$ layer and the InP layers remain undistorted, where a_0 is lattice constant of InP (=5.87A) and Δa is the difference of lattice constant between the InP and the unstrained $In_{1-x}Ga_xAs$

i.e. $\Delta a=a_0-a_0'$. The $In_{1-x}Ga_xAs$ can be in tension or in compression depending on whether Δa is positive or negative. The projection of tetragonal distortions of the $InP/In_{1-x}Ga_xAs/InP$ sandwich structure along a [001] direction with InGaAs layer in compression are shown schematically in Fig.3-13(a). The cubic lattice of InP remains with $a=b=c=a_0$, while the cubic lattice of $In_{1-x}Ga_xAs$ has changed into a tetragonal lattice with $b=c=a_0$, $a=a_0\cdot(1-3\cdot f)$ for [100] growth direction, where $f=\Delta a/a_0$. The angle between the plane (h,k,l) and the interface plane (100) is given by

$$\cos\theta = \frac{h}{(h^2+k^2+l^2)^{1/2}} \qquad 3\text{-}3$$

for cubic lattice of InP layers; and given by

$$\cos\theta' = \frac{h}{[h^2+(k^2+l^2)(1-6\cdot f)]^{1/2}} \qquad 3\text{-}4$$

for a tetragonal lattice in the InGaAs layer. If the plane (h,k,l) is parallel or perpendicular to the interface plane, we have $\theta=\theta'$, and there is no rotation for such planes of the InGaAs with respect to the equivalent InP planes. If the plane (h,k,l) is inclined to the interface plane, we have $\theta\neq\theta'$, and the plane (h,k,l) of InGaAs layer is rotated corresponding to the equivalent InP planes. The distortion changes the interplanar distance as well and as a result the correspondant Bragg angles. Hence the contours which correspond the plane

(h,k,l) of the InP layers in the LACBED patterns are rotated and displaced on crossing the InGaAs layer. According to the direction of the rotation which occurrs, we can work out whether the strain in InGaAs layer is compressive or tensile, see Fig.3-13(b). Both the displacement and the rotation are in turn related to the misfit strain

In the case of sample 5902A with an InGaAs well width of 500A, and by studying the 220 LACBEDD pattern shown in Fig.3-12(b), we conclude that the InGaAs layer was in compression. From measuring the displacement of the $\bar{2}\bar{8}0$ contour (as indicated in Fig.3-12(b)) we estimate that the misfit strain is about $9 \cdot 10^{-3}$, which is larger than that being estimated from PL studies.

Moreover we observed that the contours corresponding to inclined planes displaced in two InP layers. This can be result from the relative rotation between the InP capping layer and InP substrate due to the misfit strain, since the distortion model descrided above is rather simplified.

3-3-2 The Analysis of Interface Fringe Contrast

Usually there are four principal types of fringe contrast which can arise at interfaces inclined to a specimen surface. They are thickness fringes, δ fringes, displacement fringes and Moire fringes. The detailed discussion of these in the framework of the dynamic theory of electron diffraction can be found in the review article by R.C.Pond (R.C.Pond 1984). A brief summary of the main features of these fringe contrasts is given below.

1. Thickness Fringes: The origin of thickness fringes is due to the oscillation of the direct and diffracted wave amplitudes with depth in diffracting crystals. The fringes can be commonly observed at interfaces

inclined to the specimen surface when one side of the crystal is strongly diffracting while the other side is only diffracting weakly, or when the structure factors of the crystals are very different for a particular diffraction.

2. δ Fringes: δ fringes arise in specimens having correlated lattices but different deviation parameters $s_g\xi_g$ for the common planes in each crystal. The fringes display characteristic contrast behaviour: the outer fringes are asymmetric in bright field and symmetric in dark field.

3. Displacement Fringes: Displacement fringes are closely related to δ fringe contrast, but arises as a result of a different scattering mechanism at the interface. The scattering mechanism leading to displacement fringes is the same as that responsible for stacking fault fringes in single crystals. The general features of displacement fringes are the same as those of stacking fault fringes i.e. the fringe pattern is symmetric in bright field and asymmetric in dark field, and the fringe contrast disappears if $g \cdot \underline{R} = 0$, where g is operating diffraction vector and $\underline{R}$ is displacement vector (this is not necessarily restricted to specific values derived from the crystal structure).

4. Moire Fringes: Moire fringe patterns are a type of lattice image. The characteristic features distinguishing them from other types of fringes are that the fringes are not necessarily parallel to the intersection of the interface with the foil surface and the fringe contrast does not depend on the wavelength of the incident radiation.

In this study, fringe contrast analysis was performed on inclined heterostructure interfaces of a cross-section of an InGaAs/InP single quantum well structure. The specimen structure is clearly displayed in Fig.3-14, which was taken with the interfaces edge-on. There are two hetero-structure interfaces, A and B, and one homogeneous interface, C, as indicated in the

figure. In the observations of inclined interfaces, the specimen was tilted around operating vectors about 10° away from the edge on condition i.e. [001] or [011] zone axis. The observation geometry is shown in Fig.3-15, where the incident electron beam is either near an [001] direction or an [011] direction.

As is shown in Fig.3-16 the interface fringes arise at all three interfaces. Both micrographs were taken from an [001] cross-section with s=0 in the InP layer at a $\bar{2}\bar{2}0$ two-beam condition. The fringe contrasts of the interfaces A and C have characteristic features typical of stacking fault fringes i.e. the fringes are symmetric in bright field images and asymmetric in dark field images, The fringe contrast of interface B does not show any very clear features and cannot be characterised as any particular simple type of fringe. Similar results were obtained at 220, $2\bar{2}0$ and $\bar{2}20$ reflections under two-beam conditions with s=0. This means that the lattices are simply displaced at the interfaces A and C, but that a more complicated situation exists at the interface B.

However, a different type of fringe contrast was observed at the interfaces A and B for BF images taken in the 020 reflection of the same specimen. Fig.3-17(a) shows results for s=0 in the 020 two-beam condition. The fringes which are visible are likely to be thickness fringes since the structure factors of the InP and the InGaAs layers are very different in this case (see Section 3-2). No such fringes were observed at the interface C. Moreover, as is shown in Fig.3-17(b), no fringe contrast appeared at any of the interfaces in $02\bar{2}$ two-beam BF images taken with s=0 from an [011] cross-section specimen. The disappearance of the displacement fringe contrast when the operating reflection vectors were perpendicular to the growth direction [100] indicates that the displacement occurred parallel to the growth direction.

3-3-3 Discussion

The experiment results obtained by the LACBED technique are highly compatible with those obtained by fringe contrast analysis. Both studies were carried out in the dislocation free areas and indicated that the lattice distortion existed in InGaAs layer due to misfit strain. A simple model of tetragonal distortion along the growth direction due to the lattice misfit is proposed to estimate the strain in InGaAs layer. However, the actual situation is much more complicated than this. A dislocation network was observed in the sample which was restricted to interface B only. The actual lattice misfit of the system can be higher than that estimated from a simple model since the dislocation network releases some of the lattice misfit strain in the system. On the other hand, accumulation of impurities at the interface could also give rise to extra strain in addition to the lattice misfit strain of the system and facilitate the nucleation of misfit dislocations at the interface. In this case, growth interruption occurred at interface B in order to change to a lower growth temperature for growth of the InP capping layer. As a result there exists a possibility of a very high impurity density at interface B compared with interface A. Hence the appearance of misfit dislocations at interface B is quite likely to be the result of a high impurity density. The obvious inequivalence of the interfaces A and B observed by fringe contrast analysis is possibly due to a difference of impurity density at the two interfaces. Impurity accumulation is also almost certainly responsible for the lattice displacement at the homogeneous interface C.

Differences between the interfaces A and B may cause uneven distributions of the strain in InGaAs layer so that the lattice distortion is

asymmetric at the interfaces A and B. As is shown in Fig.3-18, which is a CBED pattern taken from the InGaAs layer at the [001] zone axis (the central disk is indicated by letter T) we noticed that the pattern is asymmetric. The asymmetry may be seen between the growth direction [100] and the opposite direction [100] although the pattern is accurately oriented according to the Kikuchi line pattern. The above mentioned asymmetry is perhaps responsible. In the LACBED experiment, a loss of symmetry for the -g and +g sides of an 020 BF pattern was also noticed. The displacements of the inclined planes are larger for the +g side. A lattice surface relaxation effect may be responsible since the specimen thickness changes in the area of observation, getting thinner towards the +g side. Such effects complicate the estimation of the strain in the system.

The failure to detect very small residual strains in the sample by PL may be explained as follows. The PL peak position of the InGaAs QW emission corresponds to the energy gap in the quantum well. From the LACBED experiments we deduced that the InGaAs layer was in compression. This means that $a_0' > a_0$ or $x < 0.47$ which in turn leads to a decrease of the energy gap of the quantum well. On the other hand, the compressing stress introduced by the misfit strain in the system tends to increase the energy gap of the quantum well. The two opposite effects may compensate so that the PL peak position does not show a detectable change.

3-4 The CAT of GaAs/AlGaAs QW

The composition analysis of thickness-fringe(CAT) was performed on a wedge-shaped specimen, which was prepared by the cleavage method

described in Section 2-2-3. The analysis was based on the shift of equal thickness fringes as a function of the composition. An detailed experimental and theoretical investigation of this method have been done (H.Kakibayshi 1985, 1986, 1987; D.J.Eaglesham 1987; A.F.de Jong 1988). The geometry of CAT observation is shown schematically in Fig.2-4. The electron beam is incident along [001] and parallel to the interface. The exact [001] zone axis condition is preferred in order to get high resolution CAT images. The advantages of CAT observation are the quick and simple specimen preparation, the straightforward evaluation of the results about interface abruptness and composition uniformity of the multilayer structures. These are very helpful in finding the proper growth conditions. Fig.3-19(a) is a CAT image taken from a GaAs/AlGaAs QW sample NU210S. As we can see, the detailed structure of the sample is clearly shown. Three sets of QW's, each containing five wells, are separated respectively by thick AlGaAs and GaAs layers. A periodic fluctuation of the thickness fringes in individual AlGaAs layers is just apparent in an enlarged picture shown in Fig.3-19(b). On the other hand, the fringes remain undisturbed in the GaAs layers. The fluctuation of thickness fringes i.e. the fluctuation of composition of the AlGaAs layer is a result substrate holder rotation during MBE growth. It can be eliminated by adjusting the rotation speed.

CAT observations were routinely performed on specimens studied in this work.

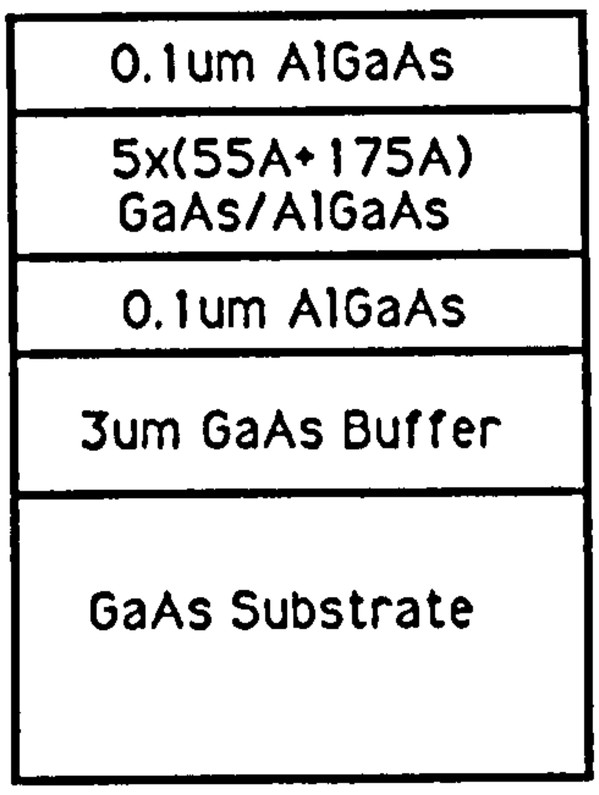

(a) Sample G43

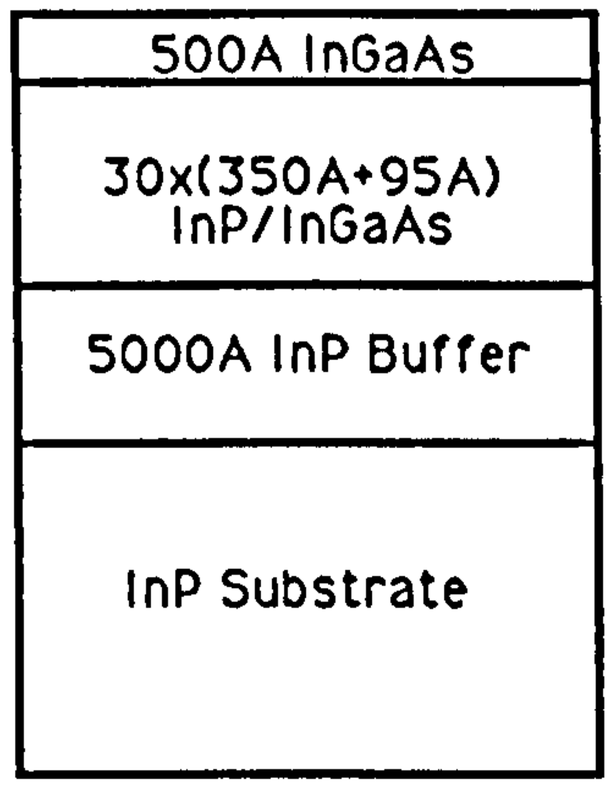

(b) Sample OE61

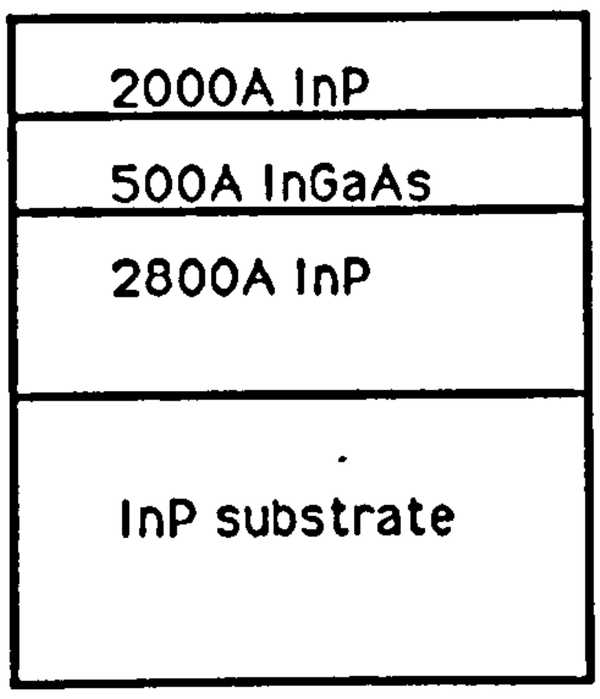

(c) Sample 5902A

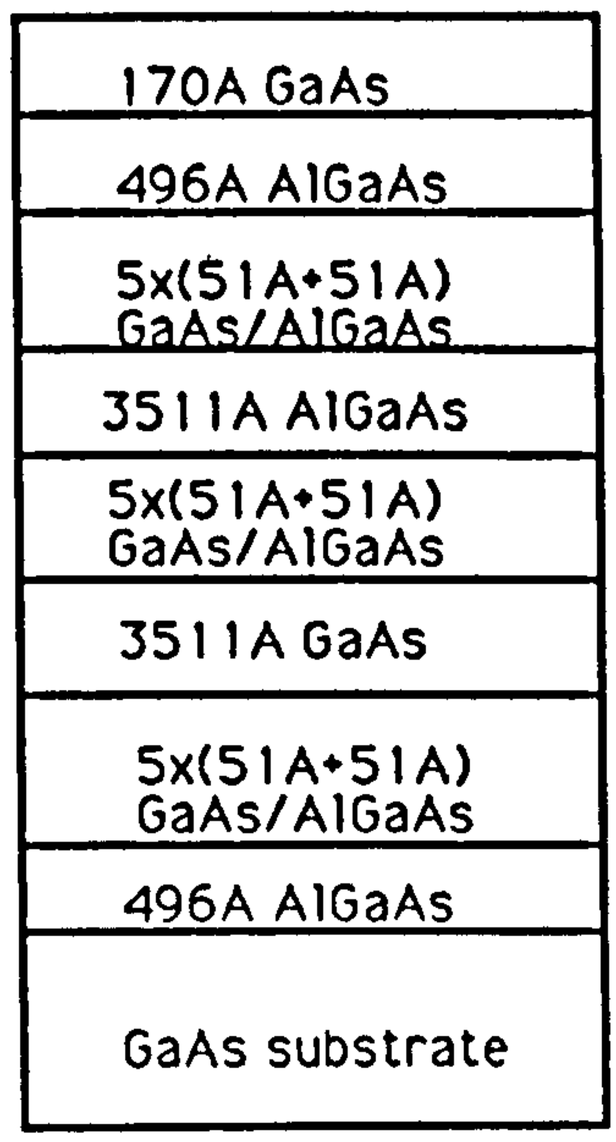

(d) Sample NU210S

Fig.3-1 The structures of sample G43,0E61,5902A & NU210S.

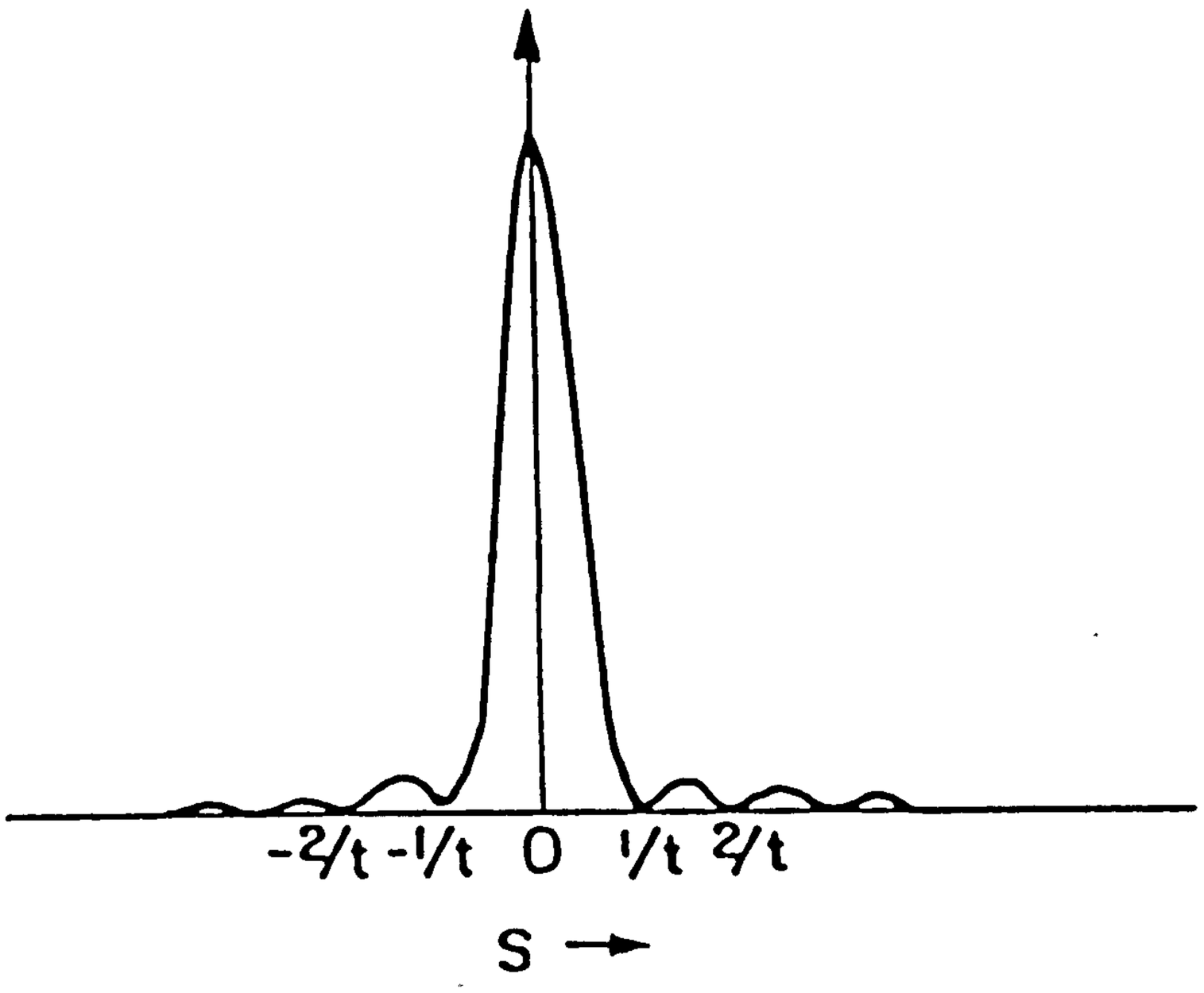

(a)

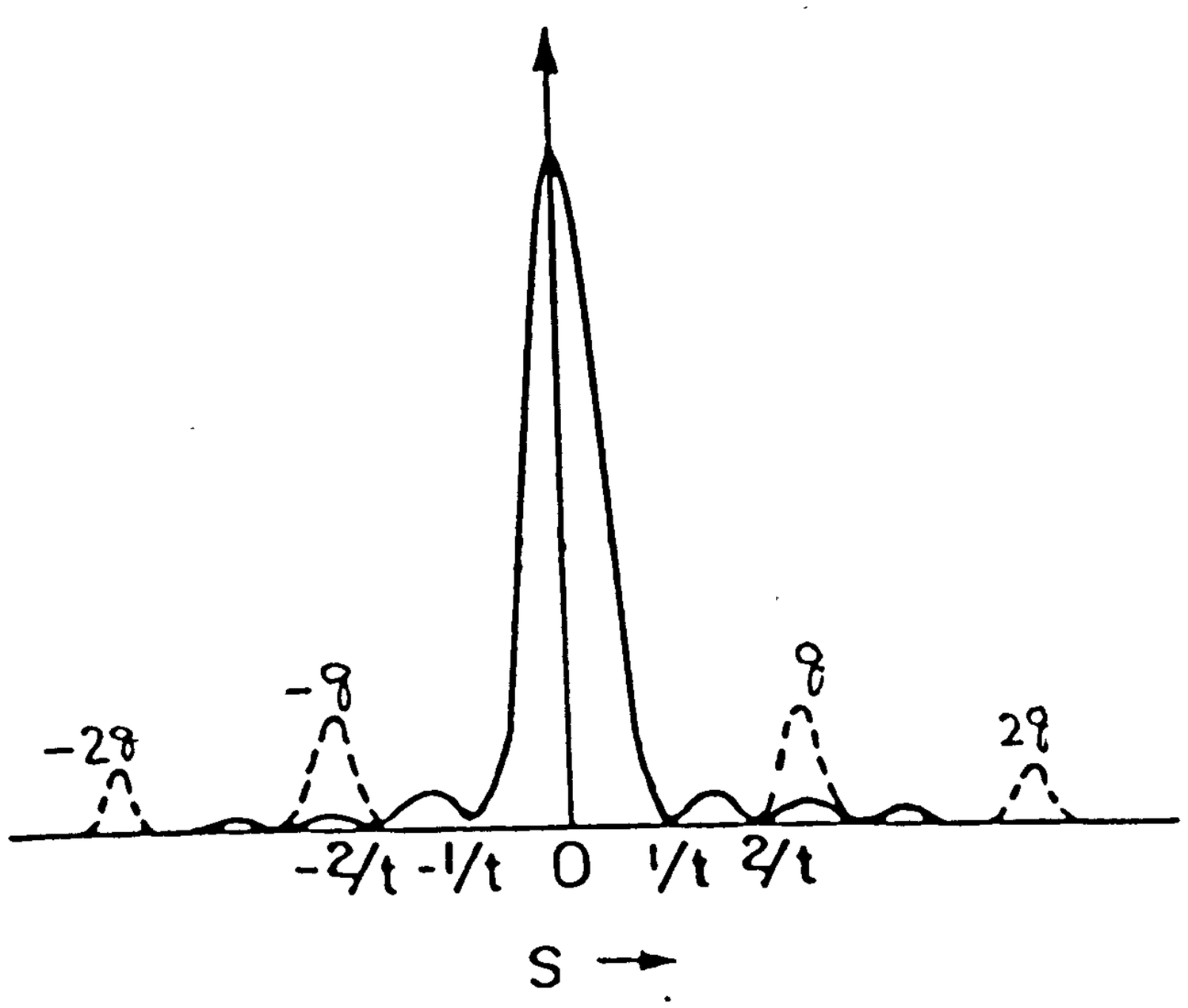

(b)

Fig.3-2 The kinematical intensity distribution along s direction
a) for thin film of single layer
b) for thin film contained mutilayer structure

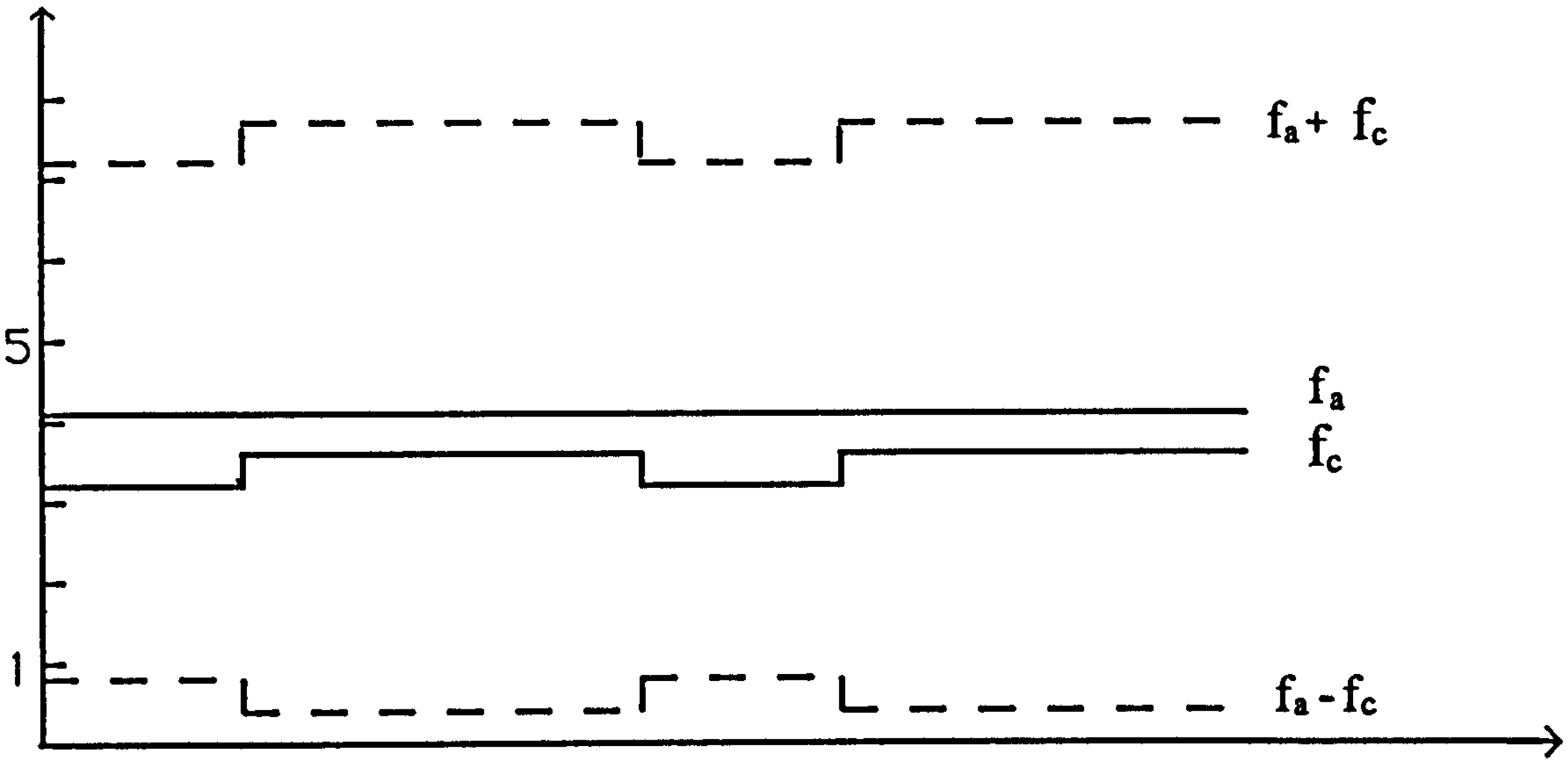

Fig.3-3 The schematic diagram of structure factor modulation in GaAs/AlGaAs multilayer structure, z is growth direction (s=0.2).

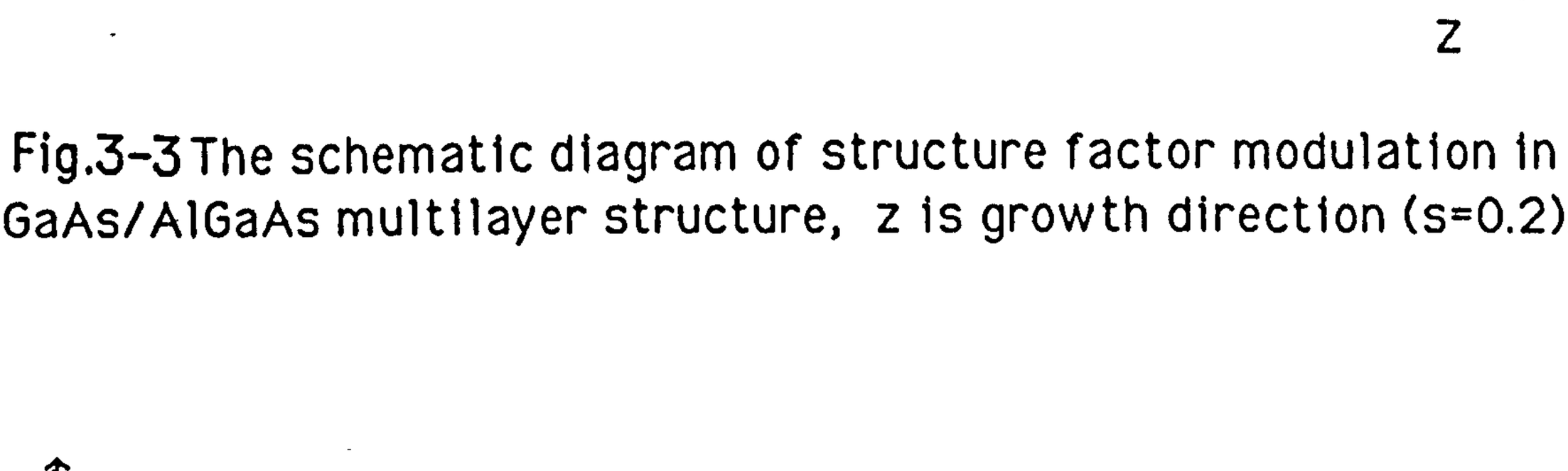

Fig.3-4 The schematic diagram of structure factor modulaton in InGaAs/InP multilayer structure, z is growth direction (s=0.2).

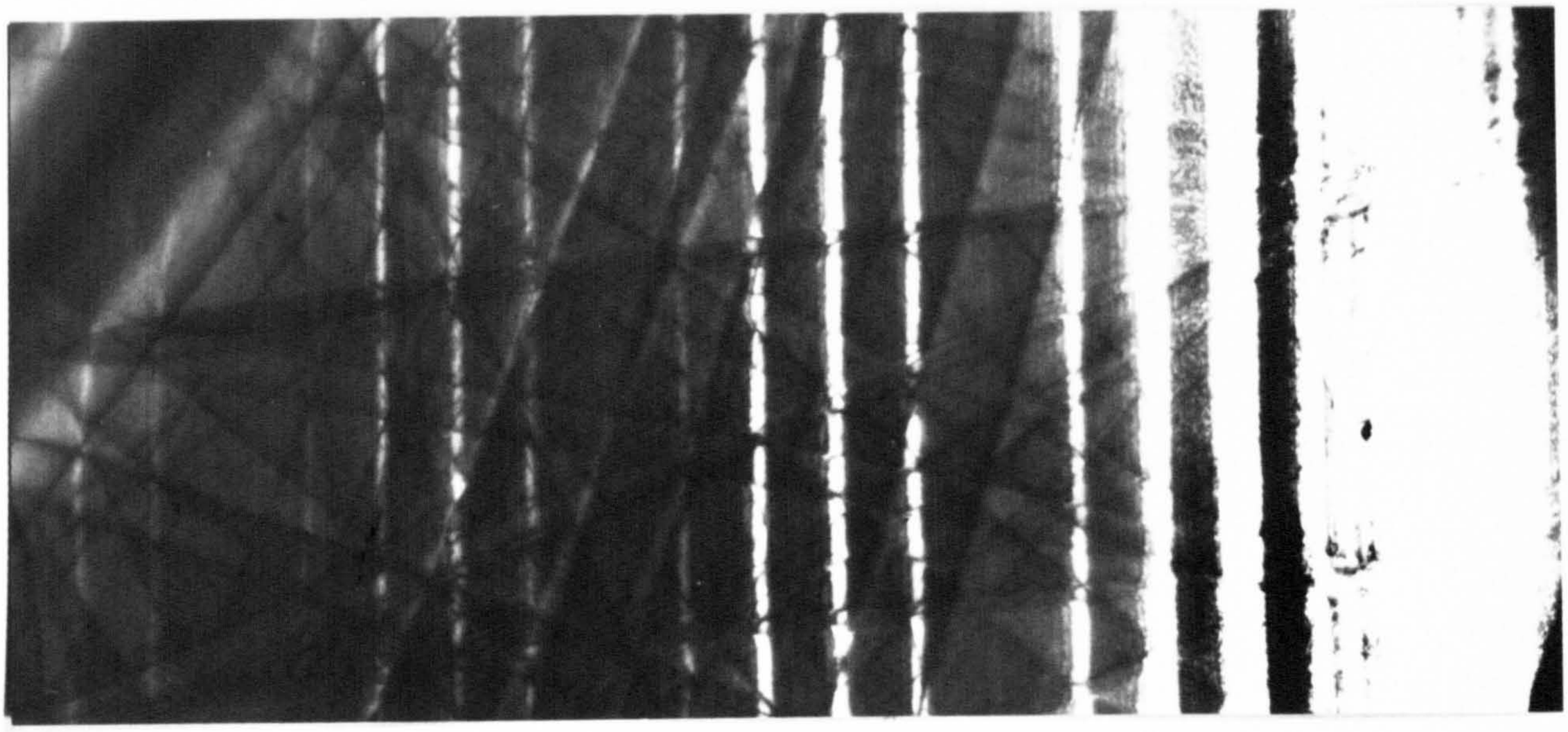

Fig.3-5 200 DF LACBED pattern from InGaAs/InP QW sample OE61

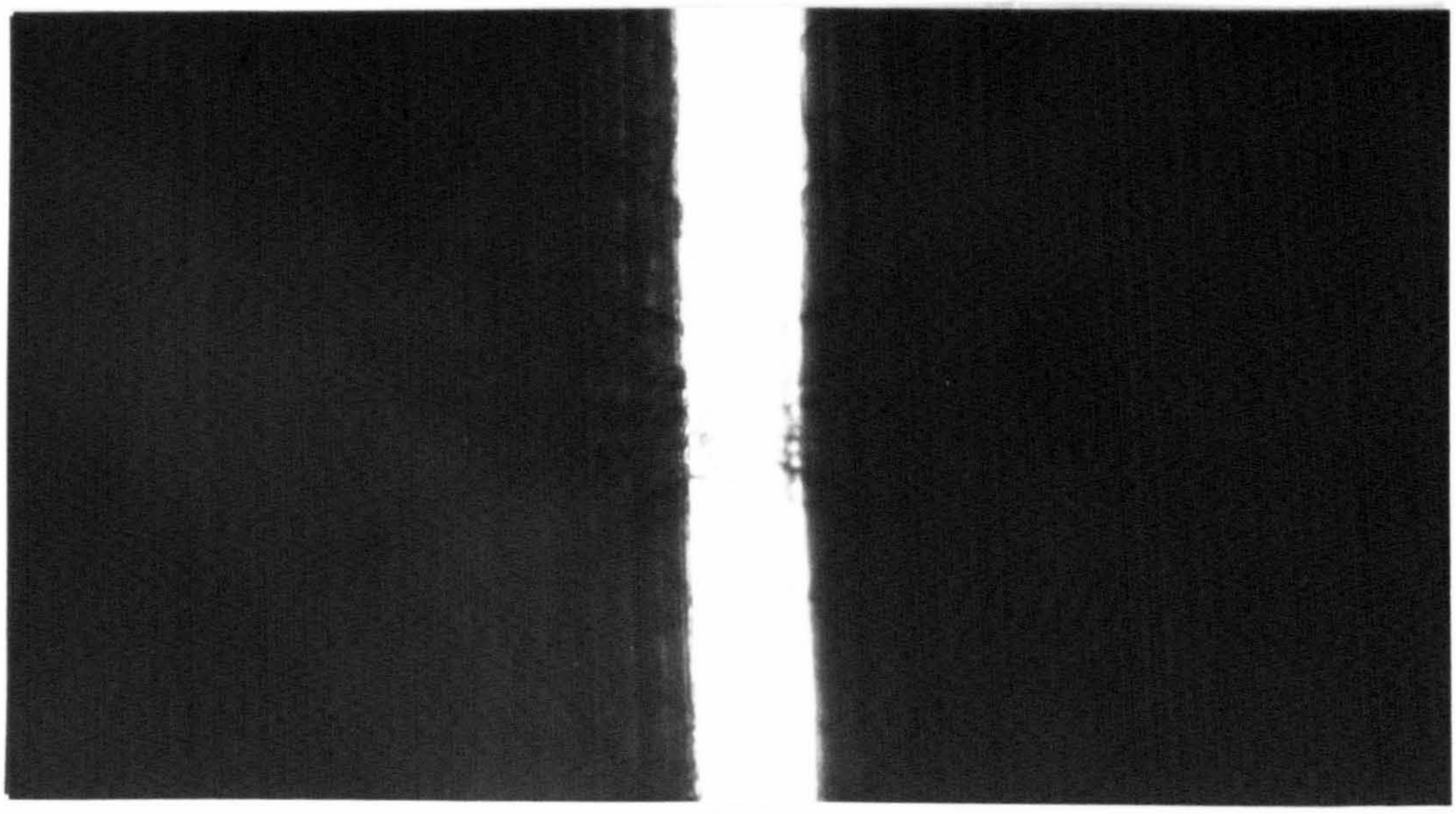

Fig.3-6 400 DF LACBED pattern from the same sample as above.

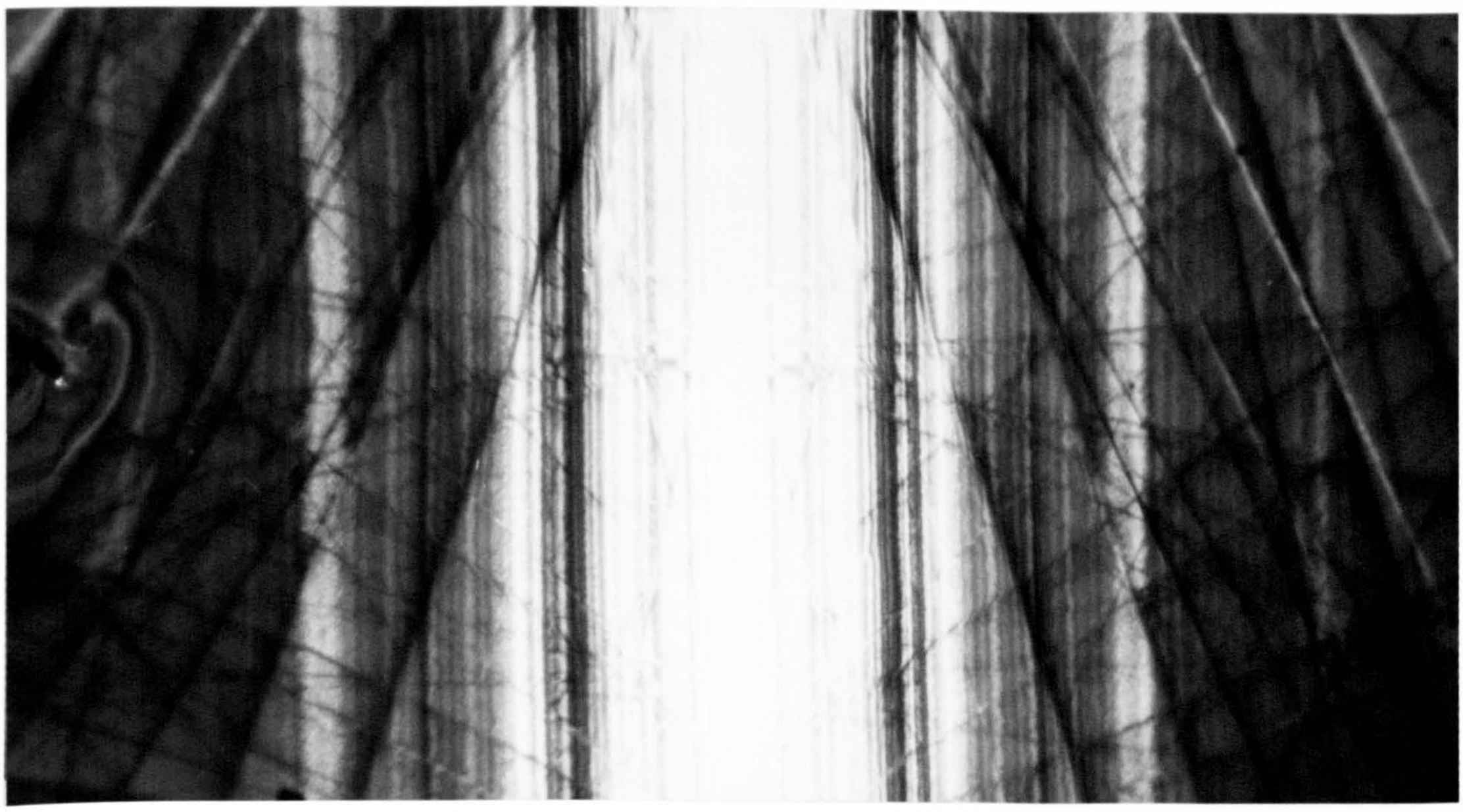

Fig.3-7 200 DF LACBED pattern from GaAs/AlGaAs QW sample G43

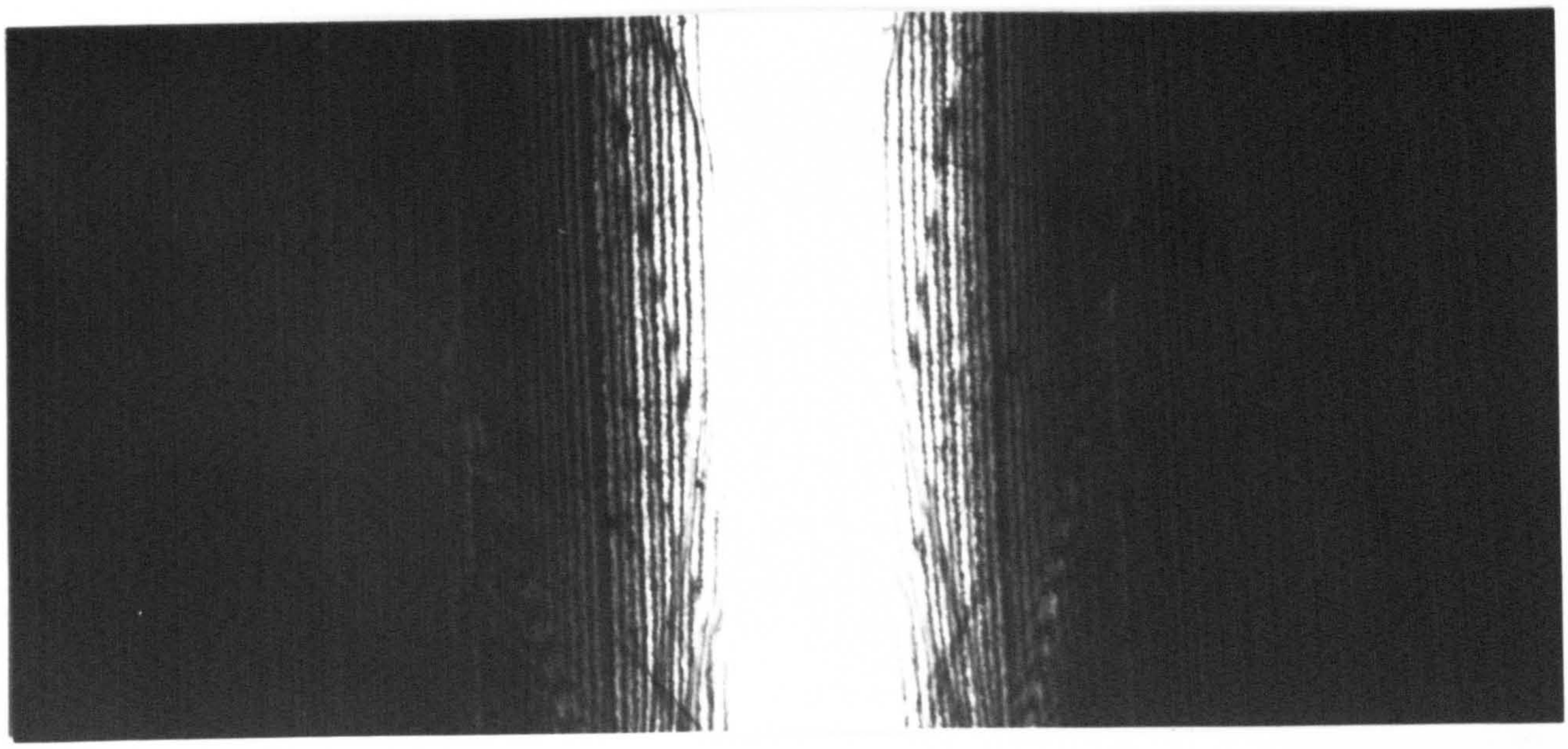

Fig.3-8 400 DF LACBED pattern from the same sample as above.

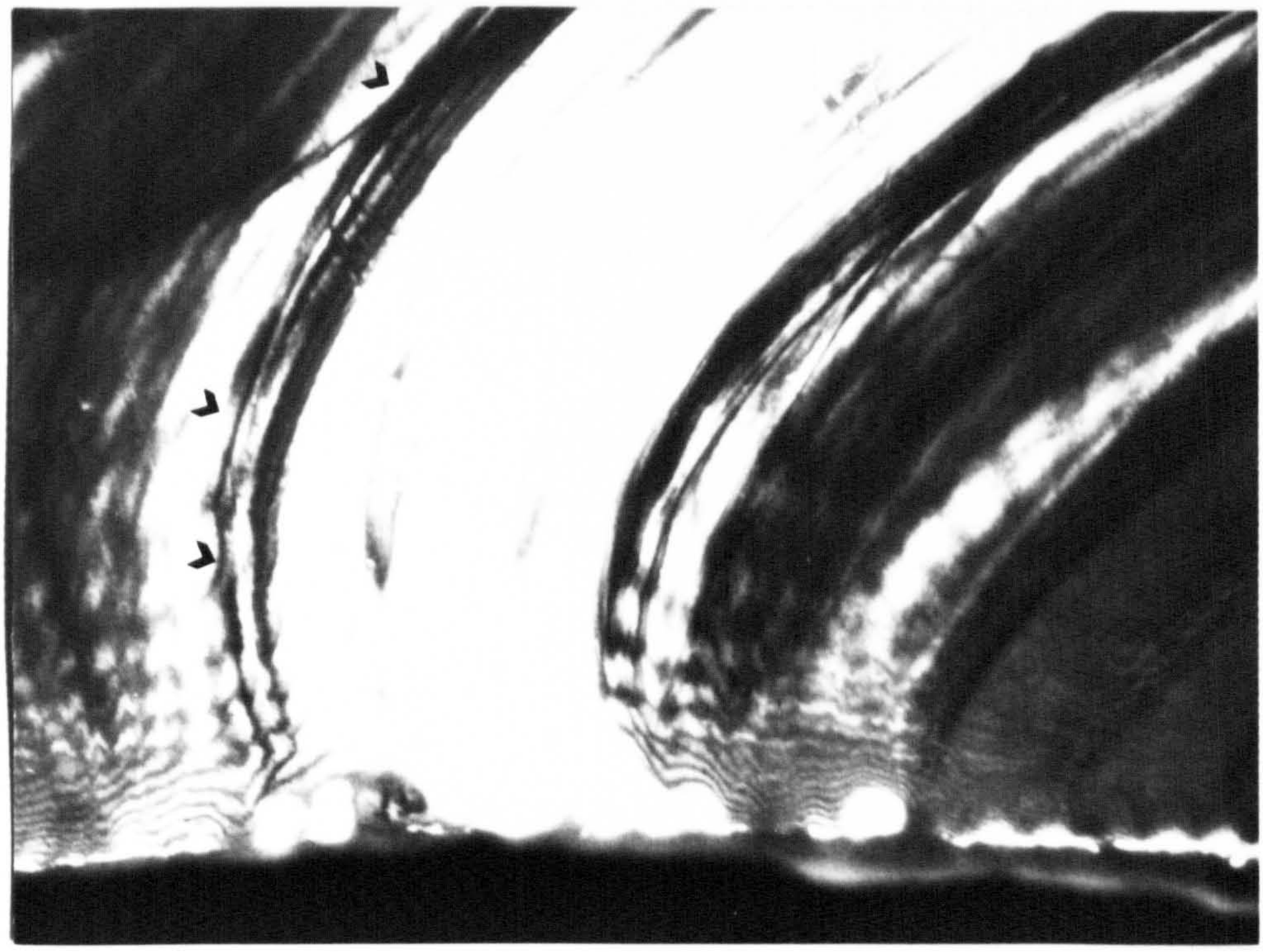

Fig.3-9 200 DF LACBED pattern from the edge of a hole created by PIMS in GaAs/AlGaAs QW sample G43.

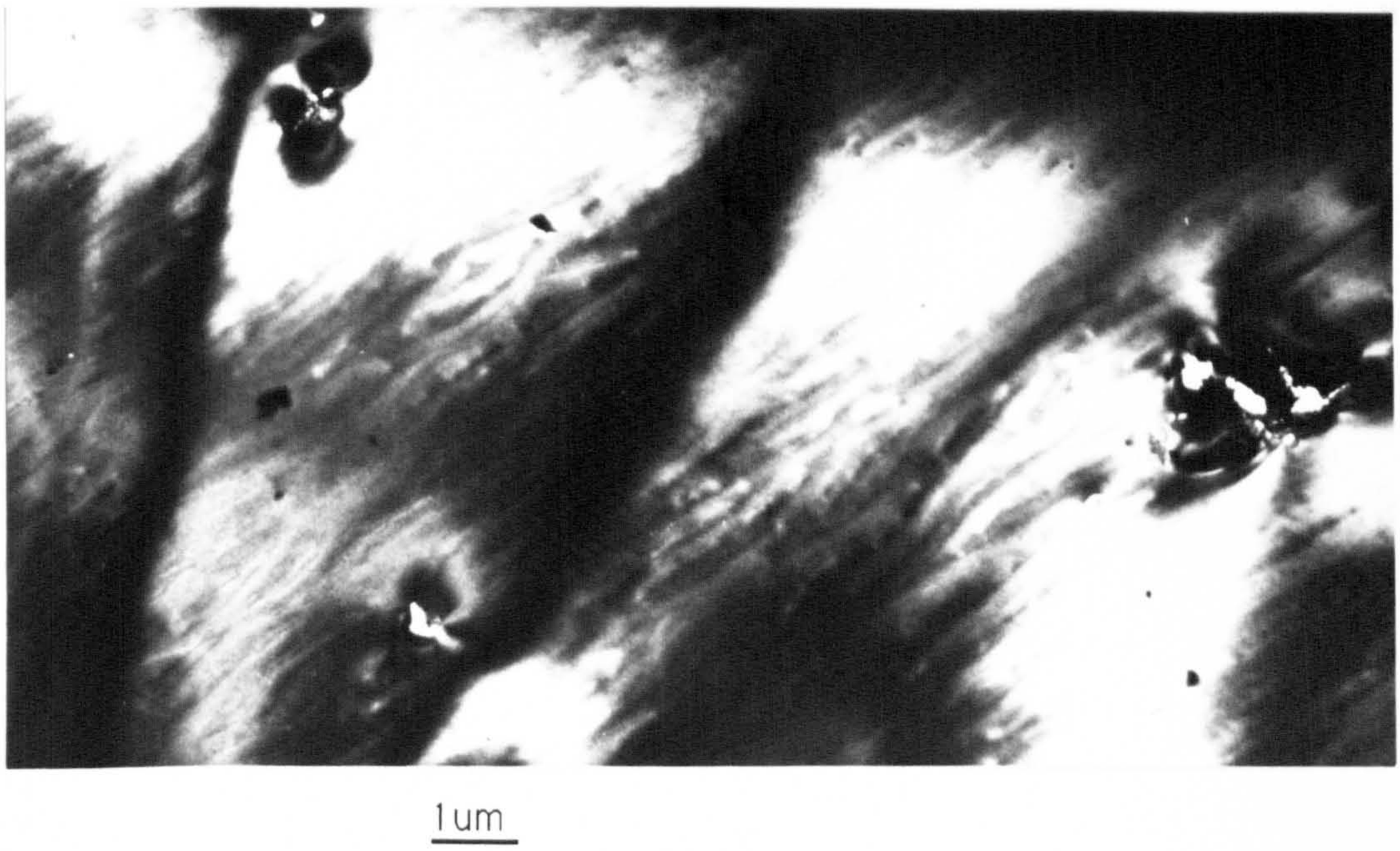

Fig.3-10 The DF image of QW reflection shows the linear contrast along a 110 direction

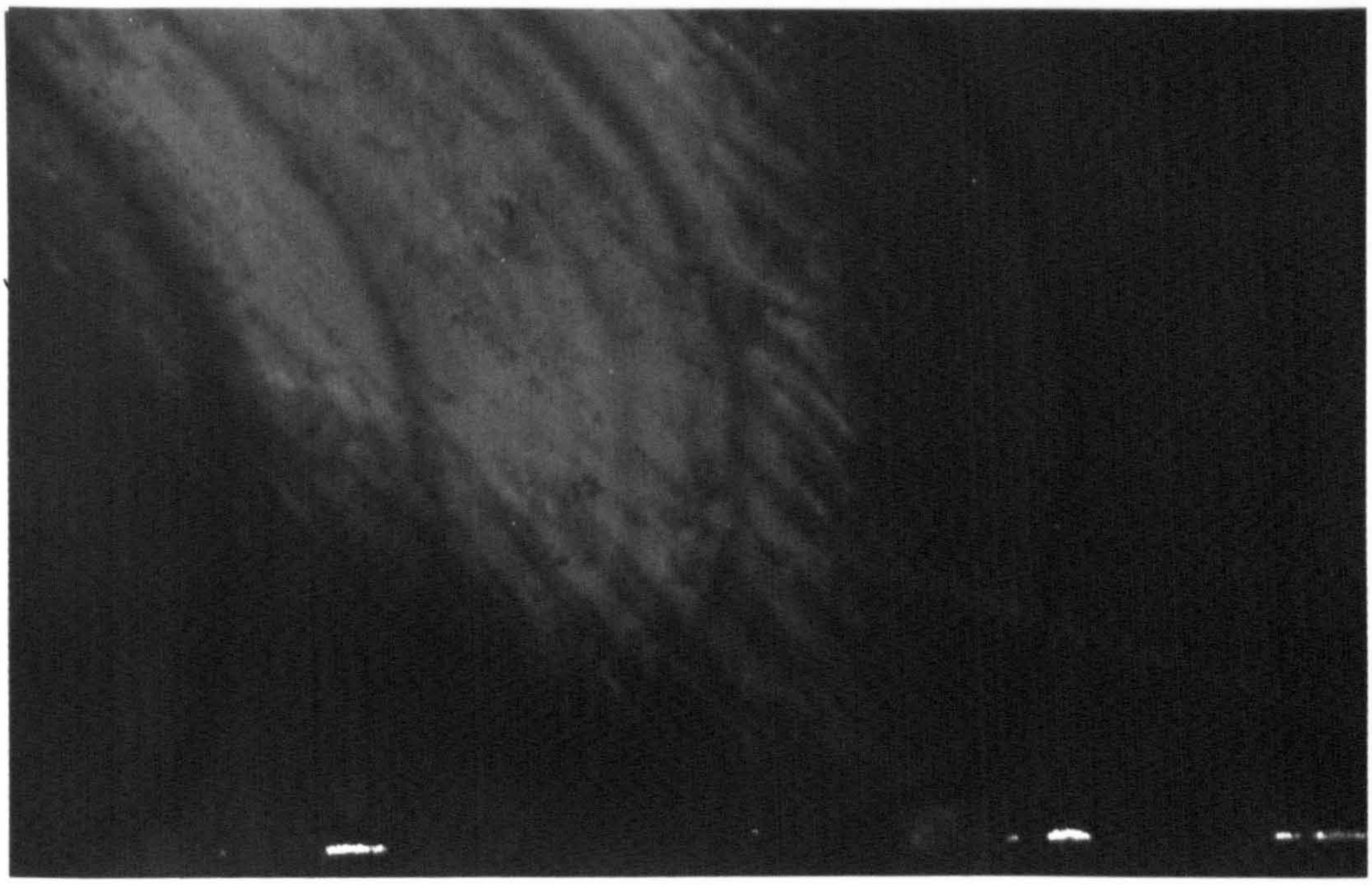

1um

(a)

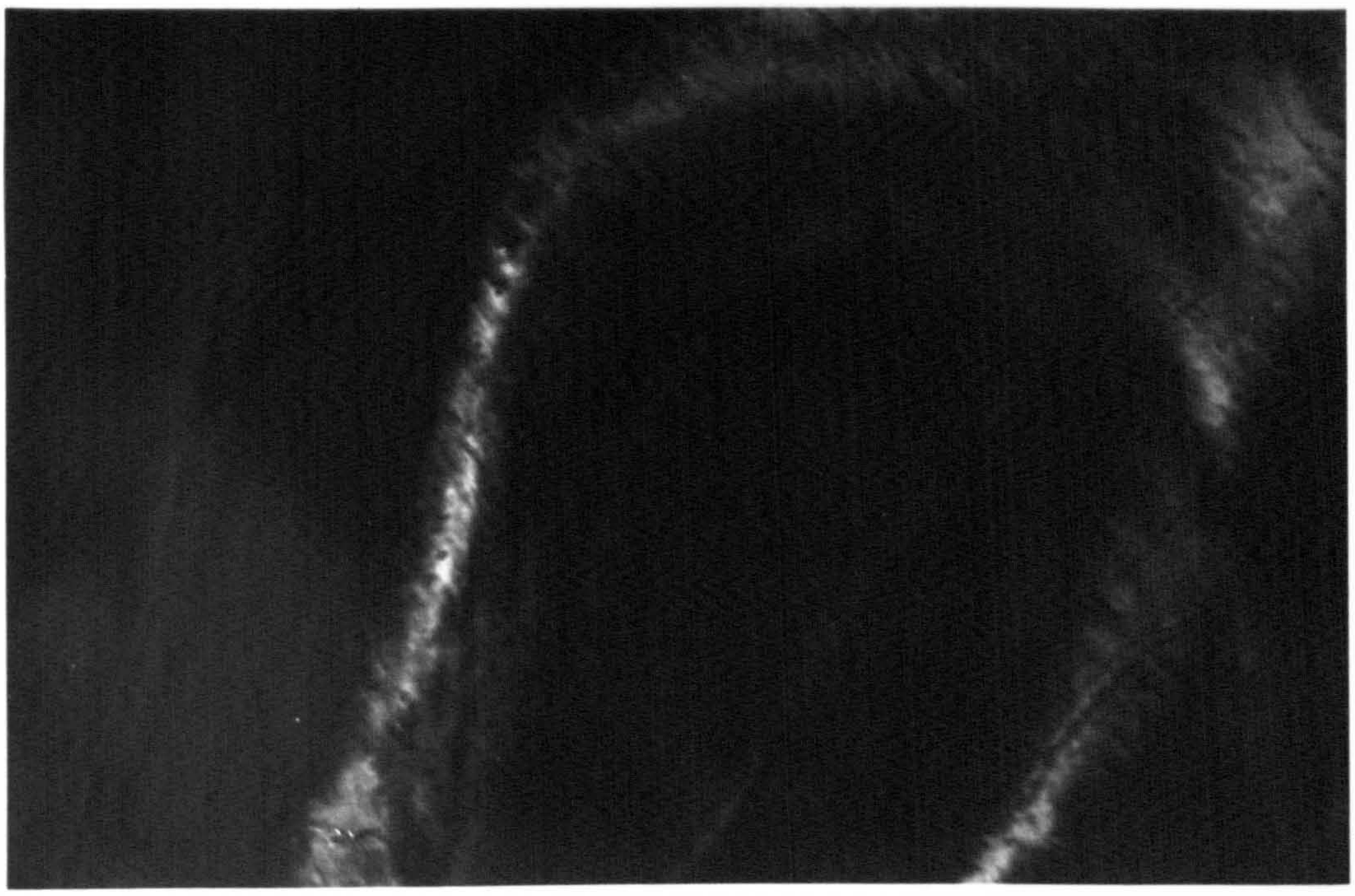

(b)

Fig.3-11 a) DF image of QW reflection from sample G43 before thinning by PIMS

b) DF image of QW reflection from the same area as above after 115 minutes thinning by PIMS

(a)

$\longrightarrow$ +g

$\bar{2}\bar{8}0$

220

(b)

080

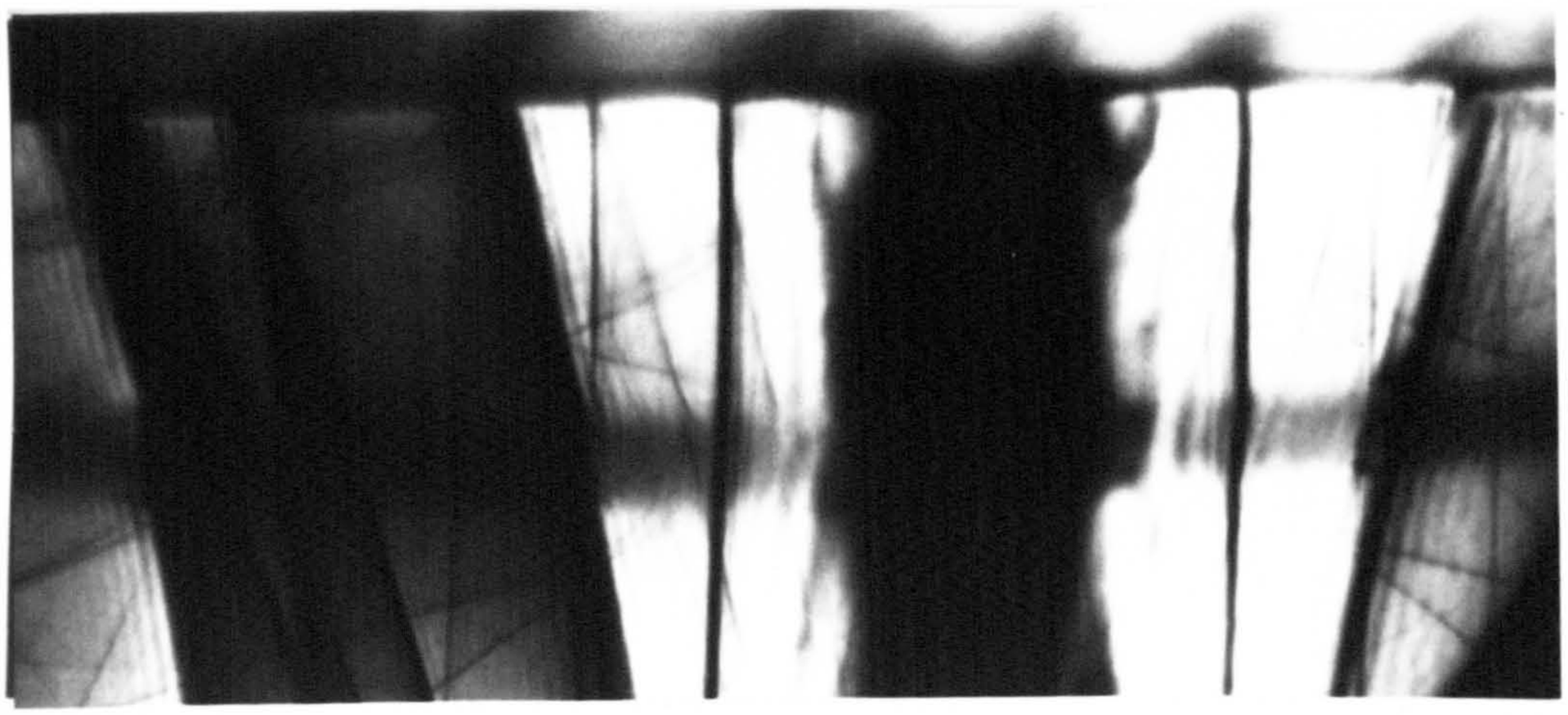

(c)

Fig.3-12 a) 020 BF LACBED pattern from [001] cross section specimen,
b) 220 BF LACBED pattern from [001] cross section specimen,
c) $02\bar{2}$ BF LACBED pattern from [011] cross section specimen.

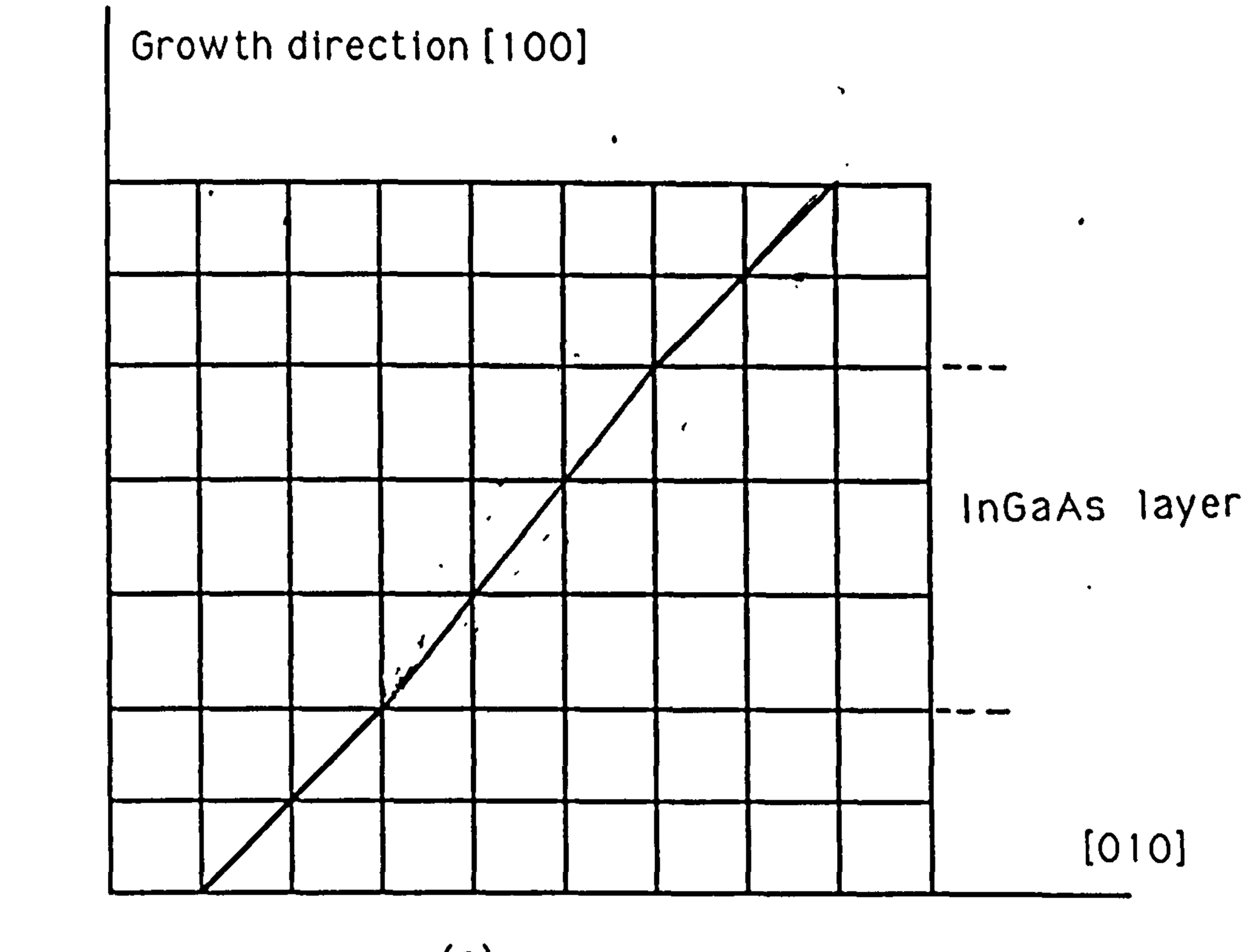

Fig.3-13 The schematic diagram showing tetragonal distortion of InP/InGaAs/InP sandwich structure, a) InGaAs layer in compress. b)

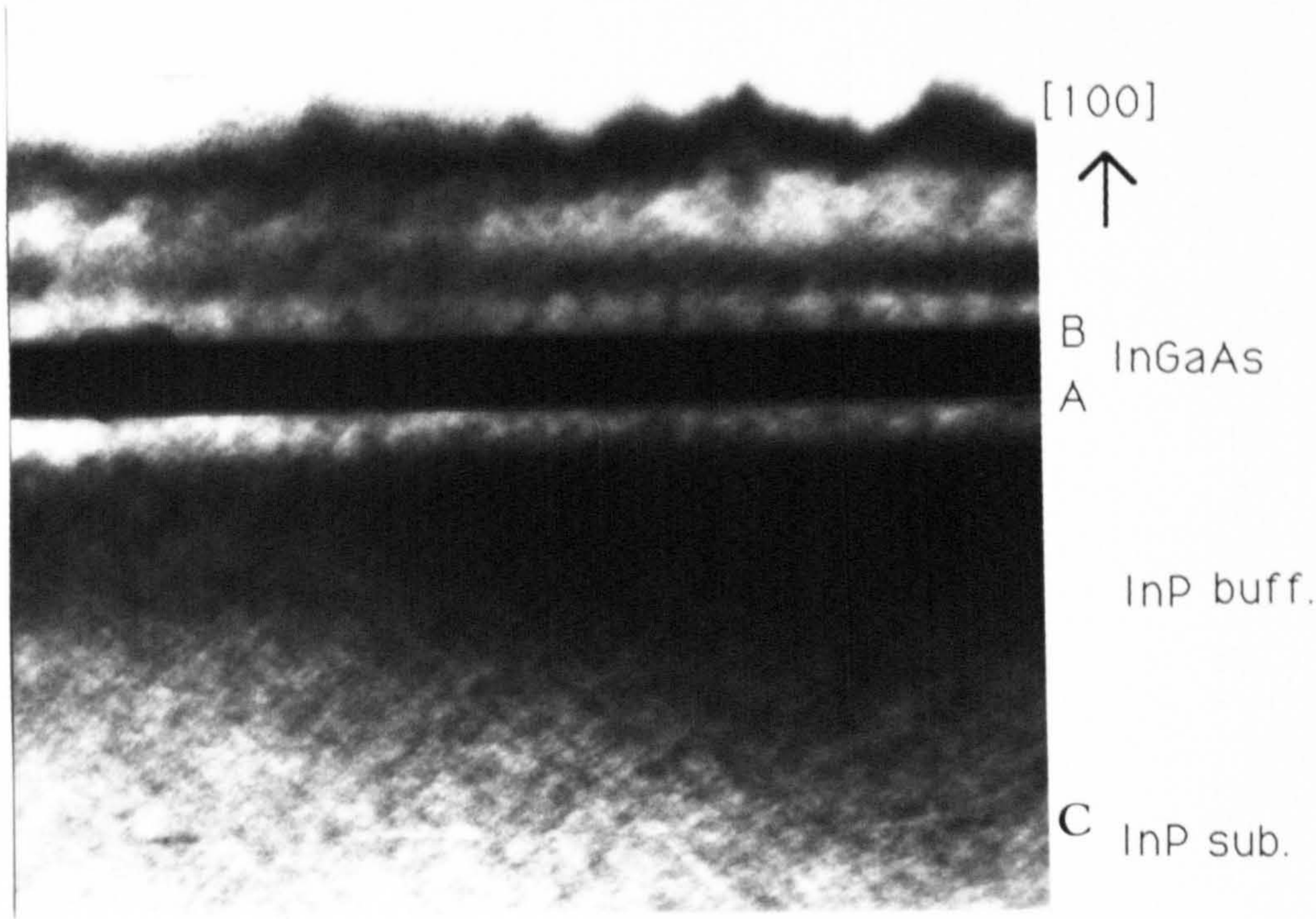

Fig.3-14 A 200 BF image showing the structure of the sample 5902A

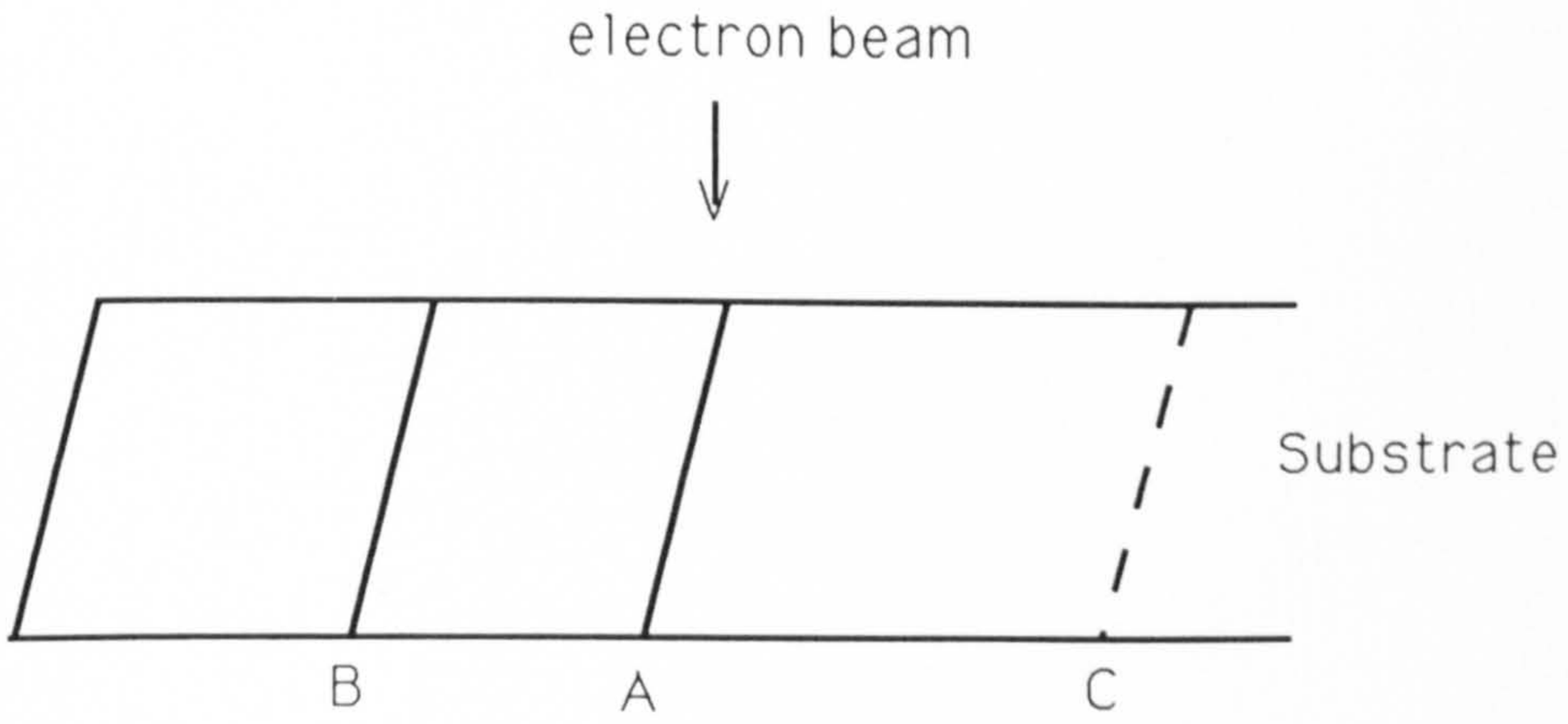

Fig.3-15 The geometry of the interfaces in a microscope after the specimen being tilted.

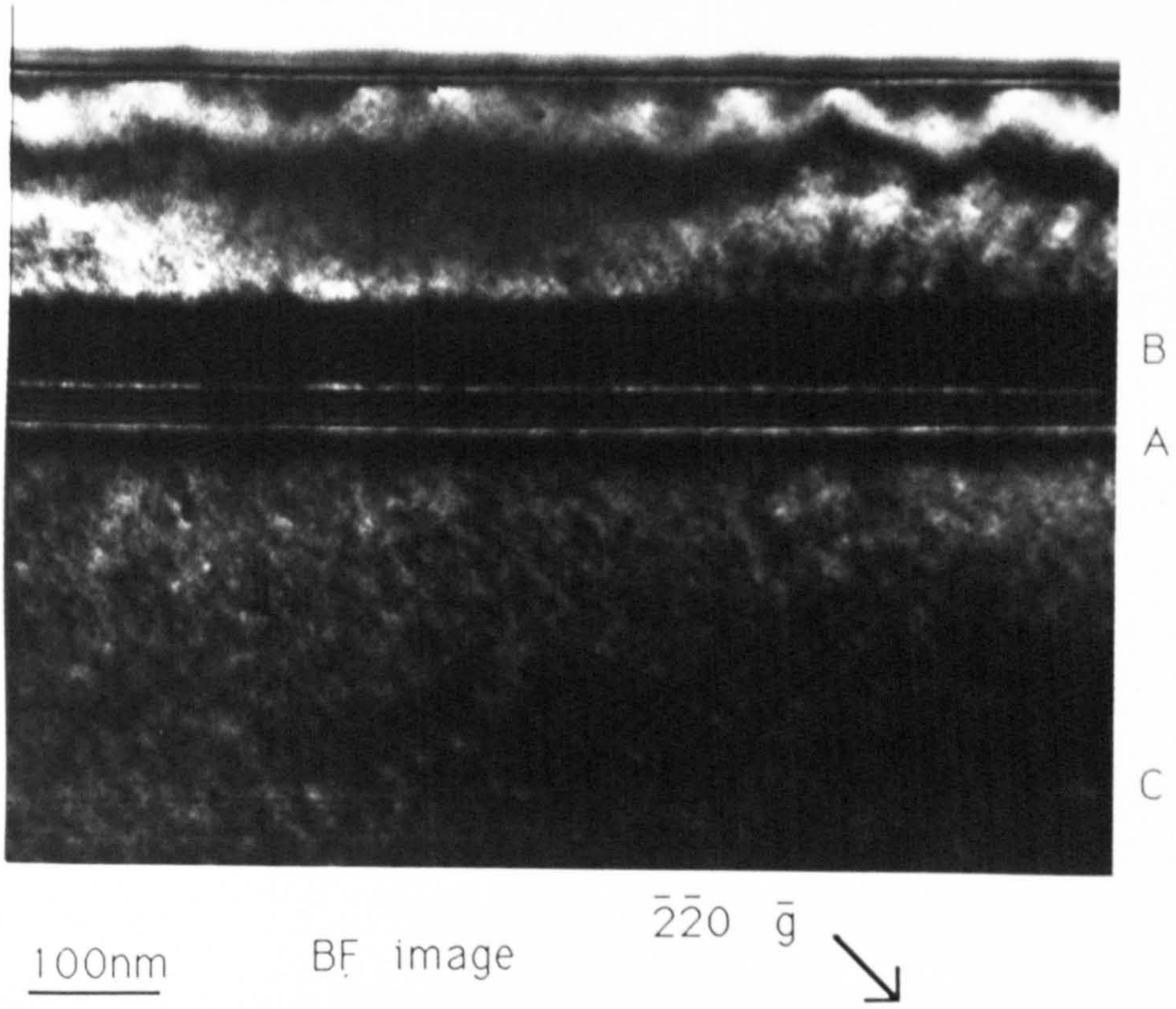

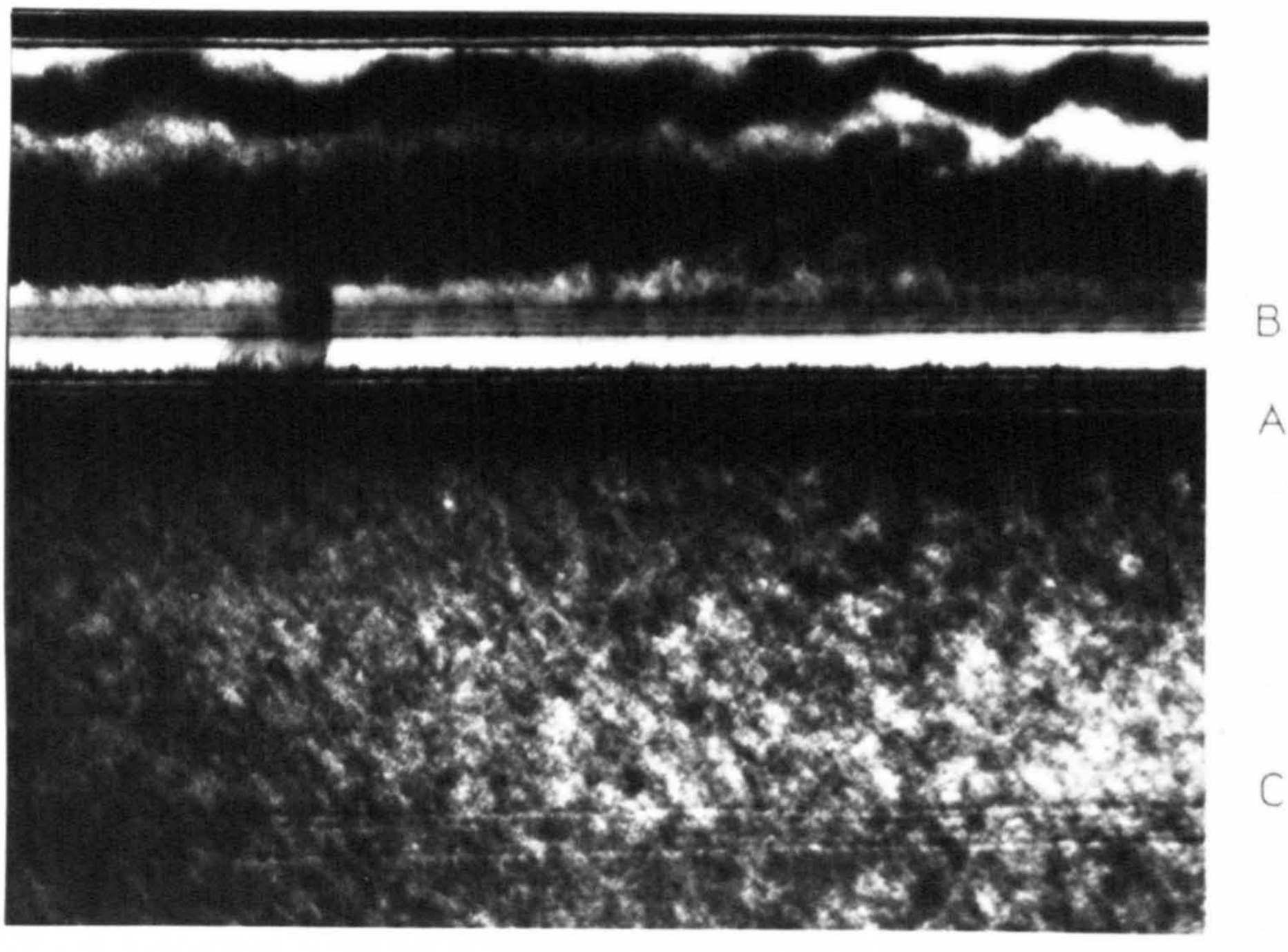

Fig.3-16 $\bar{2}\bar{2}0$ two beam BF and DF image pair at s=0 from [001] cross section specimen of sample 5902A with inclined interfaces.

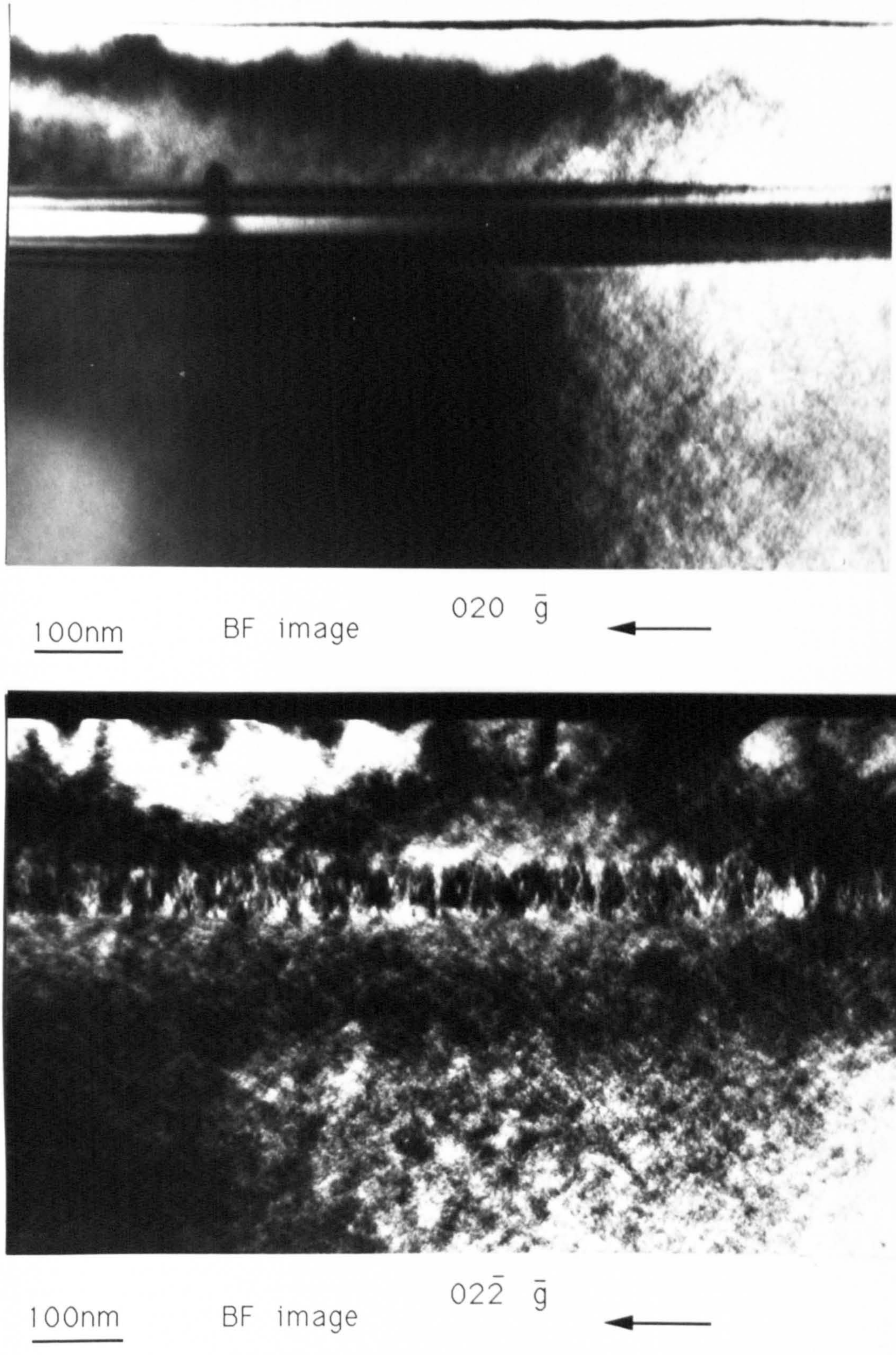

Fig.3-17 a) 020 two beam BF image with s=0, inclined angle of about 10' from [001] cross section specimen of sample 5902A. b) $02\bar{2}$ two beam BF image with s=0, inclined angle of about 10' from [011] cross section specimen of sample 5902A.

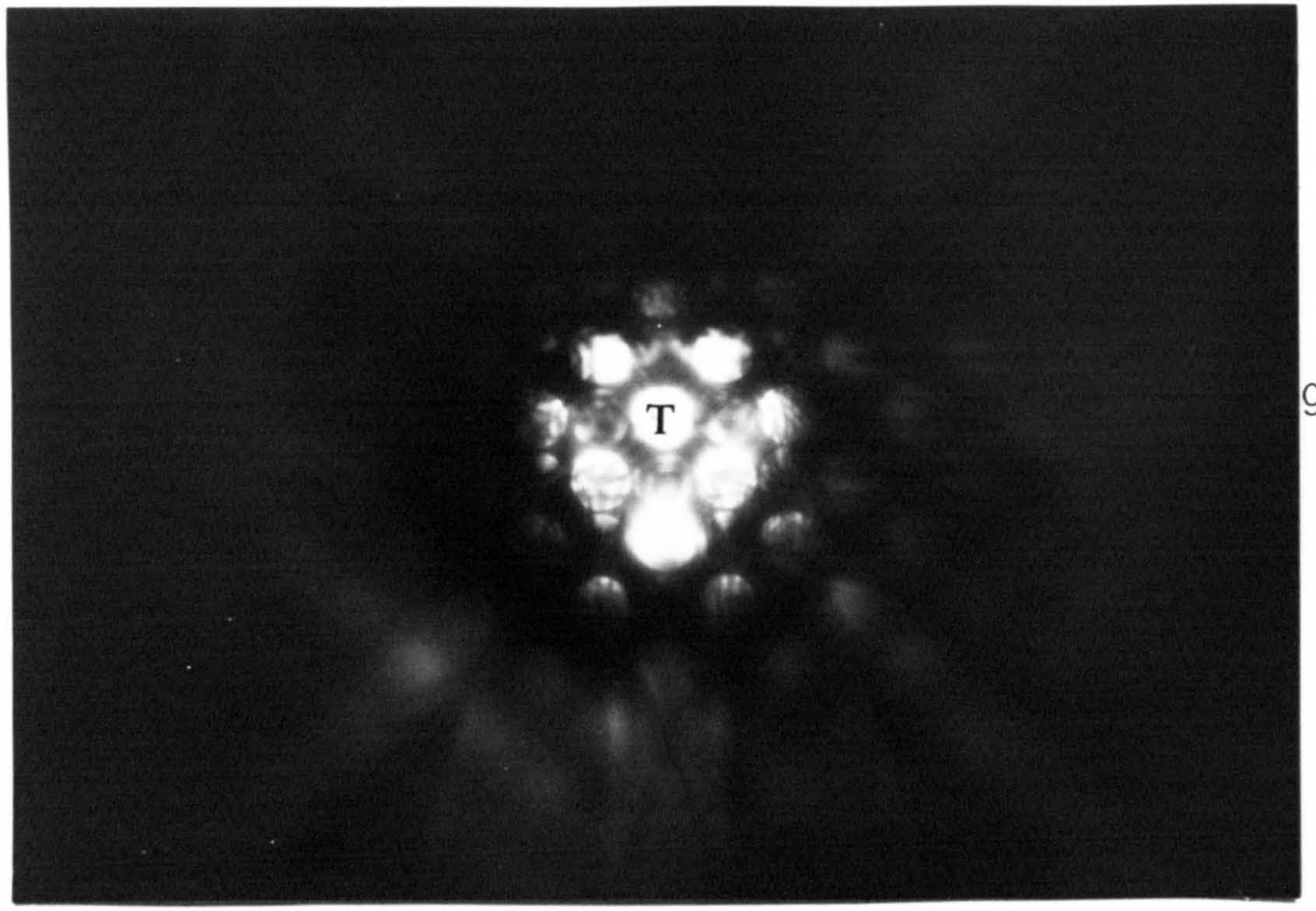

Fig.3-18 001 CBED pattern taken from InGaAs layer.

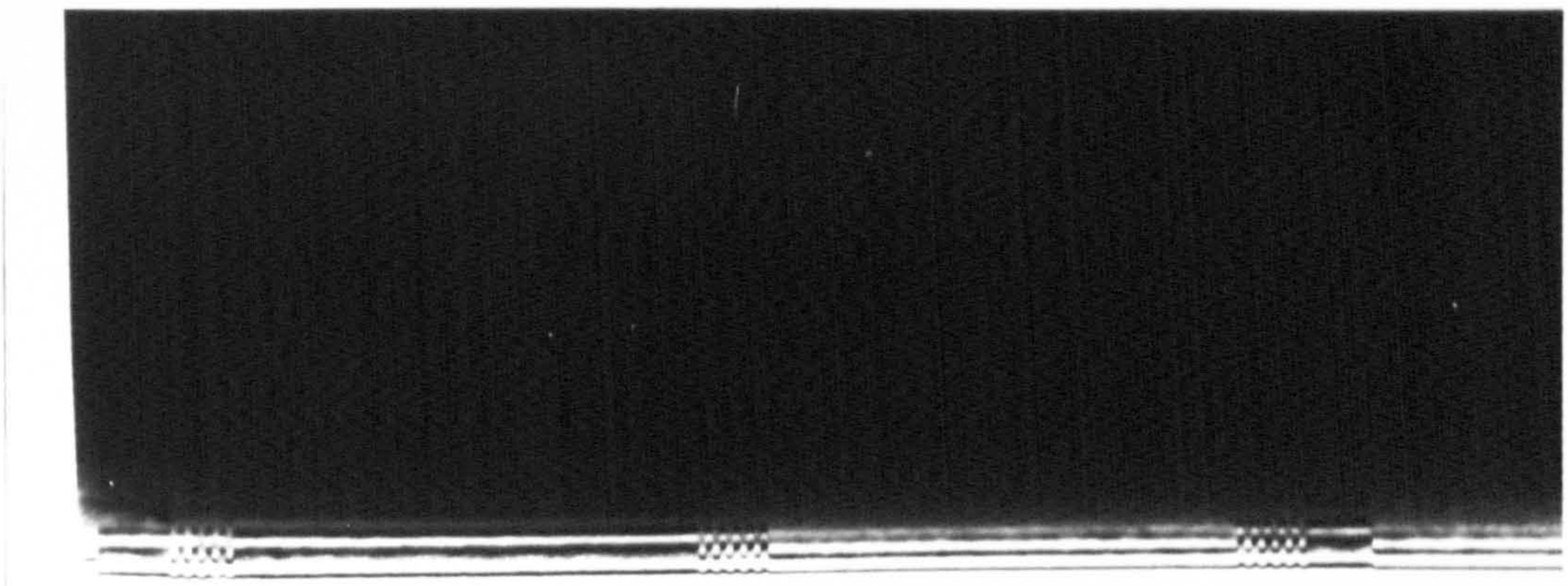

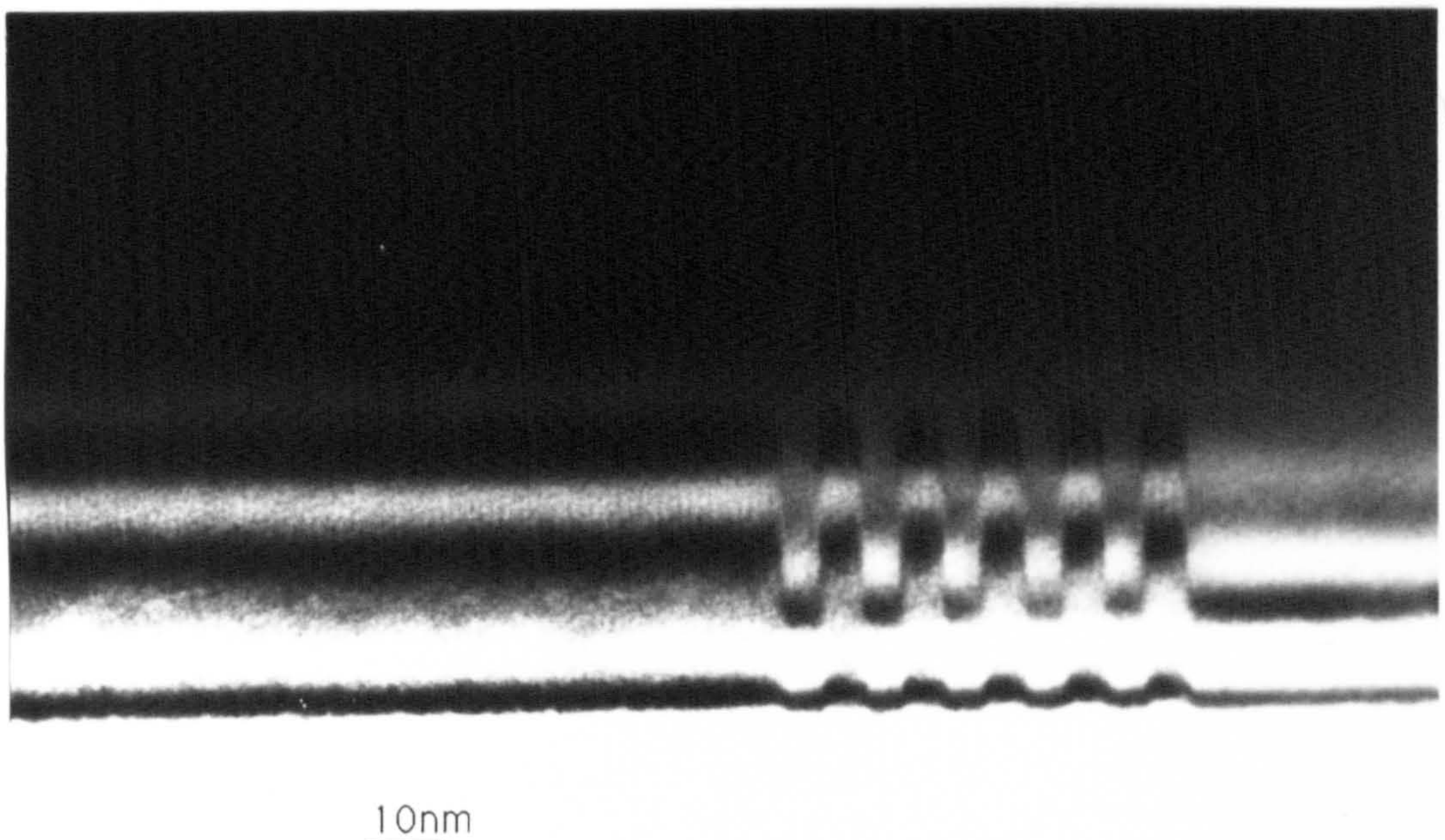

(b)

Fig.3-19 a) TEM image from a wedge-shaped specimen of sample NU210S shows the layout of the sample structure, b) Enlarged image of the above picture from the area around QW-2.

Chapter 4 The Studies of MBE-grown GaAs/AlGaAs MQW structures by CL

Low temperature CL has been applied to study MBE grown GaAs/AlGaAs MQW samples NU210S and NU305. The extrinsic luminescence properties of as-grown and thin cross section specimens of sample NU210S are discussed. The experimental results, which include the CL spectra, excitation power dependent and electron beam accelerating voltage dependent CL spectra, and monochromatic CL images and line scan profile analysis, are explained based on the discussions in Chapter 1. The effects of the AlGaAs barrier layer thickness and GaAs QW well width on the luminescence efficiency are discussed depending on the carrier capture and confinement effects.

4-1.Extrinsic Luminescence of Sample NU210S

It is well known that in high quality unintentionally doped GaAs/AlGaAs QW structures optical spectroscopies display mainly excitonic features partly due to the enhancement of the exciton binding energy (C.Weisbuch 1981 1987; G.Bastard 1988). The luminescence spectrum appears to be essentially intrinsic, in remarkable contrast with thick GaAs of

comparable purity in which the transitions due to bound excitons, electron to neutral acceptors (e-A°), holes to neutral donors (D°-h) and donor-acceptor pairs (D°-A°) are usually dominant. The simpler QW luminescence may be the result of trapping of excitons at interface defects, which prevents the excitons from reaching the impurities, or from the decrease of the exciton lifetime due to the increase of the overlap of electron and hole wavefunction in QW, which increases the exciton recombination efficiency and implies that unless the impurity separation in the QW is comparable with the free exciton diameter, the free exciton recombines before it is captured by a impurity.

However experimental observations of acceptor related features in PL spectra of non-intentionally doped MBE grown GaAs/AlGaAs QW's have been reported. It is believed that the impurities were randomly distributed throughout the wells in MQW structures (R.C.Miller 1982[1]&[2] 1983; P.M.Petroff 1984), or were segregated near the invert interfaces (AlGaAs-GaAs interface) in the case of single and double QW structures (W.T.Masselink 1984; M.H.Meynadier 1985). An explanation of the origin of the impurities is that the impurities are probably carbon which is less soluble in AlGaAs than in GaAs and is well known background impurity in MBE grown GaAs (G.B.Scott 1978). Thus , as the AlGaAs grows, an ever increasing amount of carbon floats at the AlGaAs-vacuum interface. After the growth of a thick AlGaAs layer, a great amount of these impurities is trapped in the first few QW's in a MQW structure or in the first few monolayers of GaAs and results in interface roughness.

Donor related emission in PL spectra has also been reported in nominally undoped MBE grown GaAs/AlGaAs MQW structures (B.Lambert 1982; D.C.Reynolds 1984; P.W.Yu 1985). Very sharp extrinsic emissions of

donor bound excitons (D°-X) and hole to neutral donors (D°-h) were identified in the thick MQW structures ($L_z \geq 100Å$) in their work.

In this work, a MBE grown, unintentionally doped GaAs/AlGaAs MQW sample (NU210S) was examined by the low temperature CL technique. The layout of the sample is shown in Fig.3-19(a). Three sets of QW's, each containing five wells, are separated respectively by thick AlGaAs and GaAs layers. The intentionally grown GaAs well widths and AlGaAs barrier thickness were both 51Å and the Al concentration in all of AlGaAs layers was 33%. The initial aim of studying this particular sample was to investigate the effect of different growth sequences on QW luminescence properties.

4-1-1 The observation of as-grown sample

Bulk as-grown specimens were prepared by cleaving the sample along (110) planes. The CL observations were carried out either in the plan view specimens with the incident electron beam perpendicular to the sample growth surface or in the cross-section specimens with the incident electron beam perpendicular to the cleavage surface.

A typical low temperature CL spectrum of this GaAs MQW sample, observed from as-grown specimens with the electron beam accelerating voltage at 20kV and within a period of one year after MBE growth, is shown in Fig.4-1(a). One line luminescence structure, as is well understood (C.Weisbuch 1981, 1987; G.Bastard 1988), corresponds to an n=1 electron-heavy hole (e-hh) exciton transition with the emission energy at 1.617eV. The FWHM (full width at half maximum) of the emission is 6meV and can be explained as a result of the interface roughness of one monolayer step-like islands with lateral size about 100Å in the QW (J.Singh 1984 and 1985). A change of QW emission

energy of about 10meV was observed during the study. Fluctuations of the GaAs QW width and AlGaAs barrier composition from place to place are possibly responsible. Some evidence of the latter can be deduced from CAT analysis in Section 3-4, where the CAT fringe fluctuation in the AlGaAs layers along growth direction can just be seen in Fig.3-19(b). The fact that CAT fringes are related to the substrate rotation during growth implies that an in-plane composition fluctuation exists at the AlGaAs growth front.

Apart from the e-hh exciton emission, we note that at the energy region below the QW emission there is additional luminescence. To make this feature clear, a spectrum was acquired at low excitation level and is displayed in Fig.4-1(b). A very broad extrinsic emission band with the intensity maxima at energies of 21meV and 32meV below the QW emission can just be recognized. The energy positions, the breadth and the saturation of the emission at high excitation level suggest that the emission is impurity related. The impurity binding energy E_i^B can be estimated from the expression $E_i^B = E_x^{e\text{-}hh} - E_i + E_x^B$ where E_x^B is the ground state heavy hole exciton binding energy, $E_x^{e\text{-}hh}$ is the n=1 e-hh exciton emission energy and E_i is the impurity emission energy. In this case the heavy hole exciton binding energy is about 9meV (G.Bastard 1988), so the impurity binding energies corresponding to the two intensity maxima are 30meV and 41meV respectively. Comparison with the theoretical predictions (see references listed in Section 1-3-3) and experimental results (R.C.Miller 1982[1]; R.L.Greene 1985) of shallow impurities in QW's reported by other researchers, leads us to conclude that these extrinsic emissions correspond to e-A° transitions and that the acceptor-like impurities are situated at the interfaces and the centres of the wells with binding energy of 30meV and 41meV respectively.

For a uniform distribution of impurities in the QW, we expect that a peak will appear with its maximum intensity at the energy corresponding to an impurity at the well centre according to the density of states effect (G.Bastard 1981) and the high non-radiative recombination efficiency at the interfaces as a result of interface defects. Therefore, the fact that in this experiment interface impurity-related emission appeared as well as the well-centre impurity related emission indicates that impurity segregation to the interfaces occurs.

Substantial changes of the impurity related emission intensity and shape were observed after the as-grown bulk sample was left in air for more than a year. As is shown in Fig.4-2, the integrated intensity of the impurity related emission in the CL spectrum increased from about one tenth of the intrinsic excitonic emission in the previous experiment (see Fig.4-1(a)) to about twice the intrinsic value. Only one peak was observed with its energy at 33meV below the QW intrinsic emission instead of the two-peak structure in earlier observations. According to the above discussion, we can conclude that this peak energy corresponds to e-$A^{\bullet}$ transitions with acceptors which are located at the centre of the wells. This implies that the impurity related emission line now resulted from a random distribution of impurities in the wells.

In Fig.4-3(a), the CL spectra of the sample for three different excitation powers, increasing from spectrum 1 to 3, are displayed. The QW intrinsic emission energy moved slightly towards low energy side as the excitation power increased probably due to an electron beam heating effect, while the FWHM of the emission remained unchanged. The relationship between the ratio of the integrated intensity of impurity-related emission and

the integrated intensity of excitonic emission and the excitation power is shown in Fig.4-3(b). As described in Section 1-4, the ratio is proportional to τ_{er}/τ_{ir} according to Equations 1-9 and 1-10, where τ_{ir} and τ_{er} are the carrier lifetime determined respectively by impurity related transitions and intrinsic transitions. The reduction of the ratio with increase of the excitation power in this case is due to an increase of τ_{ir} as the impurity related transition centres become saturated at high excitation levels. As a result, the integrated intensity of the excitonic emission increases superlinearly with the excitation power (see Fig.4-3(c)).

The reason for impurity redistribution in the wells and for the great enhancement in the intensity of impurity luminescence is still unknown. Moreover, in the observations described so far, it is impossible to distinguish the luminescence of each of the three sets QW's from each and hence deduce the impurity distribution among them since the generation volume of the 20kV electron beam used is much larger than the QW's separations and it is impossible to operate the TEM at a lower accelerating voltage in our equipments. A lower operating voltage would reduce the generation volume and hence permit spatial and depth resolved CL analysis at an appropriate resolution. However, monochromatic CL images were acquired from a bulk cross section specimen and are shown in Fig.4-4. The left half of the image was acquired at the impurity related emission energy 1.576eV while the right half was acquired at the QW excitonic emission energy 1.607eV. As you can see, although the three sets of QW's cannot be resolved individually, the impurity related emission profile is much narrower than that of the QW emission. Moreover the impurity related emission is concentrated at the area near to the surface. No conclusions can be made at this stage, but it seems

that the most of impurity related emission may be attributed to QW-1, which was grown after a thick AlGaAs layer and near to the surface (see Fig.3-19(a)). High resolution CL from the cross section thin specimens has been done to improve the spatial resolution as will be discussed below.

4-1-2 The Observation of Thin Cross-section Specimens

Thin cross-section specimens were prepared by the method described in Section 2-2-2. The electron beam with an accelerating voltage of 120kV and a probe size of about 1-0.1μm in diameter was used in the investigations. All observations were carried out on the thin cross-section specimens which were prepared before luminescence degradation occurred in the as-grown bulk sample.

As is shown in Fig.4-5, the luminescence spectrum of a thin cross-section specimen included both the bulk AlGaAs emission at about 1.965eV and the bulk GaAs emission at about 1.516eV but was dominated by the QW emission at about 1.607eV. This situation contrasts with what was obtained from bulk specimens where the bulk GaAs emission was dominant. This difference may result from the reduction of relative generation volume of the bulk GaAs layers (including the GaAs separation layer, the buffer layer and substrate) to the GaAs QWs for thin cross-section specimens as compared with bulk specimens. An additional contribution comes from the serious surface ion damage, introduced during specimen preparation, which almost quenched the CL emission from the GaAs buffer layer and substrate. We found that the CL intensity of the GaAs separation layer was more than three times higher than that of the GaAs buffer layer and substrate as a result of the presence of QWs on both sides of the GaAs separation layer. These QWs

act like potential barriers and result in a smaller effective lateral carrier diffusion length in the GaAs separation layer. In other words, because the carrier confinement effect in multilayer regions reduces the effective lateral carrier diffusion length and prevents carriers from reaching the surface, the effect of high surface non-radiative recombination, is decreased greatly.

Another feature of the spectrum in Fig.4-5 is that the QW intrinsic emission is also accompanied by a high intensity of impurity related emission. The impurity emission intensity is about 1.5 times that of the QW intrinsic emission, similar to what was obtained from the degraded, as-grown, bulk specimens (see Fig.4-2). It follows that the enhancement of the impurity level and of the redistribution of impurities in the sample had occurred during the process of cross-section specimen preparation. Unfortunately, this degradation effect eliminates the possibility of investigation by this method the effect of different growth sequences on the luminescence properties of QW's. However, some aspects of the native quality of the QW's can be deduced from the study of the degraded specimens.

To determine the distribution of impurities among the QW's, we obtained three CL spectra by pointing a focused electron beam at each of the three sets QW's in turn. In Fig.4-6, spectrum(a) corresponds the CL emission acquired from QW3 which was grown immediately after the GaAs buffer layer and separated from QW2 by a thick GaAs layer. As a result of the lower potential energy in the GaAs none of the excess carriers, which were generated in the GaAs adjoining QW3 by the electron beam were able to spill over into the QWs. Hence the luminescence from QW3 shown in spectrum(a) was uncontaminated by carrier diffusion from else where in the structure. The integrated intensity of the impurity emission for QW3 is about one tenth of

the value of the intrinsic emission. This is consistent with the average impurity level in the un-degraded, as-grown, bulk sample and indicates that no degradation occurred in QW3. The origin of these impurities may be residual impurities in the growth chamber or on the substrate surface. Spectrum(b) and spectrum(c) in Fig.4-6 correspond respectively to the CL emission acquired by directing the electron beam at QW2, which was grown immediately after the GaAs separation layer, and to QW1, which was grown immediately after a thick AlGaAs separation layer. The degradation of the QW luminescence is obvious and the integrated intensity of impurity emission is about one and half times the value of the intrinsic emission from QW2 and three times the value of the intrinsic emission from QW1. However, since the two sets of QW's were separated by a thick AlGaAs layer where the carriers have a higher potential energy some of the excess carriers created in this region are likely to diffuse into the adjoining quantum wells where they will recombine. Considering this effect, it is possible that a considerable proportion of the impurity emission apparent in spectrum(b) from QW2 is in fact a spill over from QW1. When the beam is directed at QW2 a certain amount of the excitation is inevitably created in the AlGaAs separation layer. Some of this excitation will diffuse to QW1 giving luminescence characteristic of QW1 although apparently arising from QW2. On the other hand, the intrinsic emission shown in spectrum-(c) for QW1 can be partly from the QW2 intrinsic emission. This assumption also explains why no significant FWHM broadening of QW intrinsic emission accompanying ~~to~~ the high impurity emission was detected in our experiments, which is in contrast to the general results reported by other researchers. Therefore, the above discussions may lead us to conclude that the luminescence degradation mainly occurs in QW1.

The uneven distribution of impurity emission among the QW's rules out the possibility that it results from contamination of the free surfaces during thinning. Both room temperature and liquid nitrogen temperature ion thinning were applied in specimen preparation and only slight differences in the impurity emission intensity were observed. This result implies the specimen heating effect due to ion beam bombardment was negligible. The effect of epoxy used in specimen preparation was tested by spreading it over the growth surface of an as-grown bulk specimen prior to low temperature CL observations. Due to surface tension, many epoxy droplets were formed on the specimen surface and were easily recognized in secondary electron images. A typical CL spectrum from a droplet free area is shown in Fig.4-7. It is undoubtedly the case that the luminescence degradation occurred because of application of the epoxy. By pointing the electron beam towards droplets, a series of spectra similar to Fig.4-6 have been obtained. This can be explained by consideration of the electron penetration. As is schematically shown in Fig.4-8, the increased epoxy thickness on the specimen surface decreased the penetration depth of the electron beam into the sample. This conclusion was confirmed experimentally by investigating the electron beam energy dependence of this phenomenon. No further degradation was observed after the specimens were left in air for more than one year.

4-1-3 Discussions

As described above, the greatest increase of impurity emission intensity was observed in QW1 of the sample. It is natural to conclude that this increase was the consequence of an increase of the number of impurities in the QW's. Since the QW1 was

situated near to the sample surface, impurity diffusion from the sample surface is the most likely explanation for the increase in the number of impurities in the QWs. However, it is hard to believe that the impurity diffusion could occur to a depth of 1000Å in a perfect crystal which had been maintained at room temperature for about one year apart from a few minutes of exposure to the epoxy at 100°C. On the other hand, this increase could also be explained by an increase of the intrinsic recombination lifetime in comparison with the extrinsic one in the QWs. It has been reported that electric field induced band bending reduces the overlap between the electron and hole wavefunctions in QWs. This will decrease the intrinsic recombination efficiency of the QWs (H.J.Polland 1985 [1] [2]; G.Bastard 1988). In this case, it is possible that the surface fields were induced by the presence of the epoxy, and created band bending penetrating into the QW1 region. This would cause a quenching effect on the intrinsic emission thereby enhancing the impurity emission, providing that there are impurities in the QWs. Since the QW1 was grown after a thick AlGaAs layer, a high impurity level was expected according to the discussion at the beginning of this section.

Whatever is the real reason for the enhanced impurity emission, the fact that it was not observed in other different samples which were subjected to exactly similar preparation procedures implies that there must have been some native lack of quality of the QW1 which was responsible for this enhancement of impurity emission.

4-2 CL Images and Line-scans of Sample NU210S

A monochromatic CL image acquired from a thin cross-section specimen of sample NU210S at the energy corresponding to the QW exciton emission is displayed in Fig.4-9 (a) together with the TEM image of the same sample for comparison in Fig.4-9 (b). Due to the effect of carrier confinement in the separate sets of quantum well, which was essential in achieving the high resolution of the CL image, the three sets of QW's are clearly resolved. As is shown in the CL line scan profile parallel to the growth direction in Fig.4-9(c), the QW2 and QW3 are very well resolved since they are separated by a thick GaAs layer (3500Å) and the intensity of the QW emission almost reached zero at the middle of the GaAs separation layer. In this case, the CL image resolution was determined only by the electron beam probe size and beam broadening; carrier diffusion does not need to be considered, since the band gap of bulk GaAs is less than that of the QWs. However, as QW1 and QW2 were separated by a thick AlGaAs layer, a low level of QW emission was detected even when the electron beam was directed at the middle of the AlGaAs separation layer. Note that the thickness of the AlGaAs layer was the same as that of the GaAs layer but in this case, the Cl image resolution was affected by the carrier diffusion length as well as the beam size and beam broadening.

Note that the apparent distance between the QW1 and QW2 in the CL image was less than that between QW2 and QW3 although they were in fact equally separated as was evident from the TEM image. This apparent discrepancy is a consequence of the fact that the carriers created in the

AlGaAs separation layer diffused into and were captured by the adjacent QWs where they recombined. This effect is further confirmed by the shrinkage of the CL image of the AlGaAs separation layer (see Fig.4-10(a)) in comparison with that of the GaAs separation layer (see Fig.4-10(b)). In the point source approximation it is possible to calculate the expected CL line scan profile between QW1 and QW2 as shown in Fig.4-9(c) as dashed line. An exponential distribution of the excess carriers and the linear relationship of the CL intensity to the excess carrier concentration was assumed. The carrier diffusion length was taken as 1000Å. For a more accurate fit, a more realistic generation function has to be taken into account. The weak image intensity in CL image for QW1 is due to its high extrinsic emission.

Fig.4-11 shows the beam accelerating voltage dependences of the CL integrated intensity of the AlGaAs bulk emission, GaAs QW emission and GaAs bulk emission for voltages between 20kV and 100kV. As you can see, the increases of the emission intensity of the AlGaAs bulk and the GaAs QW with the increase of the voltage were very slow in comparison with the emission intensity of the GaAs bulk. This may be because the increase in the number of excess carriers resulting from the increase of electron voltage was largely compensated by the decrease of generation dose within the surface layers of GaAs and AlGaAs.

4-3 CL of Sample NU305

The capture of electrons and holes by the quantum wells from their barriers is shown by the usually small luminescence from the barrier layers as compared to the QW luminescence. The carrier capture processes have been

studied both experimentally (E.O.Göbel 1983; H.J.Polland 1988; B.Deveaud 1988; U.Cebulla 1989) and theoretically (J.A.Brum 1986, 1987). The most commonly used technique was time resolved measurements.

In this experiment, the dependence of the luminescence efficiency, related to the capture of carriers by the QW, on barrier thickness was studied using the double QW structure shown in Fig.4-12. The sample used (NU305) contained a series of GaAs/AlGaAs double QW's with well widths of 59Å and barrier thickness varying from 25Å-305Å separated by thick GaAs layers (3000Å). Low temperature CL observation was carried out in a thin cross section specimen. The typical CL spectrum from these double QW structures is shown in Fig.4-13, which was acquired from the double QW with barrier thickness of 305Å. The exciton emission peak is at 1.583eV and FWHM of the peak is 6meV. No significant variations of peak position or FWHM were detected for the double QW's with different barrier thickness.

However, the CL integrated intensities of these double QW's increase superlinearly with increasing barrier thickness, as is displayed by open circles in Fig.4-14(a) . If the capture of carriers by each of these QW's from their barriers were the same, then the CL emission intensities of these QW's should increase linearly with increasing barrier thickness since the number of carriers available for capture is proportional to the barrier thickness (see the solid line in Fig.4-14(a)), i.e. the volume effect. Hence, deviation from a linear relationship between the CL emission intensity and barrier thickness implies that the capture of carriers by QW's changes with barrier thickness. In Fig.4-14(b), the evaluated CL intensity of these double QW structures after excluding the volume effect is plotted as a function of the barrier thickness. The low luminescence intensities from the QW's with thin barriers is due to

the onset of tunnelling of carriers across the barriers. This causes the reduced carrier capture by the QWs and the increase of the carriers captured by the separation layers. It is evident that some carriers generated within the wells or the central barrier were able to tunnel across the outer barriers to be captured by the GaAs separation layers. The tunnelling phenomenon across barriers, when the barriers were thin enough, was also demonstrated in the CL line scan profile of the GaAs bulk emission taken from a thin cross section specimen prepared from another sample (NU210S). As can be seen from Fig.4-15, the emission intensity reaches a maximum in the GaAs separation layer and towards the right of the profile it decreases to reach a plateau as the electron beam scans into the GaAs buffer layer and substrate. Towards the left of the profile, instead of a smooth exponential decrease to zero, it forms a little shoulder at a position corresponding to the AlGaAs separation layer. Since the region between the AlGaAs and GaAs separation layers was occupied by a set of 5 QW's with both well widths and barrier thickness of 50Å, the only reason for the appearance this shoulder is that carriers generated in the AlGaAs layer tunnelled across the set of QWs (QW2) and were captured by the GaAs layer leading to GaAs bulk emission.

The effect of changing well width on luminescence efficiency has also been studied in a sample which contains four single quantum wells with barrier thickness of 300Å and well widths varying from 15Å to 100Å. As is shown in Fig.4-16(a), the open circles indicate the measured integrated CL intensities for the single QWs of different well width while the solid line represents the volume effect on the CL intensity taking no account of the effect of carrier confinement on luminescence efficiency. Excluding the volume effect, the dependence of the modified CL intensity, which is related

to the luminescence efficiency, on well width is shown in Fig.4-16(b). A great increase of CL intensity was observed with decreasing well width. Due to the carrier confinement effect the overlap of electron and hole wavefunctions increases as the well width decreases and this results in the enhancement of carrier recombination efficiency which is responsible for the remarkable increase of CL intensity.

In conclusion, by studying the dependencies of the CL intensity on the barrier thickness and the well widths in QW structures we have demonstrated that the capture ability of carriers by QW's from the barriers is increased with increasing barrier thickness and that the carrier recombination efficiency is enhanced as the well width is reduced.

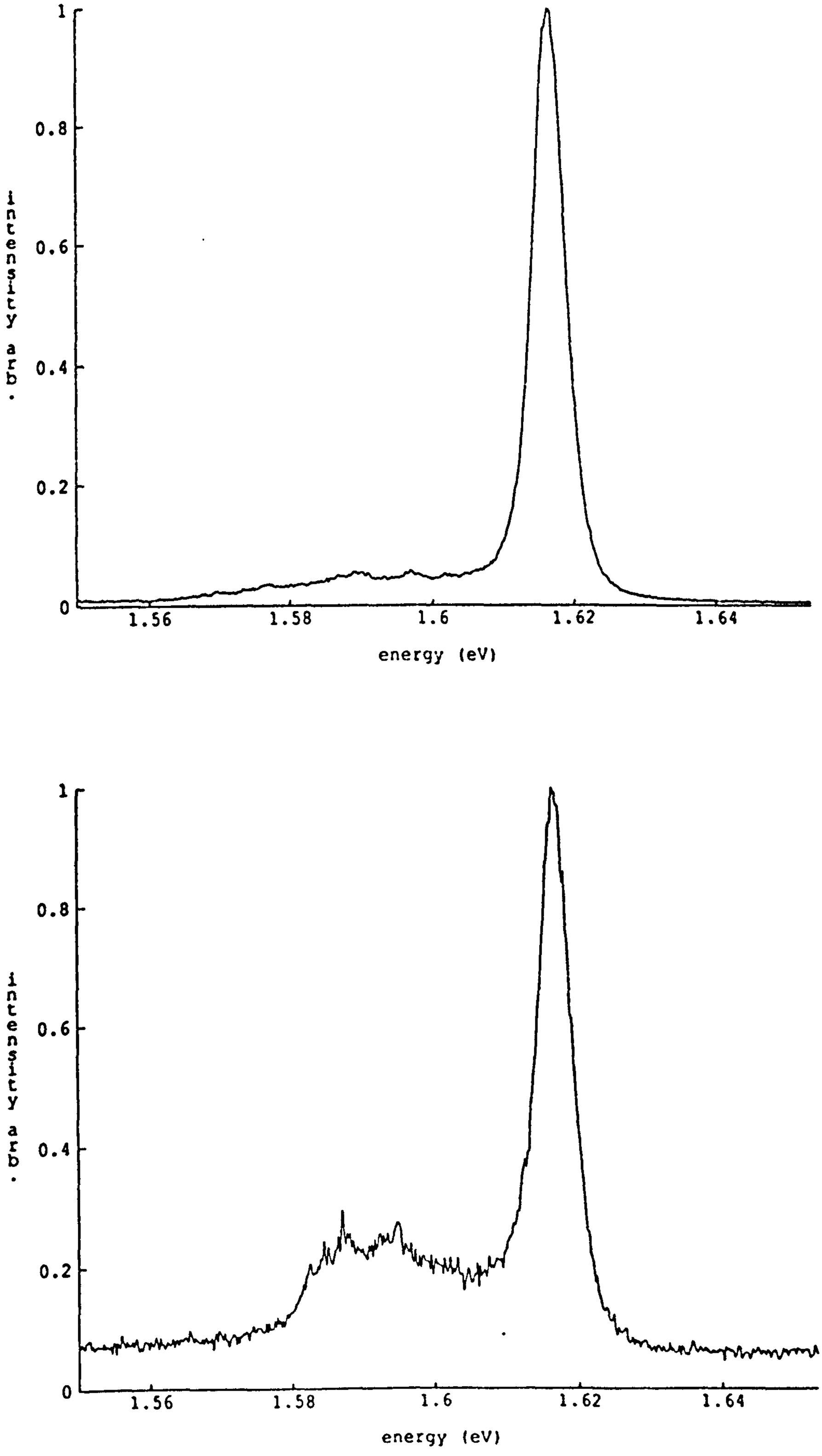

Fig.4-1 Typical CL spectrum from a bulk as-grown specimen of sample NU210S acquired at normal electron beam excitation level (a) and lower electron beam excitation level within a period of one year after MBE growth.

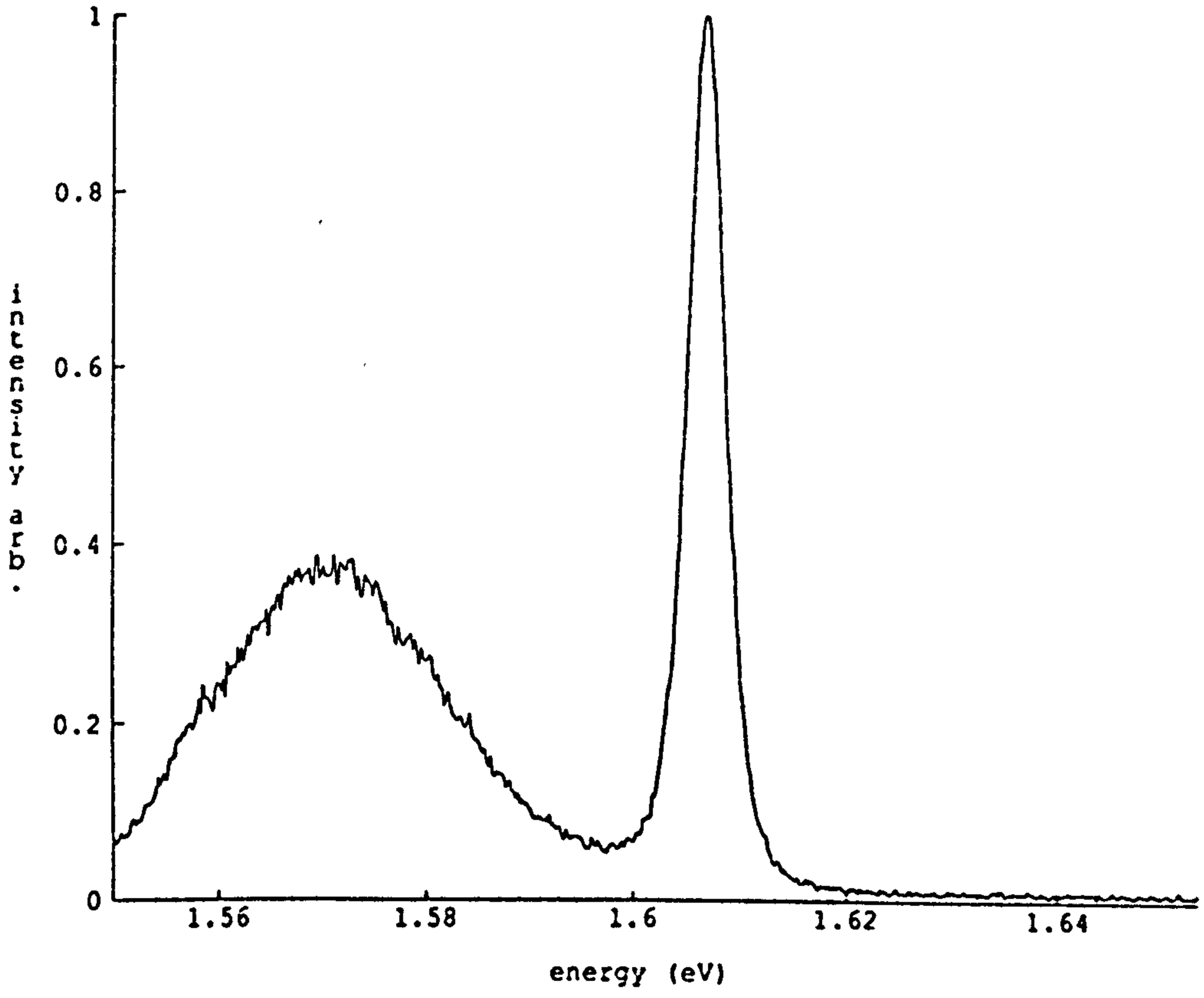

Fig.4-2 A CL spectrum from a bulk as-grown sample (NU210S) acquired after it was left in air for more than one year.

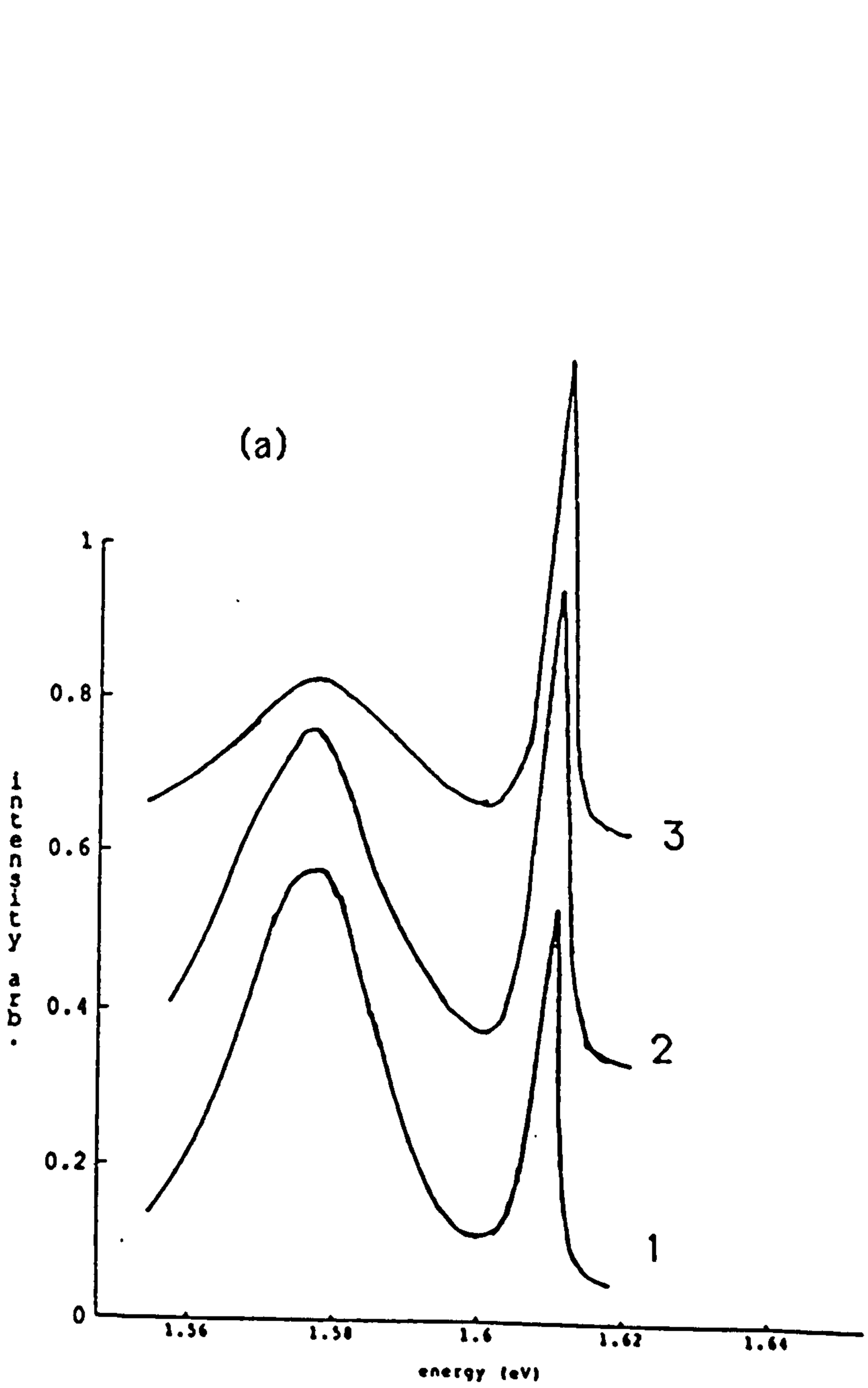

Fig.4-3 (a) The CL spectra of sample NU210S for three different electron beam excitation power, increasing from spectrum 1 to 3.

(b) The dependence of the ratio of the integrated intensity of impurity-related emission and intrinsic emission on electron beam excitation power.

(c) The dependence of the integrated intensity of the intrinsic emission on electron beam excitation power.

(b)

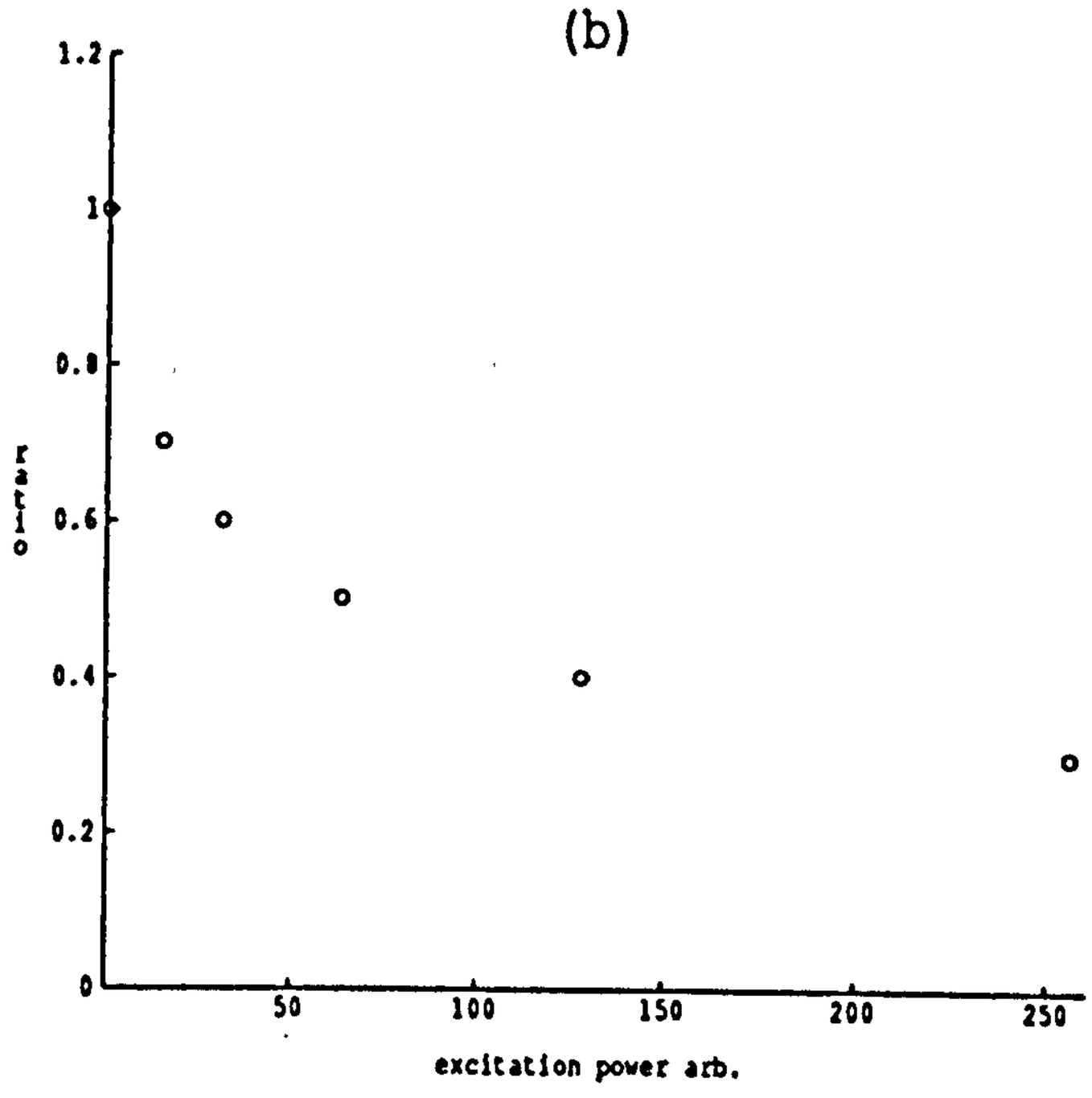

(c) GaAs QW emission

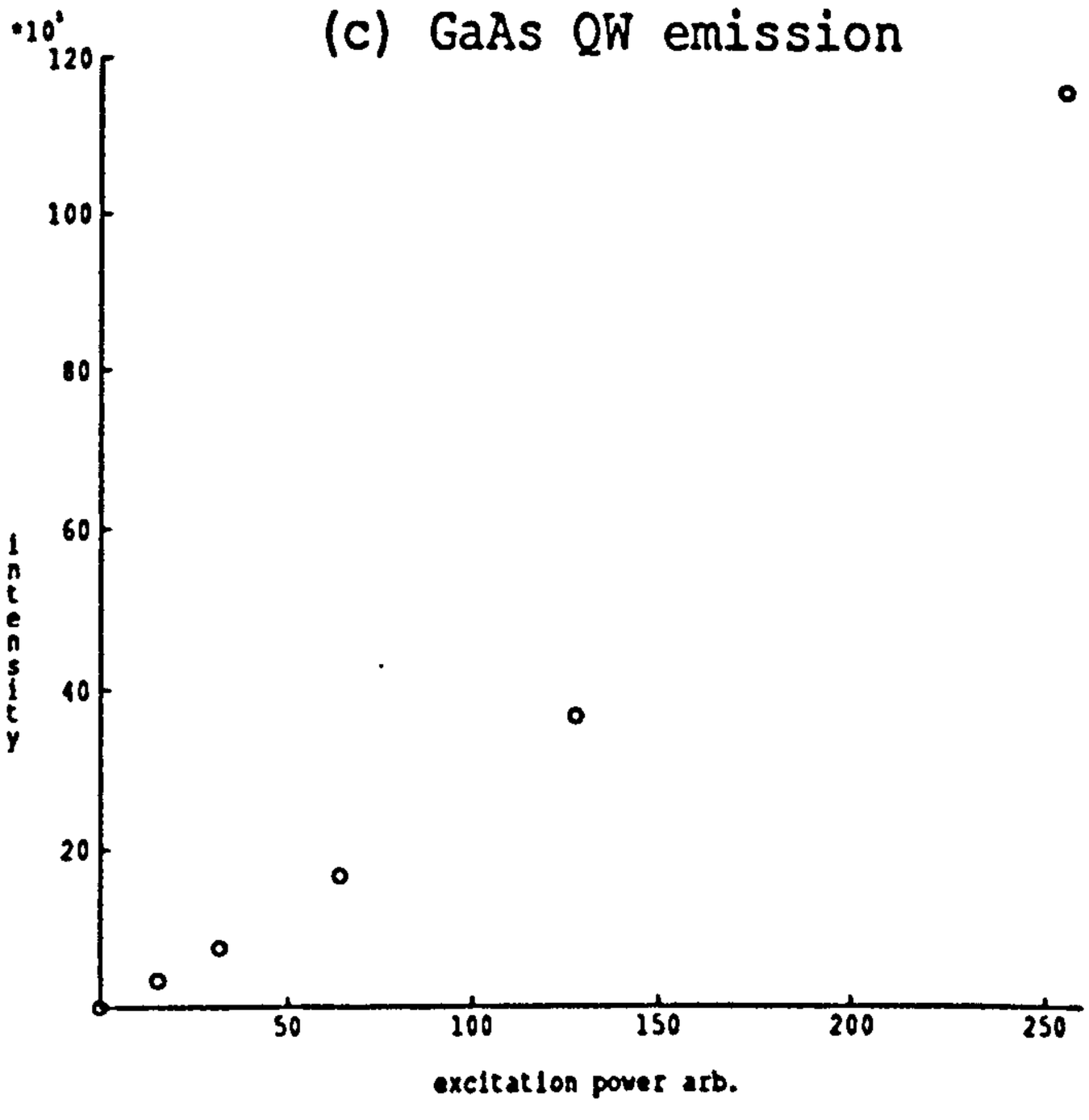

Fig.4-3

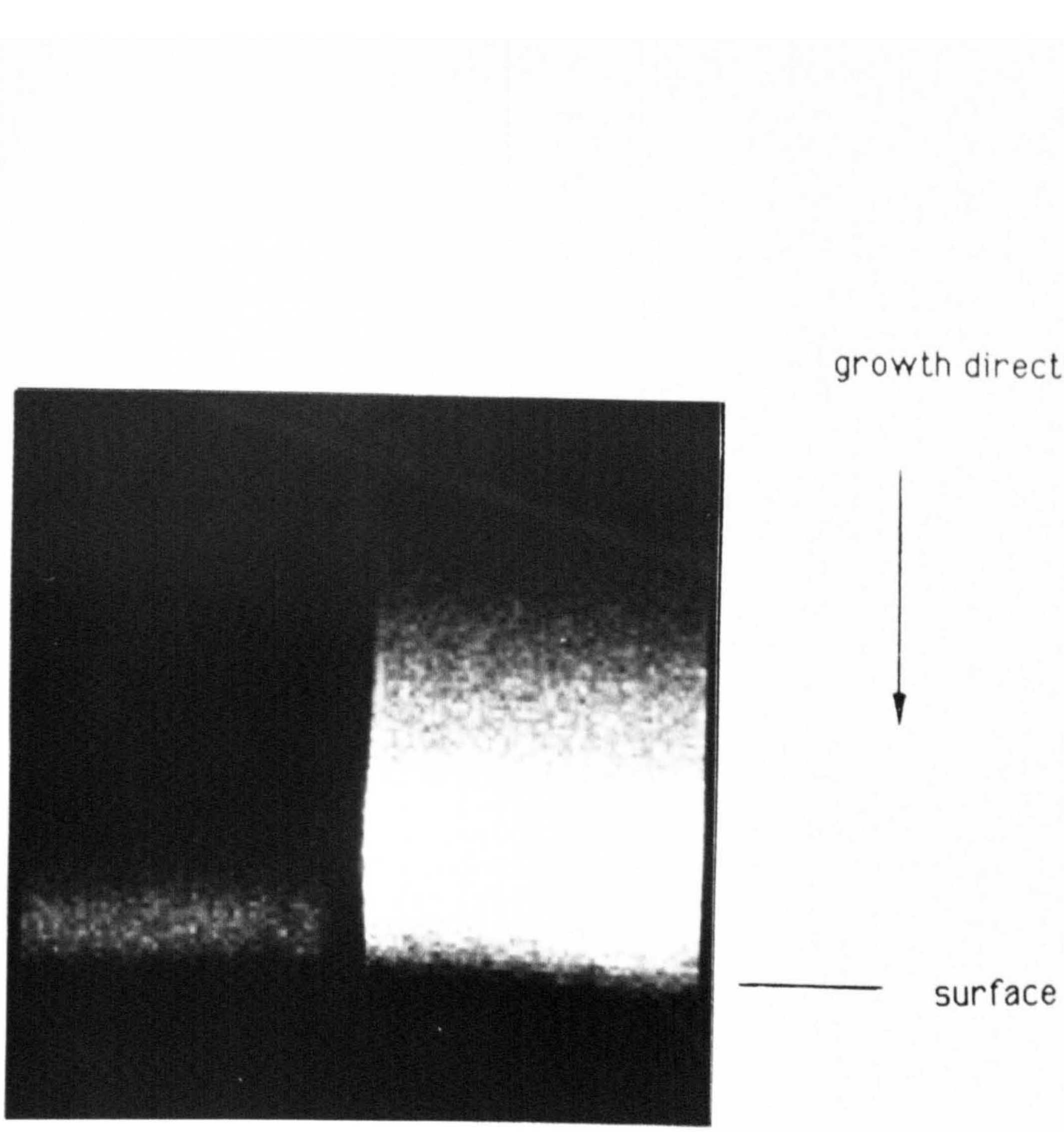

Fig.4-4 Monochromatic CL image from a bulk cross-section specimen of sample NU210S. The left half of the image was acquired at the impurity-related emission (1.576eV) and the right half of the image was acquired at intrinsic emission (1.607eV).

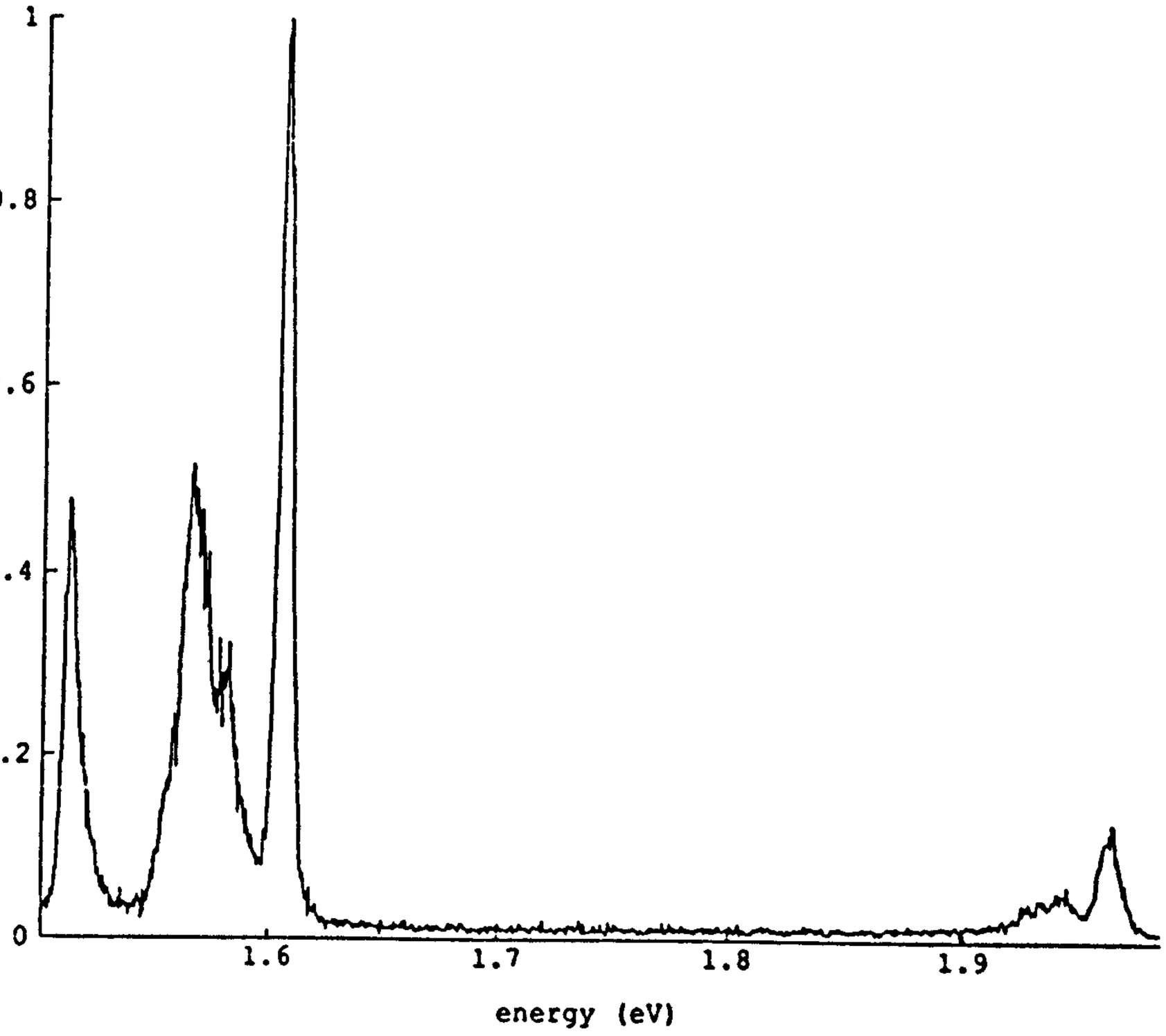

Fig.4-5 CL spectrum from a thin cross-section specimen of sample NU210S, including bulk AlGaAs emission at high energy side of the spectrum and bulk GaAs emission at low energy side.

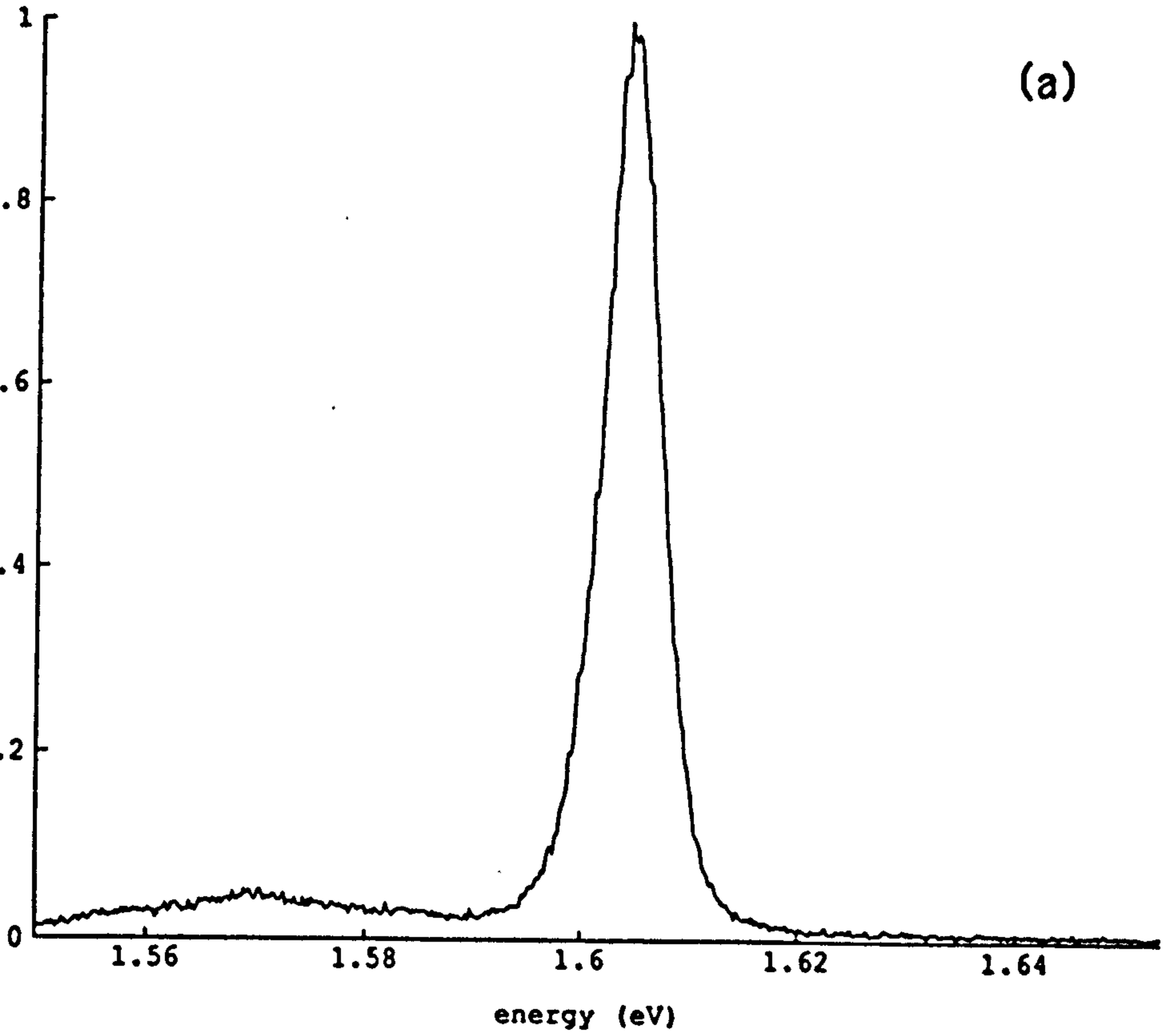
(a)
1
0.8
0.6
0.4
0.2
0
intensity arb.
1.56
1.58
1.6
1.62
1.64
energy (eV)
(b)
1
0.8
0.6
0.4
0.2
0
intensity arb.
1.56
1.58
1.6
1.62
1.64
energy (eV)

Fig.4-6

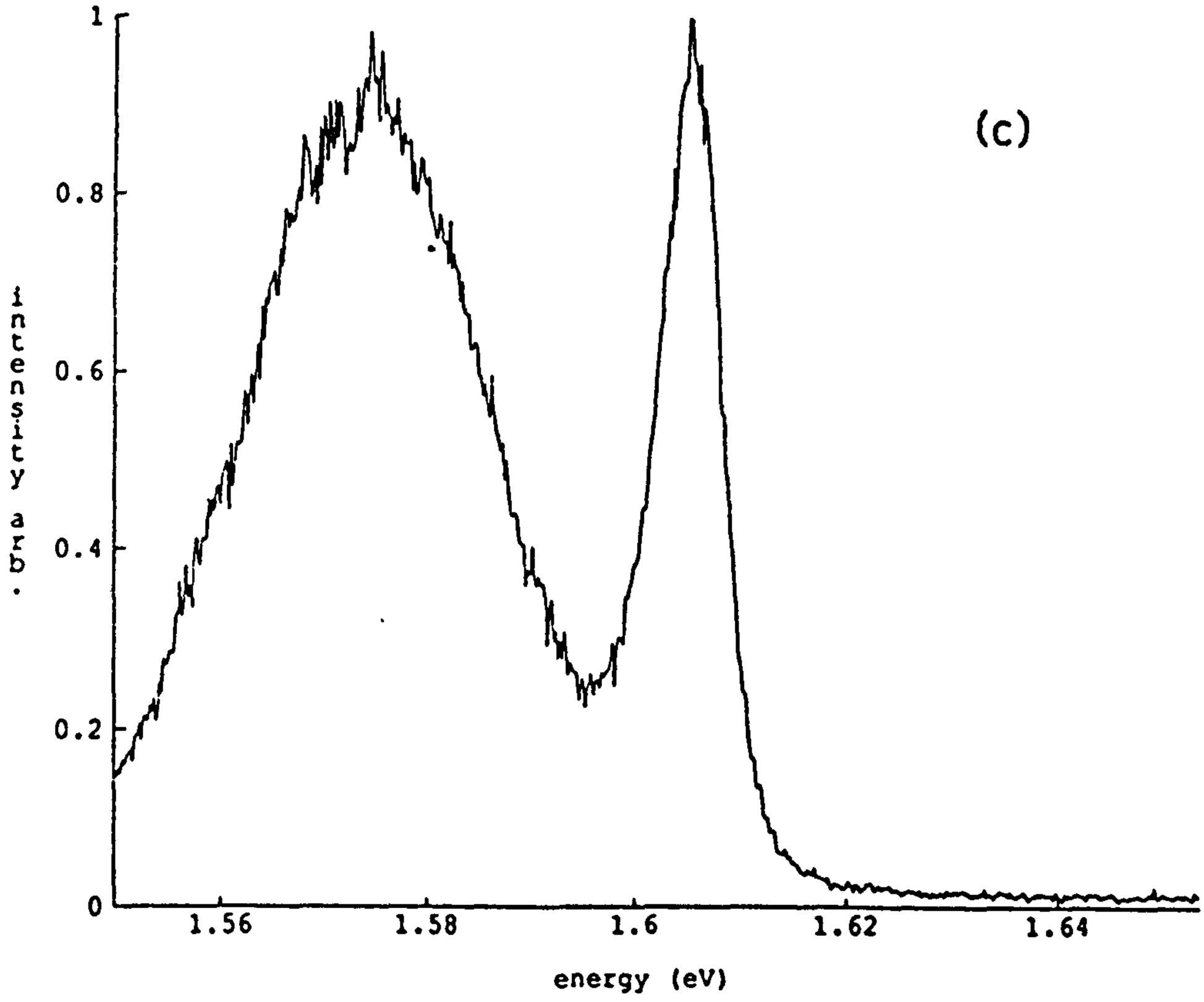

Fig.4-6 CL spectra from QW3 (a), QW2 (b) and QW1 (c) of a thin cross-section specimen of sample NU210S.

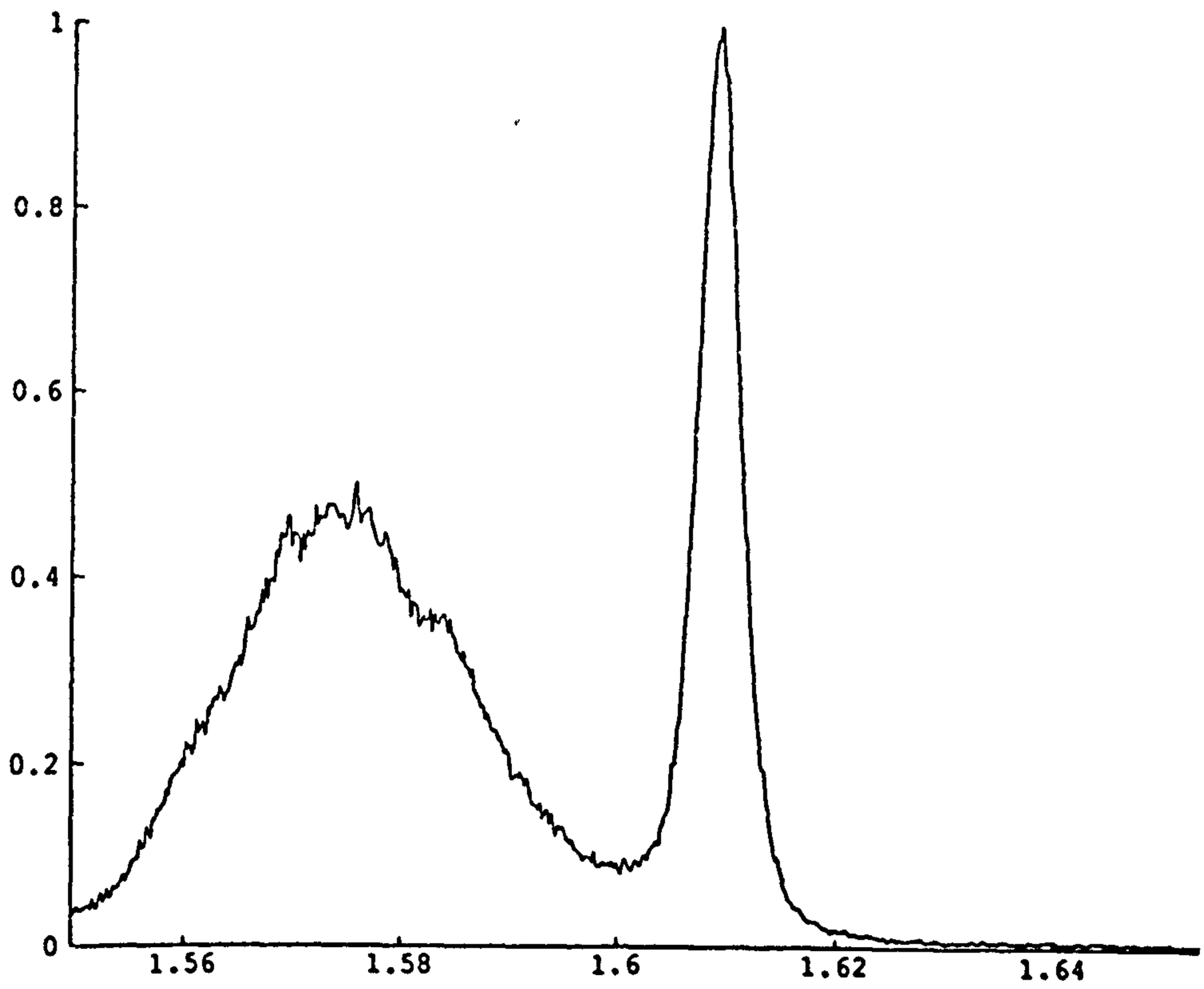

Fig.4-7 CL spectrum from a epoxy droplet free area of a plan view bulk specimen (sample NU210S) with its surface being contaminated by epoxy.

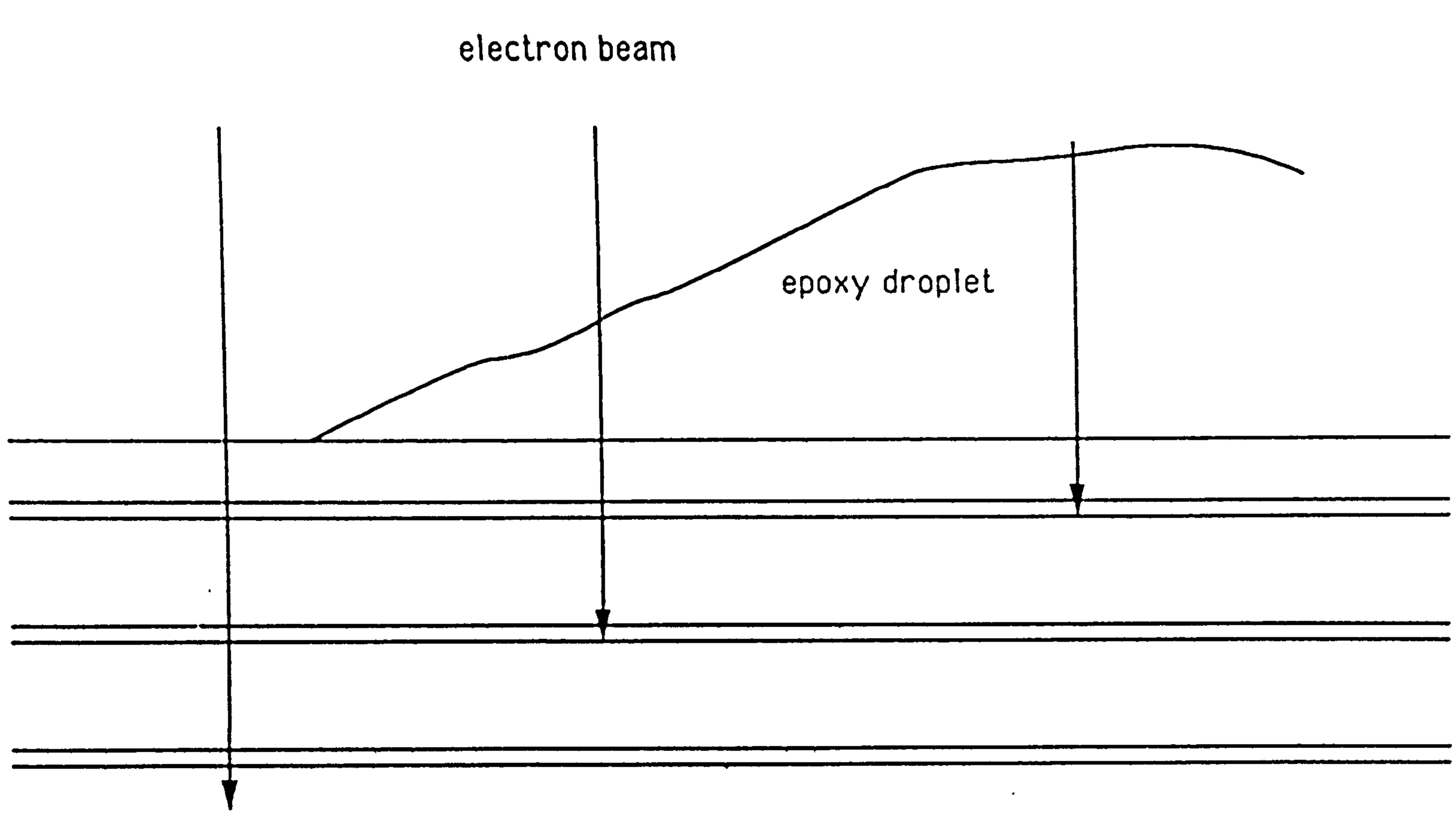

Fig.4-8 Schematic diagram showing the effect of epoxy layer thickness on electron beam penetration depth in specimen.

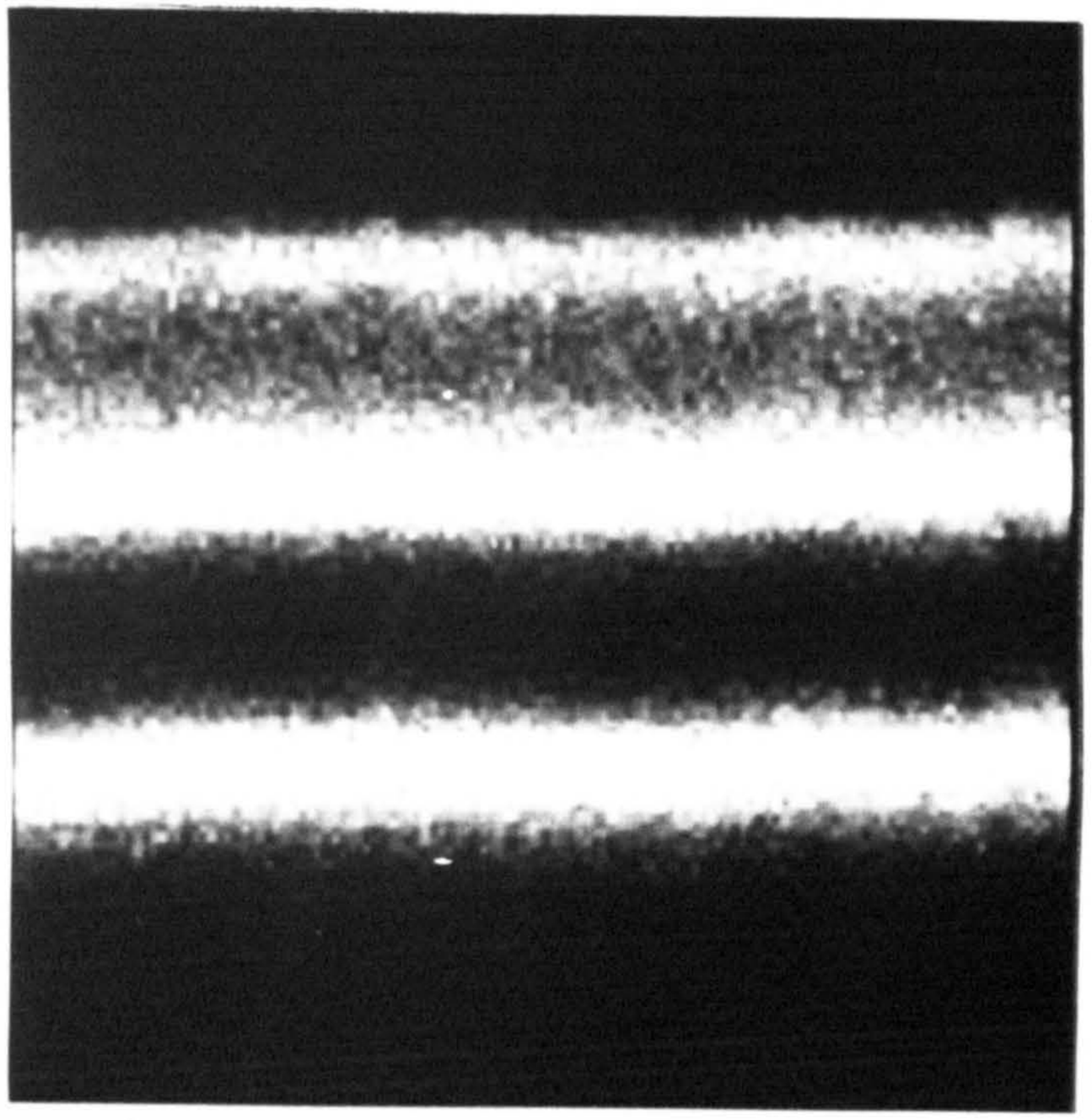

1.607eV

(a)

surface

500nm

(b)

Fig.4-9

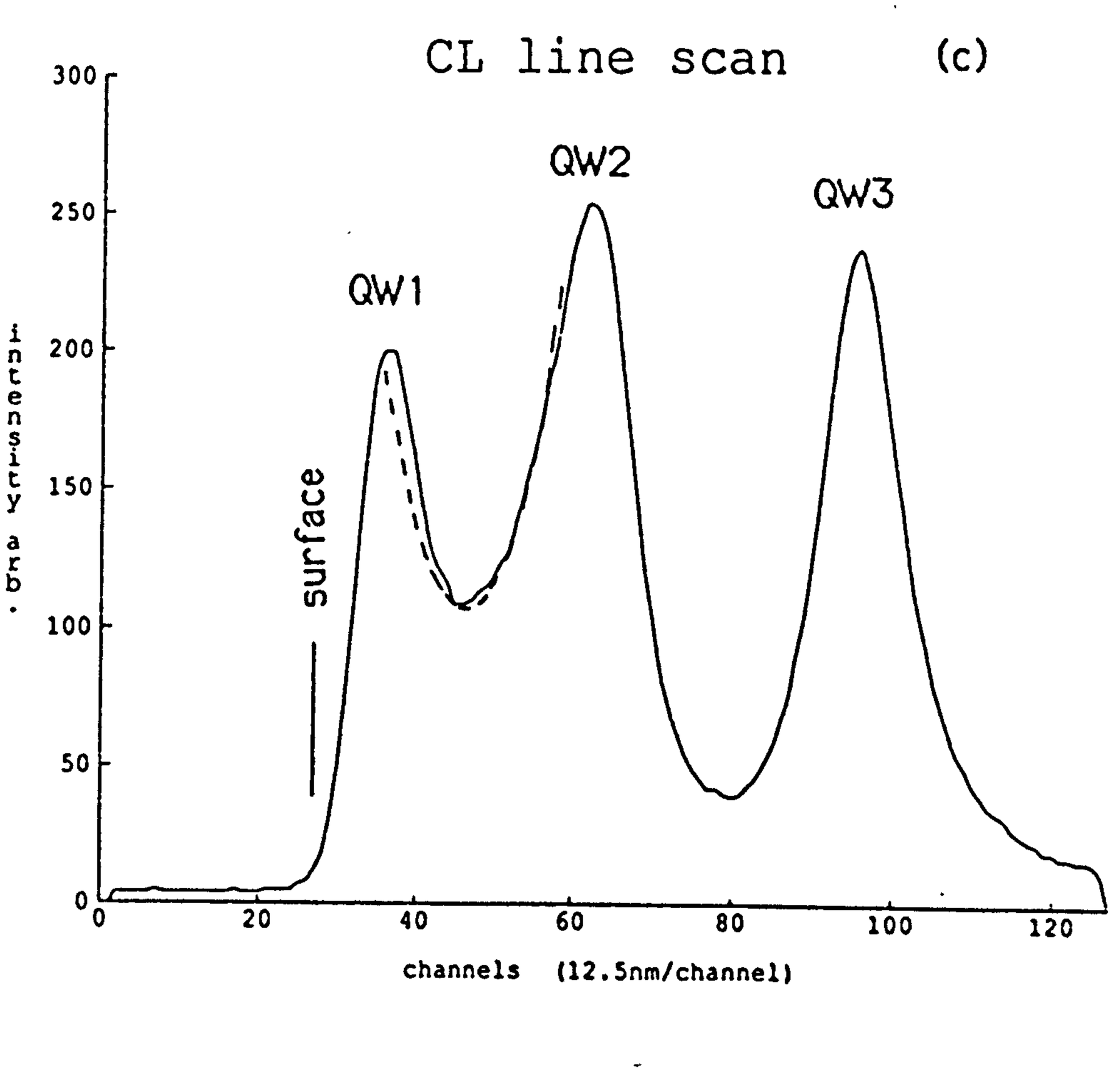

Fig.4-9 (a) Monochromatic CL image acquired from a thin cross-section specimen of sample NU210S at QW intrinsic emission (1.607eV).

(b) TEM cross-section view image of the same sample for comparison.

(c) Monochromatic CL line scan profile (1.607eV) parallel to growth direction, dashed line indicates the expected CL line scan profile by calculation.

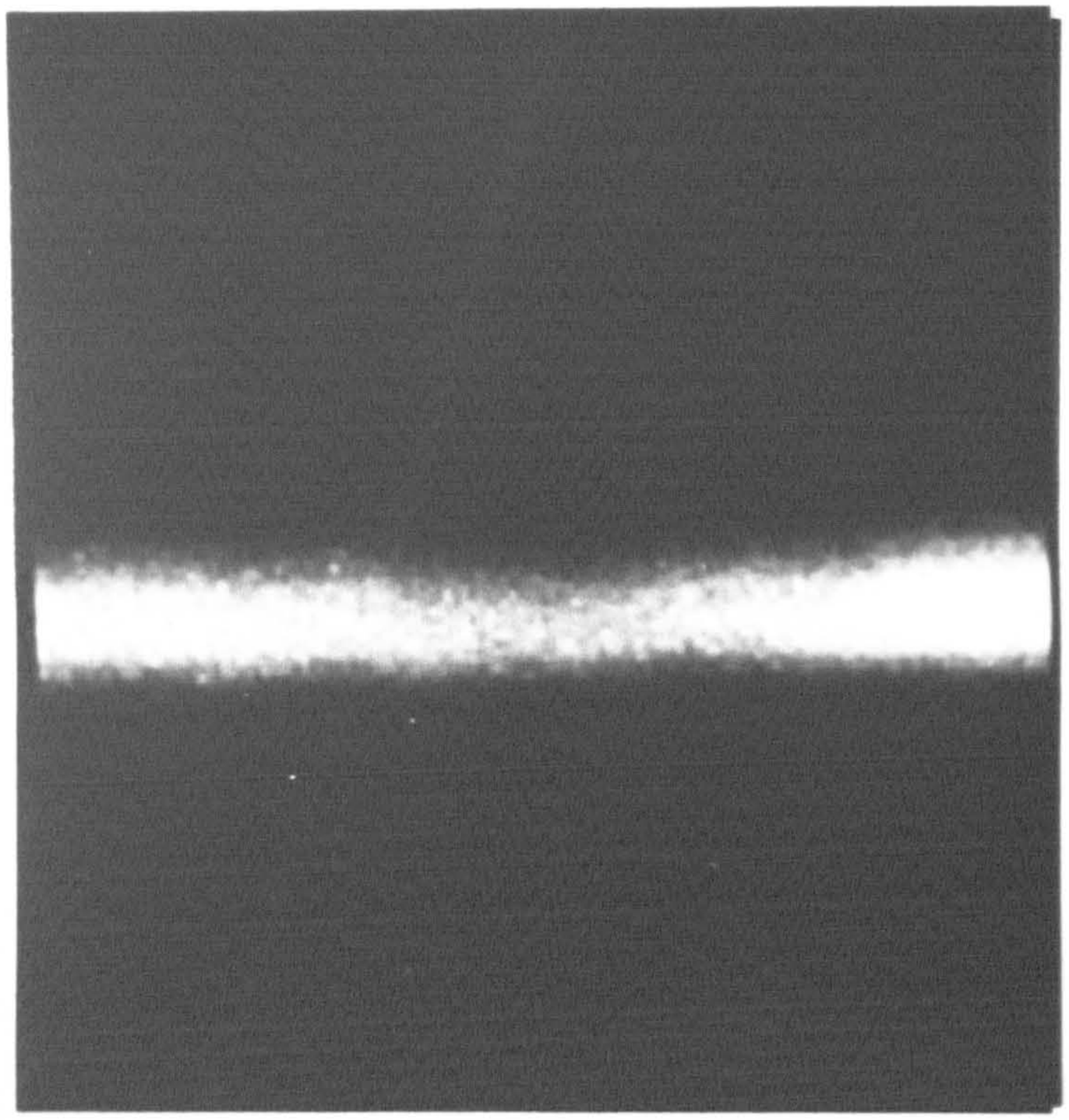

(a)

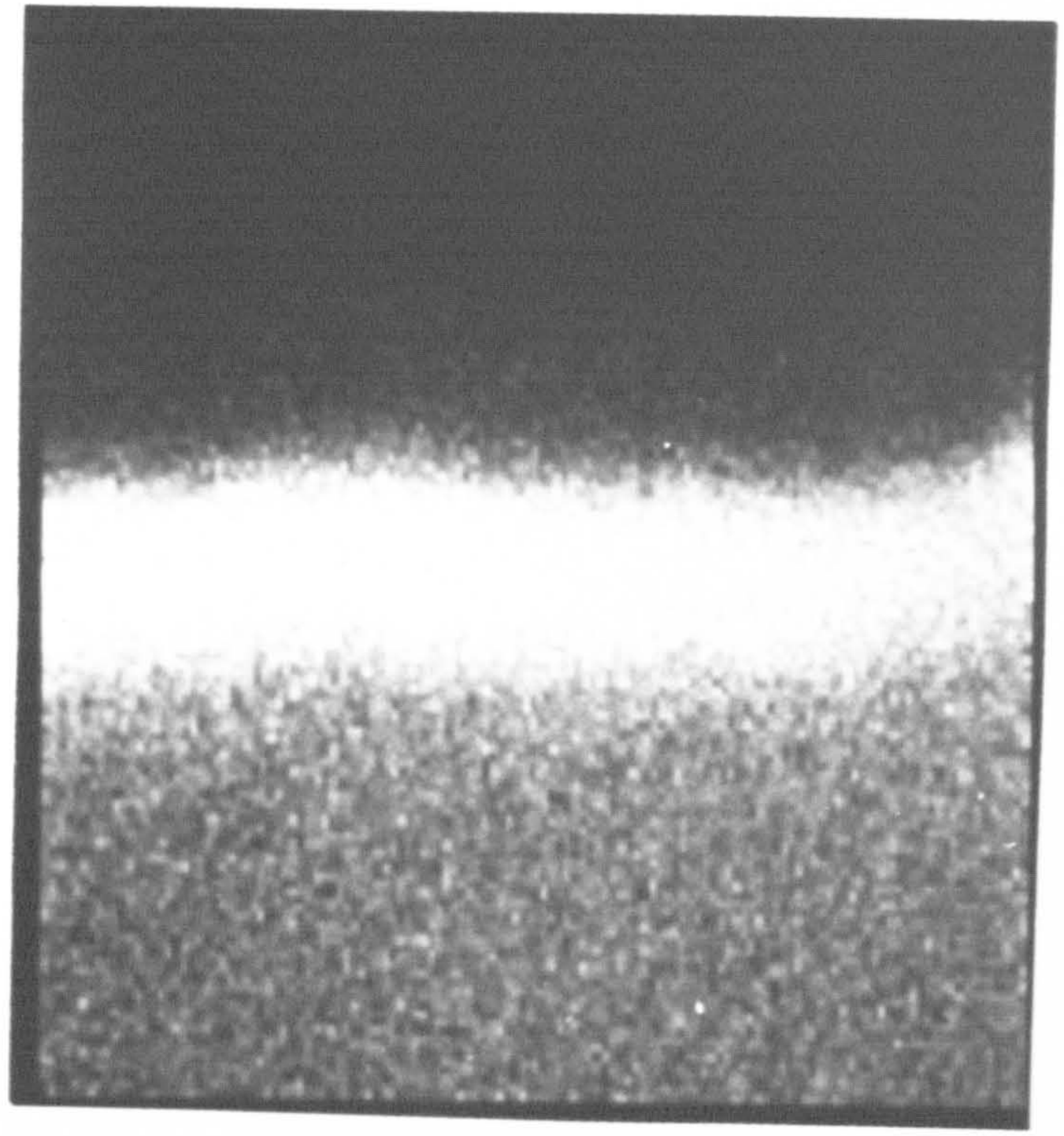

(b)

500 nm

Fig.4-10 Monochromatic CL image acquired (a) at bulk AlGaAs emission (1.965eV), (b) at bulk GaAs emission (1.513eV).

(a) AlGaAs emission

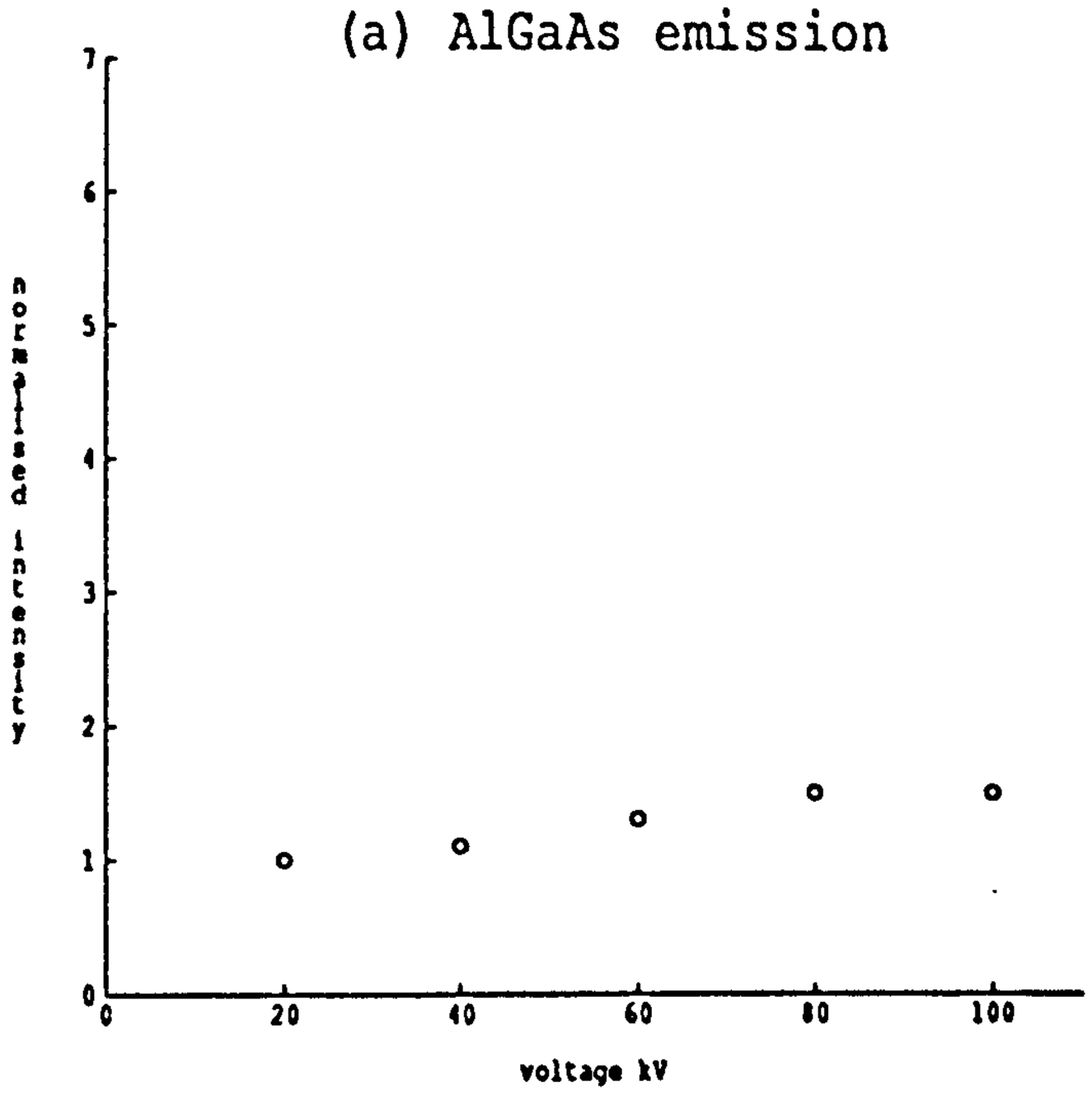

(b) GaAs QW emission

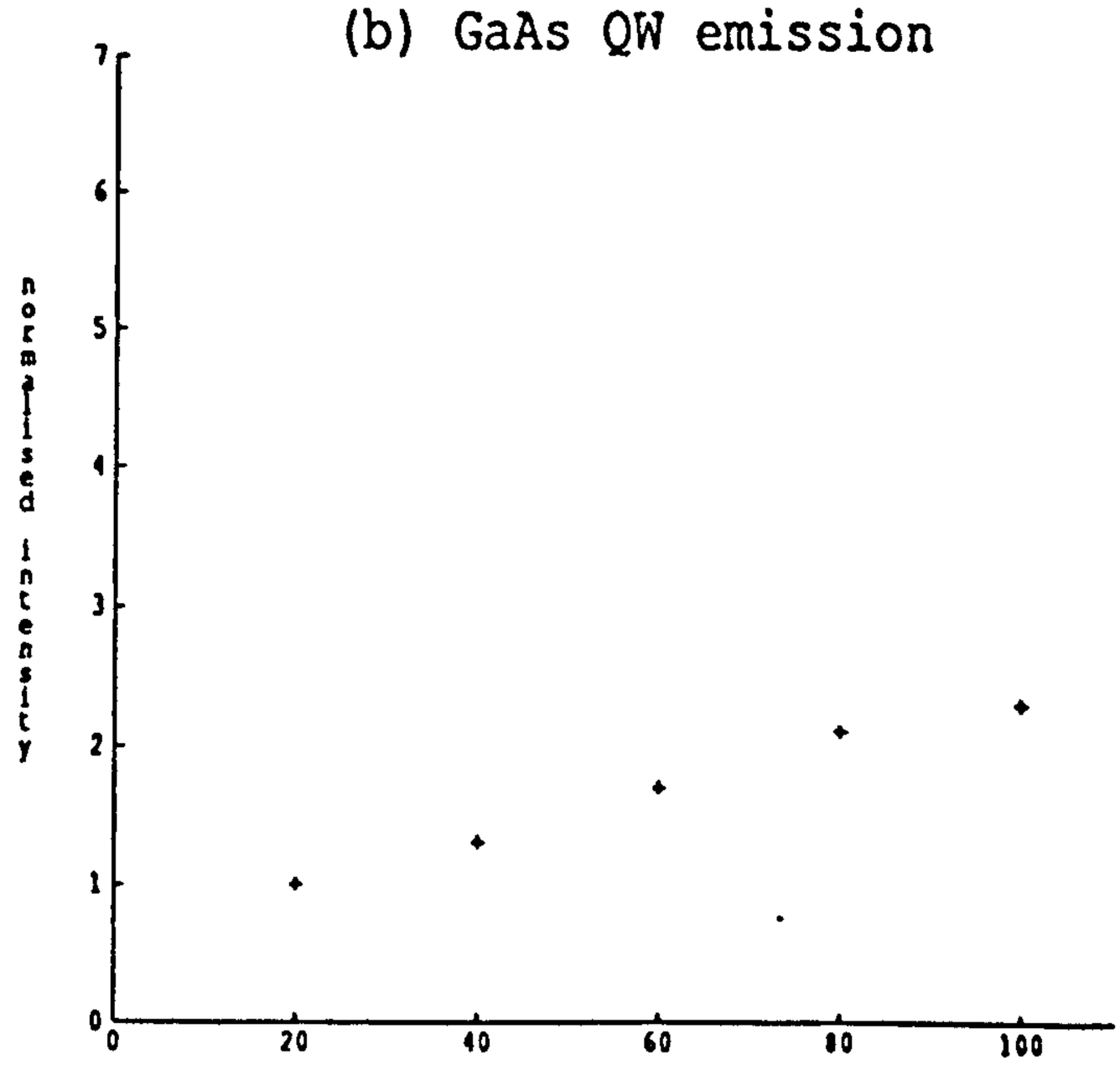

Fig.4-11

(c) GaAs emission

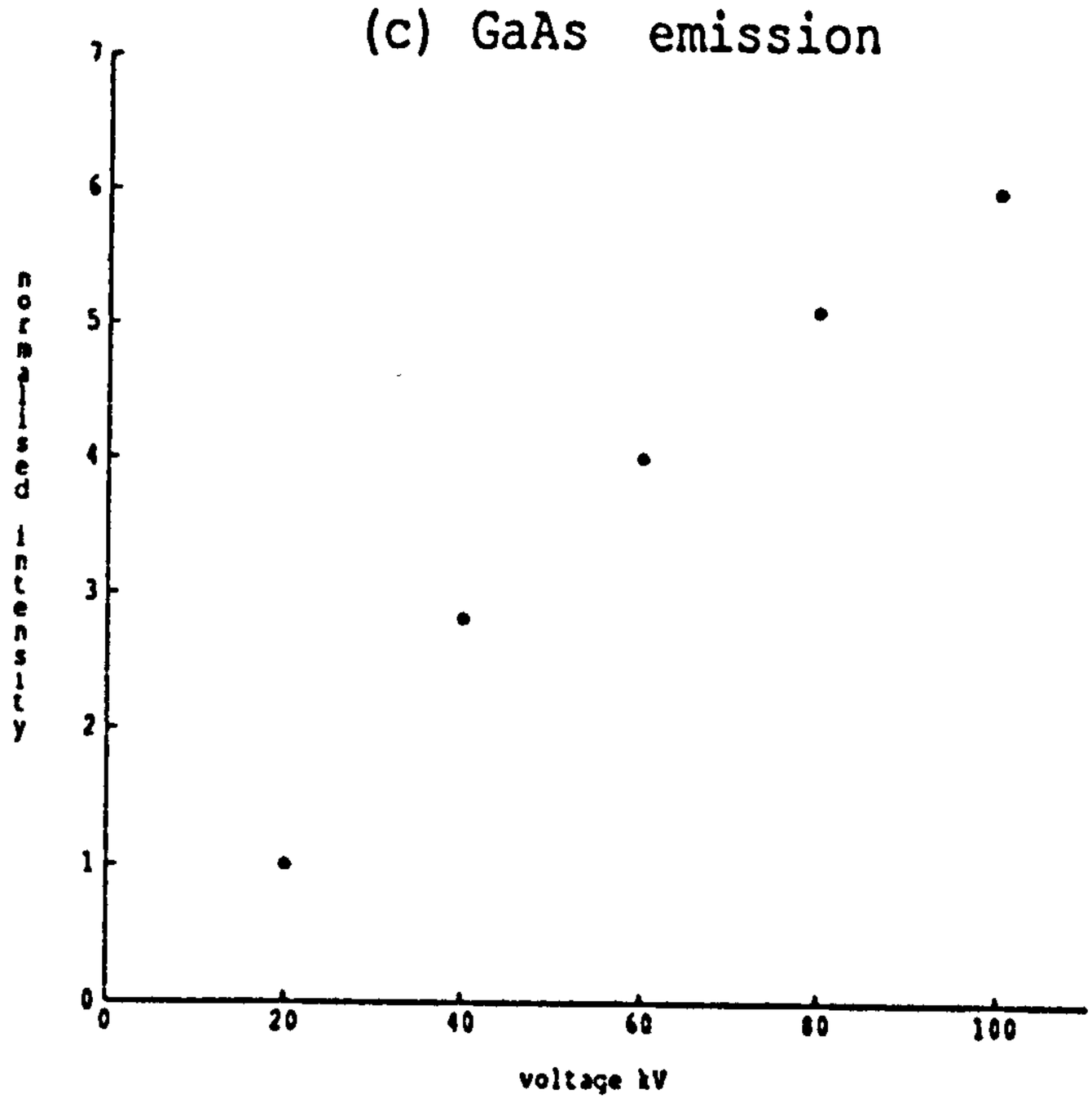

Fig.4-11 The electron beam accelerating voltage dependences of the CL integrated intensity of (a) AlGaAs bulk, (b) GaAs QW and (c) GaAs bulk emission.

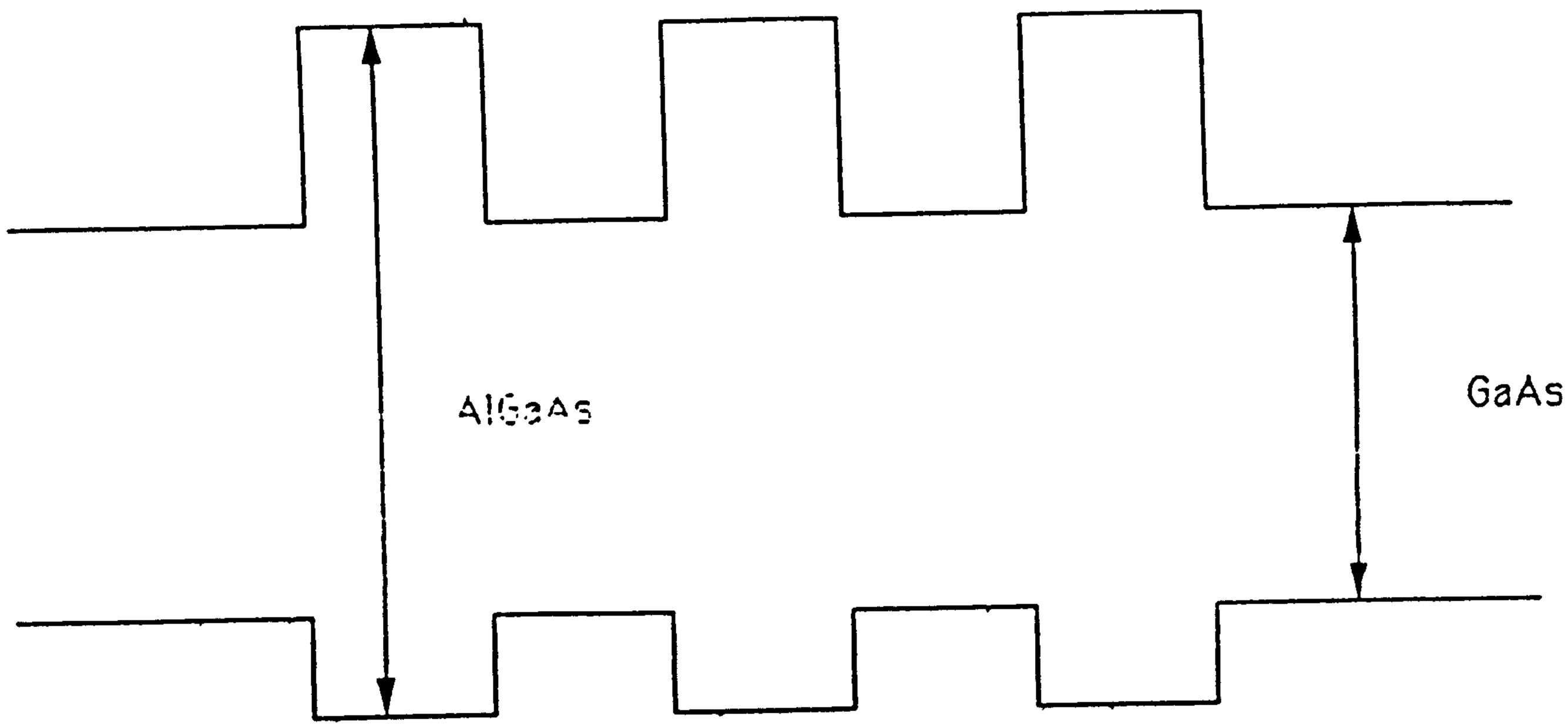

Fig.4-12 Schematic diagram showing a double QW structure in sample NU305.

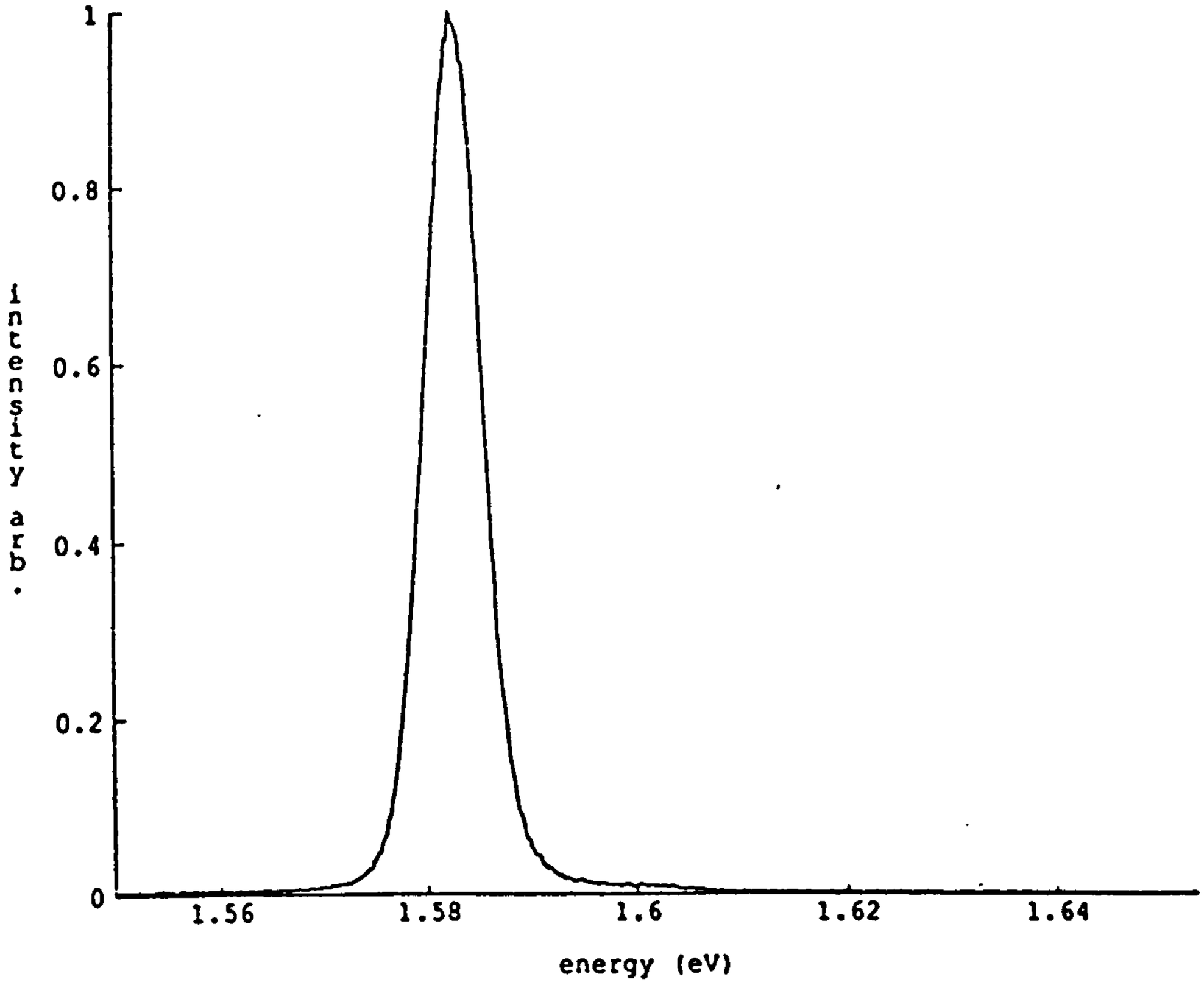

Fig4-13 CL spectrum from double QW with barrier thickness 305A and well width 59A in sample NU305.

(a) GaAs well width 59A

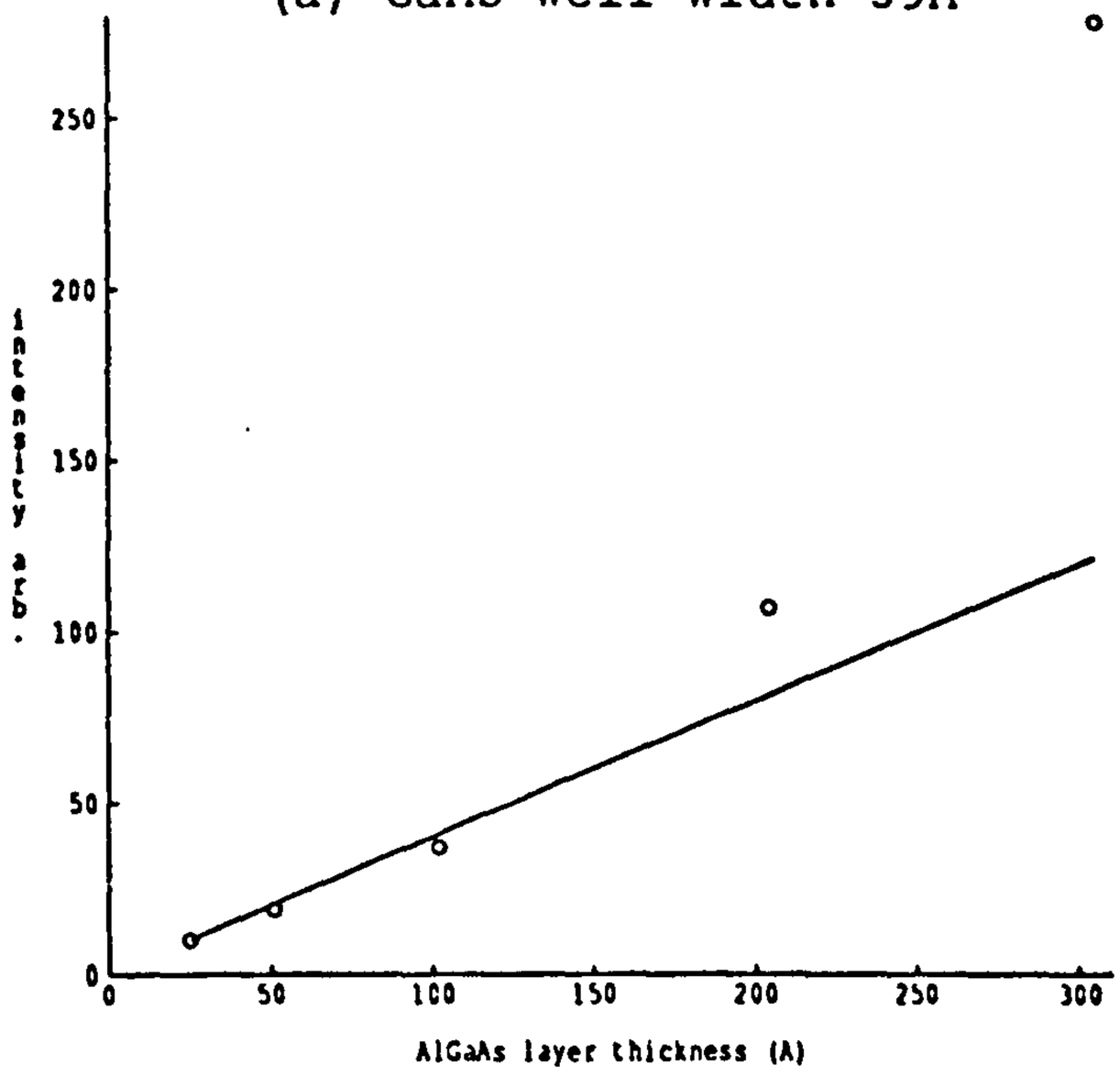

(b) GaAs well width 59A

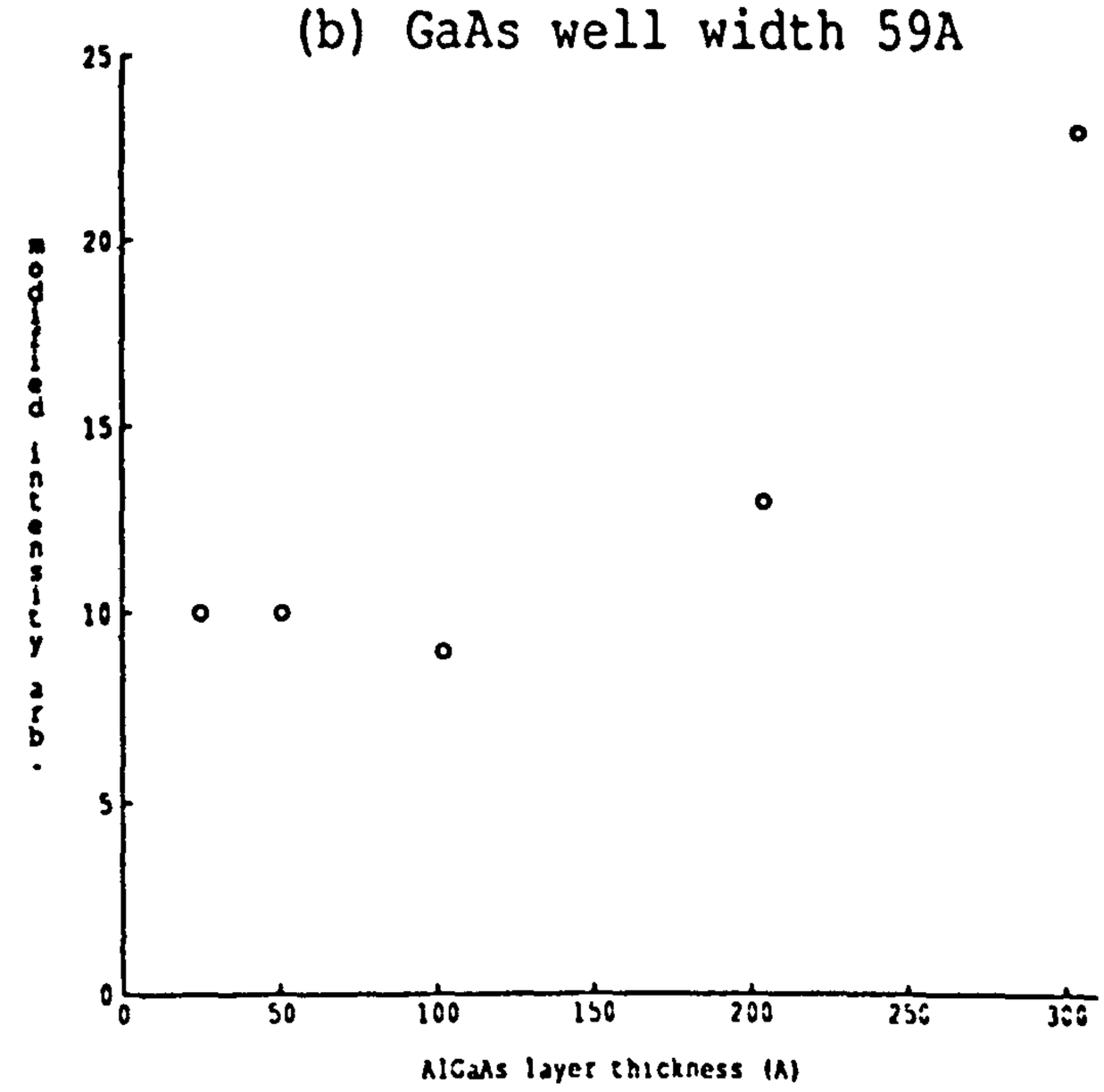

Fig.4-14 (a) The dependence of integrated CL intensity of double QW structure on the barrier thickness (open circle). Solid line indicates the volum effect.

(b) Modified CL intensity of double QW structure by volum effect as a function of barrier thickness.

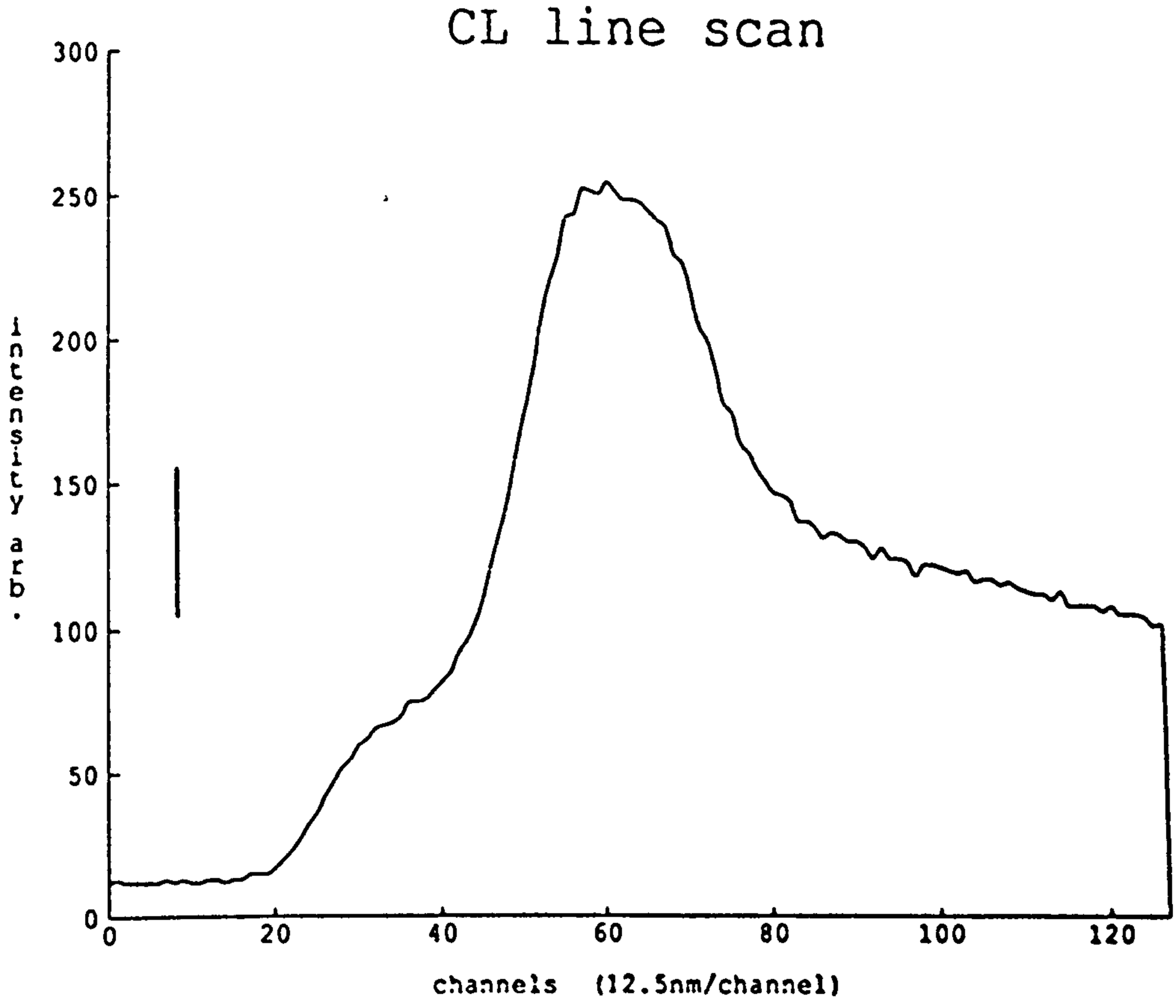

Fig.4-15 Monochromatic CL line scan profile of GaAs separation layer in sample NU210S.

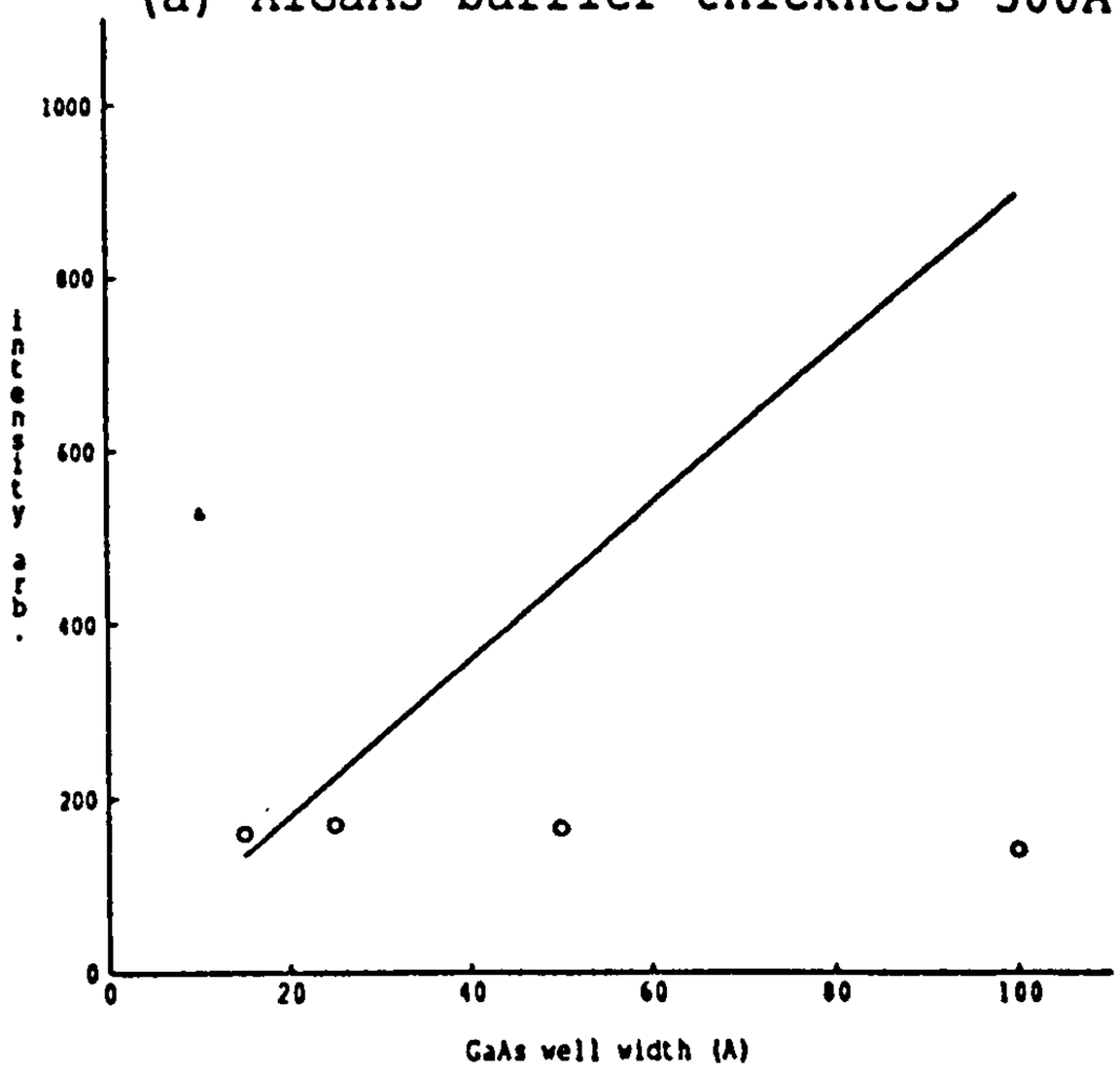

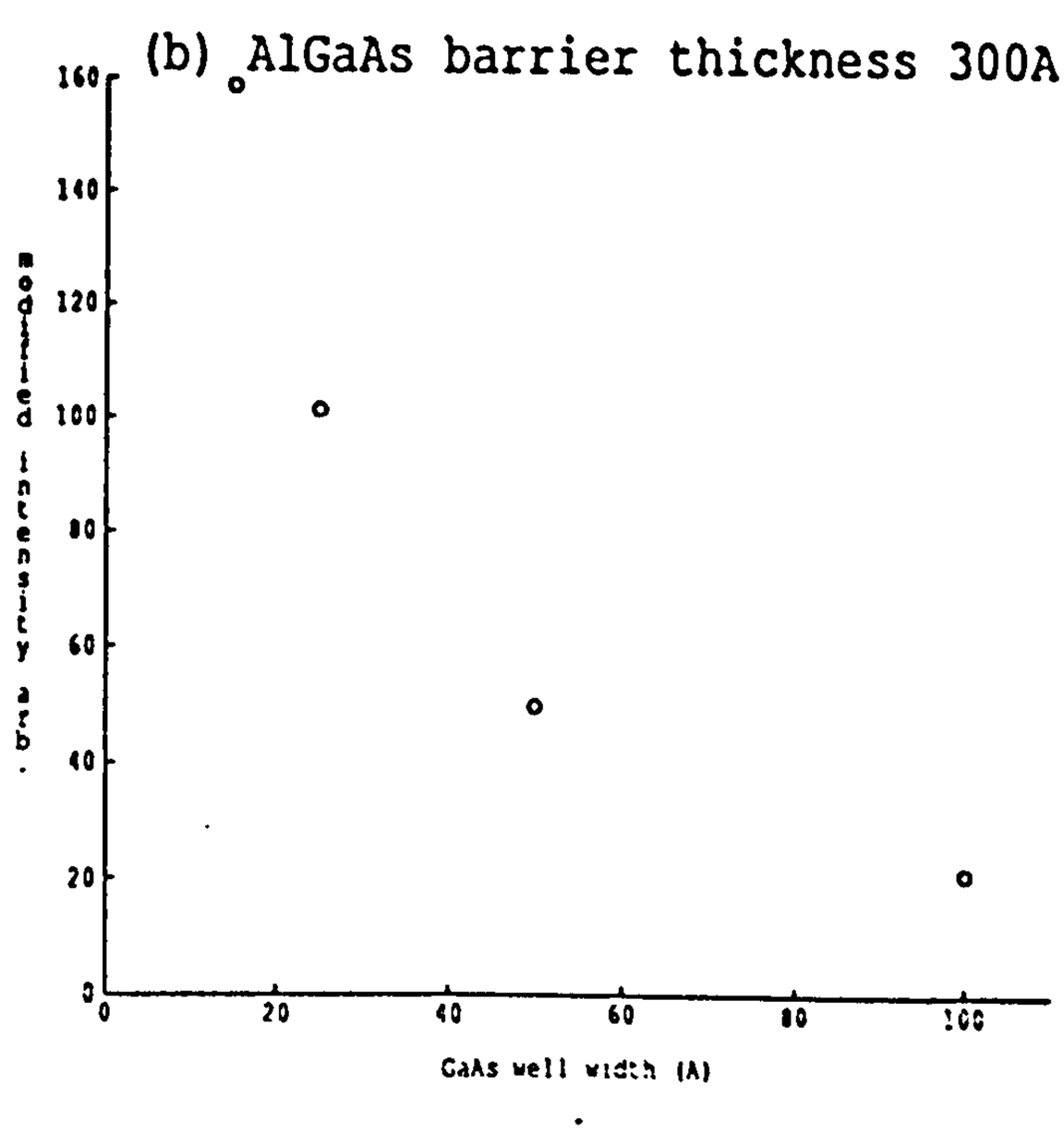

Fig.4-16 The well width dependence of CL intensity of QW emission. (a) with volum effect (open circle) and volum effect (solid line); (b) without volum effect.

Chapter 5 The CL Study of GaAs/AlGaAs SQW

In this chapter, the effects are discussed of growth interruption on the interface smoothness of MBE grown GaAs/AlGaAs single quantum well structures. High resolution TEM-CL images were obtained from the SQW structure grown with interruptions which showed local bright and dark regions. This contrast effect is the result of monolayer changes in the thickness of the QW. Studies of the dependence of the PL spectra on the sample temperature were also carried out on the SQW structures with and without growth interruption and the experimental results are reported in Section 5-2. Then in Section 5-3, an investigation is presented of the impurity distribution around a particular type of oval defect by TEM and TEM-CL. Finally, the results are described of examination of free standing quantum dots samples by STEM-CL.

5-1 CL of GaAs/AlGaAs SQWs Grown With and Without Interruption

Interfaces play an important role in many heterostructure devices that require thin layers and abrupt interfaces, such as quantum well lasers and quantum well light emitting diodes. In the MBE growth technique, which is widely used in growing GaAs/AlGaAs QW structures, it is well-known that

the growth is principally a two-dimensional monolayer-by-monolayer process, but irregularities occur. In Fig.5-1 the formation of the first two monolayers of GaAs (left) with the corresponding reflection high energy electron diffraction (RHEED) oscillations (right) is presented in real space (B.A.Joyce 1987). According to an over simplified interpretation there are maxima in reflectivity for the initial and successive smooth surfaces and minima for the intermediate stage when the growing monolayer is approximately half complete. As growth continues, a gradually damping of the maximum amplitude of the oscillation occurs due to im-perfect two-dimensional monolayer growth which results in a surface roughness statistically distributed over two or more incomplete monolayers. As a result, an interface formed on such a surface by continuous growth is not atomically abrupt. It is therefore expected that by introducing interruption in the growth prior to initiation of the interface formation, so as to provide sufficient time for surface atom migration, more smooth surfaces and more abrupt interfaces can be obtained.

This has been directly shown by the studies of RHEED and PL spectroscopy. In RHEED, the recovery of the diffraction intensity upon growth interruption has been observed and indicates the smoothing out of local roughness of the surface (J.H.Neave 1983; A.Madhukar 1985; H.Sakaki 1985; F.Voillot 1987; M.Tanaka 1988). Compared with the structures grown without interruption, the line-shape obtained by PL spectroscopy of GaAs/AlGaAs QW structures grown with interruption exhibited important changes (T.Fukunaga 1985; H.Sakaki 1985; D.Bimberg 1986; R.C.Miller 1986; B.A.Wilson 1986). The changes, which take the form of fine structure or the splitting of PL peaks, are related to the formation of the regions with well widths differing by one monolayer (ML,2.83Å) steps, with lateral size large

compared to the exciton diameter, as is schematically shown in Fig.5-2 (D.Bimberg 1986). In Fig.5-2(a) the average interface terrace size is smaller than the exciton diameter at both interfaces so that an unresolved emission peak is obtained corresponding to the well-width which is not an integral number of MLs. In Fig.5-2(b) the interface terrace size is larger than the exciton diameter, due to the growth interruption, so that three discrete emission peaks are obtained corresponding to well widths differing by one ML step and smoothing of both interfaces is assumed. In fact the smoothing process at the GaAs surfaces and AlGaAs surfaces are not equivalent due to less efficient migration of Al atoms on the AlGaAs surface (M.Tanaka 1988; D.Bimberg 1987). Increased impurity incorporation in the QW's was also reported (D.Bimberg 1987), as a result of growth interruption.

In these experiments, a series of four samples were studied by CL and PL. All samples were grown in a MBE system on an undoped SI GaAs (100) substrate and they each contain four single quantum-wells. As is shown in Fig.5-3, four SQW's with different well widths (L_z) were grown between 1000Å AlGaAs cladding layers over a 5000Å GaAs buffer layer. The nominal Lz's were 15Å, 25Å, 50Å and 100Å. The wells were separated by 300Å AlGaAs barriers and the Al content of all the AlGaAs layers was 37%. The four samples 86004, 86005, 86048 and 86049 were grown respectively without growth interruption, with growth interruption at each interface, with growth interruption at the AlGaAs-GaAs interface i.e. AlGaAs surface and at the GaAs-AlGaAs interface i.e. GaAs surface only. The duration of interruption was 2min. PL and PLE experiments of these samples have been carried out by others (C.W.Tu 1987; B.A.Wilson 1986; R.C.Miller 1986), here we report CL

spectra results from both bulk and thin specimens of these samples and the temperature dependent PL experimental results (see Section 5-2).

Fig.5-4 shows a CL spectrum of the sample 86004 which was grown continuously. Corresponding to the four single quantum wells with nominal well-widths of 15, 25, 50 and 100Å, four unresolved peaks were observed at 1.821, 1.726, 1.614 and 1.551eV. These peaks come from n=1 e-hh exciton emission and indicate that the interface terrace sizes were smaller than the exciton diameter (≈300Å). The FWHM of these peaks are 15, 12, 6 and 2meV respectively. The increase of the FWHM with the decrease of well-width results from the comparatively larger effects of well width fluctuation and barrier layer alloy composition disorder for narrower wells (J.Singh 1984, 1985). For the sample 86005, which was grown with interruption at both interfaces, significant changes in the CL spectrum were observed, as is displayed in Fig.5-5. For the well with nominal width of 100Å and major emission peak at 1.548eV, no visible changes were noted since interface roughness has little effect on the luminescence line-shape at the present spectral resolution. For the well with nominal width of 50Å, apart from the main emission peak at 1.602eV, fine structures appeared on both high and low energy sides of the main peak due to growth interruption. A dramatic decrease of FWHM from 6meV in the case of continuous growth to 2meV was obtained. The fine structures are poorly resolved and are difficult to analyze. However, as the change of the exciton emission energy due to the difference of well width by one monolayer step increases with decreasing well width, we will concentrate on studies of the spectra obtained from the narrower wells with nominal widths of 25Å and 15Å. The dominant emission peak at 1.696 and its FWHM of 5meV was observed for the well with nominal width of

25Å. The FWHM was reduced greatly in comparison with 12meV for the continuously grown quantum-well. On the high energy side of the main emission line a well resolved, weak emission peak appeared at 1.731eV while on the low energy side the additional structure was relatively poorly resolved. A temperature dependent PL study revealed that increased impurity incorporation within the quantum-well, due to growth interruption, was mainly responsible; this will be discussed in next section. For the well with nominal width of 15Å, the single emission peak of the continuously grown sample split into two discrete peaks (at 1.803eV and 1.775eV) in the case of growth interruption. The FWHMs were reduced from 15meV to 10meV. A careful study of the energy differences between these split peaks by PL and PLE determined that the corresponding well widths differed by one monolayer step (C.W.Tu 1987; B.A.Wilson 1986; R.C.Miller 1986). The appearance of the additional emission peaks and the reduction of FWHM of the main emission lines in growth interrupted samples indicate that smoothing of the interfaces occurred and that the interface terrace lengths were larger than the exciton diameter. The splitting of the emission lines into doublets rather than triplets (Fig.5-2) suggests that the terrace length is larger than the exciton size at only one of the two QW interfaces. This interface is very likely to be the GaAs-AlGaAs interface, as it is well known that the inverted interface, i.e. the AlGaAs-GaAs interface, is much rougher than the GaAs-AlGaAs interface.

By the comparison of the luminescence results from the two specimens, the model of the AlGaAs-GaAs interfaces as much more smooth after growth interruption than the same interfaces during continuous growth is confirmed. Apart from a slight decrease of FWHM of the emission peaks the sample

(86049) which was grown with interruption only at the GaAs surface revealed no other changes of CL spectrum in comparison with the results from the sample without growth interruption. In contrast, the sample (86048) which was grown with interruption only at the AlGaAs surfaces revealed noticeable fine structure in the CL spectrum, as is shown in Fig.5-11. The smaller effect of growth interruption at the GaAs-AlGaAs interface rather than at the AlGaAs-GaAs interface suggests that the GaAs-AlGaAs interface may be atomically smooth even in the case of continuous growth. Failure to observe any fine structure from sample 86049 is the result of rather rough AlGaAs-GaAs interfaces leading to very broad overlapping emission lines. The reduction of the roughness of the AlGaAs-GaAs interfaces as a result of the interrupted growth of sample 86048 decreases the FWHM of the emission lines so that the fine structures resulting from the well-width fluctuations can possibly be distinguished.

For the PL and CL spectra from a very large area of the sample with growth interruption at each interface, if the exciton thermalization effect were excluded, the relative intensity of the split peaks would reflect the average ratio of the regions of different well-width of monolayer differences thickness. No important changes in relative intensity of the split peaks were observed during bulk CL experiments on specimens of the sample 86005. This implies that the interface terrace size is much smaller than the dimensions of the generation volume which was about 5μm or more. On the other hand, significant changes in relative intensities of the split peaks were observed by moving a focused electron beam from place to place while performing CL experiments on thin specimens, from which the substrate and the buffer layer had been etched away by selective etching. This phenomenon suggests that the

interface terrace size was comparable with the generation volume size which was about 1μm in this case.

The spectral resolved CL imaging technique was also employed in these experiment to further develop and explore the work of others (P.M.Petroff 1987; D.Bimburg 1987). By this means it is possible to show direct images of regions where the interface terraces are approximately flat on the monolayer scale in the sample with growth interruption at both interfaces. The difference between our experiments and the others is the relatively high spatial resolution of our CL images as we performed them on electron-transparent thin specimens. As discussed the two discrete peaks from the growth interrupted well with nominal thickness of 15Å correspond to regions where its well-width varies by one monolayer. The highly complementary nature of the images obtained is shown in Fig.5-6. Image (a) was acquired at an emission energy of 1.803eV, corresponding to a well-width of L_z-a/2 (a/2=2.83Å is the thickness of one monolayer); image (b) was acquired at an emission energy of 1.775eV, showing the regions with well width of L_z. Image (c) in Fig.5-6 is displayed as the reversed contrast of image (a) to bring out the similarities. The sharper contrast of the image (a), bright regions of which correspond to regions with narrower well width than in image (b), indicates that there is more efficient carrier confinement in the thicker regions of the single quantum well. In an attempt to estimate the dimensions of the interface terraces, the width of the bright regions observed in image (b) in Fig.5-6 on a scale of $\approx$1μm give an upper limit since the image resolution is affected by the carrier diffusion length. Less contrast and less complementary images were obtained for the well with nominal width of 25Å, as is shown in Fig.5-7. The more uniform contrast of image (b) in Fig.5-7,

which was formed from the strongest emission line corresponding to regions with wider well width L_z, may be the consequence of a large predominance of thick regions. Because of the limitation of spectral resolution the CL images for the well with nominal width of 50Å failed to show any similar contrast effect.

LACBED patterns and quantum well diffraction contrast images, as described in Chapter 3, have been used in an attempt to correlate these results with the images obtained by CL. A typical LACBED pattern from a plan-view thin specimen of the sample which was grown with interruption at both interfaces (86005) is shown in Fig.5-8. Unfortunately we failed to observe any contrast in dark field 200 images which resembled the interface terraces observed in CL images. As the pattern in Fig.5-8 cannot be explained by the simple discussion based on kinematic diffraction presented in Chapter 3 the quantum well diffraction sidebands cannot be identified with diffraction from the single quantum wells. The failure to see relevant dark field contrast might be due to this difficulty.

5-2 Temperature Dependent PL of the GaAs/AlGaAs SQWs Grown With and Without Interruption

Standard PL experiments were performed on the samples 86004 and 86005 of which detailed structures were described in the previous section. The samples were mounted in a variable temperature He gas cryostat. The PL spectra were measured in the temperature range of 4- 150°K by use of a 514.5 nm (2.41eV) line from an Ar+ ion laser with an excitation density of about $3mW/cm^2$ and a probe size of about $1mm^2$ diameter.

Examples of the PL spectra obtained in the temperature range of 4-100°K from the 15Å and 25Å single QW's in growth interrupted sample are presented in Fig.5-9. A significant change of the spectra occurred as the temperature was increased in steps up to 100°K. The spectra obtained at temperatures lower than 40°K were qualitatively similar to the low temperature CL spectra from the same sample. For the higher temperatures, although the total PL intensity decreased with increasing temperature, the relative intensity of the high energy peaks, at 1.792eV for the 15Å well and 1.699eV for the 25Å well, increased substantially. The high energy peak started to dominate the well emission at 60°K for the 15Å well and at 100°K for the 25Å well became comparable with that of the major peak at low temperature. This effect was caused by the thermalization of carriers from thicker regions of the wells to the narrower regions. In contrast, the intensity of the weak low energy side- structure in the 25Å well emission decreased slowly with increasing temperature and completely disappeared at 100°K. This different thermalization behaviour indicates an extrinsic nature since if the emission were intrinsic, its intensity, due to the carrier thermalization effect, should decrease rapidly when the temperature was increased. We also notice that the shape of the main emission peak at 1.766eV for 15Å well is asymmetric and that it has a large FWHM. The extrinsic component of the high energy peak at 1.792eV may be responsible. Similar results have also been obtained by others (E.S.Koteles 1986; D.Bimberg 1986).

The temperature dependence of the PL peak energy of QW structures has been compared with that of bulk GaAs (T.Hayakawa 1988), with the band gap of GaAs (D.S.Jiang 1988; W.K.Ge 1987) and with that of excitation (or absorption) spectrum. The difference between the PL peak energy and its

corresponding excitation (or absorption) peak, which is commonly known as a Stokes shift, is attributed to the trapping of free excitons at interface defects. This shift is often used as a quality standard during QW structure characterization. Because the Stokes shift decreases as the temperature increases due to the thermalization of bound excitons and the change of the excitation peak energy with temperature simply follows the GaAs band gap (Eg), temperature dependent PL experiments can be used for evaluating the quality of QWs if the temperature dependence of Eg is taken as a reference. In Fig.5-10 the temperature dependencies of the n=1 e-hh exciton emission energies of the four single QW's in sample 86004 are plotted. The variation of Eg with temperature is also presented in the same figure as curve e (S.M.Sze 1981). At temperatures above 40°K, the behaviour of the peak energies of the four QWs followed Eg quite closely. But 0-5meV blue shifts of these peak energies were observed as the temperature increased from 4°K to 20°K. This results are similar to those obtained by Delalande (1985). These blue shifts are associated with the thermalization of bound excitons. At very low temperature free excitons are trapped at the interface defects before they recombine so that bound-exciton emission peaks are obtained. When the temperature increases detrapping of these bound excitons occurs and higher energy free exciton emission is observed. Moreover, we notice that the blue shift was well-width dependent and increased as the well width decreased. Since these well were grown under almost identical conditions so that wells of very similar quality would have resulted, this well- width dependent phenomenon indicates that the binding energy of free excitons at interface defect was well-width dependent. Similar results were obtained for sample 86005, but the value of

the blue shift was decreased for all the wells. This result is evidence of the improvement of interface quality by introducing growth interruption.

5-3 The Study of Oval Defect in GaAs/AlGaAs SQW

Microscopic surface defects, so called "oval defects" are commonly observed in GaAs and AlGaAs layers grown by MBE. So far, studies have been focused on the characterization of such defects, and the determination of their origins. These observations show that defects are generally elongated along the (110) directions. It is known that the origin of these defects are related to a number of factors arising out of the systems employed and the growth conditions used (S.Matteson 1986; K.Nanbu 1986). As a result, there are a number of different oval defects and many of these have now been identified. A recent thorough classification has been given by K.Fujiwara et al (K.Fujiwara 1987). However, in this work we have studied a particular type of oval defect in an MBE grown SQW sample (86048) with the detailed structure shown in Fig.5-3. TEM-CL and TEM investigations were carried out on a selectively etched, thin, plan-view specimen. The four single quantum wells contained in the specimen, which have well-distinguished emissions, allowed us to study each separately by CL.

Fig.5-11 shows the CL emission from an unfaulted area. The four peaks at 1.800eV, 1.70eV, 1.650eV and 1.540eV in the spectrum are attributed to the four single quantum-wells with nominal widths of 15Å, 25Å, 50Å and 100Å respectively. The line widths for the narrower wells are greater than those for the wider wells due to the larger effects of interface roughness and barrier composition fluctuations for the narrower wells as has been discussed

in previous section. The TEM bright field image of a typical oval defect observed in our experiment is shown in Fig.5-12. Detailed studies show that the core area of the defect is misorientation crystal and the longer oval axis is along the [100] direction. This is not the usual sense of elongation for oval defects found by other researchers (S.Matteson 1986; K.Nanbu 1986; K.Fujiwara 1987). As we can see, some twins and dislocations surround the core of the defect. At the core of the oval defect, the CL emission is totally quenched due to the high concentration of non-radiative recombination centres created by the highly faulted crystal. The CL emission from the area around the core of the defect (faulted area) where the crystal structure is unfaulted is shown in Fig.5-13. The relative intensities of the spectra in Fig.5-11 and Fig.5-13 have been adjusted for easy comparison. The differences between the spectrum from the unfaulted area and the spectrum from the faulted area are obvious. The studies of the differences for the four single QW's have been performed separately. The results show a gradual decrease of the differences in going from the 100Å well, which was grown first, to the 50Å well, the 25Å well and the 15Å well, which was grown last. In particular the emission of the 15Å well was almost unchanged between the unfaulted and faulted areas, as is shown in Fig.5-14 where spectrum (a) was obtained from the unfaulted area and spectrum (b) was from the faulted area.

However, significant changes have been observed between the emissions of the 100Å well acquired from unfaulted and faulted areas, as is shown in Fig.5-15. Spectrum (a) in Fig.5-15 is from an unfaulted area. The main peak at 1.541eV corresponds to the QW n=1 (hh-e) excitonic emission; the smaller peak on the high energy side of the main peak is from the recombination of (lh-e) excitons. Spectrum (b) is from the faulted area. The

dramatic decrease of intrinsic emission intensity in the spectrum is due to the appearance of impurities and non-radiative recombination centres in the area.

A slight shift of the intrinsic emission towards the low energy side may result from defect-related strain, or distortion of the well-width or the barrier layer composition at the vicinity of the defect. Some extra structure also appears on the low energy side of the main QW emission. The broad continuous line shape of extra structure is considered to be related to the distribution of impurities along the growth direction rather than different species of impurities as has been discussed in Chapter 1 and 4. The position of the low energy end and high energy end of the broad structure correspond to impurities with ionization energy of about 29meV and 18meV respectively. According to previously detailed discussions, we believe that this broad structure is acceptor-like impurity related emission and the impurities with ionization energy of 18meV were sitting at interfaces while the impurities with ionization energy of 29meV were distributed near the centre of the wells. The fact that emission associated with interface impurities is present in the broad impurity-related emission band implies that segregation to the interfaces has occurred. The results indicate a considerable accumulation of impurities in the 100Å well around the core of the defect. This uneven distribution of impurities along the growth direction implies that the residual impurities in the growth system were mainly trapped in the first well to be grown. These experiments were not able to address the question of whether the impurities came from the core of the defect or rather by general accumulation at the defect.

By applying the CL monochromatic image technique, we have studied the lateral distribution of impurities in the wells around the defect. The

results for the 100Å well are presented in FIg.5-16. The TEM image of the same area is shown in Fig.5-16(d). The CL image in Fig.5-16(a) was formed by choosing the QW intrinsic emission. The strong emission only appeared at regions (bottom left) remote from the defect. Fig.5-16(b) and Fig.5-16(c) show respectively the CL images formed from the interface impurity emission and well centre impurity emission. As we can see, the impurities sitting at the centre of the well are restricted to the area very near to the core of the defect, whereas those sitting at the interfaces have a much wider distribution around the defect. This suggests that interfaces are possible channels for impurity diffusion while the well centre position only becomes occupied when the impurity concentration increases no matter how the impurity diffusion occurs.

5-4 Studies of AlGaAs/GaAs Quantum Dots

As described previously, large changes of the optical and transport properties have been observed between three-dimensional bulk materials and two-dimensional quantum well structures. One expects new physical phenomena to emerge if the dimension of the materials can be reduced further. In Fig.5-17 the changes of the energy dependent density of states in going from a three-dimensional bulk system to a two-dimensional quantum well structure, a one-dimensional quantum wire and a zero- dimensional quantum dot are shown (A.Forchel 1988). In contrast to the parabolic density of states function for the three-dimensional system, a discrete series of states is obtained for the extreme case of a zero dimensional quantum dot. At the approximation of infinite potential barriers, the confinement energies for an

electron or a hole in a rectangular shape quantum dot can be given as (W.Y.Wu 1987)

$$E = \frac{\pi^2 h^2}{2 m^*} \left(\frac{n_1^2}{L_x^2} + \frac{n_2^2}{L_y^2} + \frac{n_3^2}{L_z^2} \right) \qquad n_i = 1,2,3, \qquad 5\text{-}1$$

where m^* is the effective mass of an electron or a hole; E is the confinement energy measured upward from the bottom of the conduction band or downward from the top of the valence band and L_x, L_y and L_z are the lateral sizes and the vertical size of the quantum dot respectively. The ground state sub-band of the electrons in the conduction band or the holes in the valence band corresponds $n_i=1$.

Generally speaking, two different methods have been applied to produce the quantum dots from quantum well structures. By a combination of ion-implantation-induced interdiffusion in QW structures with high resolution electron beam lithography, buried quantum dots can be formed (J.Cibert 1986, 1987; P.M.Petroff 1987; A.Forchel 1988), as is schematically shown in Fig.5-18. On the other hand, by the application to the quantum well structures of electron-beam lithography patterning and dry etching free-standing quantum dots can be fabricated (see Fig.5-19). The results of luminescence studies of etched AlGaAs/GaAs quantum dots are inconsistent so far. Due to the sidewall surface damage induced during the etching process, a high surface recombination velocity is expected. In addition there will be a surface layer depleted of carriers. A degradation of luminescence efficiency was observed as the lateral size of the dots approached the carrier diffusion length ($\approx 1\mu m$) (A.Forchel 1988; E.M.Clausen 1989) and a depletion layer with depth of 100-

150nm at the sidewall surface was obtained by optical measurements (A.Forchel 1988) and magnetotransport measurements (T.Demel 1988). However, another study has claimed no degradation of luminescence efficiency occurred in etched quantum dot structures with the lateral sizes of the dots as small as 40nm (K.Kash 1986; H.Arnot 1988).

In this experiment, the AlGaAs/GaAs quantum dots were formed from the quantum well structure shown in Fig.5-20. This contained four single quantum wells with GaAs well widths of 50Å, 100Å, 200Å and 800Å and AlGaAs barrier thickness of 340Å. The free-standing quantum dots were produced by electron beam lithography patterning and reactive ion-etching using either silicon tetrachloride ($SiCl_4$) or methane/hydrogen (CH_4/H_2). The etching depth was varied from 800Å to 1200Å, which ensured that the 50Å and 100Å wells were formed into dots. Dots with diameters between 60nm and 0.5μm have been studied. When the dots were examined in an SEM patterning defects were discovered. Fig.5-21 shows some examples for the case of the 300nm dot array. In STEM the dots could also be recognized in secondary electron images, although the image quality was very poor in comparison with the SEM images. The STEM images enabled us to identify the dot areas so that individual dots could be studied by low temperature CL.

Each sample it contained a large unetched area (50μm-100μm in size). The luminescence spectrum from such areas is shown in Fig.5-22. This represents the QW emission from the structure prior to etching. The peaks at 1.591eV, 1.543eV and 1.521eV correspond to the QW excitonic emission from the 50Å, 100Å and 200Å wells respectively. Emission from 800Å well overlapped the GaAs bulk emission at 1.514eV from the buffer layer and substrate. The low energy tail of this emission may have resulted from the

impurities in the GaAs buffer and substrate. After the fabrication of the quantum dots, the luminescence spectrum from the etched area, which still contained the 200Å and 800Å quantum-wells, had changed greatly. As shown in Fig.5-23, the low-energy tails in Fig.5-22 from the bulk GaAs layers dominated the whole spectrum. The high energy shoulder at 1.517 and 1.513eV may correspond to the 200Å and 800Å well emissions but with their energies both shifted from the values prior to etching. By acquiring CL monochromatic images at the energies corresponding the supposed 200Å and 800Å well emissions from a region which included both etched and unetched areas, from a sample with an etching depth of 800Å, we noticed a great decrease of CL intensity in the etched area, see Fig.5-24 (a) & (b). The rectangular shaped frames are the unetched areas. These changes in emission line shape and intensity from etched areas suggest that the process of fabrication of the quantum dots induced surface damage, probably during the ion etching process.

Quantum-dots produced from the 50Å and 100Å quantum wells with diameters of 60nm, 90nm, 100nm, 150nm, 250nm, 300nm and 500nm were examined by STEM-CL. No luminescence signal corresponding the 50Å or 100Å well-emissions was detected in our experiments for dot diameters equal to or less than 300nm. The spectra obtained from these dots are similar to one shown in Fig.5-23. This result indicates that severe sidewall surface damage occurred due to ion etching and a carrier depletion layer i.e. luminescence dead layer formed with a depth of more than 150nm. These results are reasonably consistent with those of A.Forchel (A.Forchel 1988) and T.Demel (T.Demel 1988) who estimated a carrier depletion layer thickness of 100nm-

150nm at the sidewall surface. This depletion layer width determines the smallest dot size that will still emit light.

However, for the quantum dots with diameters of 500nm the luminescence signal corresponding to the 50Å and 100Å wells was obtained from individual dots. As is shown in Fig.5-25, no changes in the emission energies and FWHM were detected in comparison with the quantum-well emissions of Fig.5-22. According to Equation 5-1, the changes of the effective energy gap caused by lateral confinement of carriers for quantum dots with diameters larger than 120nm are less than 1meV, so for 500nm dots the energy shift would be unobservable. Moreover, we observed a degradation of luminescence efficiency for these quantum wells. After taken into account of volume effect, there was a decrease by a factor of 0.5 for the 50Å wells and of 0.2 for the 100Å well in comparison with the luminescence efficiency of the unetched structures. This degradation was due to the very high non-radiative recombination velocity at the sidewalls. The different degradation factors for the 50Å and 100Å wells may be explained by the lower carrier diffusion coefficient for the narrower quantum wells due to the carrier confinement effect. This means that the narrower the QW, the smaller the number of carriers which could reach the sidewall surface, so the weaker the surface effect. The integrated CL intensities from the dots formed by 100Å wells was also weak as compared with that of the 50Å wells, as is shown by the CL monochromatic images in Fig.5-26. Image (a) in Fig.5-26 was taken at an energy corresponding to the emission of the dots formed by the 50Å wells while image (b) was taken from the emission of the dots formed by the 100Å wells. The ratio of the dot image intensity to the background is much higher for the dots formed by the 50Å wells than that for the 100Å wells as is

indicated by the corresponding line scan curves. The bright patch at the left of the images is a processing fault and there is a dot missing in image (a) but not in image (b). This study indicates that high resolution STEM-CL is very useful for studying the performance of individual dots.

In integrated CL images of the quantum-dot samples we observed some irregularly scattered bright spots here and there. Apart from the same broad peak shown in Fig.5-23 on the low energy side of the spectra, the CL spectra obtained from these bright spots all contained a group of two or three peaks with energies falling between 1.642eV and 1.851eV. These energies are much higher than any quantum well emission from the structures. Fig.5-27 gives a example of such spectra. If these energy shifts were caused by carrier confinement effects in a lateral direction, then these bright spots must correspond to dot sizes of 7nm-16nm in diameter according to Equation 5-1. However, this is unlikely to be the explanation as no light was emitted even from the dots with diameters of 300nm. Hence the origin of the high energy peaks remains unknown.

In conclusion, our studies of free-standing quantum dots, fabricated by reaction ion etching reveal that severe surface damage occurred at the sidewall surfaces. This resulted in a total loss of luminescence from quantum dots with diameters less than 300nm and represents a major obstacle to the observation of new phenomena induced by decreasing dimensions of the structures.

Text cut off in original

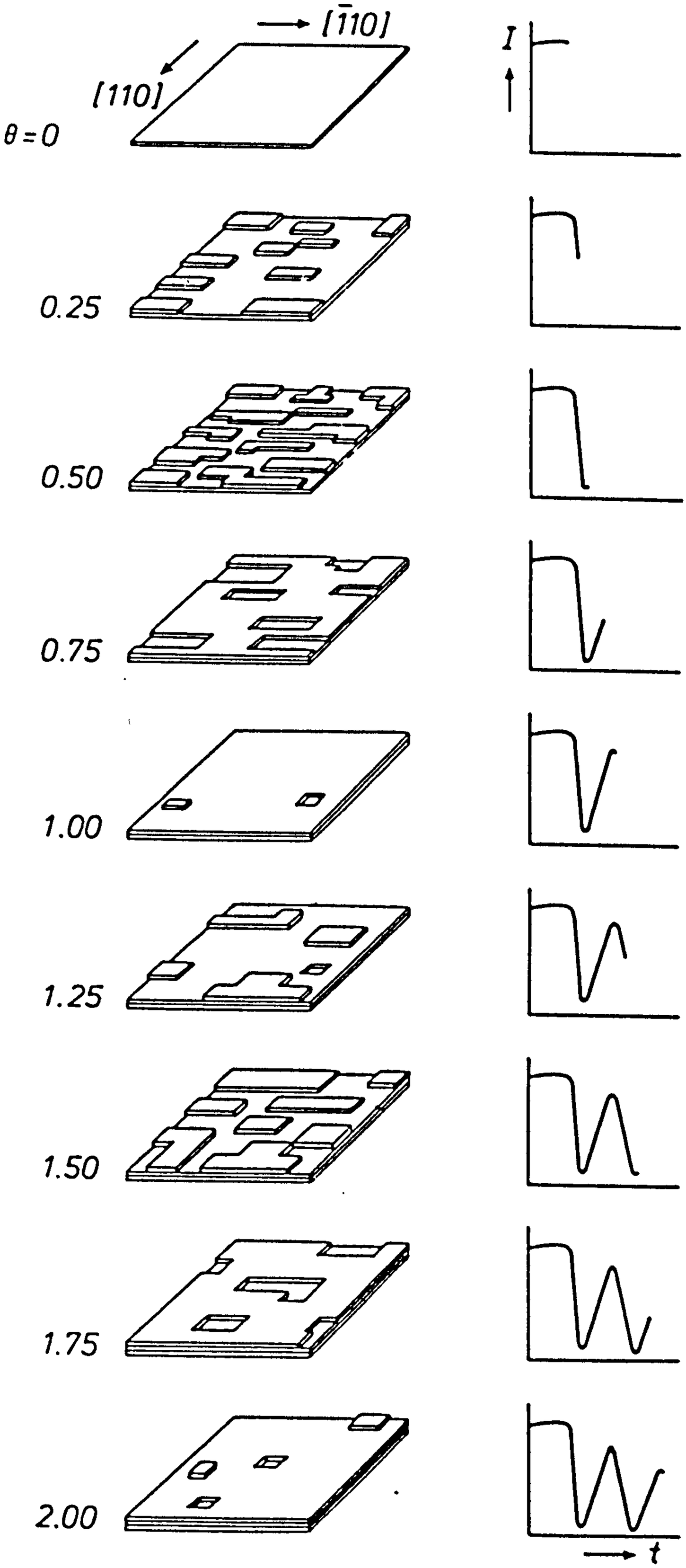

Fig.5-1 The schematic diagram of the formation of the MBE grown first two monolayers of GaAs (left) with the corresponding RHEED oscillations (right) (after B.A.Joyce 1987)

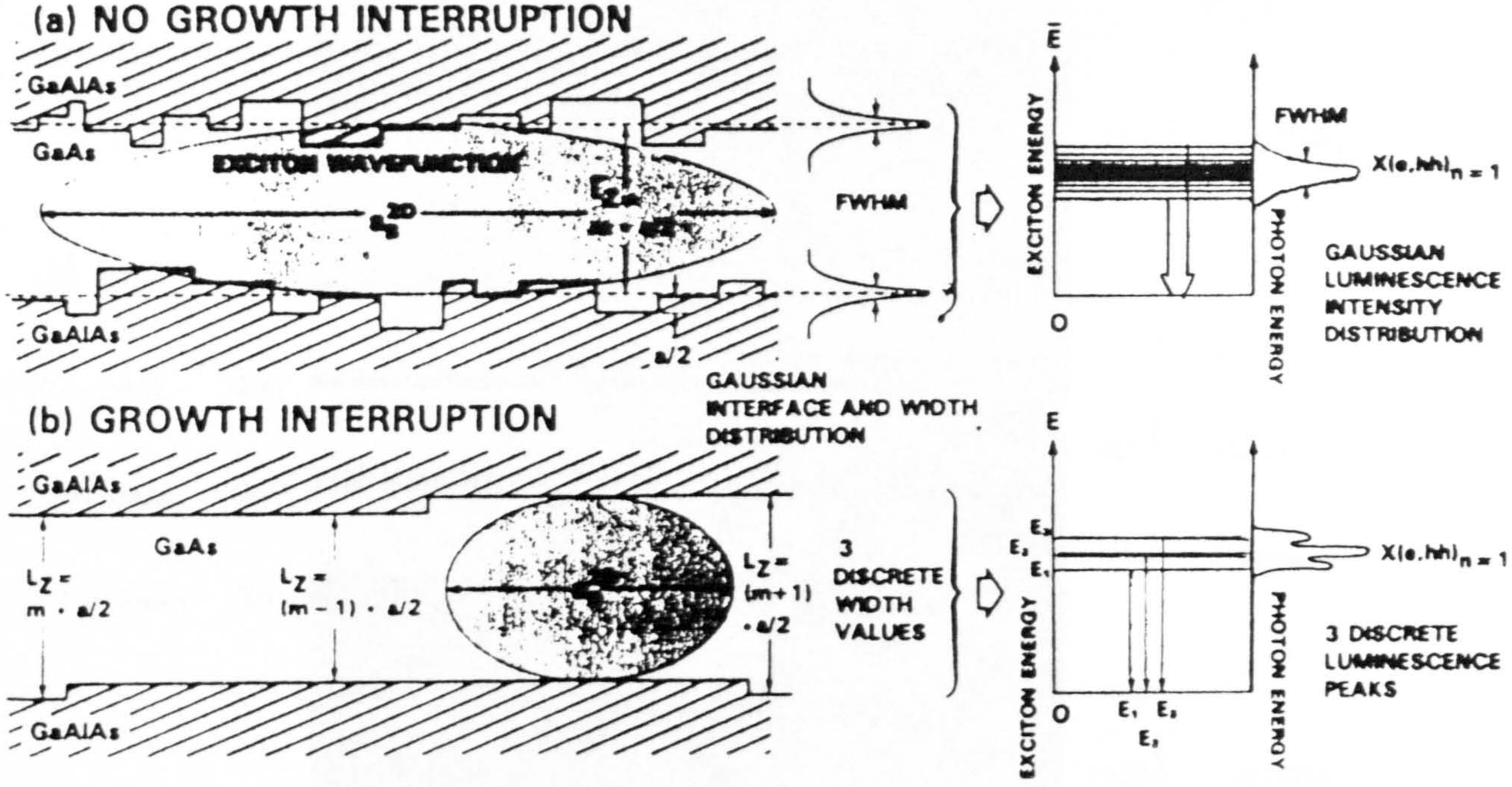

Fig.5-2 Model showing interface roughness of GaAs/AlGaAs QW grown without (a) and with (b) interruption and corresponded n=1 e-hh exciton emission lines.

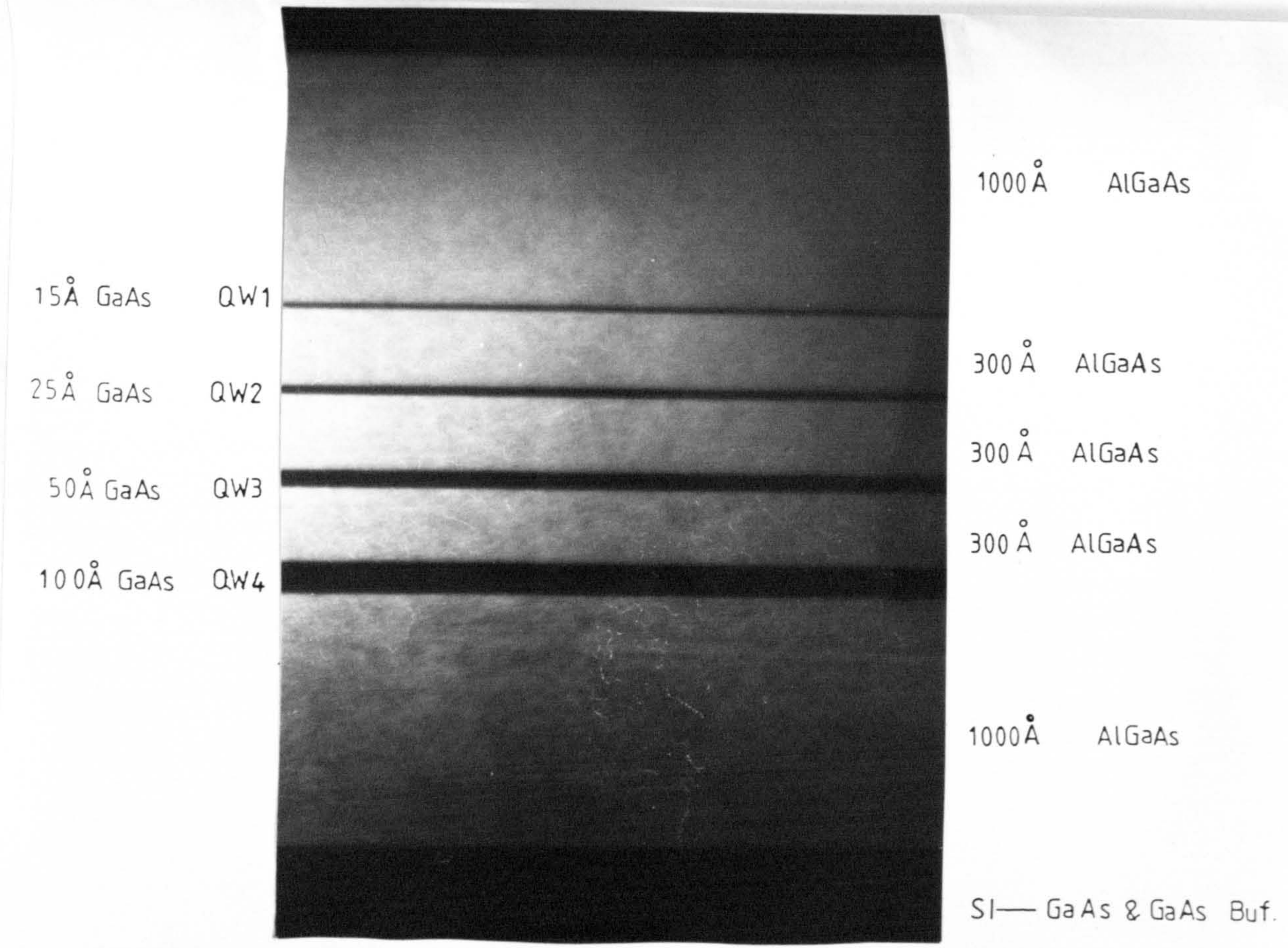

Fig.5-3 Cross-section TEM image showing the layout of the samples (86004, 86005, 86048 and 86049).

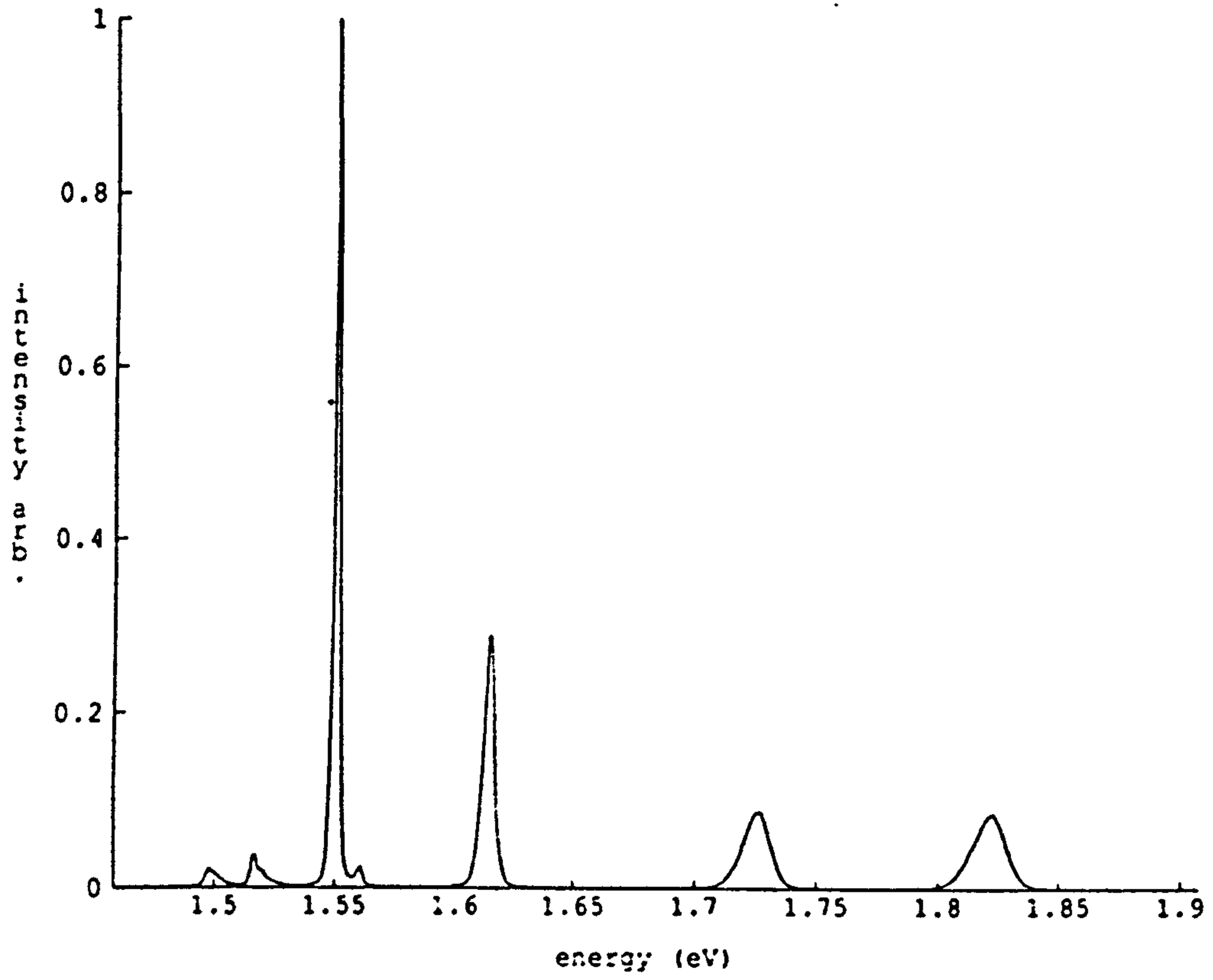

Fig.5-4 CL spectrum from sample 86004 grown without interruption.

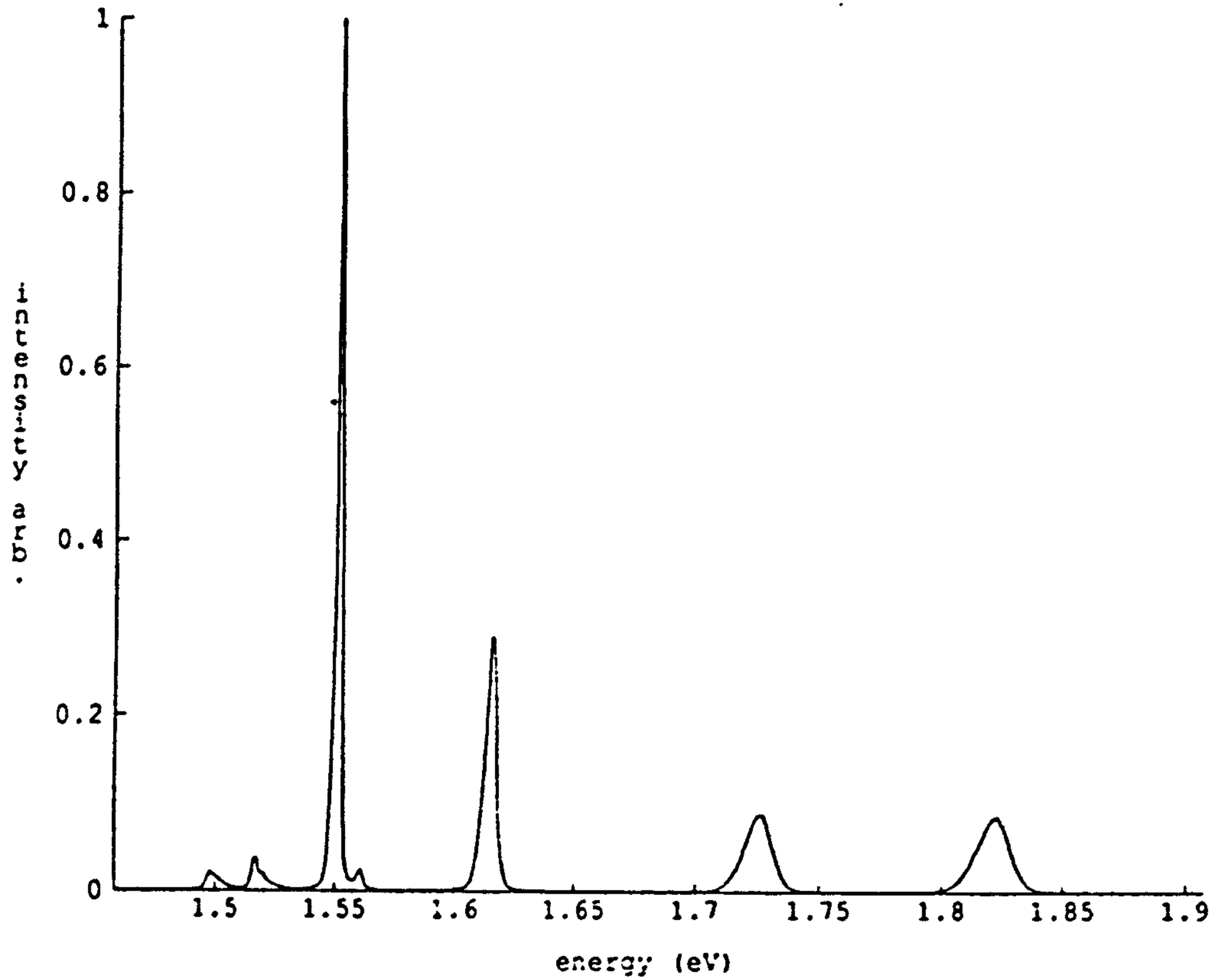

Fig.5-4 CL spectrum from sample 86004 grown without interruption.

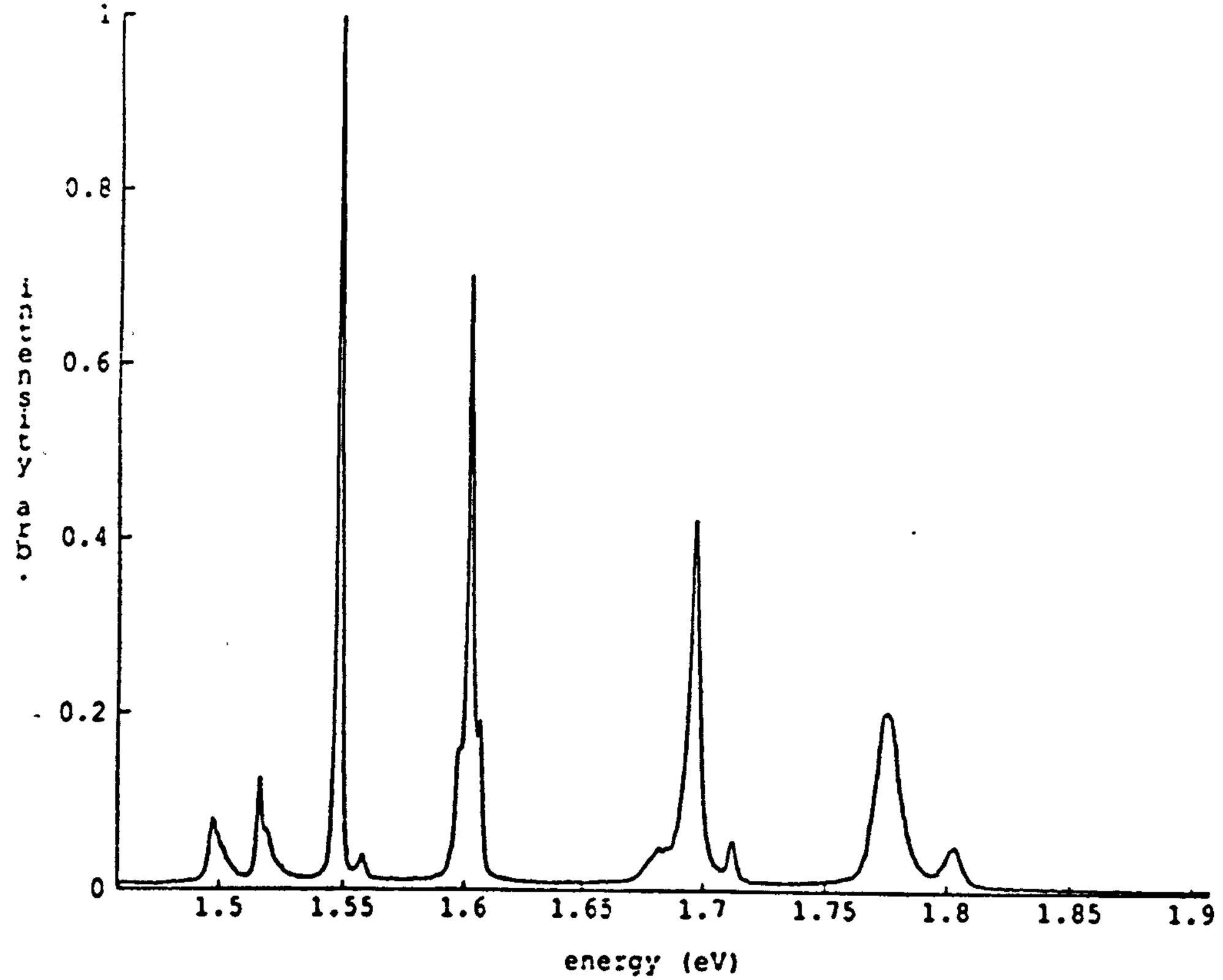

Fig.5-5 CL spectrum from sample 86005 grown with interruption at each interface.

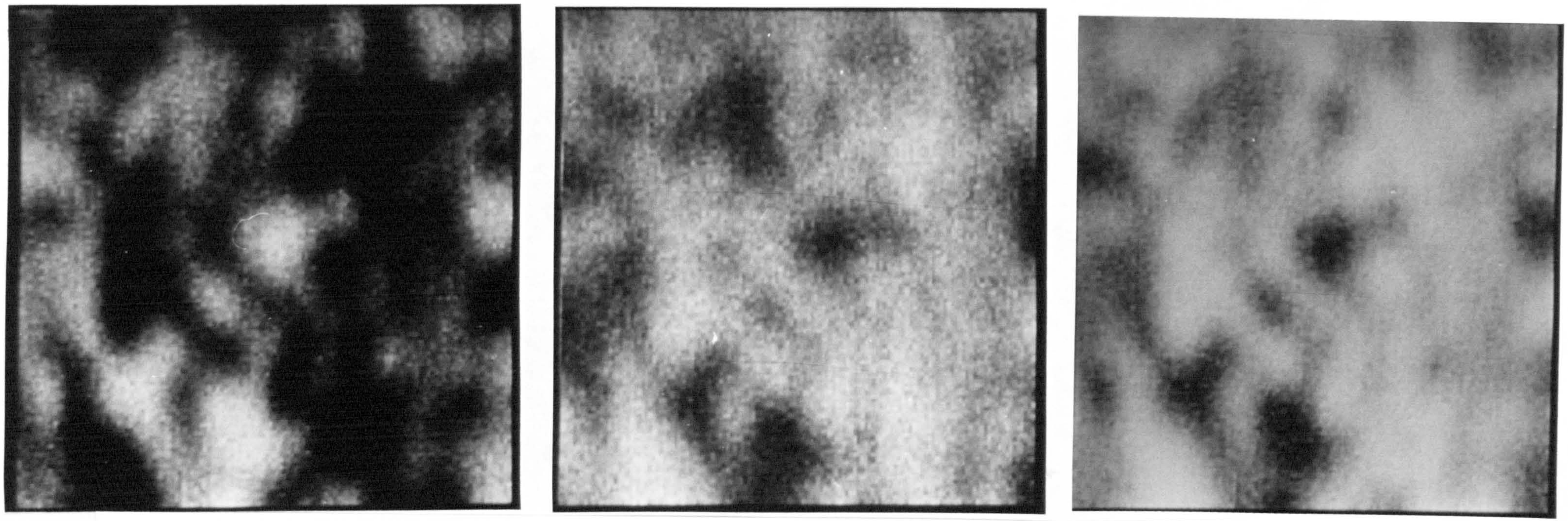

Fig.5-6 Monochromatic CL images acquired (a) at 1.803eV and (b) at 1.775eV corresponding QW emission of 15A well in sample 86005. Image (c) is a invert contrast of image (a).

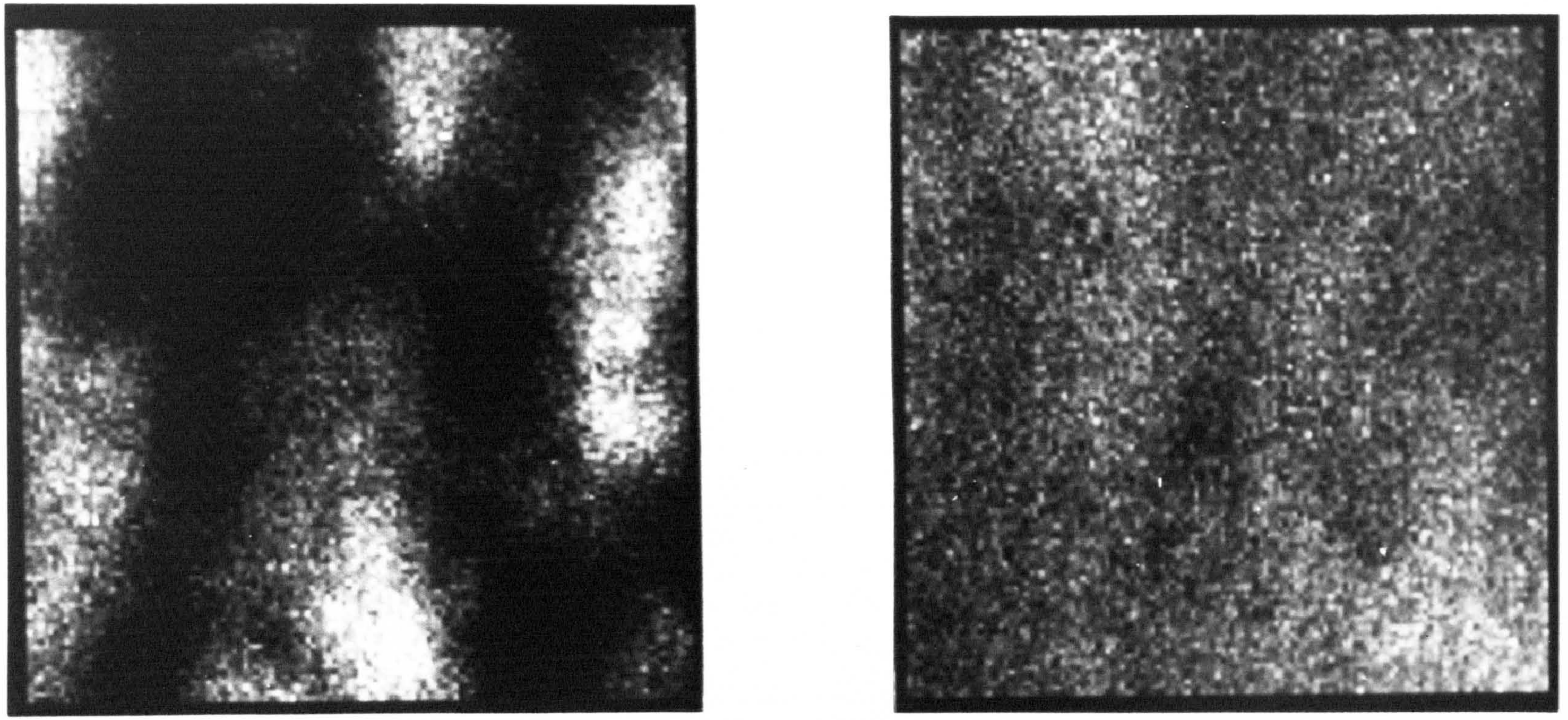

(a) 1.713eV

500nm

(b) 1.696eV

Fig.5-7 Monochromatic CL images acquired (a) at 1.713eV and (b) at 1.696eV corresponding QW emission of 25A well in sample 86005.

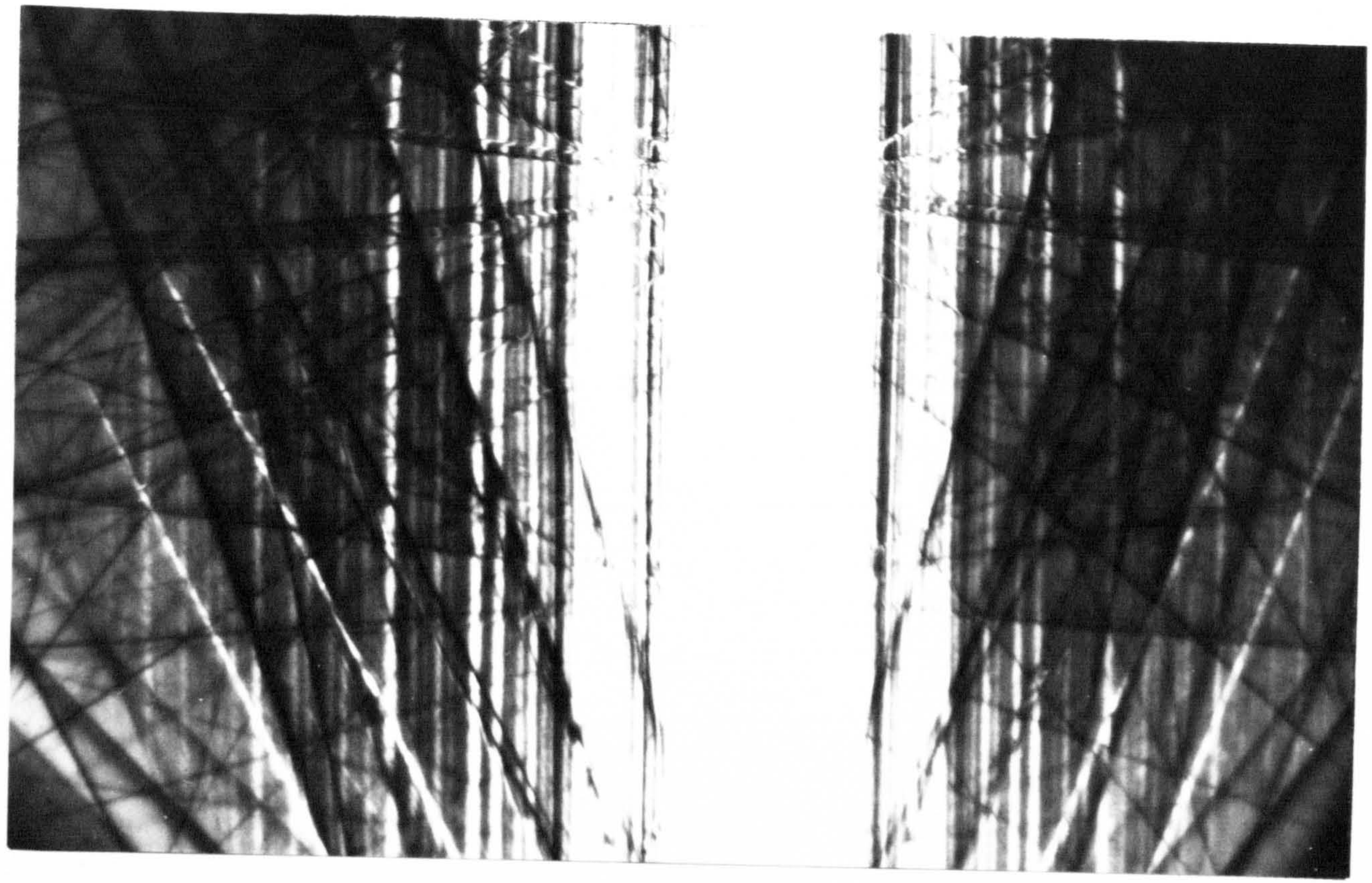

Fig.5-8 200 dark field LACBED pattern from a plan view specimen of sample 86005.

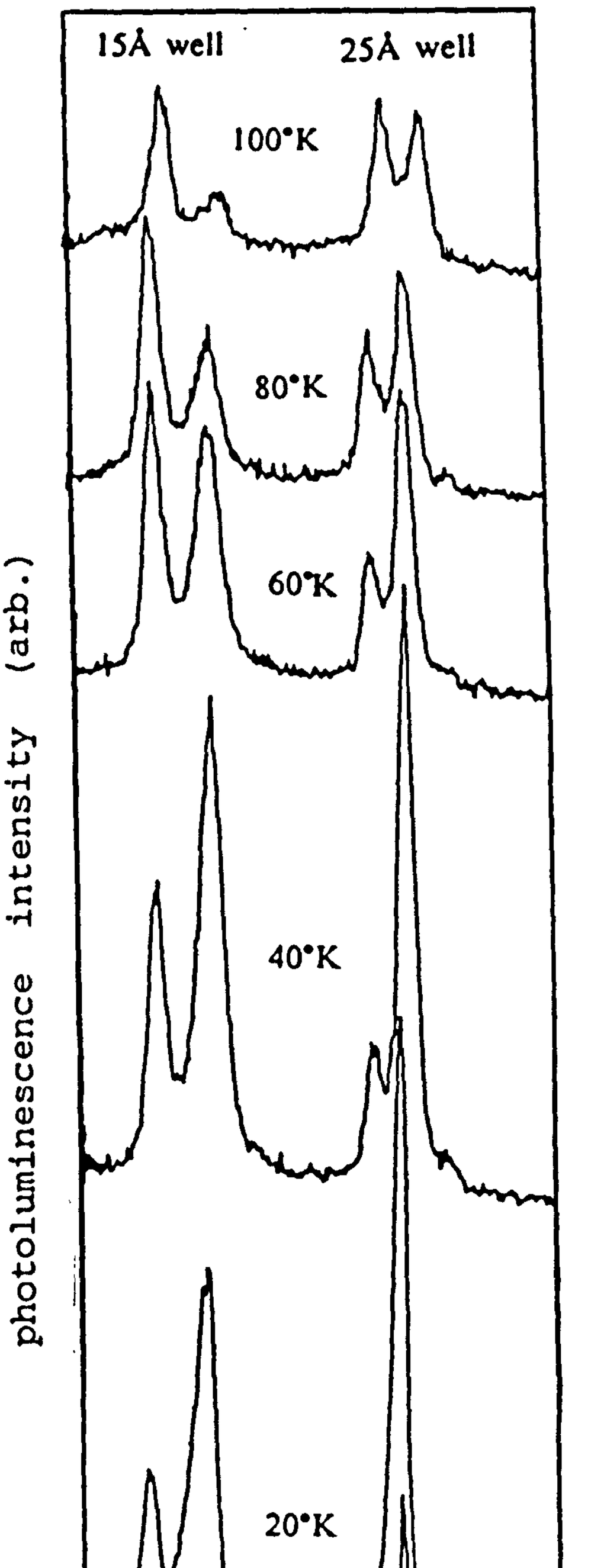

Fig.5-9 CL spectrum of 15A and 25A well emission as a function of sample temperature.

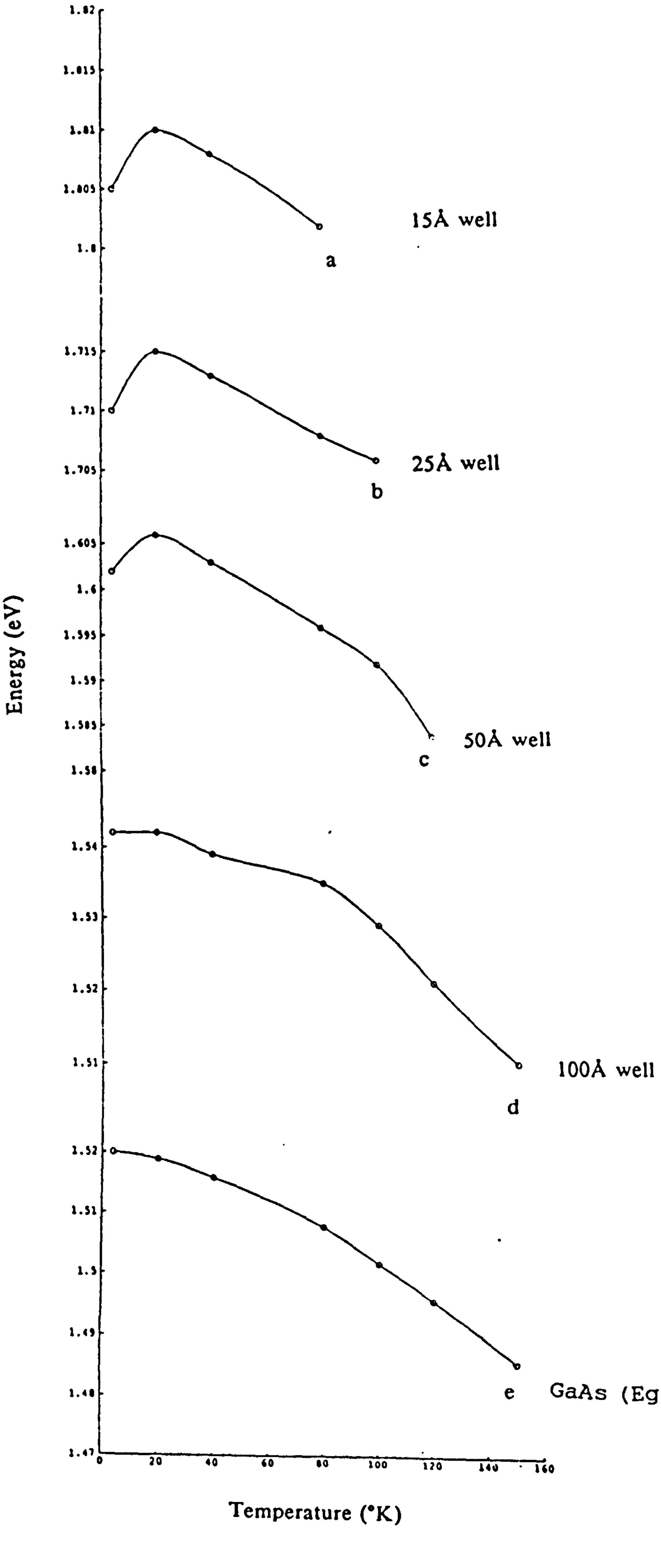

Fig.5-10 Temperature dependence of four single QWs (Lz=15A, 25A, 50A & 100A) emission energy together with GaAs band gap Eg.

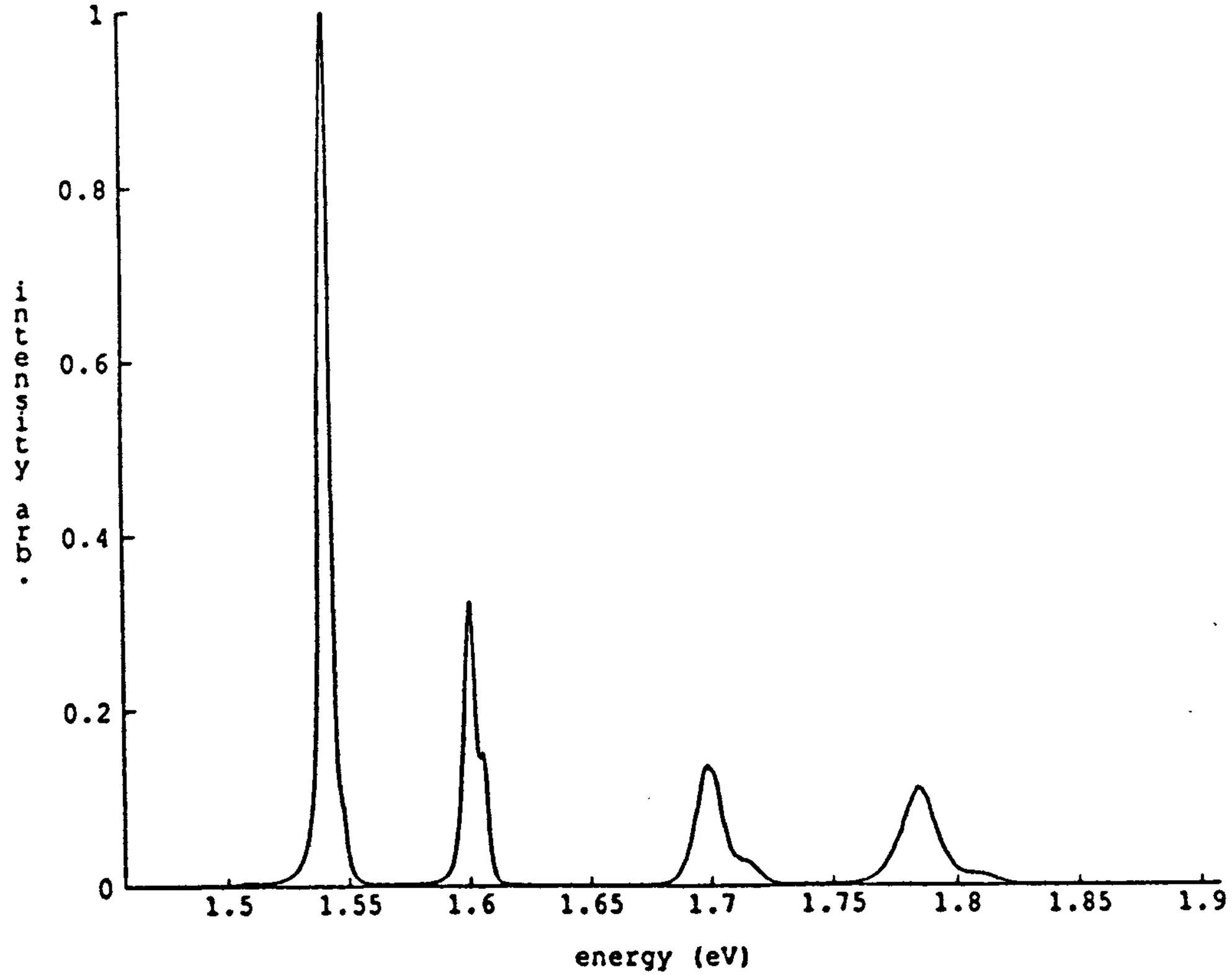

Fig.5-11 CL spectrum from unfaulted area.

Fig.5-12 TEM BF image of a typical oval defect.

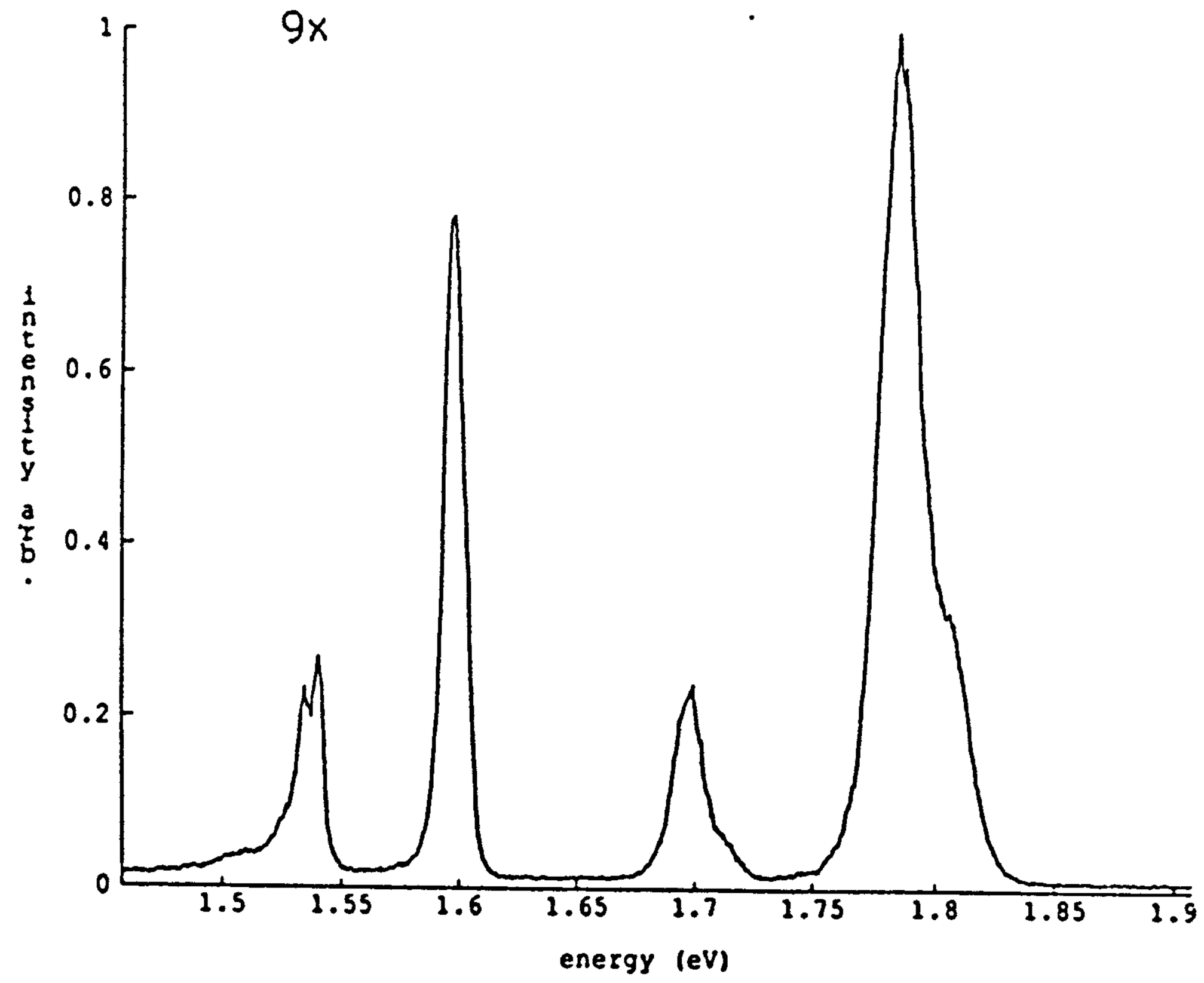

Fig.5-13 CL spectrum from faulted area.

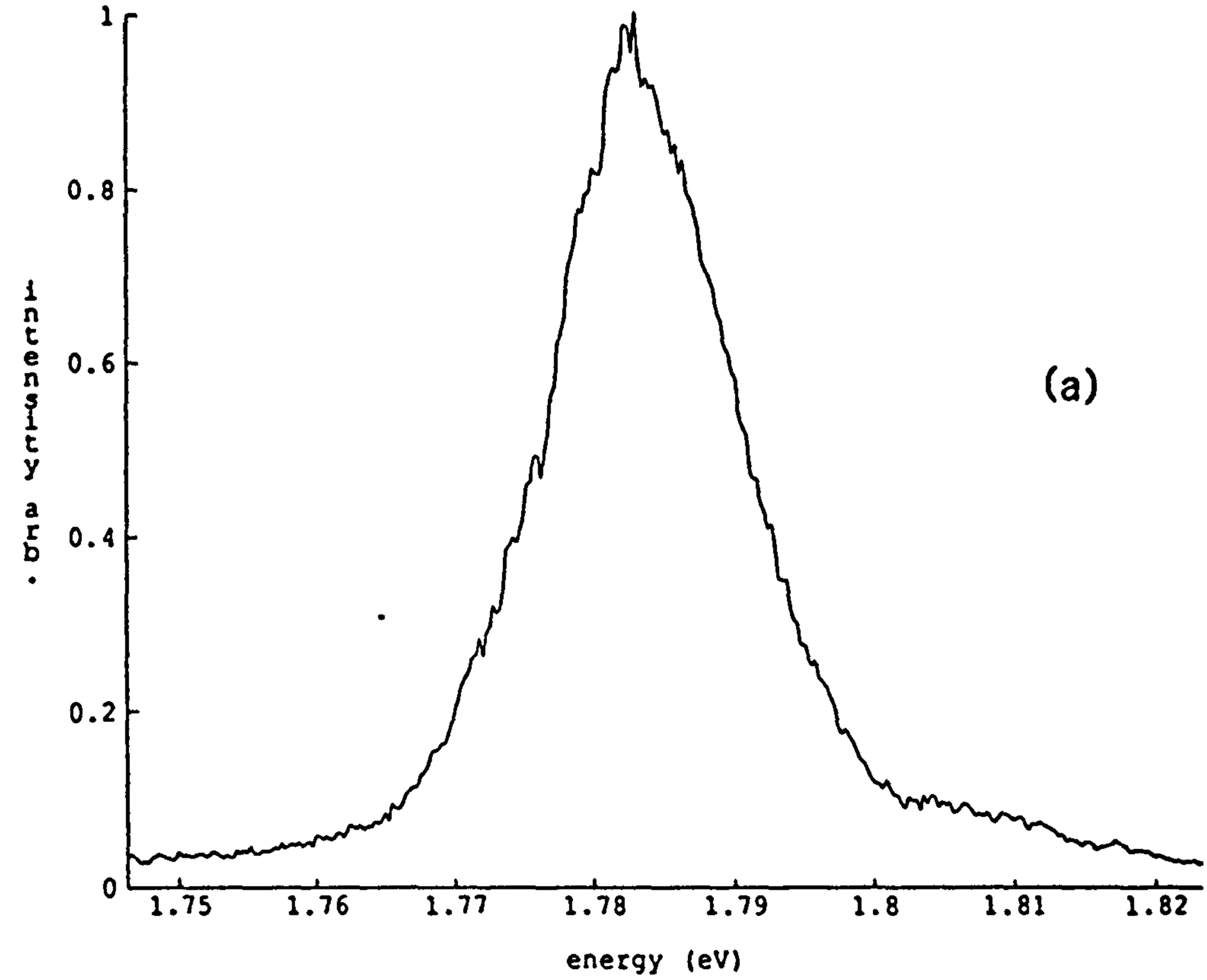

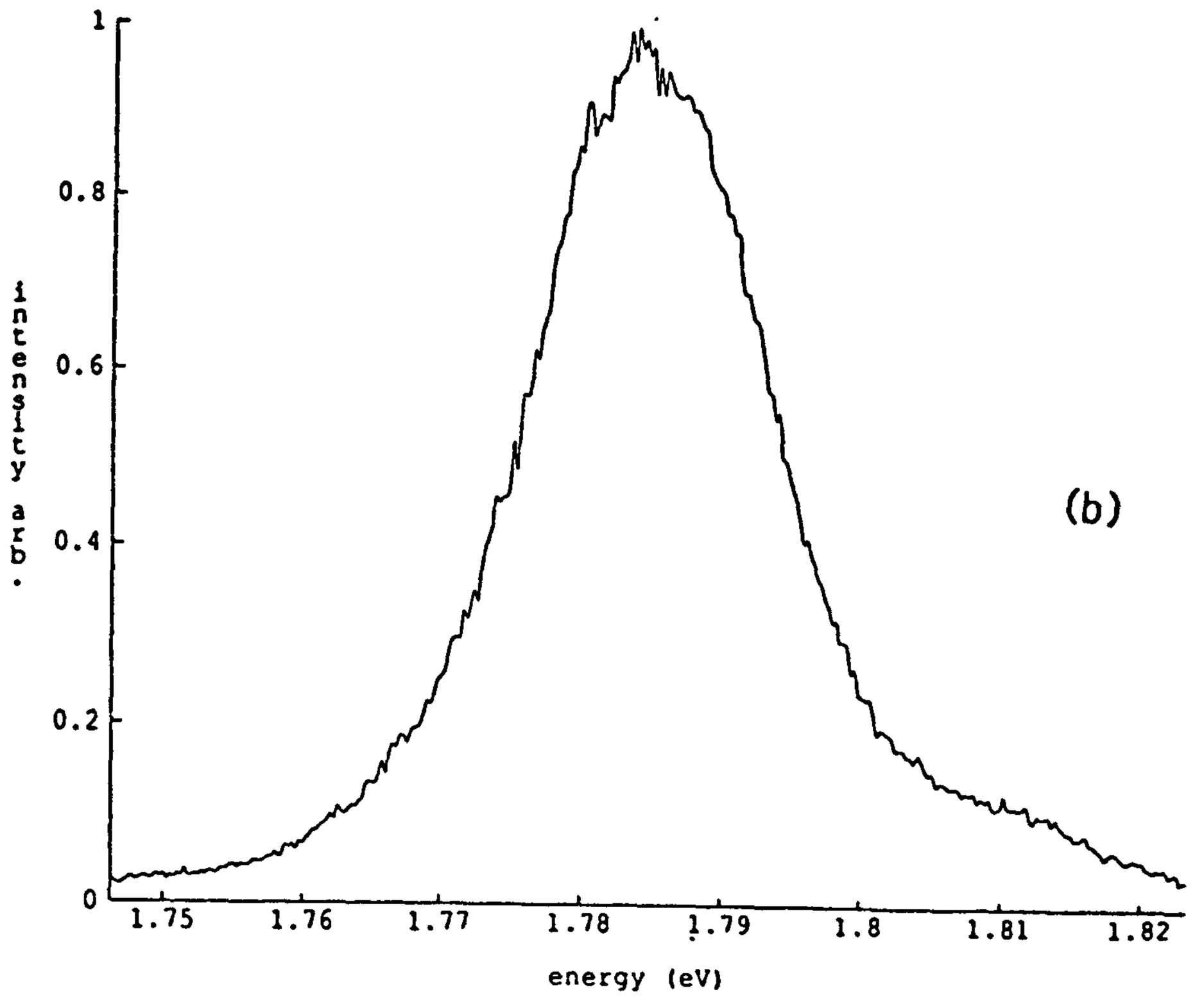

Fig.5-14 (a) CL spectrum of 15A well from unfaulted area;
(b) CL spectrum of 15A well from faulted area.

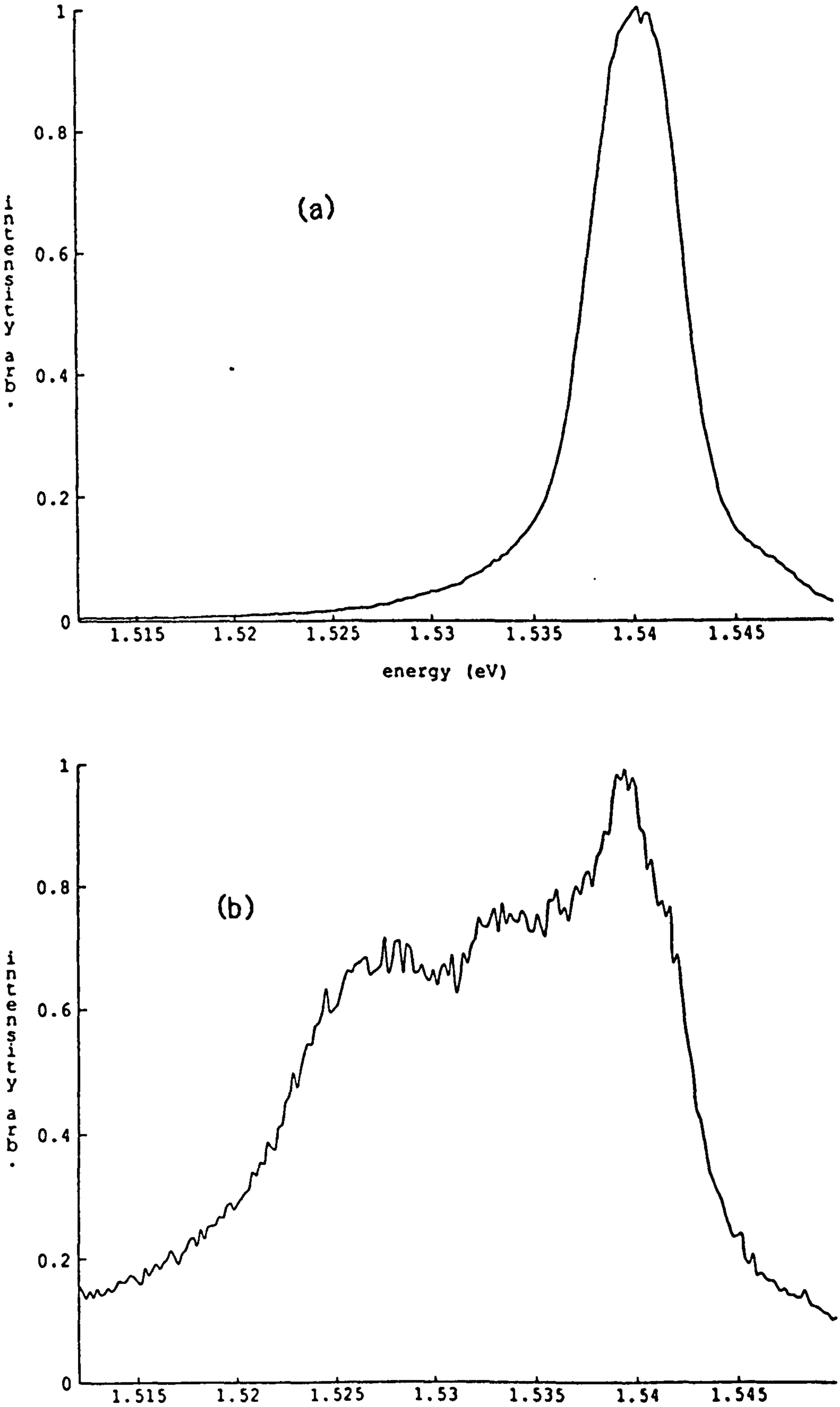

Fig.5-15 (a) CL spectrum of 100A well from unfaulted area;
(b) CL spectrum of 100A well from faulted area.

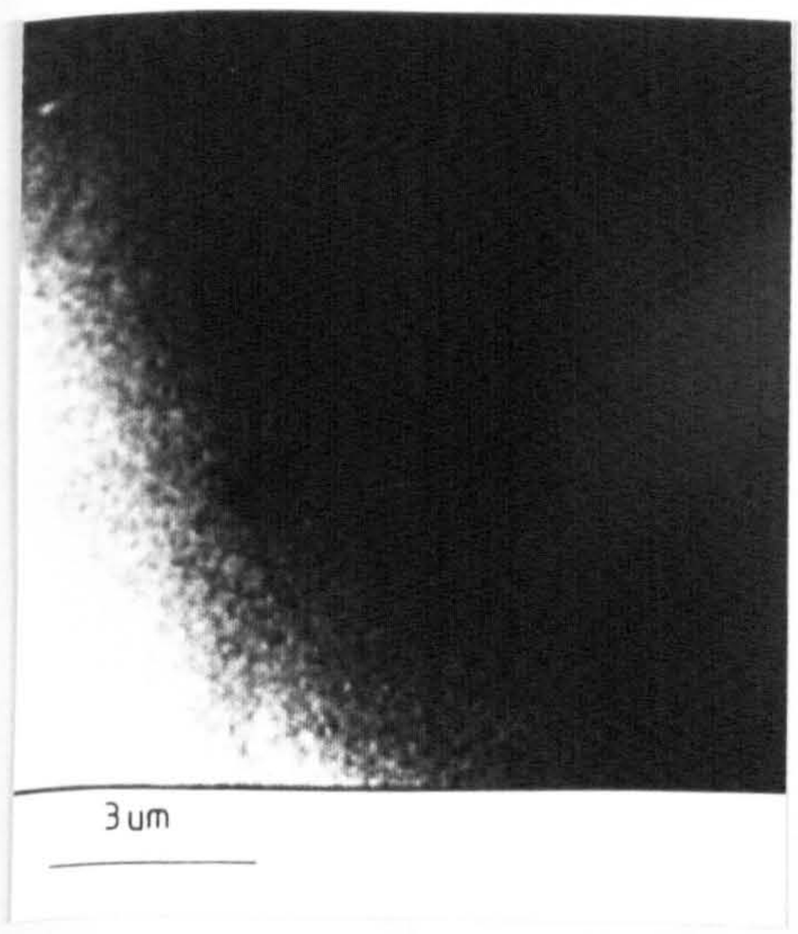

(a)

(b)

(c)

(d)

Fig.5-16 (a) Monochromatic CL image choosing QW emission at 1.541eV;
(b) Monochromatic CL image choosing impurity emission at 1.535eV;
(c) Monochromatic CL image choosing impurity emission at 1.527eV;
(d) TEM image of the area of CL acquisition.

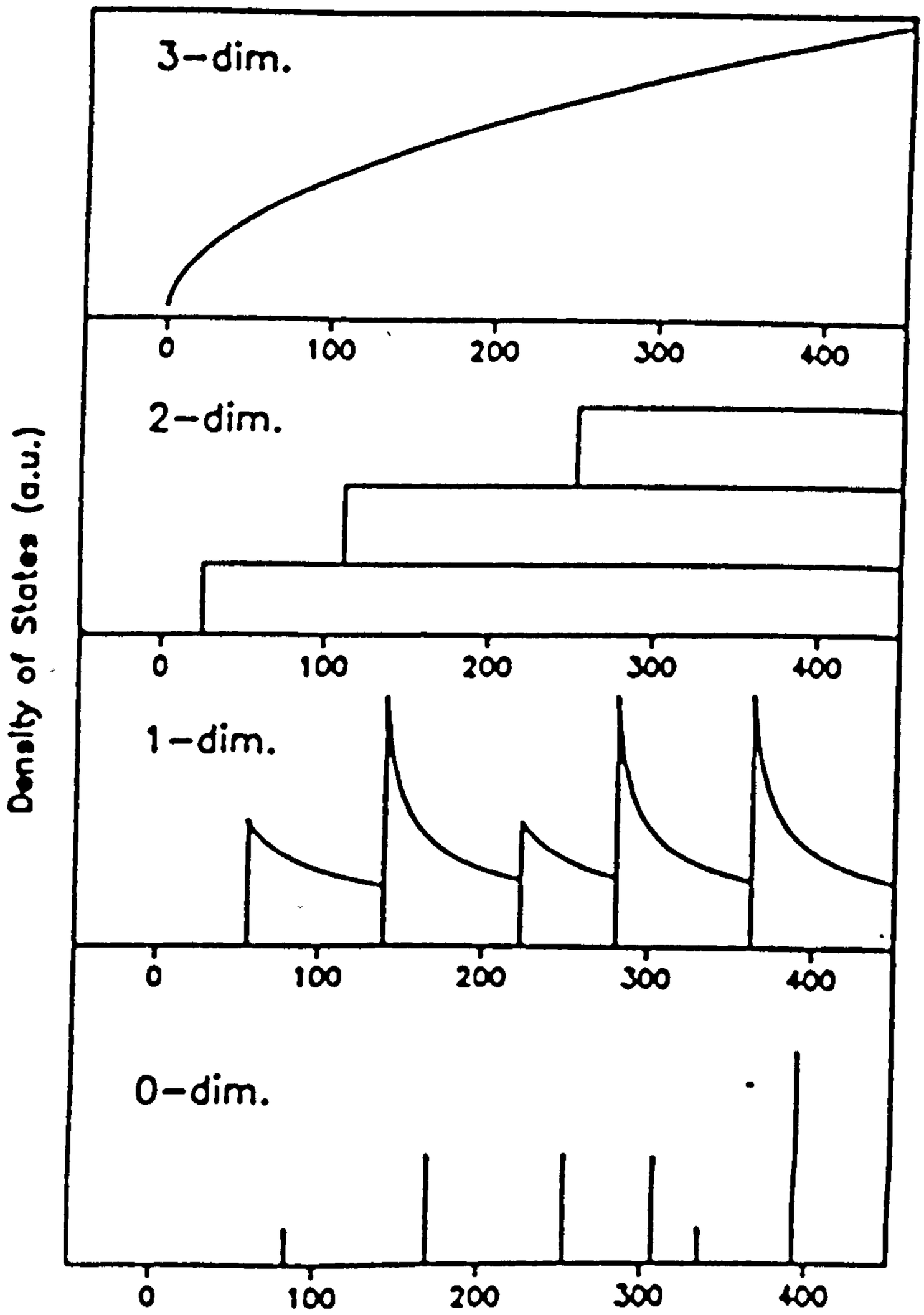

Fig.5-17 Schematic diagram of the energy dependence of the density of states for a three-, two-, one- and zero-dimensional structure (after A.Forchel 1988)

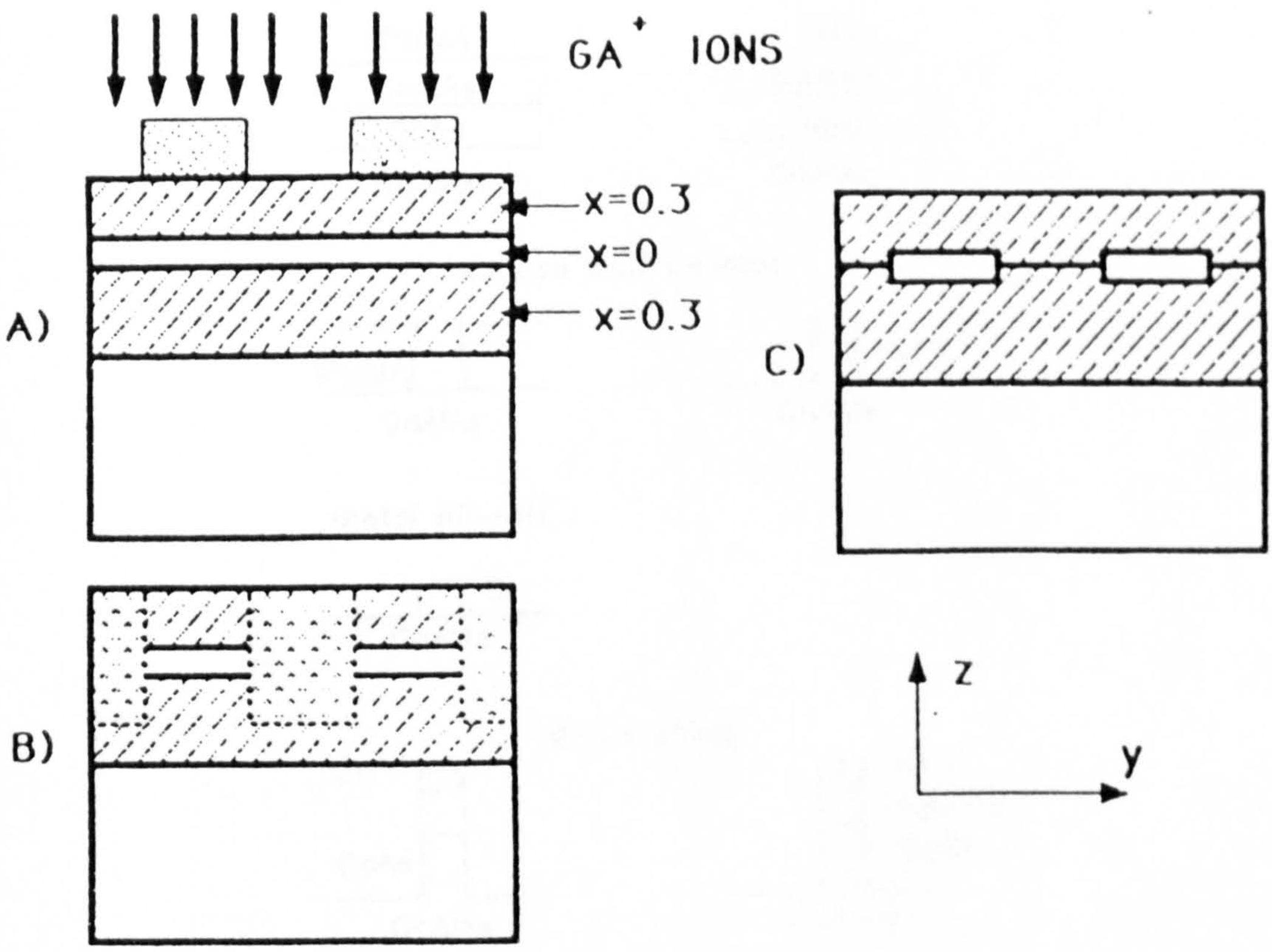

Fig.5-18 Schematic diagram showing the processing of buried quantum dots by ion-implantation-induced interdiffusion. Dotted areas in (A) indicate the metal masks. A rapid thermal annealing treatment is applied in (C) (after P.M.Petroff 1987).

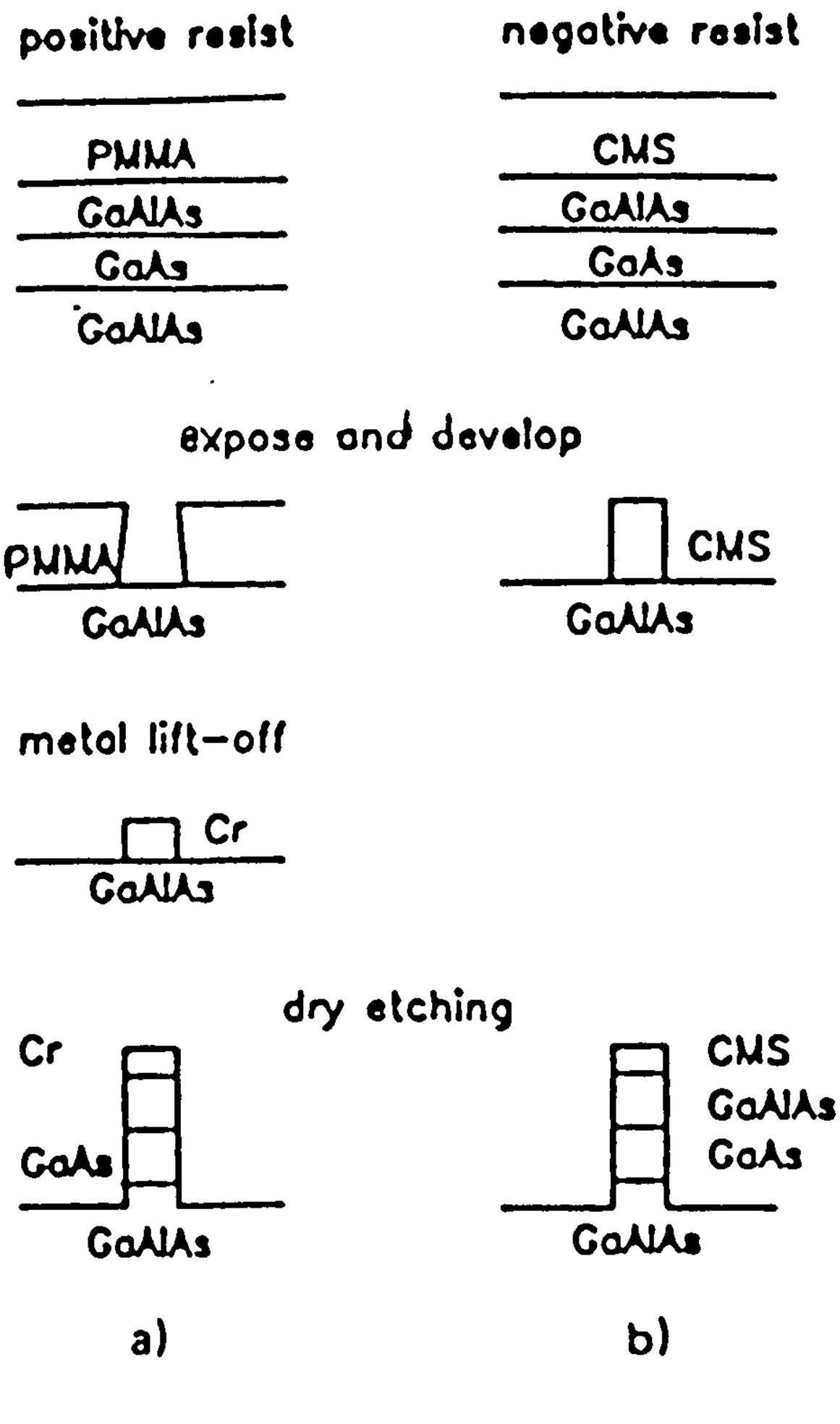

Fig.5-19 Process sequence for free-standing quantum dots formation. (a) A positive resists; (b) a negative resists (after A.Forchel 1988).

MISSING

PRINT

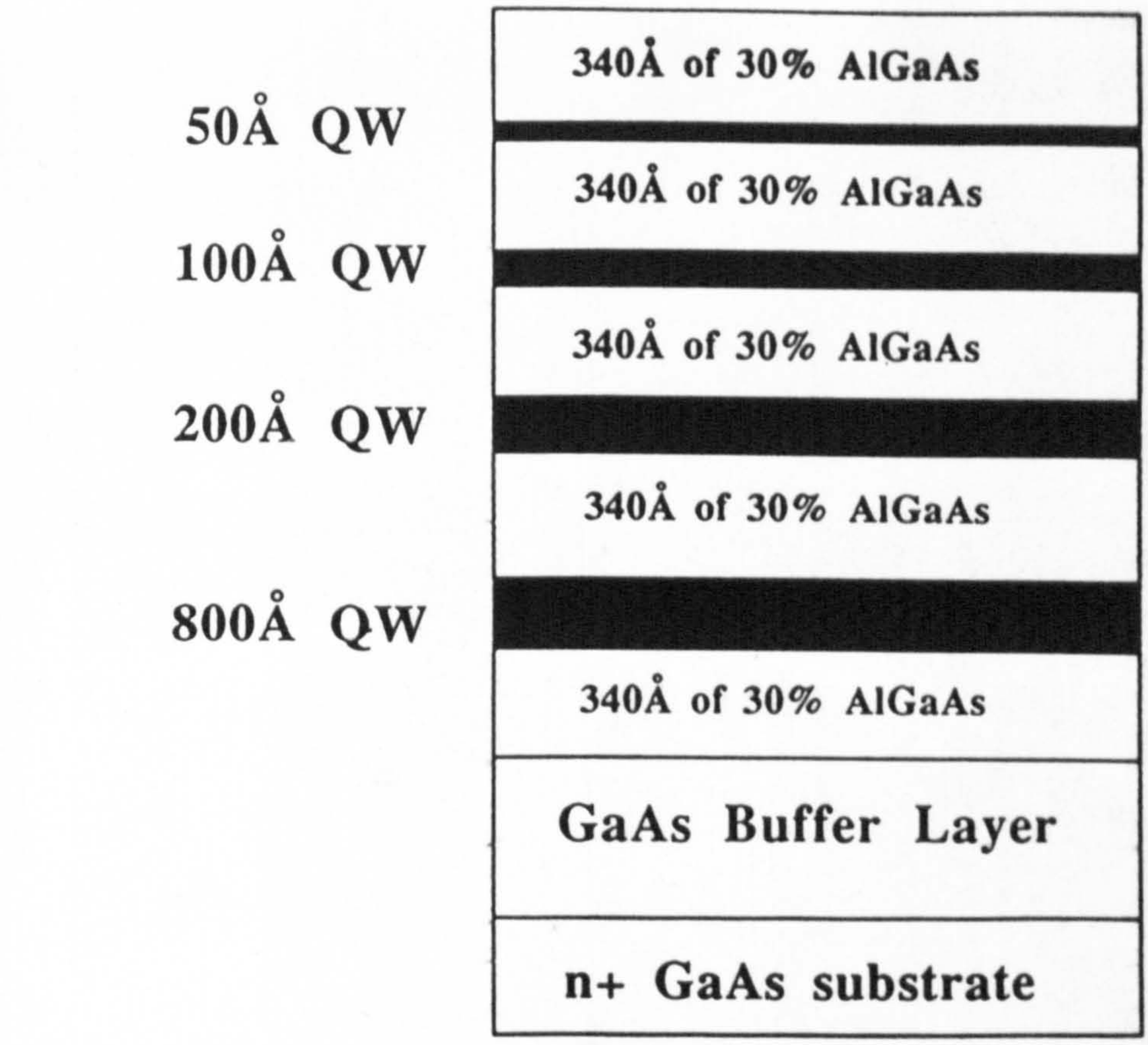

Fig.5-20 Schematic diagram showing the detailed structure of th QW sample DB36 from which the quantum dots were formed.

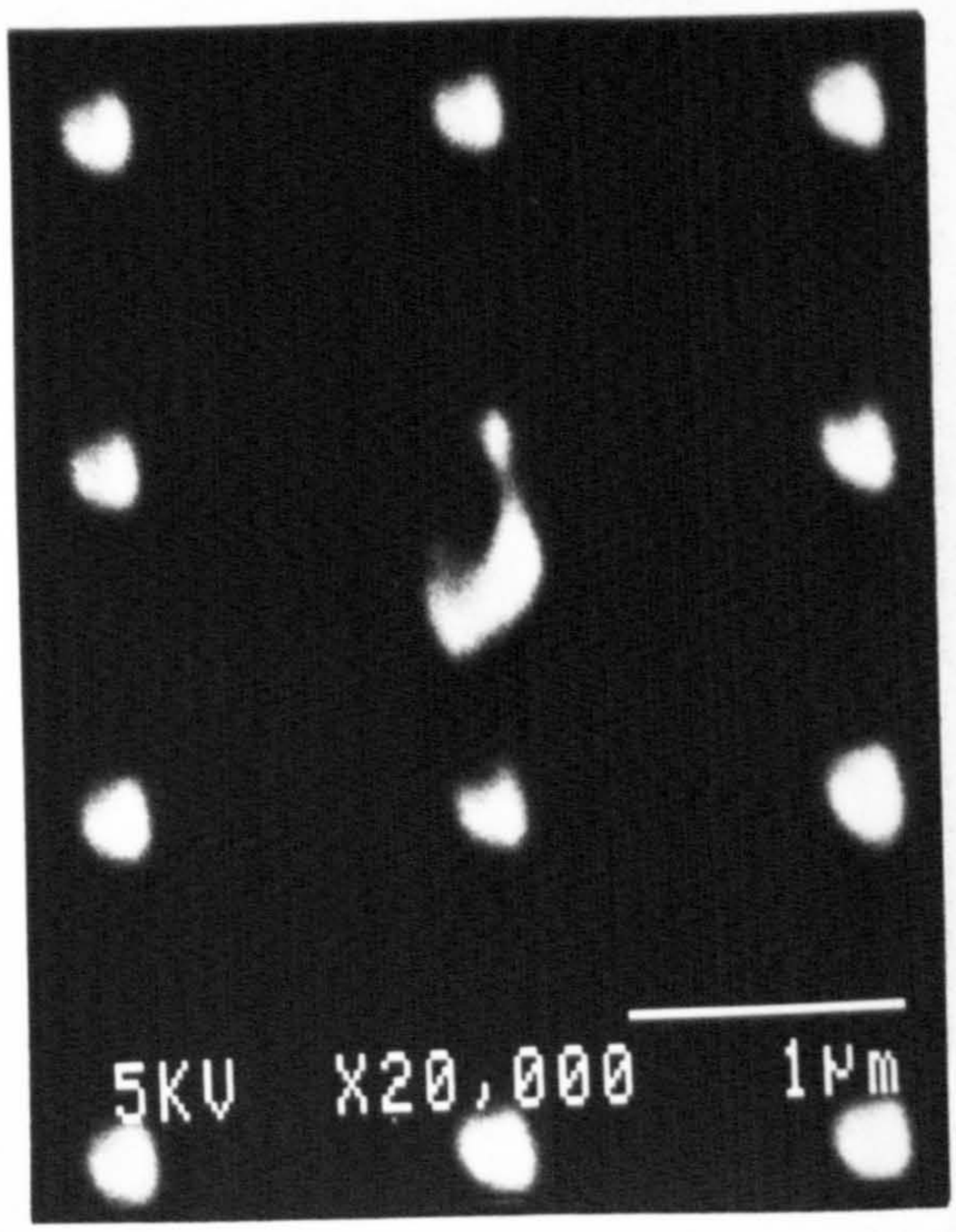

Fig.5-21 SEM image from a 300nm dot array showing a patterning defect.

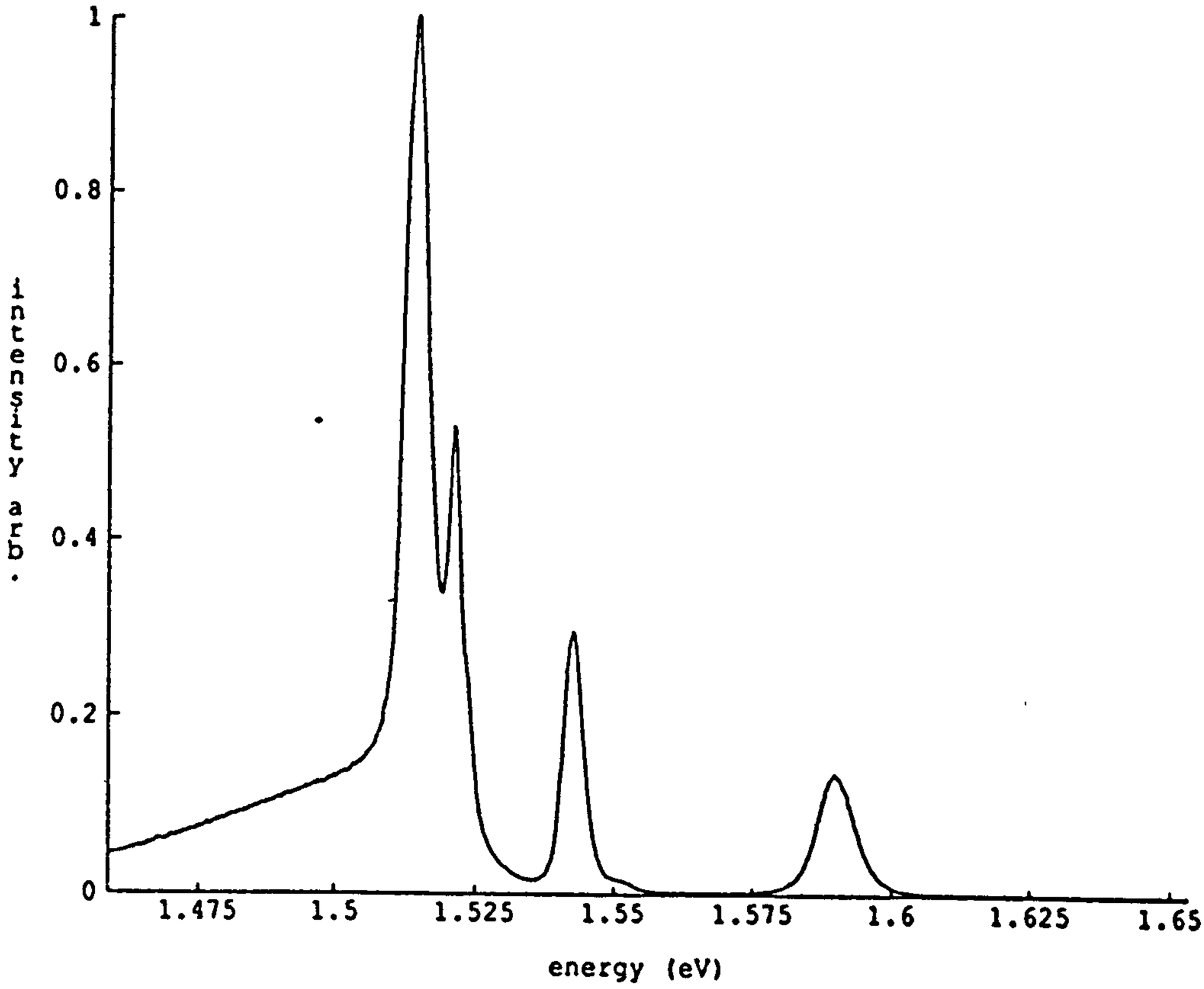

Fig.5-22 CL spectrum from a unetched area representing the QW emission.

Fig.5-23 CL spectrum from a etched area.

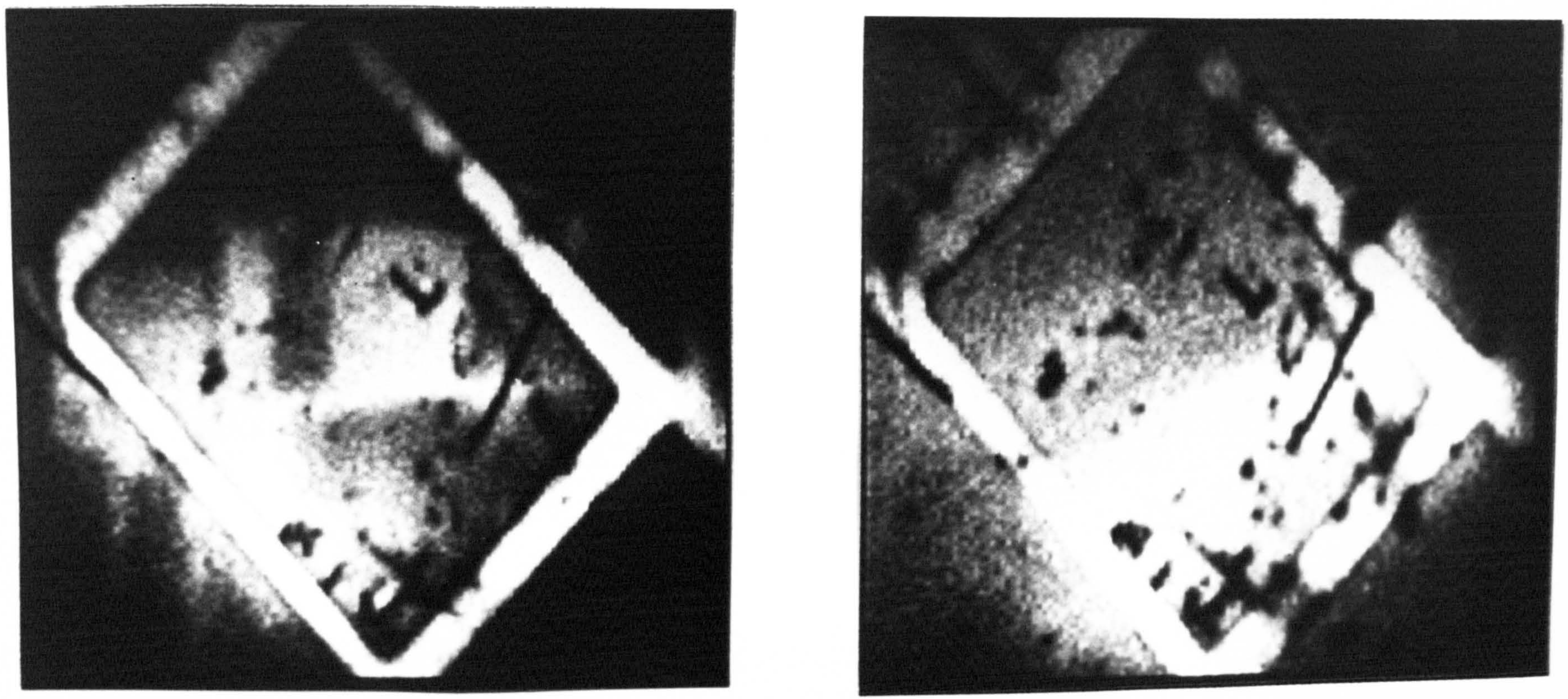

(a) 1.521eV

10 um

(b) 1.514eV

Fig.5-24 Monochromatic CL image choosing at (a) 200A well emission (1.521eV) and (b) 800A well emission (1.514eV) showing a region containing unetched (rectangular shaped frame) and etched areas.

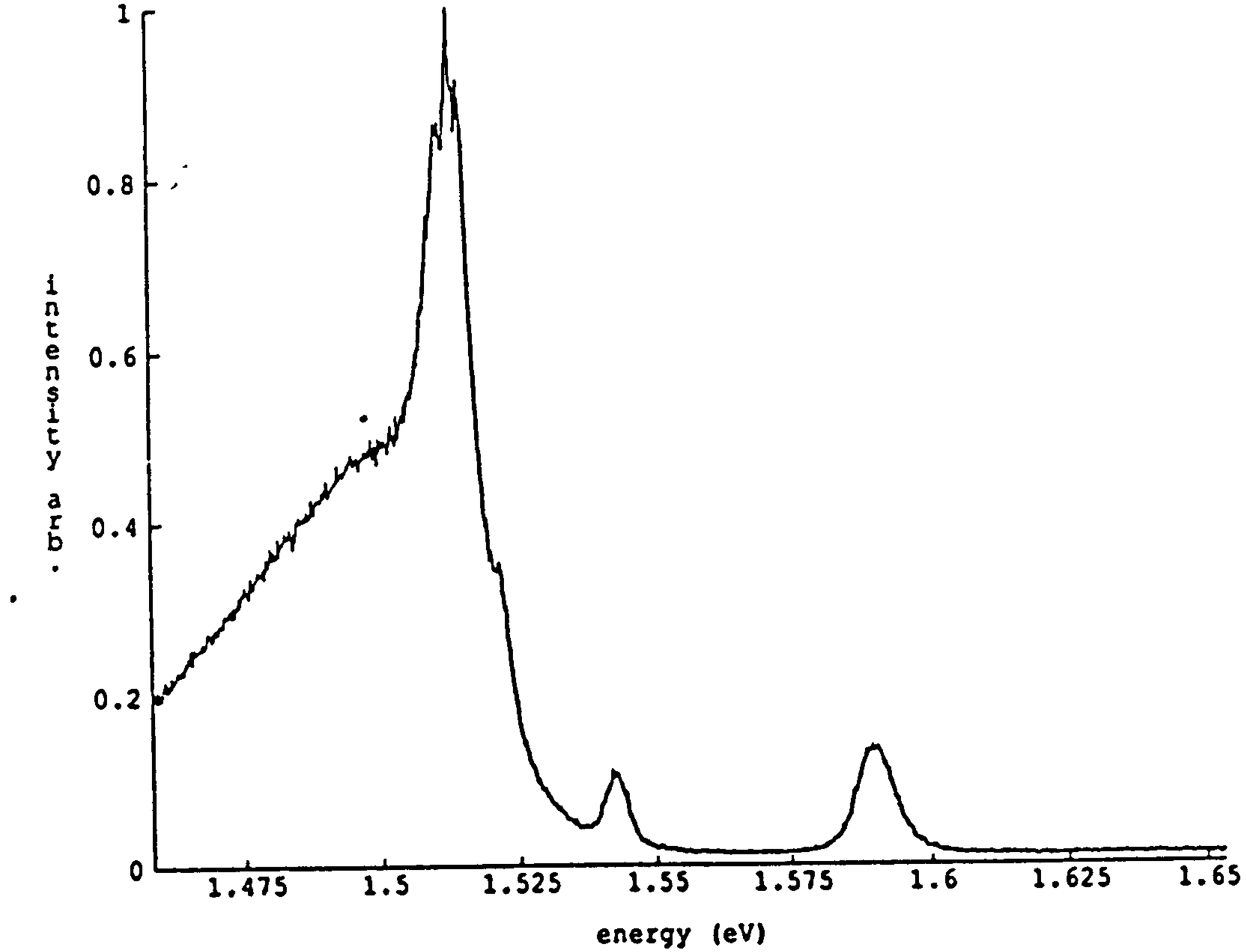

Fig.5-25 CL spectrum from an individual quantum dot with diameter of 500nm.

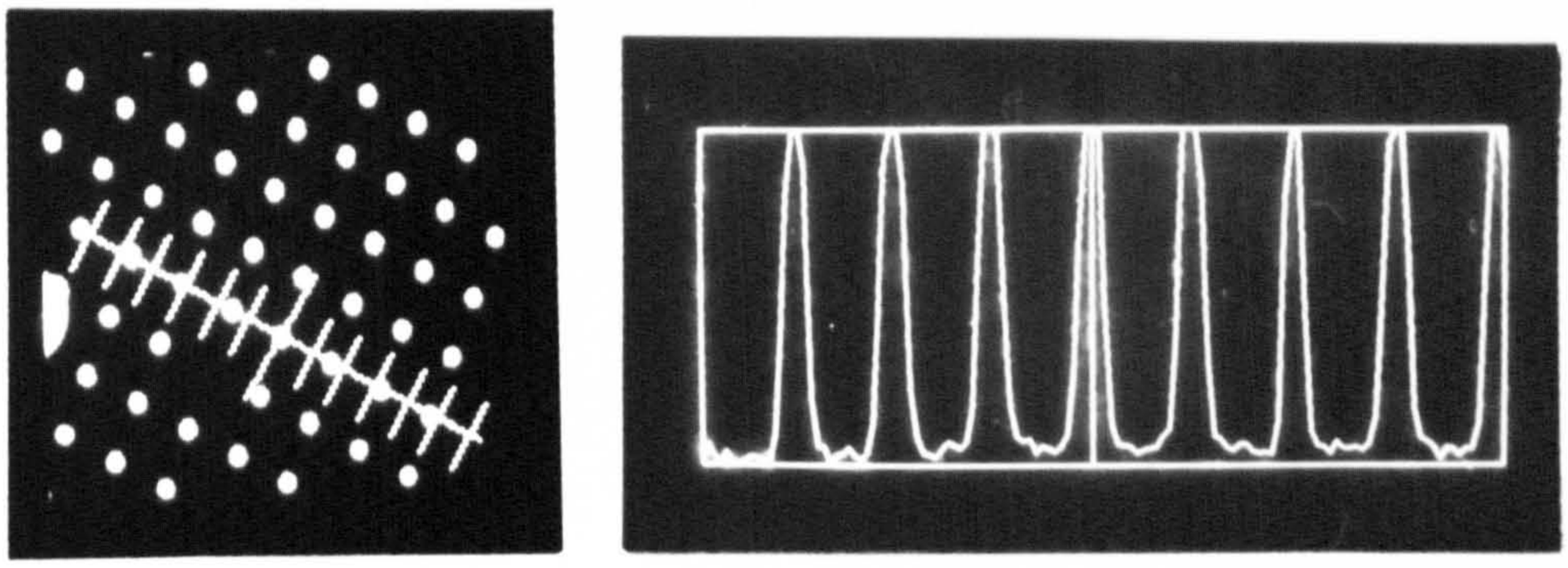

(a) 1.591eV

10um

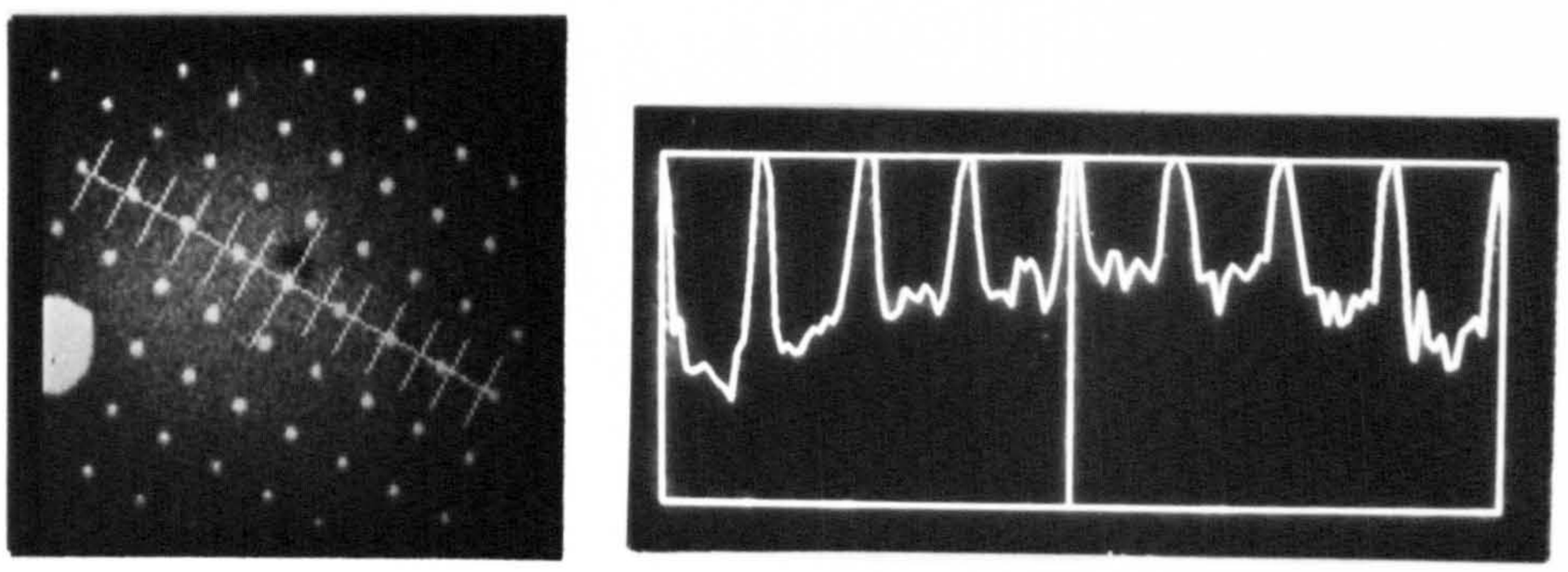

(b) 1.543eV

Fig.5-26 Monochromatic image and line scan profile acquired at (a) 1.591eV, the emission of a dot formed by 50A well and 1.543eV, the emission of a dot formed by 100A well. The marks in the images indicate the dot array where the line scan profile were taken.

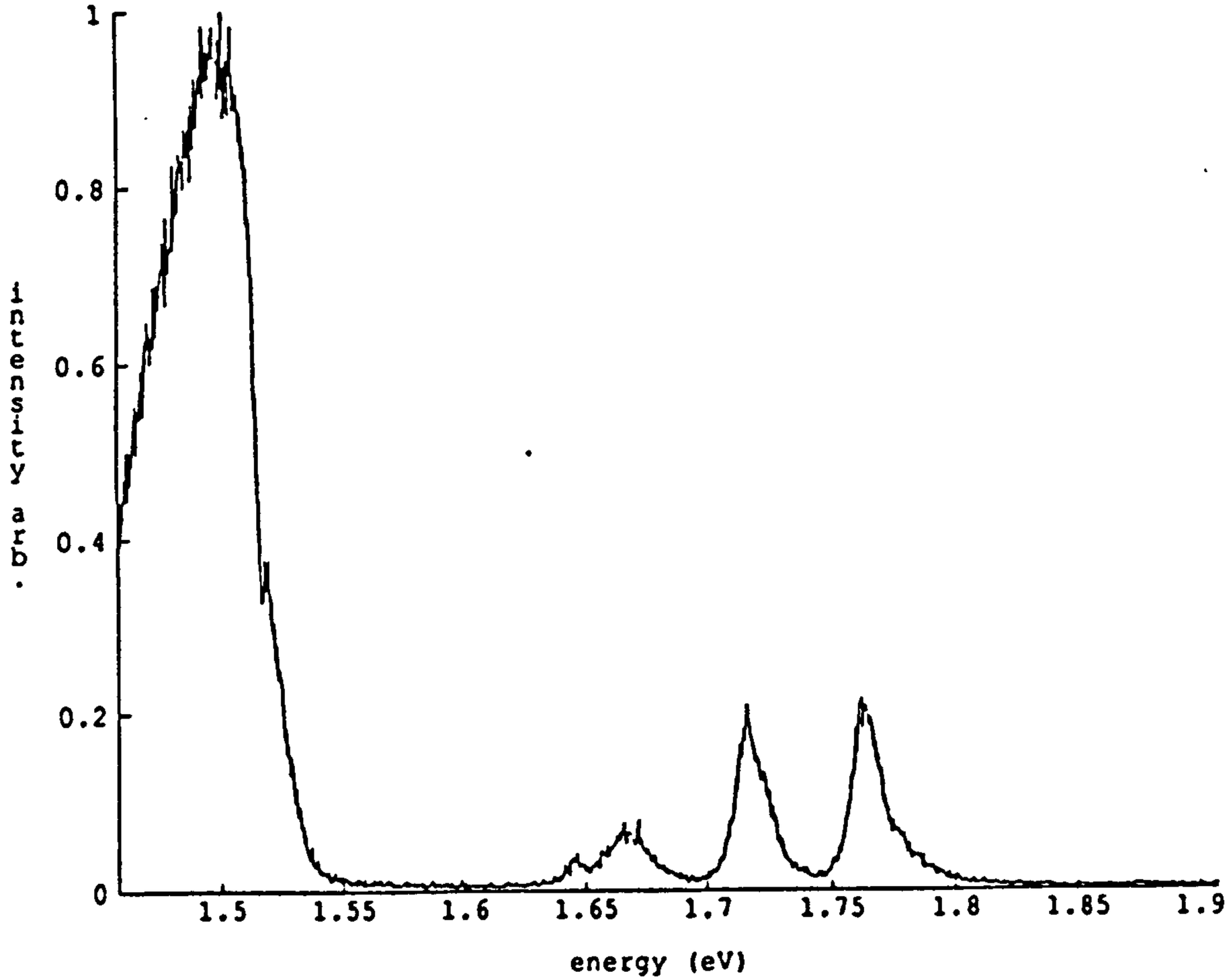

Fig.5-27 CL spectrum from an irregularly scattered bright spot.

Chapter 6 Conclusions and Suggestions for Further Work

Major results described in Chapter 3, 4 and 5 are summarized in this chapter.

LACBED patterns were taken from the plan view specimens of the GaAs/AlGaAs and InGaAs/InP multiple quantum well structures. A series of sidebands were observed resulting from a periodic compositional modulation in the structures and were explained qualitatively by a kinematic theory. In dark field images formed by multilayer structure reflections a linear contrast along one [110] direction was observed from the plan view specimen of a GaAs/AlGaAs MQW structure. This contrast was related to the quantum well thickness fluctuations. These preliminary results showed that the applications of LACBED and imaging from multilayer structure reflections to the plan view specimens of the multilayer structures were of considerable potential interest as a way to complement information obtained by X-ray diffraction and cross sectional TEM.

LACBED was first applied to the [001] and [011] orientation cross-section specimens of an InGaAs/InP single quantum well structure. Lattice distortion due to misfit strain was readily observed. Based on a tetragonal distortion model, the value and the type of the misfit strain in the InGaAs layer was estimated. In this experiment, a compression misfit strain as small as

9×10^{-3} could be detected. A diffraction contrast analysis of the interface fringes observed from the inclined interfaces of the structure also led to a similar result.

TEM-CL spectra and images were first obtained from the thin cross-section specimens of a GaAs/AlGaAs MQW structure. The experimental results revealed an uneven distribution of impurities in the structure. High impurity emission intensity for QW1 was largely due to epoxy which was applied to the sample surface in the specimen preparation process, as well as some native lack of quality of QW1, which might result from its having been grown after a thick AlGaAs layer.

The carrier capture by the quantum wells from their barriers was indicated by the increase of the luminescence efficiency with increase of barrier thickness from the study of the GaAs/AlGaAs double QW structures with constant well width and different barrier thickness. On the other hand, the study of a single QW structure with different well widths and constant barrier thickness revealed the enhancement of luminescence efficiency with decreasing well width due to the carrier confinement effect.

The influence was investigated of growth interruption on interface smoothness of MBE grown GaAs/AlGaAs SQW structures. Split CL emission peaks were observed for the sample grown with interruption but not for the sample grown without interruption. This split was a result of enlargement of the interface terrace width due to growth interruption, to dimensions larger than the exciton diameters. The improvement of the interface smoothness due to growth interruption was also evident in temperature dependent PL experiments, in which a decrease of the blue shift (Stokes shift) was observed relative to that in the sample grown with interruption. A great effect of

growth interruption on AlGaAs-GaAs interface smoothness was deduced by comparing the CL spectra of the sample grown with interruption at the AlGaAs-GaAs interfaces and that interrupted at the GaAs-AlGaAs interfaces. High resolution TEM-CL images were obtained from the SQWs grown with interruptions and showed local bright and dark contrast resulting from monolayer changes in the well widths. An interface terrace size of about 1μm was estimated from these images. The thermalization of carriers from thicker regions of a well to the narrower regions was demonstrated in a temperature dependent PL experiment. A increase of blue shift with decreasing well width was also observed.

The distribution of impurities around a particular type of oval defect was studied by TEM-CL in a GaAs/AlGaAs SQW sample. An uneven distribution of impurities along the growth direction was discovered. A considerable accumulation of impurities was found at the first grown quantum well around the core of the defect. The lateral distribution of impurities was much wider for interface impurity than for well centre impurity. This suggested that interfaces were possible channels for impurity diffusion.

The studies of free-standing quantum dots, fabricated by reactive ion etching, revealed that severe surface damage occurred at the side wall surfaces. This resulted in a total loss of luminescence from quantum dots with diameters less than 300nm and represented a major obstacle to the observation of new phenomena induced by decreasing the dimensions of the structures. But the CL spectra and images from a 500nm dot array were obtained and indicated that STEM-CL was very useful for studying the performance of individual dots. A weaker side wall surface effect was also observed for the narrower quantum wells in the dots due to the carrier confinement effect.

Suggestions for Further Research

This project has proved that transmission electron microscopy, cathodoluminescence spectroscopy and imaging techniques are very useful in observation of microstructure and microstructure related optical properties of materials.

However, the major shortcoming of this work is the lack of detailed theoretical work which will lead to quantitative information about the materials which have been characterized. Dynamical electron diffraction theory is needed for more accurate explanation of the LACBED patterns from multilayer structures. A suitable sample is necessary to correlate the linear contrast observed in DF images using multilayer structure reflections with TEM-CL images so that definite conclusions can be deduced.

Surface relaxation should be included in the estimation of residual strains from LACBED of cross-section specimens containing multilayer structure. Calculation of the image intensity is needed in the diffraction contrast analysis of inclined interfaces for obtaining quantitative information about lattice displacements at the interfaces.

Auger electron spectroscopy, C-V measurements and other surface examination techniques should be used to understand more about surface related degradation of a GaAs/AlGaAs MQW sample.

References

Abe,M.; Mimura,T.; Nishiuchi,K.; Shibatomi,A.; Kobayashi,M.; Misugi,T. 1987 Semiconductors and semimetals Vol.24 p249

Aplin,P. 1983 unpublished work

Arnot,H.; Andrews,S.R.; Beaumont,S.P. 1988 Proc. Microcircuit Engineering Conf. Vienna Austria

Bailey,S.J. 1987 Ph.D Thesis

Balkanki,M. (editor) 1980 Handbook on Semiconductors Vol.2 Optical and Opto-electronic Properties

Bangert,U.;Charsley,P. 1987 Microsc. Semicon. Mater. Conf., Inst. Phys. Conf. Ser. No.87 p89

Bangert,U.;Charsley,P. 1989 Phil. Mag. A Vol.59 p629

Bartels,W.J.; Hornstra,J.; Lobeek,D.J.W. 1986 Acta. Cryst. Vol.A42 p539

Bastard,G. 1981 Phys. Rev. Vol.B24 p4714

Bastard,G.; Delalande,C.; Guldner,Y.; Voisin,P 1988 Advances in Electronics and Electron Physics Vol.72 p1 (ed. P.W.Harkes)

Besser,R.S.;Helms,C.R. 1988 Appl. Phys. Lett. Vol.52 p1707

Bimberg,D.; Bauer,R.K.; Oertel,D; Mars,D.; Miller,J.N. 1987 J. de Physique Vol.48 pC5-93

Bimberg,D.; Mars,D.; Miller,J.M. 1986 J. Vac. Sci. Technol. Vol.B4 p1014

Brown,L.M. 1981 J. Phys. Vol.F11 p1

Brum,J.A.; Bastard,G. 1986 Phys. Rev. Vol.b33 p1420

Brum,J.A.; Bastard,G. 1987 Superlatt. Microstruct. Vol.3 p51

Cebulla,U.; Bacher,G.; Forchel,A.; Schmitz,D.; Jürgensen,H.; Razeghi,M. 1989 Appl. Phys. Lett. Vol.55 p933

Chang,L.L. 1980 Handbook of Semiconductors Vol.3 p563

Chang,Y.C. 1987 Physica Vol.146B p137

Chew,N.G.; Callis,A.G.; Bass,S.J.; Taylor,L.L.; Skolnick,M.S.; Pitt,A.D. 1987 Microsc. Semicon. Mater. Conf., Inst. Phys. Conf. Ser. No.87 p231

Clausen,E.M.; Jr.; Craighead,H.G.; Worlock,J.M.; Harbison,J.P.; Schiavone,L.M.; Florez,L.; Van der Gaag,B. 1989 Appl. Phys. Lett. Vol.55 p1427

Dapkus,P.D. 1982 Annu. Rev. Materials Science Vol.12 p243

Day,J.C.C. 1988 Ph.D Thesis

Delalande,C.; Meynadier,M.H.; Voos,M. 1985 Phys. Rev. Vol.B31 p2497

Delalande,c. 1987 Physica Vol.146B p112

Demel,T.; Heitmann,D.; Grambow,P.; Ploog,K. 1988 Appl. Phys. Lett. Vol.53 p2176

Deveaud,B.; Shah,J.; Damen,T.C.; Tsang,W.T. 1988 Appl. Phys. Lett. Vol.52 p1886

Dingle,R. 1975 Festkorperprobleme Vol.15 p21

Dupuy,M. 1983 J. De Physique Vol.C4 p277

Eaglesham,D.J.; Hetherington,C.J.D.; Humphreys,C.J. 1987 MRS Symp. Proc. Vol.77 (Interfaces Superlattices and Thin Films) p473

Edington,J.W. Practical Electron Microscopy in Materials Science Vol.1-4

Forchel,A.; Leier,H.; Maile,B.E.; Germann,R. 1988 Festkorperprobleme Vol.28 p

Franzosi,P.; Salviati,G. 1986 J. Cryst. Growth Vol.75 p521

Fukunaga,T.; Kobayashi,K.L.I.; Nakashima,H. 1985 Japanese J. Appl. Phys. Vol.24 pL510

Ge,W.K.; Xu,Z.Y.; Yan,Y.; Zu,Z.J.; Zheng,Z.B.; Sun,D.Z. 1987 J.de Physique Vol.48 pC5-131

Gibert,J.; Petroff,P.M. 1987 Phys. Rev. Vol.B36 p3243

Göbel,E.O.; Jung,H.; Kuhl,J.; Ploog,K. 1983 Phys. Rev. Lett. Vol.51 p1588

Goldstein,J.I.; Costloy,J.L.; Lorimer,G.W.; Read,S.J.B. 1977 Scanning Electron Microscopy 1977 Vol.1 p315

Greene,R.L.; Bajaj,K.K.; Phelps,D.E. 1984 Phys. Rev. B Vol.29 p1807

Greene,R.L.; Bajaj,K.K. 1985 Solid State Comm. Vol.53 p1103

Halliwell,M.A.G.; Lyons,M.H. 1984 J. Cryst. Growth Vol.68 p523

Hayakawa,T.; Takahashi,K.; Yamamoto,S.; Hijikata,T. 1988 Japanese J. Appl. Phys. Vol.27 pL979

Hergert,W.; Pasemann,L. 1984 Phys. Stat. Sol. (a) Vol.85 p641

Hergert,W.; Reck,P.; Pasemann,L.; Schreiber,J. 1987 Phys. Stat. Sol. (a) Vol.101 p611

Hillmer,H. 1988 Appl. Phys. Lett. Vol53 p1937

Hirsch,P.B.; Howie,A.; Nicholson,R.B.; Pashley,D.W.; Whelan,M.J. Electron Microscopy of Thin Crystals

Holt,D.B.; Datta,S. 1980 Scanning Electron Microscopy 1980 vol.1 p259

Jakubowicz,A. 1986 J. Appl. Phys. Vol.59 p2205

Jiang,D.S.; Jung,H.; Ploog,K. 1988 J. Appl. Phys. Vol.64 p1371

Jong,A.F.de; Janssen,K.T.F. 1988 Inst. Phys. Conf. Ser. No.93 Vol.2 (EUREM'88) p153

Joyce,B.A.; Foxon,C.T. 1987 Philips Tech. Rev. Vol.43 p143

Jung,H.; Fischer,A.; Ploog,K. 1984 Appl. Phys. A Vol.33 p97

Kakibayashi,H.; Nagata,F. 1985 J. J. Appl. Phys. Vol.24 pL905

Kakibayashi,H.; Nagata,F. 1986 J. J. Appl. Phys. Vol.25 p1644

Kakibayashi,H.; Nagata,F. 1987 J. J. Appl. Phys. Vol.26 p770

Kash,K.; Scherer,A.; Worlock,J.M.; Craighead,H.G.; Tamargo,M.C. 1986 Appl. Phys. Lett. Vol.49 p1043

Kervarec,J.; Baudet,M.; Caulet,J.; Auvray,P.; Emery,J.Y.; Regreny,A. 1984 J. Appl. Cryst. Vol.17 p196

Koteles,E.S.; Elman,B.S.; Jagannath,C.; Chen,Y.T. 1986 Appl. Phys. Lett. Vol.49 p1465

Leamy,H.J. 1982 J. Appl. Phys. Vol.53 pR51

Linh,N.T. 1987 Semiconductors and semimetals Vol.24 p203

Lohnert,K.; Kubalek,E. 1984 Phys. Stat. Sol. (a) Vol.83 p307

Loretto,M.H. Electron Beam Analysis of Materials

Liu,X.; Petrou,A.; McCombe,B.D.; Ralston,J.; Wicks,G. 1988

Madhukar,A.; Lee,T.C.; Yen,M.Y.; Chen,P.; Kim,J.Y.; Chaisas,S.V.; Newman,P.G. 1985 Appl. Phys. Lett. Vol.49 p1148

Masselink,W.T.; Sun,Y.L.; Fischer,R.; Drummond,T.J.; Chang,Y.C.; Klein,M.V.; Morkoc,H. 1984 J. Vac. Sci. Technol. Vol.B2 p117

Meynadier,M.H.; Brum,J.A.; Delalande,C.; Voos,M.; Alexandre,F. 1985 J. Appl. Phys. Vol.58 p4307

Miller,R.C.; Gossard,A.C.; Tsang,W.T.; Munteanu,O. 1982(a) Phys. Rev. Vol.B25 p3871

Miller,R.C.; Tsang,W.T.; Munteanu,O. 1982(b) Appl. Phys. Lett. Vol41 p374

Miller,R.C. 1984 J. Appl. Phys. Vol.56 p1136

Miller,R.C.; Dupuis,R.D.; Petroff,P.M. 1984 Appl. Phys. Lett. Vol.44 p508

Miller,R.C.; Tu,C.W.; Sputz,S.K.; Kopf,R.F 1986 Appl. Phys. Lett. Vol.49 p1245

Myhajlenko,S.; Batstone,J.L.; Hutchinson,H.T.; Steeds,J.W. 1984 J.Phys. Part-C Vol.17 p6477

Neave,J.H.; Joyce,B.A.; Dobson,P.J.; Norton,N. 1983 Appl. Phys. Vol.A31 p1

Oliveira,L.E. 1988 Physical Rev. B Vol.38 p10641

Oliveira,L.E. 1989 Superlattices and Microstructures Vol.5 p23

Opdorp,C.Van 1977 Philips Res. Repts. Vol.32 p192

Ourmazd,A.; Tsang,W.T.; Rentschler,J.A.; Taylor,D.W. 1987 Appl. Phys. Lett. Vol.50 p1417

Pankove,J.I. 1971 Optical Processes in Semiconductors

Pennycook,S.J. 1981 Ultramicroscopy Vol.7 p99

Pettroff,P.M.; Miller,R.C.; Gossard,A.C.; Wiegmann,W. 1984 Appl. Phys. Lett. Vol.44 p217

Pettroff,P.M. 1987 Inst. Phys. Conf. Ser. No.87 p187

Ploog,K. 1982 Annu. Rev. Materials Science Vol.12 p123

Ploog,K.; Dohler,G.H. 1983 Advances in Physics Vol.32 p289

Polland,H.J.; Horikoshi,Y.; Höger,R.; Göbel,E.O.; Kuhl,J.; Ploog,K. 1985(a) Physica Vol.B134 p412

Polland,H.J.; Schultheis,L.; Kuhl,J.; Göbel,E.O.; Tu,C.W. 1985(b) Phys. Rev. Lett. Vol.55 p2610

Polland,H.J.; Leo,K.; Dother,K.; Ploog,K.; Feldmann,J.; Peter,G.; Göbel,E.O.; Fujiwara,K.; Nakayama,T.; Ohta,Y. 1988 Phys. Rev. Vol.B38 p7635

Pond,R.C. 1984 J. Microscopy Vol.135 Part 3 p213

Razeghi,M. 1985 Semiconductors and Semimetals Vol.22 Part-A p299

Roberts,S. 1981 Inst. Phys. Conf. Ser. Vol.60 p377

Sakaki,H.; Tanaka,M.; Yoshino,J. 1985 Japanese J. Appl. Phys. Vol.24 pL417

Sandroff,C.J.;Nottenburg,R.N.;Bischoff,J.C.;Bhat,R. 1987 Appl. Phys. Lett. Vol.51 p33 1987

Schiller,C.; Boulou,M. 1975 Philips Tech. Rev. Vol.35 p239

Scott,G.B.; Roberts,J.S. 1978 GaAs and Related Compounds 1978 p181

Shanabrook,B.V. 1987 Physica Vol.146B p121

Singh,J.; Bajaj,K.K. 1985 J. Appl. Phys. Vol.57 p5433

Singh,J.; Bajaj,K.K.; Chaudhuri,S. 1984 Appl. Phys. Lett. Vol.44 p805

Smith,S.H. 1978 Semiconductors

Sollner,T.C.L.G.; Goodhue,W.D.; Tannenwald,P.E.; Parker,C.D.; Peck,D.D. 1983 Appl. Phys. Lett. Vol.43 p588

Spindt,C.J.; Besser,R.S.; Cao,R.; Miyano,K.; Helms,C.R.; Spicer,W.E. 1989 Appl. Phys. Lett. Vol.54 p1148

Spivak,G.V.; Petriv,V.I.; Antoshin,M.K. 1986 Sov. Phys. Usp. Vol.29 p364

Stobbs,W.M.; Baxter,C.S. 1988 EUREM'88, Inst. Phys. Conf. Ser. No.93 Vol.2 p83

Sze,S.M. 1981 Physics of semiconductor devices

Tanaka,M.; Saito,R.; Ueno,K.; Harada,Y. 1980 J.Electron Microscopy Vol.29 p408

Tanaka,M; Sakaki,H. 1988 Superlattices and Microstructures Vol.4 p237

Thomas,G.; Goringe,M.J. Transmission Electron Microscopy of Materials

Tsang,W.T. 1985 Semiconductors and Semimetals Vol.22 Part-A p1

Tsang,W.T. 1987 Semiconductors and semimetals Vol.24 p397

Vincent,R.; Cherns,D.; Bailey,S.J.; Morkoc,H. 1987 Phil. Mag. Lett. Vol.56 p1

Vincent,R.; Wang,J.N.; Cherns,D.; Bailey,S.J.; Preston,A.R.; Steeds,J.W. 1987 EMAG'87, Inst. Phys. Conf. Ser. No.90 p233

Weisbuch,C.; Miller,R.C.; Dingle,R.; Gossard,A.C.; Wiegmann,W. 1981 Solid State Comm. Vol.37 p219

Weisbuch,C. 1987 Semiconductors and Semimetals Vol.24 p1 (Volume ed. by R.Dingle)

Wilson,B.A.; Moller,R.C.; Sputz,S.K.; Harris,T.D.; Sauer,R.; Lamont,M.G.; Tu,C.W.; Kopf,R.F. 1986 Inst. Phys. Conf. Ser. No.89 p215

Wu,W.Y.; Schulman,J.N.; Hsu,T.Y.; Efron,U. 1987 Appl. Phys. Lett. Vol.51 p710

Yacobi,B.G.; Holt,D.B. 1986 J. Appl. Phys. Vol.59 pR1

Yuan,J.; Berger,S.D.; Brown,L.M. 1989 J.Phys. Condens. Matter Vol.1 p3253